ABSTRACT

Title of dissertation: HOLLOW BESSEL TUNNEL GUIDE: THEORY AND EXPERIMENT

Narupon Chattrapiban
Doctor of Philosophy, 2012

Dissertation directed by: Professor Wendell T. Hill, III
Department of Physics

The main objectives of this thesis were to create and investigate properties and applications of all-optical atomic guides, which are potential building blocks for atom optics experiments. Specifically, we investigated experimentally and theoretically the evolution of the transverse and longitudinal atomic distributions in blue-detuned Bessel tunnels. These tunnels provide confining potentials that are comparable to or higher than the average kinetic energy of cold (hundreds of microKelvin) ensembles. The new work highlighted in this thesis include investigations of the following: 1) the generation of Bessel beams using a 2D spatial light modulator (SLM) (both experimental measurement and numerical simulations were performed), 2) the efficiency of the SLM for converting light from a Gaussian beam to a Bessel beam, 3) the behavior of several propagating structures that might be useful for guiding atoms, 4) the atom-tunnel dynamics, 5) an atom switch and delay line (along with measurements of the switch efficiency), and 6) the single-mode propagation in an idealized tunnel. To the best of our knowledge, the work in this thesis constitutes the first time that (1) an atom switch and a delay line have been demonstrated using blue detuned tunnels and (2) the atom-tunnel dynamics and the phase-space distribution of a non-interacting dilute gas in a non-equilibrium state has been tracked experimentally.

HOLLOW BESSEL TUNNEL GUIDE: THEORY AND EXPERIMENT

by

Narupon Chattrapiban

Dissertation submitted to the Faculty of the Graduate School of the
University of Maryland, College Park in partial fulfillment
of the requirements for the degree of
Doctor of Philosophy
2012

Advisory Committee:
Professor Wendell T. Hill, III, Chair/Adviser
Professor Rajarshi Roy
Professor Gretchen Campbell
Professor Michael A. Coplan
Professor Julius Goldhar

Acknowledgments

I am grateful to my mom, my dad and my older brother to continuely support me with their love.

I would like to sincerely thank my advisor, Prof. Wendell T. Hill, III, for his supports, advises and teachings, and for giving me an opportunity to work in his lab. He had been extremely patient with me through out the years of my graduate studies. Without him this work would not be possible. I would like to thank my colleague and friend, Ilya Arakelyan, for his collaborations and invaluable advises. I learned from him a great deal of necessary skills and knowledge I needed to know in the lab.

I truly appriciate the friendship I had with Balmeeki Bandyopadhyay, Hailu Bantu, Guan-Yu Chen, Yung-Fu Chen, Lee Elberson, Jang Hyoung-uk, Min-Young Kim, Sandip Mitra, Sheung Wah Ng, Hanhee Paik, Kun Zhao and Junjie Zhu. They made my life enjoyable while studing at the university of Maryland.

I am greatly thankful to receive helps from David Cofield, Edward J. Cole, Ryan Van Fleet, Arseni Goussev, Jeff Heward, Phillip Land, Jeff Lee, Elizabeth A. Rogers, Dr.Ming H. Wu (Hamamatsu), Prof. M. Anisimov, Prof. Charles Clark, Prof. J. R. Dorfman, Prof. Mark Edwards, and Prof. Rajarshi Roy.

My special thanks also go to: (1) our alumnus, Dr. Yonho Song, for the invaluable notes he left behind, (2) faculties and staffs from the department of physics, IPST and OIS, especially Barbara Ferguson, Nancy L. Gong, Jane Hessing, Linda O'Hara, Debbie Pruett, and Pauline Rirksopa, for their help with all the paper works, (3) all the funding agencies including ARO (grant No. ARO-DAAD190110695), NSF (grant No. PHY0426696), NIST (grant No. PHY0099489), NSF/DARPA (Photonics Technology Access Program grant for the SLM), Laboratory for Physical Sciences, and DPST Thailand, (4) all the authors in the reference section, and (5) the creators and communities of many softwares, which help producing this thesis and all the work in it, including Adobe reader, Blender, C/C++, GIMP, GSView, Ghostscript, Inkscape, Mathematica, Matlab, Microsoft Office, Microsoft windows, MiKTeX, OpenOffice, Scribus, and TeXnicCenter.

Table of Contents

List of Tables

List of Figures

List of Abbreviations

$\hbar$	Reduced Plank constant
Γ	Natural line width (FWHM), Decay rate
γ	Reduced natural line width ($= \Gamma/2\pi$)
τ	Lifetime ($1/\Gamma$)
Δ	Detuning
δ	Reduced detuning ($= \Delta/2\pi$)
η	Index of refraction
Λ	Grating's spacing
Δt	Time increment
Φ	Spatial phase profile
Ψ	Wave function
ω	Angular frequency
ω_0	Gaussian beam waist
λ	Wavelength
ζ	Distribution function
I	Intensity
I_s	Saturation intensity
J_n	Bessel function of the first kind of order n
n	an integer, a vortex's charge
k	Wave number
k_B	Boltzmann constant
R	Photon absorption rate
t	Time
t_H	Hold time
T	Temperature
Q	Scalar field
U	Potential energy
E	Total energy

2D	Two Dimension
3D	Three Dimension
AOM	Acousto-Optic Modulator
Ar	Argon
BEC	Bose-Einstein Condensate
BNC	Bayonet NeillConcelman
CCD	Charge-Coupled Device
DDG	Digital delay/pulse generator
LE	Liouville Equation
MC	Monte-Carlo Calculation
MOT	Magneto Optical Trap
Nd:YAG	Neodymium-doped Yttrium Aluminium Garnet
Nd:YVO_4	Neodymium-doped Yttrium Orthovanadate
PZT	Piezoelectric transducer
Rb	Rubidium

SAS	Saturated Absorption Spectroscopy
SF	Shape factor
SLM	Spatial Light Modulator
SQUID	Superconducting Quantum Interference Device
Ti:Saph	Titanium-Sapphire
TOF	Time of flight
TTL	Transistor-transistor logic
UHV	Ultra-high vacuum
VGA	Video Graphics Array

Chapter 1

Introduction

A magneto-optical trap (MOT) [1] was developed in the past decades to study cold dilute gases using laser cooling techniques [2, 3]. The temperature of trapped gas can very well be within millikelvin regeme [4, 5, 6]. Recently techniques had been developed such that it might be possible to cool most of the atoms in the periodic table to within or below milikelvin temperature [7, 8, 9, 10].

An inexpensive laser source with $\sim$ 100 mW of power can be used to trap or manipulate such a cold atomic ensemble. A research related to an optical neutral atom circuit [11, 12] might one day become commonly accessible. Examples of proposed basic atom circuits, in analogy to their electronics counterparts, are: atomtronic batteries [11], atomtronic diodes [13, 11, 14], atomtronic conductors [11, 15], atomtronic transisters [11, 16] and atom-based SQUIDs [17, 18, 19, 20].

With even colder temperature within sub-milliKelvin regime and a much higher phase-space density of the order of 10^{12} cm^{-3}, the cold gaseous ensemble condenses to a Bose-Einstein condensate (BEC) [21]. Exploiting coherency of the BEC, the atom circuit can turn to an interference based device, e.g. an atom interferometer [22, 23, 17, 24, 25, 26, 19], with high fringe visibility. A common structure present in all atom circuits is a network of channels that connect or transport atoms between different sites. Achieving durable and flexible control in the network requires robust elements (1) to move ensembles along arbitrary paths and (2) to divide, delay, recombine and reshape ensembles at any location along the path, in the absence of decoherence. A number of different techniques for switching and dividing neutral atom clouds have been proposed and demonstrated over the past several years. Exploiting atomic magnetic moments, for example, guides and switches have been produced

with magnetic potentials from current carrying wires [27, 28, 29, 30, 31]; circuits have been fabricated on surfaces (atom chips) [32, 33]. More recently, chip-based interferometers have been demonstrated where Bose-Einstein condensates have been split with an optical grating (via diffraction) [26] and double-welled magnetic potentials [24]. Light-based techniques have been used as well to divide clouds of atoms in free-space [34, 35]. Free-space elements have attractive features not easily realized with contemporary material-based element designs making them potentially versatile compliments to the atom optical element arsenal. Light-based elements [36, 37, 38, 39, 40, 41, 42, 43], for example, do not require atomic magnetic moments. Furthermore, they eliminate the need for material in close proximity to the atoms, which can affect the ensemble adversely [44]. More importantly, they can be formed anywhere in space and modified in real time [45, 46, 47, 48], making them compatible with a variety of cold atom sources.

1.1 Single all-optical tunnel and its comparison to other approaches to guide atomic clouds

A light-based element such as an optical tunnel has been shown to be able to transport atoms successfully in many applications. Due to their flexibility, optical tunnels can be arranged to coexist with a variety of atom traps and guides. For example, atom transfer to optical fibers has been demonstrated for both red- [49, 50] and blue-detuned [51, 52, 53] tunnels. Transferring atoms between two spatially separated traps via both red- [54] and blue-detuned [55] tunnels has also been shown. Among these results, the transport efficiencies for both types of tunnels were measured and reported. The efficiencies was also studied theoretically especially for the case of a blue detuned beam by Xu *et al.* [56, 57, 58]. A robust atom guide from a blue-detuned tunnel, several gigahertz off resonance, can be used to transport atoms for long distances (a few tens of centimeter) with a few photon scatterings per millisecond per atom [36]. Such a guide, a hollow tunnel, with a diameter of 1 mm and a potential height equivalent to 1 mK, for instance, can be achieved using

a laser power below 100 mW. With a similar power as in the blue-detuned case, a red-detuned Gaussian beam, several tens of giga-Hertz off resonance, with a spot of ~ 500 μm and a divergence half-angle of 0.8 mrad was demonstrated to guide atoms for ~ 1 cm [59].

In this thesis, we extended the study of Song *et al.* [36, 60]. What distinguishes Song's and our work from others is that (1) we used a hollow tunnel that maintained its shape and size while propagating, and (2) we studied the dynamics of the atomic ensemble in the tunnel. For the latter, we employed a probe along the tunnel to observe the spatial distribution of the ensemble. This allowed us to monitor a projection of the 3D distribution onto a transverse plane, plane perpendicular to the beam propagation. Thus, our analysis of the ensemble dynamics reduced to a 2D problem.

The fundamental difference between Song's work and ours, however, lies in the energy scales related to our experiments and the type of the tunnel. The potential height of Song's tunnel, as mentioned earlier, was 1 mK whereas ours was ~ 100 μK. The fact that Song's ensemble had a temperature of a few hundred micro Kelvins, similar to ours, his tunnel contained most of the atoms inside the tunnel, while the hot atoms in the tail of the thermal distribution leaked through the tunnel in our case, providing a dramatic change in the velocity distribution.

Based on the conditions of Song's experiments, the averaged photon absorption rate of the atoms can be calculated from the shape of the tunnel itself. Including spontaneous emission in his model, Song found that the calculated heating and the acceleration of his ensemble agreed well with those obtained from his experiments.

For us, we extracted the ensemble's velocity distribution, based on several models, from measured free expansions at three particular times while the ensemble was propagating inside the tunnel. The measurements were similar to the experiment done by Pruvost *et al.* [61] for a red-detuned Gaussian beam where the ensemble was adiabatically cooled from the expansion inside the enlarging optical guide. From the velocity distributions we deduced equivalent equilibrium temperatures. These temperatures were compared with the values obtained from our simulations.

We note that, to the best of our knowledge, although the atom guiding efficiency and the time-of-flight measurement along the tunnel were reported in the past [51, 54, 62, 55, 63], the investigation of the dynamic of the *transverse* velocity distribution of the atoms inside the tunnel was not.

1.2 Overview of the thesis

This thesis is devoted primarily to the classical behavior of thermal clouds in near diffraction-free, blue detuned Bessel tunnels. In this thesis, descriptions of the main theories and experimental procedures related to creating/manipulating ensembles and measuring/modeling dynamics of ensembles guided inside a Bessel hollow beam will be provided. In addition, because light tunnels are compatible with both thermal ensembles and Bose-Einstein condensates (BEC) [64, 46], while at the same time interferometry is possible with thermal atoms [25], all-optical light tunnels appear to be an attractive complement to optical lattices [65, 66] or holographic traps [67] for pursuing fundamental studies of cold atoms. As a consequence, a thorough understanding and quantitative modeling of the evolution of quantum ensembles in light tunnels is essential.

In Chapter 2, optical vortices and their implementations are discussed. The focus is on the generation of Bessel tunnels and the description of their properties. The implementation of the Bessel beam via a spatial light modulator (SLM) is investigated by means of numerical calculations. The SLM is described in detail in Appendix D. The implementation of optical vortices provides ways to embed dark channels in a light beam, creating various exotic patterns. Their applications to atom optics are proposed. The efficiency of the SLM for producing the tunnels and the quality of the tunnels are also measured and discussed in detail.

In Chapter 3, a detailed description of our experimental setup will be provided. Sufficient detail is given so that those who wish to verify or replicate our experiment can do so easily. All the hardware and their manufacturers are given (except for some common optics such as lenses and mirrors). The software that was used to

automate control of the experiments is also briefly described. The source codes for the software are provided in Appendix G.

In Chapter 4, experimental procedures for obtaining the dynamics of the atom distribution in a single tunnel is provided and discussed. Several velocity-distribution models are proposed and procedures used to relate these distributions to the experimental data are provided. Results from two numerical simulations were compared to the experimentally measured value to get a better understanding of the data obtained from the experiments.

In Chapter 5, a preliminary test of the tunnel as a building block for an atom network is demonstrated via an "*atom lock*". A few characteristics of the atom lock are discussed.

In Chapter 6, we focus on an atom guide with restrictd dimension, where quantum effects are strong. Quantum calculations for *single-* and *multi-mode* propagation of a single atom inside Bessel tunnels in analogous to a single- and multi-mode optical fiber are reported and discussed.

In Chapter 7, the summary of the thesis and future plans are provided.

Lastly, detailed discussions, calculations and important computer codes related to the text in the main thesis will be provided in the appendices.

Chapter 2

Light Modulation and Efficiency of SLM

As mentioned in Chapter 1, an atom network requires flexibility to maneuver atoms in a way analogous to controlling electrons through wires in an electronical circuit. Utilizing atom-photon interactions, networks can be realized by manipulating the light field to form a complex structure in free space. There are several ways to manipulate the field. One way is to change the mode structure of coherent light by changing geometries of optical elements inside a laser cavity [68, 69, 70, 71]. The drawback of this method is that the alignment of optical elements inside the laser cavity requires delicate adjustments and thus are not flexible to use. Another way to manipulate light fields is to alter the amplitude or phase of the coherent field directly outside the laser cavity using an optical element or a combination of optical elements such as lenses, gratings or phase plates. A very simple example is a double slit experiment. Other examples are an axicon [36] and hollow-core fibers [72], which can be used to form all-light waveguides. More complex structures can be achieved through a hologram first developed by Gabor [73] and a method based on the phase contrast technique pioneered by Zernike [74, 75].

Gabor originally created a hologram via an interference pattern between the field of his desire and a coherent reference beam. The pattern was recorded on a mask consisted of photo-sensitive material. Upon redirecting the reference beam through the mask after the recording, the desired field can be recreated. In modern day, this task and its variations can be done on a personal computer. The mask that creates desire field can be computed by various techniques such as the Gerchberg-Saxton algorithm [76], the adaptive-additive algorithm [77], and phase selection based on the genetic algorithm [78]. Usually, the desired pattern is created at a plane in

the far field or in the image plane of a converging lens. Thus, the calculation of the mask on a computer can be done straightforwardly by using a 2D Fourier transform. To create a desired field in 3D, e.g., that of split tunnels or curved tunnel, the computation can be laborious. In addition to the above mentioned algorithms, there is a more intuitive and perhaps naive technique for creating masks that generate a small set of patterns we desire. This technique involves embedding vortices in a mask [79, 80, 81, 82] by a process that we will describe in the following sections in this chapter. One advantage of that technique is that a vortex is persistent. For a particular type of beams with embedded vortices, the mask produces a pattern that changes slightly or does not change at all for a long propagation distance. For example, Bessel-modes propagate nearly diffraction-free for tens of meters [83], in contrast to the diffraction properties of Laguerre-Gaussian modes, which also have hollow profiles, making them ideal for creating networks or long, narrow tunnels.

Typically a piece of glass or plastic can be etched to produce a mask that alters the phase or amplitude of the light field. The disadvantage is that this mask is static and requires laborious work to produce. However, recently a device called a *Spatial Light Modulator* (SLM) [1] has became commercially available that can be used to provide arbitrary control the phase or amplitude of the light field in real time. To our advantage, beams with embedded vortices can be generated straightforwardly with the SLM, including hollow waveguides with Bessel modes ($J_{n>0}$) [84, 85]. In brief, we used the SLM as a phase mask to redistribute the input Gaussian intensity profile peaked on axis to a hollow profile with an intensity void due to the formation of *phase dislocations* in laser field.

In the following sections, we begin with the description of optical vortices (point phase dislocations) and line phase dislocations in a laser beam. We especially focus our attention on the creation of Bessel beams, which we will use again in later chapters. Simulations are also provided that will help us explain several peculiar diffraction patterns we observed in the laboratory and characterize propagation of Bessel beams. Later in the chapter, we will present the results of a study of the

[1] The technical details of the SLM are provided in Appendix D.

conversion efficiency from a Gaussian beam to Bessel $J_{n>0}$-modes, with n ranging from 1 to 15. We show that the efficiency for conversion of power into the first ring depends on both the spatial resolution (number of pixels defining the phase features) and the phase quantization level [86] (the number of steps between 0 and 2π) of the mask. The effectiveness of the Bessel mode to hold atoms as a function of vortex parameters was also studied. The key for lossless atom transport is the intensity (i.e. a potential height) of the first Bessel ring. Near the end of this chapter, we show the versatility of the SLM by creating propagating beams containing an assortment of exotic vortices. These could be used in fundamental studies and important applications in atom optics associated with coupling the optical orbital angular momentum of light to an atomic ensemble [87, 88, 41, 89, 90] as well as statistical mechanics and chaos [91]. Finally, we discuss the capture and propagation of cold Rb atoms in several of these exotic vortices.

2.1 Creating Vortices

As mentioned in the beginning of the chapter, the intensity void of the waveguide is due to a vortex established by the phase mask. A vortex, in our context, is a singularity in the phase of the wavefront. A singularity can be created, for example, when the phase around a fixed point in the front changes continuously by $2n\pi$. Thus, the phase at the fixed point is undefined. This condition is called a vortex of *charge* $\pm n$ depending on the sign change of the phase for counterclockwise rotation; the charge is the total phase shift, in units of 2π, around a closed loop and is an integer for a vortex. When embedded in a coherent light beam, the singularity produces an intensity null that we exploit to construct hollow modes along with several other patterns that can be used as optical potentials for atoms. The phase of a simple ideal phase mask can be written as

$$\Phi^{Vor}(r, \phi) = (n\phi) \bmod 2\pi, \tag{2.1}$$

where n is the *charge* of the vortex and ϕ is the azimuthal angle about the singularity. By ideal we mean the mask that transforms a plane wave. The surfaces of constant

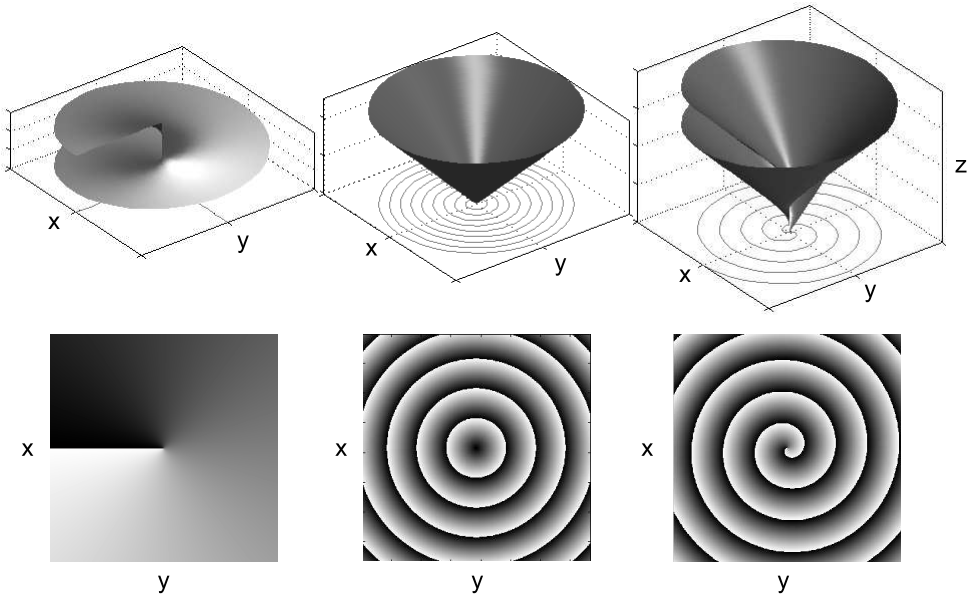

Figure 2.1: Surfaces of constant phase (left) of a vortex beam of charge 1 as described in Eq. 2.1, (middle) a conical beam or a Bessel beam of charge 0 in Eq. 2.10 with $n = 0$, and (right) a Bessel beam of charge 1 as in Eq. 2.10 with $n = 1$. The z-axis represents the propagation axis, whereas the x-axis and y-axis represent the transverse coordinates of the beam. Each phase profile in the bottom row is the 2D projection of the corresponding surface in the top row.

phase are helical as shown in the first column of Fig. 2.1. The phase is constant along a radius away from the center of the beam in a plane perpendicular to the direction of propagation, but changes with angle. One can picture the surface for a charge 1 vortex as a spiral staircase or the circular ramp connecting a multistory garage.

In contrast to the integer charge that produces a vortex localized to a point as described by Eq. 2.1, laser beams with half-integer charge have also been demonstrated [92]. Half-integer charges produce line singularities with phases that can be written as

$$\Phi^{half} = \left[\left(\frac{2n'+1}{2}\right)\phi + \vartheta\right] \bmod 2\pi, \tag{2.2}$$

where $n = (2n'+1)/2$ is the charge and n' is an integer. The parameter ϑ is added

to shift the azimuthal phase and thus rotate line singularities.

An example of a line singularity is shown in Fig. 2.2, where $n = 7/2$. It is a phase discontinuity along the interface of $\phi = 0$ (black) and π (grey). Also known as a row of edge dislocations, this type of vortex was first reported by Nye *et al.* [93] in ultrasonic waves; we exploit them here to create exotic channels in light.

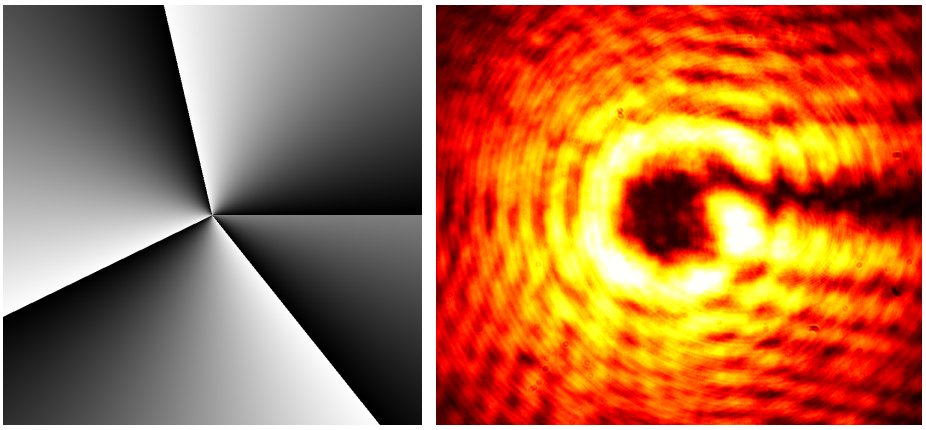

Figure 2.2: From left to right, a phase mask and corresponding beam profile of a channel beam for a vortex with half-integer charge embedded in plane background (Eq. 2.2, with $n = 7/2$ and $\vartheta = 0$). The mask has four sections; three of which have phase variation of 0 to 2π (black to white). The fourth contains a phase variation of 0 to π (black to gray). The location of the π-dislocation currently along the positive x-axis can be rotated by changing ϑ.

2.2 Bessel Beam

The Bessel beam, first introduced by Durnin in 1987 [83], is a beam of light that carries the intensity profile proportional to $J_n^2(k_r r)$, where k_r is a parameter known as *radial frequency*. This profile maintains its shape upon the beam's propagation and therefore can be listed in the family of non-diffracting beams [94, 95]. The non-diffracting property of the beam can be seen by observing that substituting the field of the form

$$Q(x, y, z) = q(x, y)e^{ik_z z}e^{-i\omega t}, \tag{2.3}$$

into the scalar wave equation,

$$\nabla^2 Q = \frac{\eta^2}{c^2}\frac{\partial^2}{\partial t^2}Q, \tag{2.4}$$

requires the transverse field $q(x, y)$ to satisfy the Helmholtz equation

$$\nabla_\perp^2 q + k_r^2 q = 0. \tag{2.5}$$

In Eq. 2.3, we note that z is the coordinate along the beam's propagation axis, x and y are the transverse coordinates, t denotes time, ω is the angular frequency of the field, and k_z is a constant. In Eq. 2.4, η is the index of refraction, c is the speed of light in vacuum. In Eq. 2.5, the radial frequency, k_r, is related to η, c and k_z through the relation

$$k^2 = k_r^2 + k_z^2, \tag{2.6}$$

where $k = \eta\omega/c = 2\pi/\lambda$ is the wavenumber and k_z is the projection of the wavevector $\vec{k}$ on z.

Now if Eq. 2.5 has a solution, then the time averaged intensity of the field Q can have the non-diffracting property, i.e.,

$$I(x, y, z > 0) = \frac{|Q(x, y, z > 0)|^2}{2} = \frac{|q(x, y)|^2}{2} = \frac{|Q(x, y, z = 0)|^2}{2} = I(x, y, z = 0). \tag{2.7}$$

By rewriting Eq. 2.5 in cylindrical coordinates,

$$\frac{1}{r}\frac{\partial}{\partial r}r\frac{\partial}{\partial r}q(x, y) + \frac{1}{r^2}\frac{\partial^2}{\partial \phi^2}q(x, y) + k_r^2 q(x, y) = 0, \tag{2.8}$$

and substituting $q(x, y) = A(r)\exp(in\phi)$, $A(r)$ must satisfy

$$r^2\frac{\partial^2}{\partial r^2}A(r) + r\frac{\partial}{\partial r}A(r) + \left(k_r^2 r^2 - n^2\right)A(r) = 0. \tag{2.9}$$

The equation 2.9 is known as the Bessel's equation, which has a solution called the Bessel function of the first kind denoted as $A(r) = J_n(k_r r)$. Thus the intensity profile is proportional to $J_n^2(k_r r)$ and the field provides an infinitely long hollow tunnel in free space. As an example, comparisons of the intensity profiles of the Bessel beams with the same peak radius, r_p, and radial frequency, k_r, for different values of n are shown on the left and right panels of Fig. 2.3 respectively.

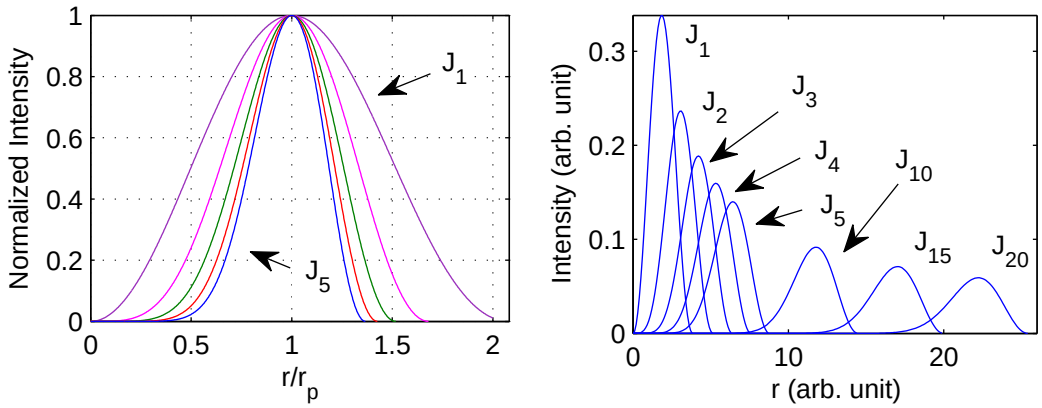

Figure 2.3: A comparison of the intensity profiles of the ideal Bessel beams with the same peak radius, r_p (left column), and radial frequency, k_r (right column). For the figure in the left column, the width of the profiles decrease as the charge, n increases from 1 to 5.

In the experiment, we used an SLM to produce a beam with an embedded vortex. A Bessel beam can be generated when a term of the form $\Phi^{Bes} = -k_r r$ is added to Eq. 2.1,

$$\begin{aligned} \Phi^{Bes-Vor}(r,\phi) &= \Phi^{Vor} + \Phi^{Bes} \\ &= (n\phi - k_r r) \bmod 2\pi, \end{aligned} \tag{2.10}$$

where the minus sign in front of k_r is to indicate that Φ^{Bes} decreases as r increases. In Eq. 2.10, k_r is a parameter that controls the size of the vortex by changing the location of the zeros in $J_n(k_r r)$. The surfaces of constant phase are again helical but in this case, the phase is no longer constant along r. This is shown in the rightmost column of Fig. 2.1. One again pictures a spiral ramp but now it slopes upward as one moves away from the center of the beam to form a conical helix similar to the shape of a drill bit. Without the vortex term, the surface of constant phase is just a cone as shown in the middle column of Fig. 2.1 and the SLM produces a Bessel beam of order zero. While the non-diffracting nature of Bessel beams is ideal for our purpose, other structured beams have also been demonstrated [96].

Vasara *et al.* [79] has shown that an aperture limited field, Q_0 at $z = 0$ with

the phase as described in Eq. 2.10, produces a Bessel beam by calculating the field for $z > 0$ using the Fresnel diffraction integral [97]. If we write Q_0 as

$$Q_0(r, \phi, z = 0) = \exp\left(i\Phi^{Bes-Vor}\right) = e^{in\phi}e^{-ik_r r}\Theta(r - D), \tag{2.11}$$

where $\Theta(r - D)$ is an aperture function with a value of one when $r \leq D$ and zero elsewhere, the Fresnel diffraction integral can be written as

$$\begin{aligned} Q(r, \phi, z > 0) &= \frac{e^{ikz}}{i\lambda z}\int_{r'=0}^{\infty}\int_{\phi'=0}^{2\pi} e^{ik(|\vec{r}-\vec{r'}|)^2/2z}Q_0(r', \phi', z = 0)\, r'dr'd\phi' \quad (2.12)\\ &= \frac{e^{ik(z+r^2/2z)}}{i\lambda z}\int_{r'=0}^{D} dr'r'e^{ik(r'^2/2z-k_r r'/k)} \\ &\quad \times e^{in\phi}\int_{\phi'=0}^{2\pi} d\phi' e^{in(\phi'-\phi)}e^{-ikrr'\cos(\phi-\phi')/z} \quad (2.13)\\ &= \frac{e^{ik(z+r^2/2z)}}{i\lambda z}2\pi(-i)^n e^{in\phi}\int_{r'=0}^{D} dr' f(r')e^{ik\mu(r')}, \quad (2.14) \end{aligned}$$

where $\mu(r') = r'^2/2z - k_r r'/k$, $f(r') = r'J_n(krr'/z)$, the prime variables denote the coordinates on the transverse plane at $z = 0$, and in the last step we have used the integral representation of J_n, i.e.,

$$J_n(\alpha r) = \frac{i^n}{2\pi}\int_0^{2\pi} e^{-i\alpha r\cos\xi}e^{in\xi}d\xi. \tag{2.15}$$

The integral can be approximated using the stationary phase method [79, 98] in the form

$$\int_{r'=0}^{D} dr' f(r')e^{ik\mu(r')} \approx \left[\frac{2\pi}{k\mu^{(2)}(r'_c)}\right]^{1/2} f(r'_c)e^{ik\mu(r'_c)}, \tag{2.16}$$

where the critical point for the stationary phase method, $r'_c = k_r z/k$, can be found by setting the first derivative of $\mu(r')$ to zero, and $\mu^{(2)}(r'_c) = 1/z$ is the second derivative of $\mu(r')$ evaluated at $r' = r'_c$. By substituting the value of r'_c into Eq. 2.16 and using the result in Eq. 2.14, $Q(r, \phi, z > 0)$ can be written as

$$Q(r, \phi, z > 0) \approx (-i)^{n+1}\left(2\pi\frac{k_r^2 z}{k}\right)^{1/2} e^{ikr^2/2z}e^{-ik_r^2 z/2k}e^{ikz}e^{in\phi}J_n(k_r r), \tag{2.17}$$

and the intensity profile is given by

$$I(r, \phi, z > 0) \propto |Q(r, \phi, z > 0)|^2 \propto zJ_n^2(k_r r). \tag{2.18}$$

The intensity profile in Eq. 2.18 has the form of the Bessel function as expected. However, the value of the intensity also depends on z unlike the *ideal* Bessel beam that we obtained from Eq. 2.9. Note that the ideal Bessel beam carries an infinite amount of energy because the peak intensity of the side lobes falls roughly as $1/r$ while the area increases by r^2. Thus the ideal Bessel beam cannot be obtained experimentally. Another remark regarding Vasara's Bessel beam in Eq. 2.18 is that the beam does not propagate indefinitely due to the aperture function that limits the source field. The critical point, $r'_c = k_r z/k$, that we used to approximate the diffraction integral in Eq. 2.14 is restricted to a range from 0 to D by the aperture. Outside this range there is no critical point and Vasara pointed out that the integral falls as $1/z$. The range where r'_c exists also limits the propagation distance to within $0 < z < kD/k_r$. This propagation limit can be explained intuitively considering geometrical optics as shown in the following section.

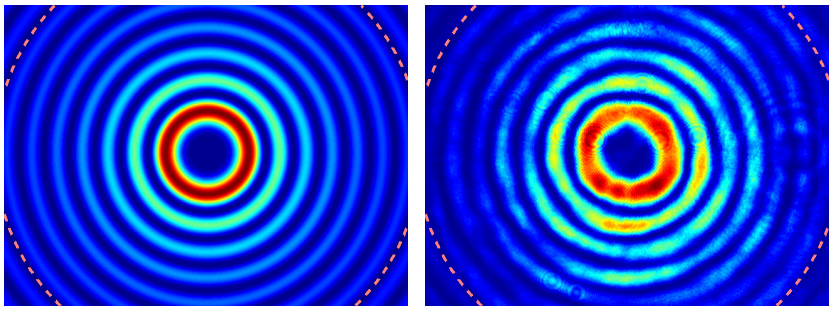

Figure 2.4: An ideal Bessel beam profile (left) derived from Eq. 2.9 compared with an experimental profile (right) generated from an SLM as described by Eq. 2.21.

Aside from Vasara's example above, in a typical experiment, the source field is normally Gaussian, the field at $z = 0$ is not aperture limited as described in Eq. 2.11 but rather

$$Q_0(r', \phi', z = 0) = e^{in\phi'} e^{-ik_r r'} Q_{GS}, \tag{2.19}$$

where we have replaced the aperture function in Eq. 2.11 with the field of a Gaussian beam, Q_{GS}. As an example, we choose Q_{GS} that has the minimum radius of curvature of the wavefront [99], i.e.,

$$Q_{GS} = Q_0 e^{-ikr'^2/4\, z_R} e^{-r'^2/2w_0^2}, \tag{2.20}$$

where Q_0 is a constant and the maximum field amplitude, $z_R = \pi w_0^2/\lambda$ is the Rayleigh range, and w_0 is the beam waist. The field for $z > 0$ can be calculated in the same way as before, using the Fresnel diffraction integral and the stationary phase method. The critical point for the stationary phase method occurs at

$$r_c' = \frac{2z_R z}{2z_R - z}\frac{k_r}{k}.$$

In a case where $z/z_R \ll 1$, the critical point becomes $r_c' \approx k_r z/k$, and the resulting intensity profile can be written as

$$I(r, \phi, z > 0) \propto z \exp\left(-\frac{z^2}{w_0^2 k^2/k_r^2}\right) J_n^2(k_r r). \tag{2.21}$$

We can see that the propagation range is now limited by the size of the beam waist, i.e. $0 < z \lesssim w_0 k/k_r$.

In Fig. 2.4, we show the transverse intensity profiles of the ideal Bessel beam on the left and that of the Gaussian-limited Bessel beam, as in the case of Eq. 2.21, that we obtained from the experiment on the right. Both beams have the same charge $n = 4$ and k_r. The angular-averaged radial profile of the J_4 Bessel beam (Fig. 2.5d) from the measured 2D intensity distribution (Fig. 2.5a) is shown to be in a reasonable agreement when fit to the function $J_4^2(k_r r)$. However, the peaks are not very well matched because of some intensity imperfections in the beam. The comparison of the power in different rings of the J_4 beam (Fig. 2.5c) shows that the power levels off at a high ring number for the ideal Bessel beam (filled black square), where the ring number one starts from the peak closest to the origin. This repeats the notion that the ideal Bessel beam carries infinite amount of energy. On the other hand, we can see a decline in the experimental values for higher ring numbers (green circles). The declination can also be seen in the plot (filled red triangle) obtained from a numerical evaluation via 2D angular spectrum or a paraxial approximation [97].

For Bessel beams in general, the values of radial position of the first peak (r_{p0}) and the first zero (r_{z0}) are tabulated in many textbooks for $k_r = 1$. For $k_r \neq 1$, if

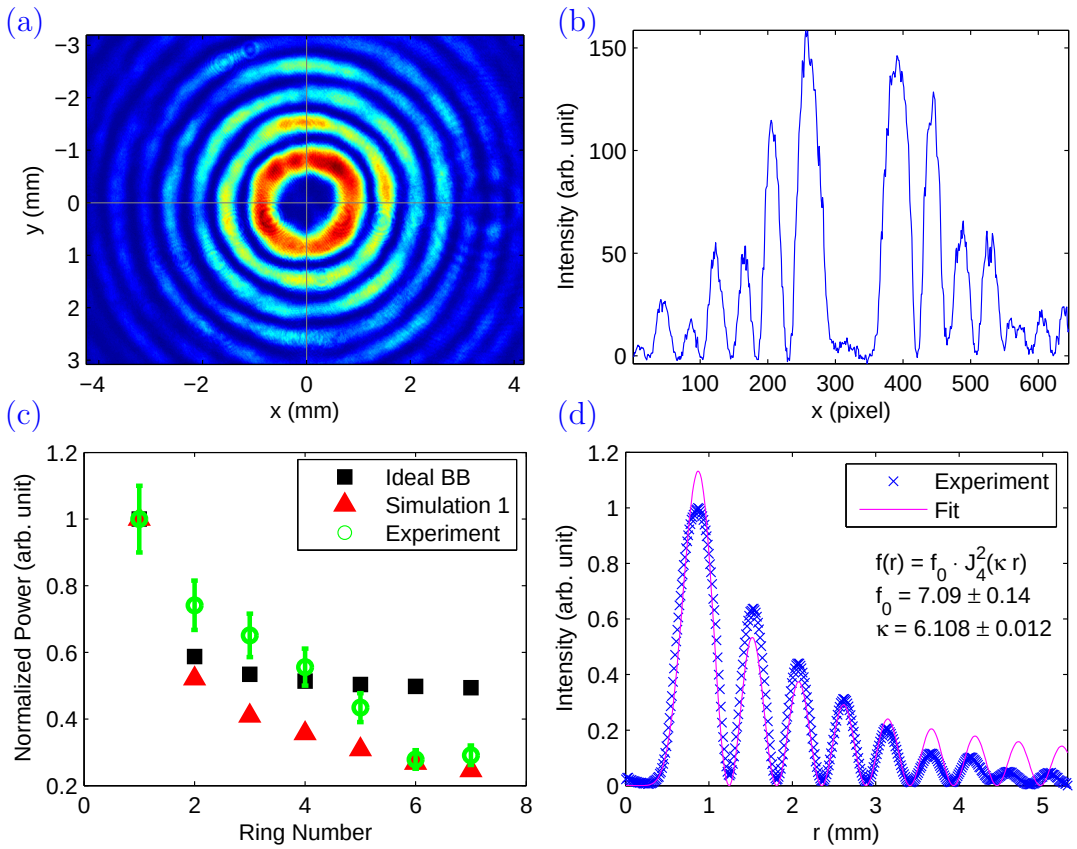

Figure 2.5: The figures show (a) measured intensity profile of a J_4 Bessel beam generated from a Gaussian beam embedded with the phase as in Eq. 2.19, (b) a line profile along the x-axis of the 2D profile in (a), (c) power in the ring of the J_4 Bessel intensity profile as a function of the ring number, counted from the center of the beam, and (d) the azimuthal average radial profile (cross plot) of the intensity profile in (a). The pink solid line is the non-linear fit of the cross plot to $J_4^2(k_r r)$.

we want our beam to have its peak at r_p, we can rewrite $J_n(k_r r)$ as

$$J_n(k_r r) = J_n\left(\frac{r_{p0}}{r_p} r\right), \tag{2.22}$$

and to have the first zero at r_z, we can rewrite $J_n(k_r r)$ as

$$J_n(k_r r) = J_n\left(\frac{r_{z0}}{r_z} r\right). \tag{2.23}$$

For example, if we want our J_4 beam to have a peak at $r_p = 0.5$ mm away from the origin, the value of k_r should be $k_r = r_{p0}/r_p \approx 5.3176/(0.5\text{mm}) \approx 10.635\text{mm}^{-1}$. Using Eq. 2.22, when $r = r_p$, $J_4(k_r r)$ becomes $J_4(r_{p0})$, where it has its maximum value.

From the constraint $k_r^2 + k_z^2 = k^2$ as in Eq. 2.6, we can see that when $k_z = 0$, k_r is its largest possible value. This value of k_r limits the achievable size of the Bessel beams, i.e. the smallest structure of the beam occurs at $k_r = \omega/c = 2\pi/\lambda$, where λ is the wavelength of the radiation composing the field, not the grating spacing [83]. For example, for J_0, the zero occurs at $r_z = r_{z0}/k_r = r_{z0}\lambda/2\pi \approx 3\lambda/4$. For J_1, the peak occurs at $r_p = r_{p0}\lambda/2\pi \approx 7\lambda/12$.

2.3 Bessel-Beam Generation: Geometrical Consideration

In this section we will discussed the geometrical construction of a Bessel beam using a conical glass and a binary grating [2]. This will provide the reader with an intuitive picture of how a Bessel beam behaves. We will use the small angle approximation to connect the axicon parameter with the grating parameter. At the end we will discuss using an axicon to produce a Bessel beam with a diameter of the order of a few microns. This micron-sized beam will be useful for atom-optics as discussed in Chapter 6.

In the previous section, we saw that the propagation range of a Bessel beam generated from an aperture limited field (Eq. 2.11) and a Gaussian limited field (Eq. 2.19) are kD/k_r and kw_0/k_r respectively, where D and w_0 are the radii of the aperture and the beam waist respectively. Both ranges are independent of the charge, n, of the Bessel beam. From the geometrical consideration, we trace a ray of light from an optical element that produces the Bessel beam to estimate this propagation range. We first start by noticing that a cone-shaped transparent medium, called an *axicon*, produces a propagation-limited Bessel beam. This was demonstrated experimentally by Arlt *et al.* [101]. It follows from the previous section that a conical phase $\Phi^{Bes} = -k_r r$ is responsible for generating the Bessel beam. In a plane containing the cylindrical symmetry axis, the projection of the axicon is a tringle in 2D as shown in Fig. 2.6a, together with principal rays. From the Fig. 2.7a, according to the Snell's law, we have $\eta \sin\iota = \sin\beta$, where η is the axicon's index of

[2] Another way to describe a Bessel beam is in terms of a superposition of Hankel beams [100].

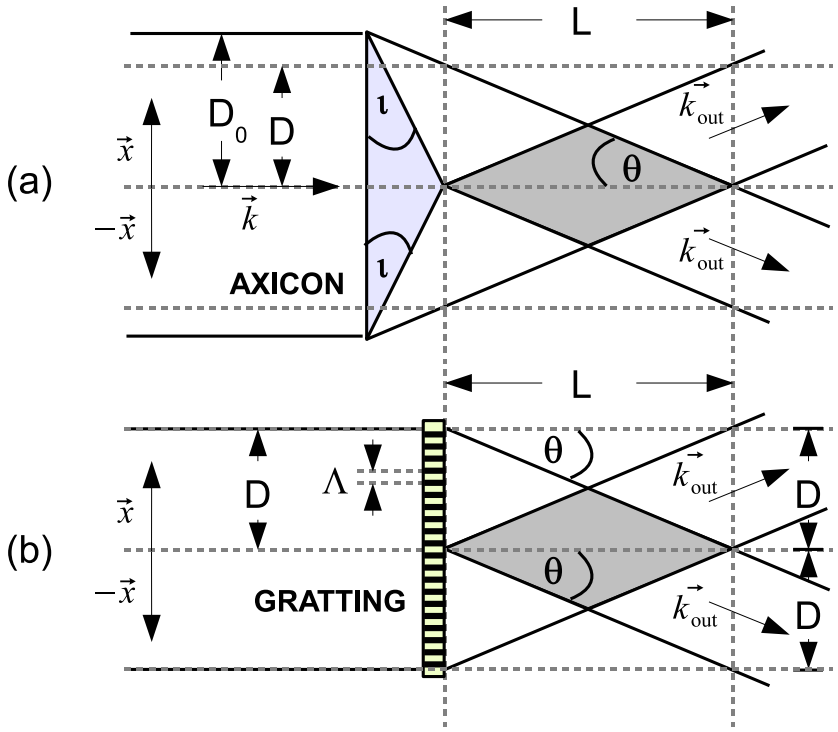

Figure 2.6: Principal rays for (a) an axicon and (b) a grating. The base angle of the axicon is ι and can be related to a particular grating parameter Λ ($= 2\pi/k_r$) as described in the text. A Bessel beam only exists in the shaded areas in the figure.

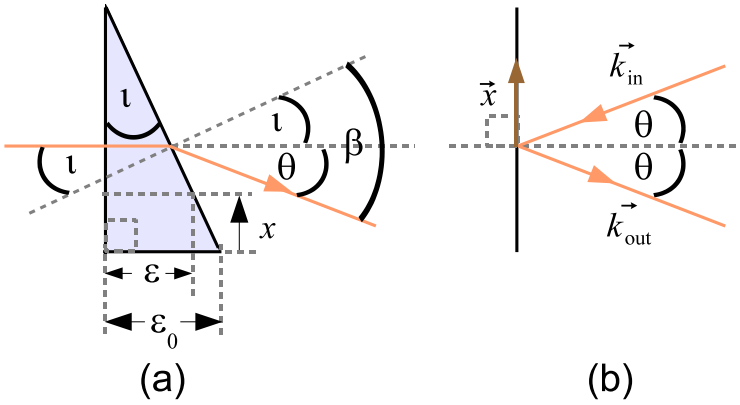

Figure 2.7: Principal rays for (a) refraction through an axicon and (b) reflection from a flat surface when the reflection angle is the same as the deviation angle θ. The maximum thickness of the axicon measured from the base is ϵ_0.

refraction, and ι and β are the incident and refraction angle respectively as shown in Fig. 2.7a. For small ι and β, $\eta\iota \approx \beta$. Thus, the refraction angle, θ $(= \beta - \iota)$, becomes $\theta \approx (\eta - 1)\iota$. The phase change, $\Delta\Phi$, corresponding to this refraction angle can be calculated by considering the difference between the phase of a plane wave traveling a distance of ϵ through the axicon and that traveling the same distance in vacuum i.e.,

$$\Delta\Phi = k\epsilon(\eta - 1) = k\epsilon_0\eta - k\epsilon_0 - kx(\eta - 1)\tan\iota, \tag{2.24}$$

where we used $\epsilon_0 - \epsilon = x\tan\iota$ from the geometry in Fig. 2.7a. For small ι, and dropping the constant terms that do not contribute to the refraction of the principle rays, $\Delta\Phi = -kx\iota(\eta - 1)$.

Now, instead of using the axicon to generate the Bessel beam, we can encode $\Delta\Phi$ onto a binary grating to diffract light to create the beam as shown in Fig. 2.6b. By *binary* we mean the grating has only two levels. For example, a binary amplitude grating will either transmit or block the light. In the case of a binary phase grating, light is either be phase-shifted by 0 or π. If we assign the spatial frequency of the grating to

$$k_x = \Phi/x = -k\iota(\eta - 1), \tag{2.25}$$

the angle of the first diffraction order, assuming the small angle approximation, is found to be the same as the refraction angle of the axicon we have mentioned earlier. To prove this, we note that, for a 1D grating with a spacing Λ[3] $(= 2\pi/k_x)$, the diffraction angle can be calculated from the grating formula

$$\Lambda\sin\theta_m = m\lambda, \tag{2.26}$$

where λ is the wavelength of light, m is the diffraction order and θ_m is the diffraction angle for order m. For the case when $m = -1$, the upper half of the grating in Fig. 2.6b, Eq. 2.26 becomes $k\sin\theta = -k_x$, which is just the projection of the $\vec{k}$ onto the x-axis (see Fig. 2.7b). For the small angle approximation, valid in our experiments with an SLM, the diffraction formula gives $\theta \approx -k_x/k \approx \iota(\eta - 1)$. In the case of an axicon in 3D, we can encode its phase change onto the SLM by expressing

[3]An example of Λ of a 2D mask is shown in Fig. 2.27.

$k_r = -k\theta = -k\iota(\eta - 1)$, where we use k_r instead of k_x by exploiting cylindrical symmetry without loss of generality. This equation also relates the grating parameter $k_r = 2\pi/\Lambda$ with the axicon parameter ι, the base angle of the axicon.

For a glass axicon with index of refraction $\eta = 1.5$, $\lambda = 780$ nm, and $\iota = 1^\circ = \pi/180$ rad, we have $\Lambda \sim 89.4$ μm ($k_r = 70.296$ mm^{-1}). If we use this value for k_r to make a Bessel beam of charge four, we will have a tunnel with a peak radius $r_p \approx 76$ μm. Thus, to make a tunnel 10 times smaller, i.e. $r_p \approx 8$ μm, in the small angle approximation, we can approximate the base angle ι to be roughly ten times larger, i.e., $\approx 10^\circ$. To create a smaller tunnel, we could increase the axicon's index of refraction. For $k_r = 8$ mm^{-1}, the value that we normally used to make our Bessel tunnel with the SLM, the base angle of the axicon would be 0.002 rad ($= 0.114^\circ$), which would be an incredibly thin piece of glass. As a consequence it is clear that the axicon approach is not viable. As mentioned above the region where the Bessel beam exists is the shaded trapezoidal area in Fig. 2.6. The maximum range of propagation, L, can be calculated from geometry, i.e.

$$L = \frac{D}{\tan\theta} \sim \frac{D}{\theta} = \frac{D}{k_r/k} = \frac{D}{(\eta - 1)\iota}. \tag{2.27}$$

2.4 Numerical Calculations of the SLM-Generated Bessel-Beam

In this section, we will discuss several features of the Bessel beam generated by the SLM in addition to the properties of the intensity profile discussed in the previous sections. To examine these features, we simulated them using the scalar diffraction theory. First, we will revisit the propagation range of the Bessel beams and its dependency on charges. Moreover, we will look at the dependency of its peak radius and peak intensity on the propagation distance. Second, we will consider the divergence of the Bessel beam after it passes through a lens. Third, we will show that in practice the SLM modulates not only the phase but the amplitude of the incoming light wave as well. That results in dips in the intensity of the Bessel profile where a phase jump from 0 to 2π in the phase mask. Fourth, we will demonstrate the intensity profiles for the case when the SLM has an inherent inactive area that

resembles a mesh grating. The size of the spacing of the mesh is around 30 μm which is about the size of the SLM's pixel. The inherent structure produces additional diffraction patterns that reduces the power of the intended patterns by about 20%. Fifth, we will show results of a phase function that tilts the propagation direction of the output patterns generated from the SLM, away from the specular direction. Lastly, we will discuss how to correct an ellipticity in a Bessel beam generated from a Gaussian beam of an oblique incidence on the SLM. This can be done by changing the aspect ratio of the phase mask that produces the Bessel beam [102].

2.4.1 Propagation Characteristics

The propagation of the aperture limited Bessel beams, as previously discussed in Sec. 2.2 and Sec. 2.3, can be numerically evaluated. In Figure 2.8, we use a cylindrical angular spectrum method, via the Hankel transform (see Appendix C.2), to calculate the propagation dependent values of (a) the peak radius position, r_p, (b) the radius of the first zero, r_z, (c) the first ring power, P_1, and (d) the maximum intensity, I_{max}. The masks for all four cases generate the Bessel beams with $r_p = 0.67$ mm. The integer, n, is set to vary from 0 to 5. A MATLAB code used for this simulation is provided in Sec. G.5.1. From Fig. 2.8a, it can be seen that r_p for a small n remain constant with respect to z for longer distances than they do for a large n. This is because the vortex with a large n value is susceptible to a small disturbance in azimuthal asymmetry causing the fields of each constituent vortex with $n = 1$ to interfere. The diffraction contribution from the edge of the square aperture is one of the causes that introduces this asymmetry. In Fig. 2.8b, the values of r_z for each n are different because we intentionally make r_p the same for all n.

In Fig. 2.8c and Fig. 2.8d, the magnitude of the slopes of P_1 and I_{max}, as a functions of z, is higher for the beam with larger n. The largest I_{max} for $n = 5$ is 1.5 times of that for $n = 1$.

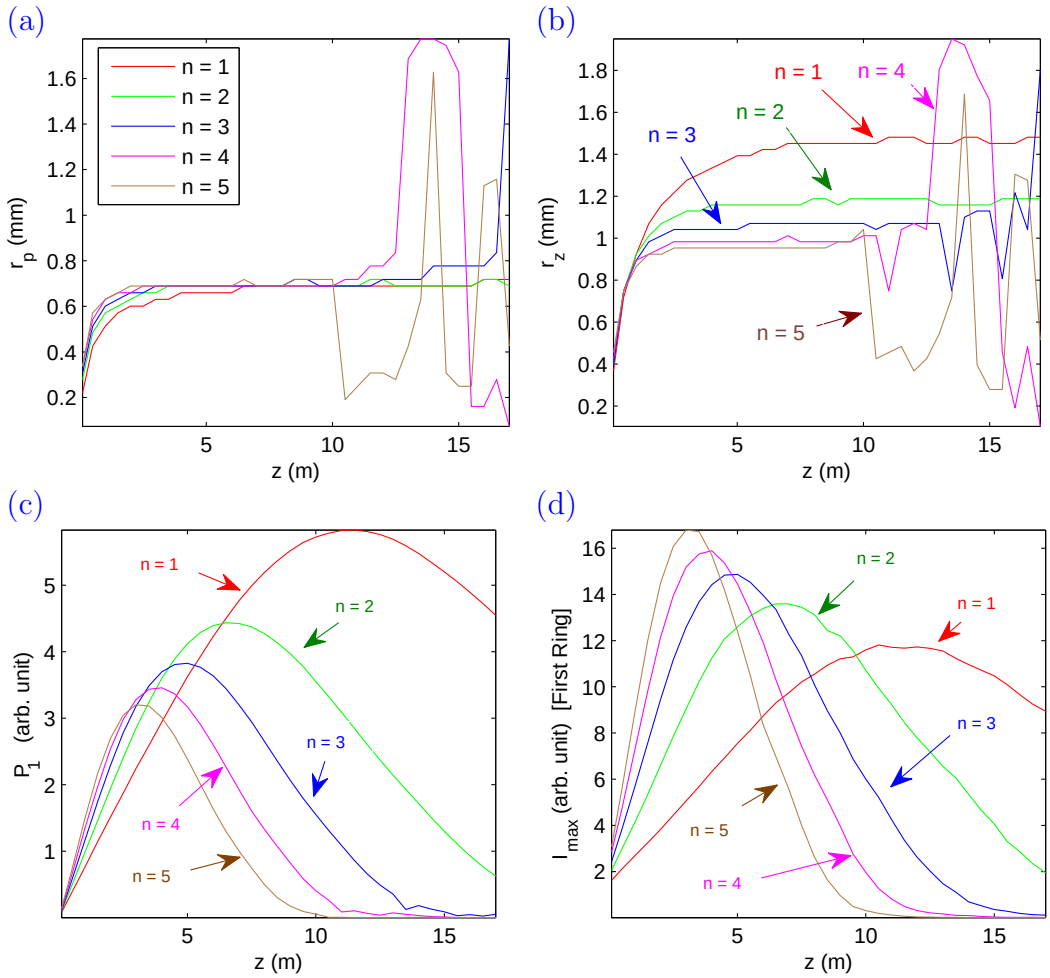

Figure 2.8: Propagation characteristics of the aperture-limited J_n-Bessel beam. The charge n of the Bessel beam varies from 1 to 5. The figures show the dependency on the propagation distance z of (a) the location of the peak radius, r_p, (b) the location of the radius of the first zero, r_z, (c) the power in the first ring, P_1, of the Bessel beam, and (d) the maximum intensity, I_{max}.

2.4.2 Propagation with Divergence

By using a converging lens, the size of the model J_n-Bessel beam can be made much smaller than that generated by the SLM, due to the finite spatial resolution of the SLM. The SLM used in our experiment has 384 pixels/cm. Thus, to encode a phase $\Phi = (2\pi x/\Lambda) \bmod 2\pi$ on the SLM, Λ must be larger than 2/384 cm.

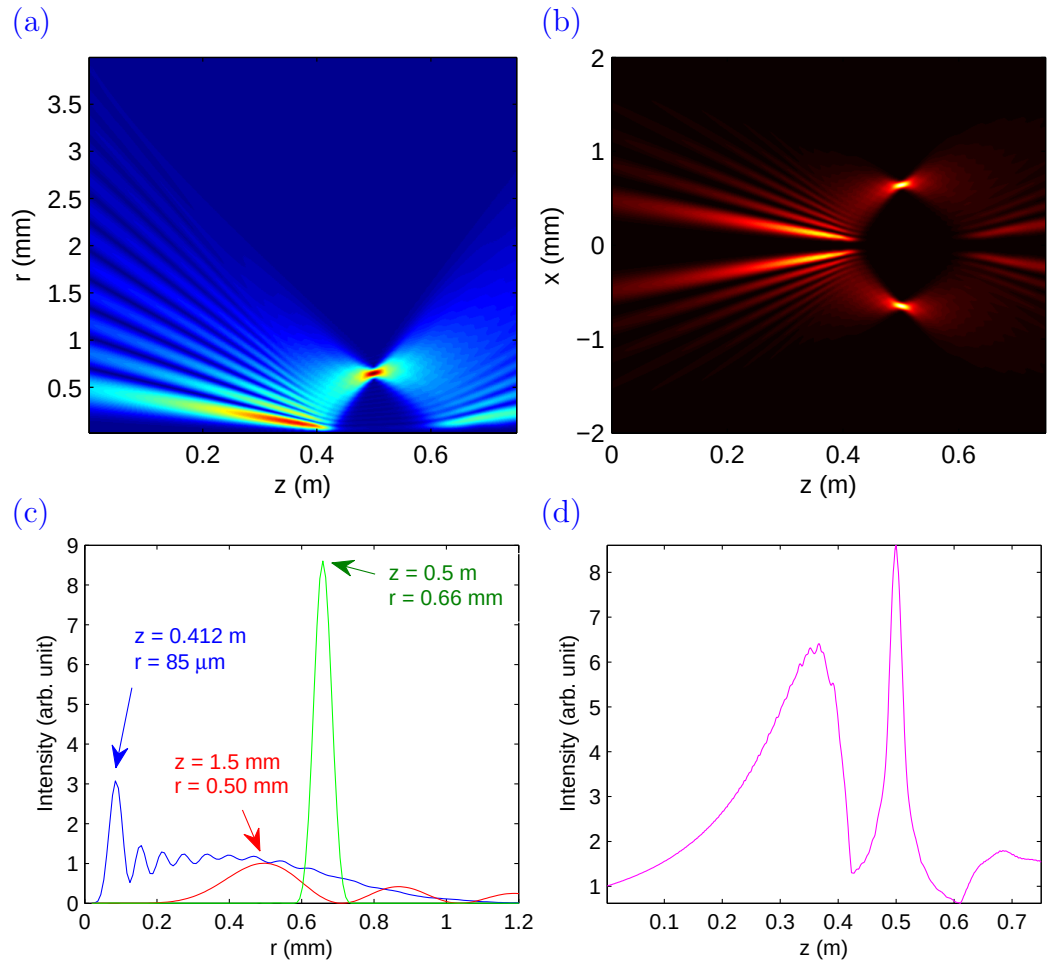

Figure 2.9: Propagation of a focused aperture-limited model Bessel beam with the field as described in Eq. 2.28, using the method in Ref. [103]. The focal length (f) of the lens used to focus the beam is 0.5 m and $r_p = 0.5$ mm at $z = 0$ ($f/r_p = 1000$). The propagation of the field and the intensity over the propagation distance z is shown in (a) and (b) respectively. In (c), radial intensity profiles for three different z values are shown. The smallest radius of the peak intensity ($r_{p,\min}$) occurs at $z = 41.2$ cm with a value of 85 μm. The plot in (d) shows a trace of I_{max} versus z.

We simulated the propagation of the field using the cylindrical angular spectrum (see Appendix C.2) as was done in the previous section. In Fig. 2.9 the amplitude and intensity patterns of the focused J_4- Bessel beam are shown as examples. The transverse source field, at the lens ($z = 0$), was expressed as

$$Q_1(r, z = 0) = J_4(k_r r) \exp(-r^2/w_0^2). \tag{2.28}$$

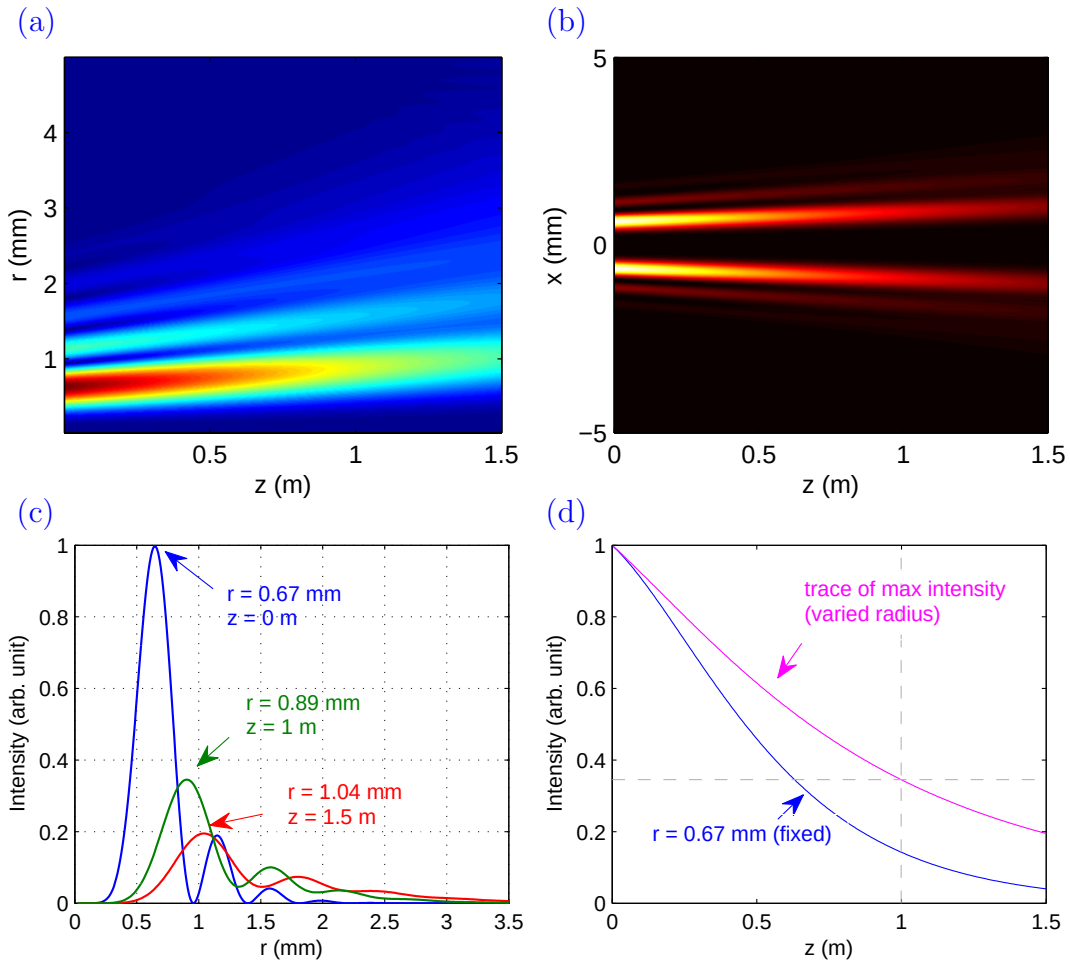

Figure 2.10: Propagation of a diverging aperture-limited model Bessel beam with the field as described in Eq. 2.28. The description of this figure is similar to Fig. 2.9 except that the focal length of the lens is -2.7 m, producing a diverging beam with a half angle of divergence of 0.22 mrad.

The lens used in the numerical calculation attaches additional phase shift Φ_{lens} to the field according to

$$\Phi_{lens}(r) = -\frac{kr^2}{2f}, \tag{2.29}$$

where the focal length of the lens f is chosen to be 50 cm for Fig. 2.9. The value of k_r is chosen to produce a beam with $r_p = 0.5$ mm. The smallest peak radius, $r_{p,\min}$, for the field Q_1 occurs at $z_{\mathrm{r,min}} = 41.2$ cm and has a value of $r_{p,\min} = 85$ μm. At $z = f$, all rings in the Bessel beam are focused to form a bright narrow ring of light with $r_p = 660$ μm. It is useful to write the quantities mentioned above in terms of r_p, i.e, $f = 1000 r_p$, $z_{\mathrm{r,min}} = 824 r_p$ and $r_{p,\min} = 0.17 r_p$, for the field Q_1. To derive

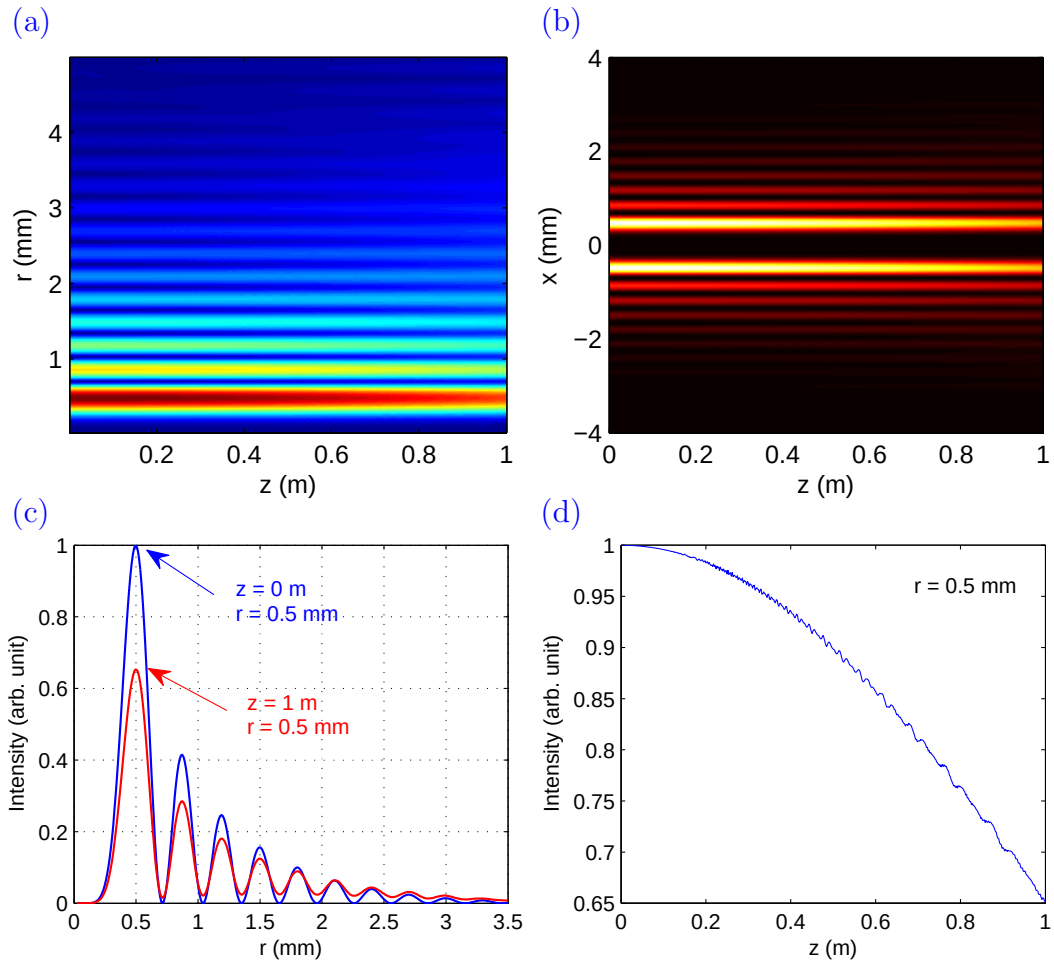

Figure 2.11: Propagation of a collimated aperture-limited model Bessel beam with the field as described in Eq. 2.28. The description of this figure is similar to Fig. 2.9 except that no lens is used to modified the field at $z = 0$. Note that the peak intensity of the beam at $z = 1$ m drops to 60% of the peak intensity at $z = 0$ m.

$z_{\mathrm{r,min}}$ and $r_{p,\mathrm{min}}$ in terms of f and r_p, a diffraction integral, such as that shown in Eq. 2.12, needs to be evaluated analytically.

For a diverging lens r_p is a linear function of z. As an example, the propagation of the field Q_1 can be seen in Fig. 2.10, where k_r is chosen to produce a beam with $r_p = 0.67$ mm and $f = -2.7$ m is chosen to produce a beam with the same divergence as that in the experiment (in Chapter 4). The peak radius changes from 0.67 mm to 0.89 mm over a 1 m range for z. This corresponds to a half angle of divergence of 0.22 mrad. The peak intensity drops approximately linearly as the beam propagates from 0 to 1 m. The peak intensity at $z = 1$ m falls by 60% under these conditions.

The peak intensity chanages by 10% over the last 15 cm.

Without any lenses, Q_1 propagates as shown in Fig. 2.11. The peak intensity drops by 40% during the first 1 m while r_p remains the same.

2.4.3 Mixed Phase and Amplitude Modulation

In the experiment, we observed various curious diffraction patterns generated from the SLM that affects our desired patterns. In the top row of Fig. 2.12, images obtained from an experimental trial are displayed. The images from the left to the right show the intensity of diffraction patterns taken in transverse planes as z increases. The two leftmost columns display curious spiral stripes closely resembling the pattern on the phase mask as seen in the bottom row of the third column of Fig. 2.1. Even though the spiral pattern could be generated from a phase mismatch at the spiral 0–2π junctions on the mask generated from the modulo 2π operation, the mismatch can always be minimized by fine tuning the phase modulation range of the SLM.

One possible way for these discontinuities to be present in the diffraction pattern is that the SLM not only introduces a pure phase modulation but also an amplitude modulation as well. In our simulation, we assume that the modulation of the amplitude is a linear function of the phase shift from the SLM. In this way, the spiral intensity dip is directly encoded into the Bessel intensity profile. The simulated diffraction patterns and their phases based on mixed phase and amplitude modulation are shown in the second and third row of Fig. 2.12 respectively. The simulation exploits a 2D Cartesian angular spectrum method as described in Appendix C.2. The MATLAB code for the simulation is shown in Appendix G.5.2. The results from the simulation agree well with the patterns observed in the experiment. In our simulation, the field at the SLM surface can be written as

$$Q(r,\phi) = \tilde{Q}(r,\phi)\exp[i\Phi^{Bes-Vor}(r,\phi)]\exp(-r^2/w_0^2), \tag{2.30}$$

where

$$\tilde{Q}(r,\phi) = (1-\sigma) \ + \ \sigma \ \Phi^{Bes-Vor}(r,\phi)/2\pi$$

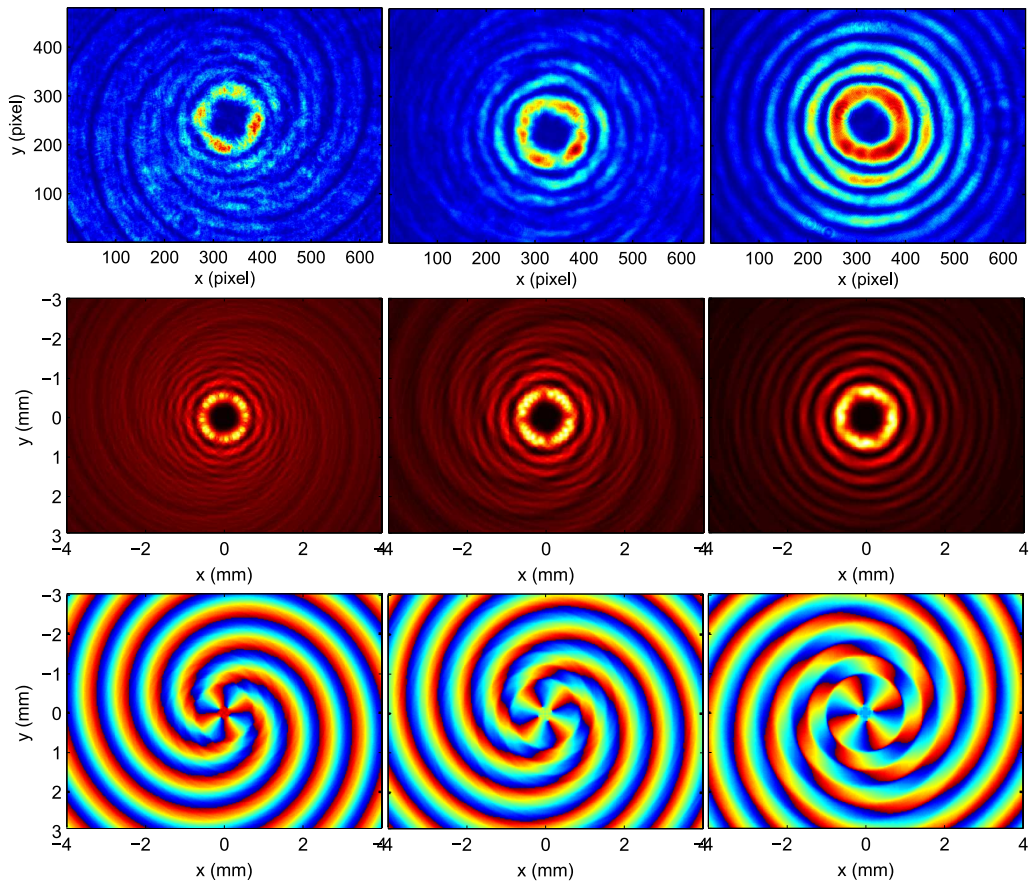

Figure 2.12: Mixed- phase- and- amplitude- modulation intensity patterns from the experiment (top row) and from the simulation (middle row). From left to right, the pictures in each column correspond to the propagation distance $z = 0.5$ m, 1 m and 2 m away from the surface of the SLM respectively. Each phase profile in the bottom row corresponds to the simulated intensity profile of the row above it in each column. The spiral patterns seen in the two leftmost columns and four dips in the smallest ring of the model Bessel beam comes from the mixture of phase and amplitude modulation as described in the text.

is the amplitude modulation function, $\Phi^{Bes-Vor}(r, \phi)$ is previously shown in Eq. 2.10, and σ is the strength of the amplitude modulation induced by the phase mask. In our case, we let the Gaussian parameter $w_0 = 1$ cm, $\sigma = 0.4$, and let $n = 4$ and $k_r = 7.597$ mm^{-1} so that $r_p = 0.7$ mm, similar to the value used in our experiments. The wavelength of light, λ, is set to 780 nm. More simulated diffraction patterns

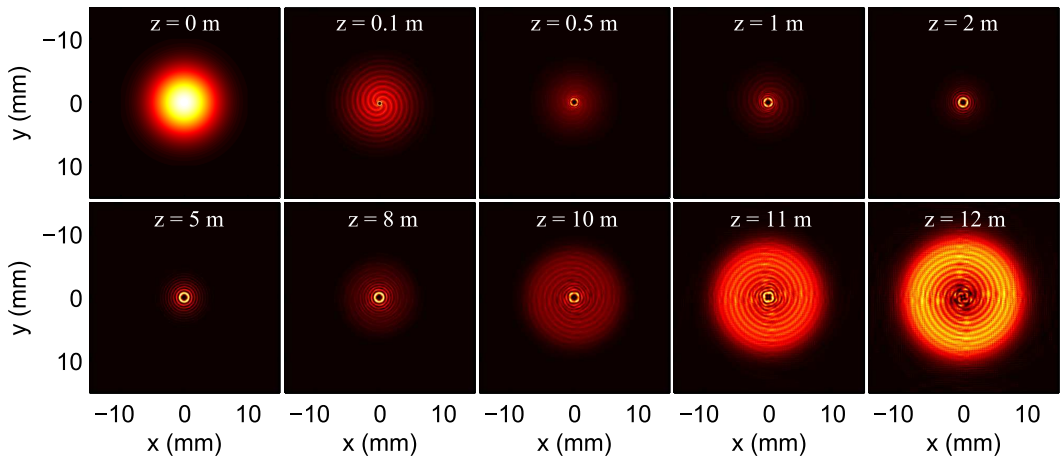

Figure 2.13: The simulated transverse intensity profile at a distance z, as labeled in each figure, away from the surface of the SLM. The source field is described by Eq. 2.30 with $\sigma = 0.4$. The profiles at $z = 0.5$ m, 1 m and 2 m are the same as that in Fig. 2.12. Notice that the profile has a ring shape at $z = 12$.

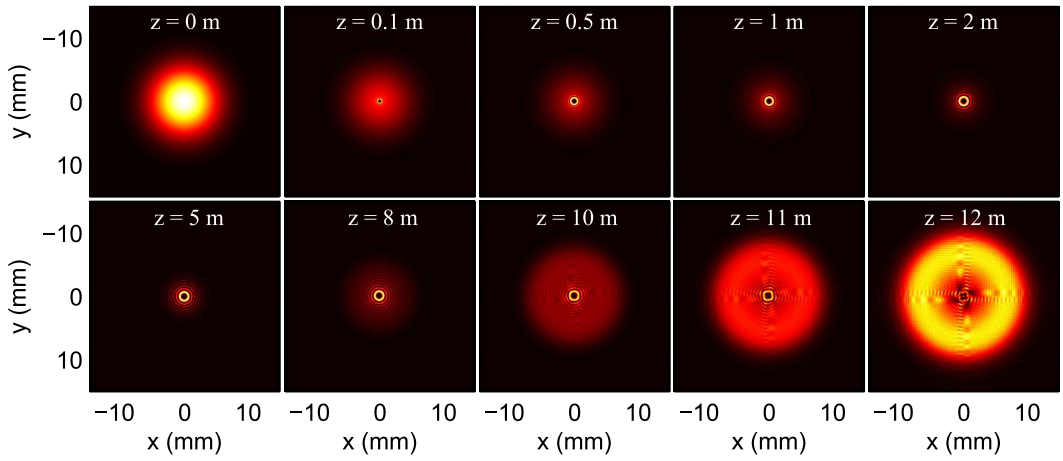

Figure 2.14: This figure has the same description as that of Fig. 2.13 except $\sigma = 0$.

are shown in Fig. 2.13 for a larger selection of the z values. The patterns can be compared to those obtained from the simulation of the pure phase modulation (i.e. $\sigma = 0$) as shown in Fig. 2.14. Note that the diffraction patterns at large distance, i.e. $z \geq 12$, approach a ring shape. Those patterns are expected outside the overlap region at large z in Fig. 2.6. Magnified views of Figs. 2.13 and 2.14 are shown in Fig. 2.15. From the latter figure, we can see that the interference from the mixed phase and amplitude modulation in the second and fourth rows introduces intensity

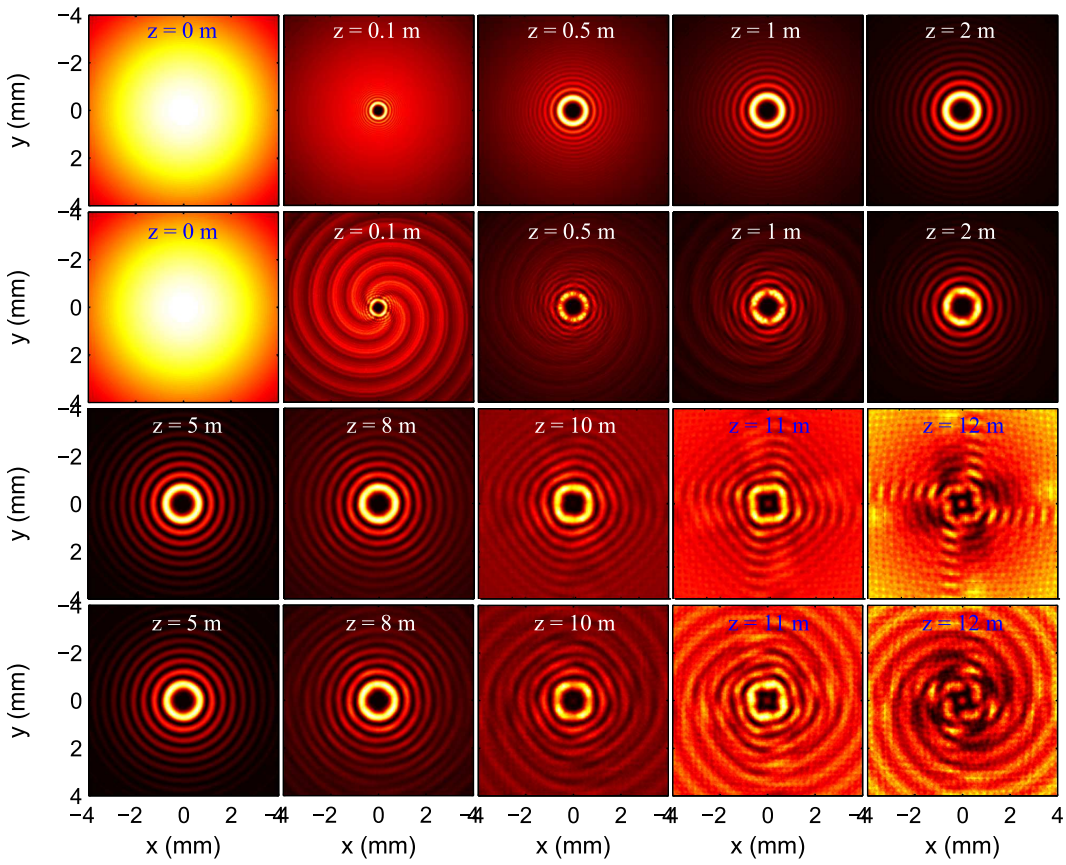

Figure 2.15: The figures show the zoomed in version of Fig. 2.14 (in the first and the third rows) and that of Fig. 2.13 (in the second and the fourth rows) at various distance of propagation z.

anomalies in the first ring of the beam. However, the anomalies are less apparent when $z = 5$ m, which is about the middle of the propagation range, L, as seen in Fig. 2.6 and as described by Eq. 2.27. Note that the size of the axicon aperture, D, in Eq. 2.27 should be replaced with the waist, w_0, of the beam according to Eq. 2.21, i.e., $L = w_0 k/k_r$. For the values of w_0, k and k_r as mentioned earlier, $L \approx 10.6$ m, roughly twice the size of the 5 m range obtained from the simulation.

2.4.4 A Mesh in SLM

In addition to the modulation of the amplitude of the input light field mentioned in Sec. 2.4.3, the SLM we used also introduces an amplitude modulation in

a form of a mesh as shown in the leftmost column of Fig. 2.16. We believe that the cause is from the SLM's pixelation as we will argue shortly, later in this subsection. For the phase mask of a J_1-beam, as described in Eq. 2.10, the output diffraction pattern contains a mesh of vortices as shown in the second column of Fig. 2.16. From the same figure, the intensities of the zeroth and first diffraction order of the meshed vortices are shown in the third and last column respectively.

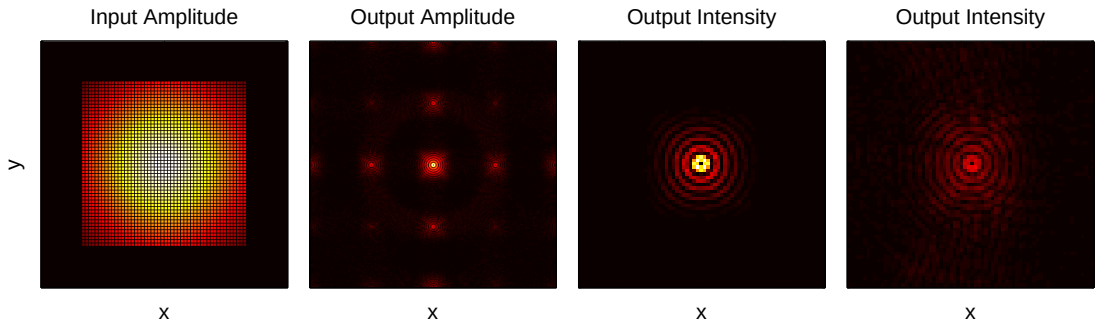

Figure 2.16: From left to right: (1) a mesh pattern and a square aperture embedded on a Gaussian amplitude at the SLM's surface. (2) the mesh diffraction patterns calculated numerically in the far field. The input field at the SLM's surface has a phase $\Phi^{Bes-Vor}$ (Eq. 2.10) in addition to the mesh pattern. (3) The magnified view of the central intensity of (2). (4) The magnified view of one of the four first-diffraction-order of (2).

We found that when we choose the center-to-center spacing of the mesh to be the same as the size of the SLM pixel, which is $\sim$ 30 μm (2 cm/768 pixels), the diffraction angle of the first order obtained from the grating formula (Eq. 2.26) matches well with the experimental value. We believe that the mesh pattern in the SLM might correspond to the pixelation of the SLM (see Appendix D for a detail of the SLM).

By calculating the diffraction pattern in the far field using Fraunhofer diffraction theory, we observed that as much as 20% of light was reflected into the diffraction orders other than zero. Furthermore, the charges of the vortices in all diffraction orders are the same as the charge n set by the mask.

2.4.5 Tilt Control

The Bessel beam generated from the phase $\Phi^{Bes-Vor}$ in Eq. 2.10 can be steered away from the usual specular direction via an addition of a tilt phase, $\Phi^{Tilt} = \vec{k} \cdot \vec{r}$, to $\Phi^{Bes-Vor}$, i.e.,

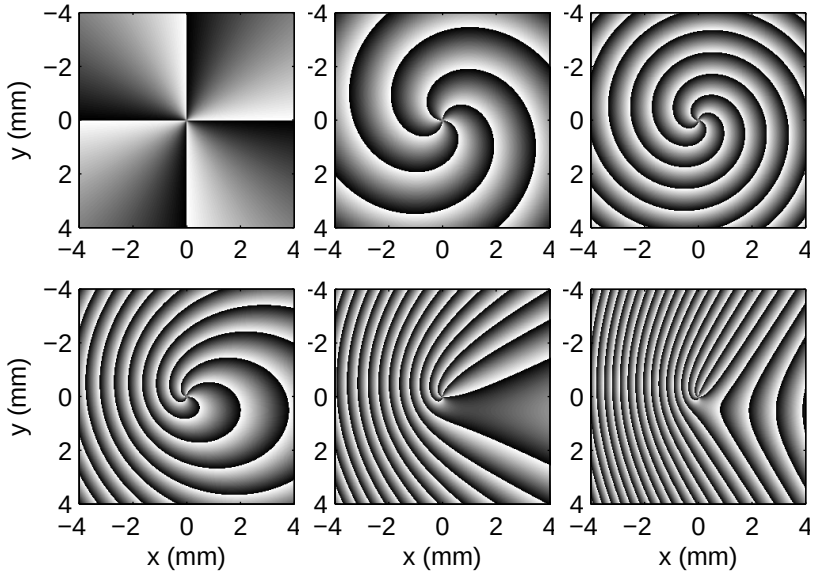

Figure 2.17: Phase mask produced from Eq. 2.31. All the masks contain the vortex of charge four. In the top row, $\vec{k} \cdot \vec{r} = 0$, and k_r of each figure is 0, 3.798 and 7.597 mm^{-1} from left to right. In the bottom row, $k_r = 7.597$ mm^{-1} corresponding to $r_p = 0.7$ mm, $\vec{k} = k_x \hat{x}$, and k_x of each figure increases from left to right.

$$\Phi^{Bes-Vor-Tilt}(r, \phi) = \left(n\phi - k_r r + \vec{k} \cdot \vec{r} \right) \bmod 2\pi, \tag{2.31}$$

where $\vec{k}$ is the wave vector of a virtual beam that makes an angle θ with the normal axis of the SLM and $\vec{r}$ a radial vector in the plane of the phase mask. The term $\vec{k} \cdot \vec{r}$ can be understood by first considering a special case when $\vec{k} = k_x \hat{x}$ such that $\vec{k} \cdot \vec{r} = k_x x$ as we have already described in Sec. 2.3, especially in Fig. 2.7b. When encoded into the SLM, the term $(k_x x) \bmod 2\pi$ produces an additional grating structure, as can be seen in the bottom row of Fig. 2.17. The grating deflects the Bessel beam across the x-axis. For the small angle approximation, the first diffraction order is deflected by an angle equals to $\theta = k_x/k$ as described in Sec. 2.3.

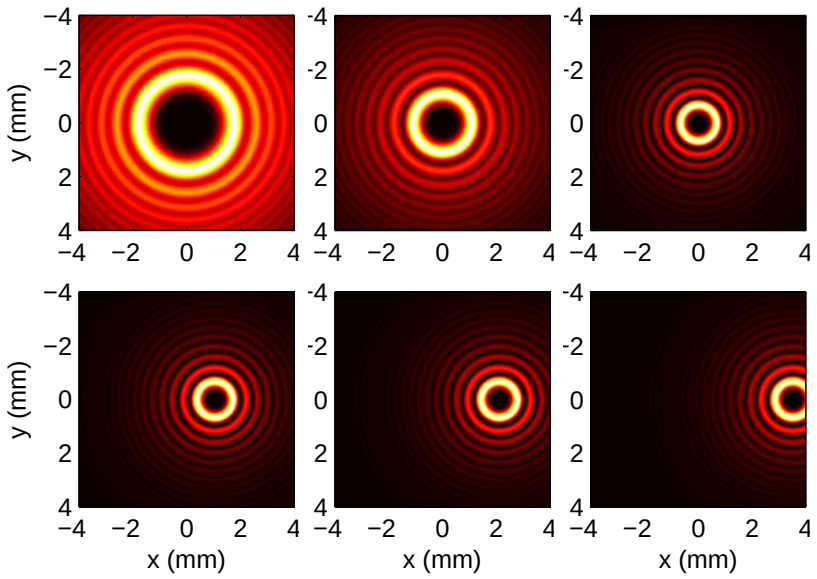

Figure 2.18: The figures show the intensity profiles corresponding to the phase masks shown in Fig.2.17. Three figures in the bottom row show the deflection of the Bessel beam across the $x-$ axis.

The discussion for the special case can be generalized to an arbitrary $\vec{k}$, i.e., a grating produced from the term $\vec{k}\cdot\vec{r}$ deflects the beam across the axis in the direction of the projection of $\vec{k}$ on the SLM's surface. When $\vec{k}\cdot\vec{r}\neq 0$, $\vec{k}$ makes an angle with the SLM surface, resulting in the modulated beam being deflected away from the specular direction. Thus, $\vec{k}\cdot\vec{r}$ provides a knob allowing the transformed beam carrying the vortex to be deflected through different angles in real time. When $\vec{k}\cdot\vec{r}=0$, the phase in Eq. 2.31 produces a non-deflected Bessel beam.

The phase masks calculated from Eq. 2.31 are shown in Fig. 2.17. All the masks contain the vortical charge of $n=4$. In the top row, $\vec{k}\cdot\vec{r}=0$, and the masks are shown in order of increasing strength of k_r from left to right. The values of k_r are 0, 3.798 mm^{-1} and 7.597 mm^{-1} respectively. In the bottom row of Fig. 2.17, $k_r = 7.597$ mm^{-1} and $\vec{k}\cdot\vec{r}=k_x x$. The values of k_x of each figure from left to right are 4.218 mm^{-1}, 8.436 mm^{-1} and 14.059 mm^{-1} respectively. Notice that the spiral phase pattern turns into a fork pattern, which resembles a grating structure as k_x becomes large. For each of these phase masks, we generated the corresponding

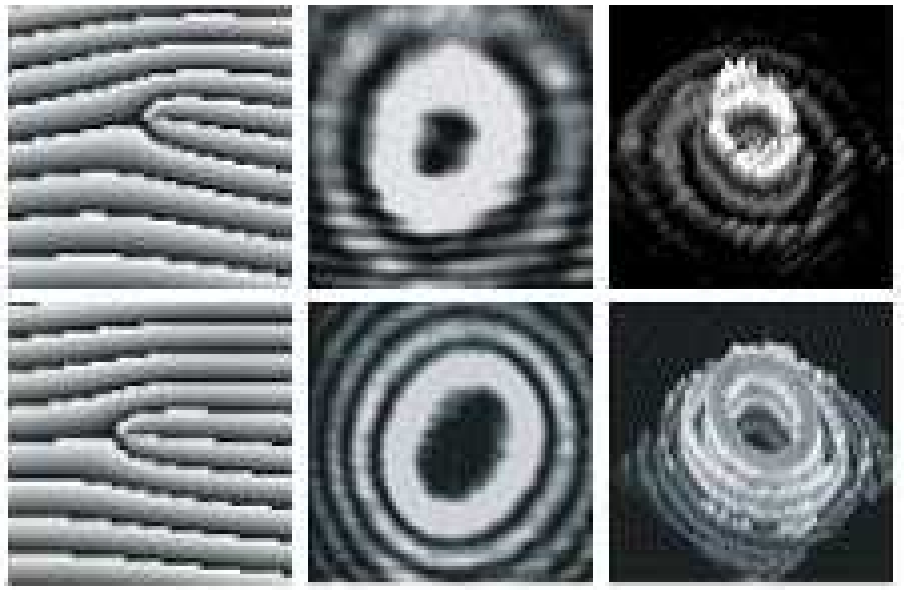

Figure 2.19: The phase masks used to produce two different sizes of the dark core of a J_2- Bessel beam. The first column consists of the actual phase masks including a term $\vec{k} \cdot \vec{r} \neq 0$. The peak radius ($r_p$) is 1.4 mm for the top, notice the larger amount of deviation from horizontal of the fork at the center of the mask due to the smaller magnitude of r_p. This results in a smaller hole. The parameter for the bottom is $r_p = 3.2$ mm resulting in a smaller bent fork pattern from horizontal for the singularity of the grating, causing a larger hole. The middle column is a 2D contour of the Bessel beam generated from the gratings to their left, where the intensity is represented by brightness. The column on the far right is a 3D profile of the hollow beam, where both brightness and height represent intensity. The inclination of the input laser beam with respect to the SLM surface results in ellipticity in the beam.

intensity pattern using a 2D angular spectrum as described in Appendix C.2. Each intensity pattern is shown in Fig. 2.18.

In the middle column of Fig. 2.19, we show two experimental Bessel beam profiles of k_r generated from masks with $\vec{k} \cdot \vec{r} \neq 0$. When we interfere these beams with a Gaussian beam, a spiral phase pattern or the fork phase pattern of the Bessel beam is revealed as seen in Fig. 2.20. Clearly, this is one method for identify the

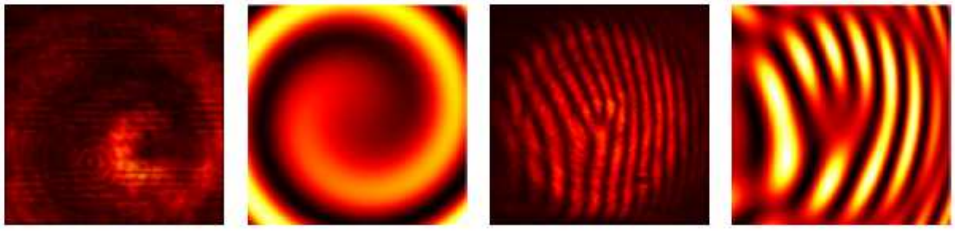

Figure 2.20: Interference patterns of $J_{n>0}$ Bessel beam with a Gaussian beam. From the left, the first and third panels are patterns obtained from the experiment; the second and fourth are simulations. The spiral interference patterns in the two left-most column reveal $n = 1$ as there is only one spiral of destructive interference. The fork interference patterns of the other two panels show that $n = 2$ because there are two destructive interference forking out from a constructive interference (compare to the left most column of Fig. 2.19). The spiral pattern is due to the Bessel beam colinear with the Gaussian beam, while the fork pattern is caused by the two beams intersecting at an angle.

value of vortical charge in a coherent beam. Note also, that the intensity profiles in the middle column of Fig. 2.19 are elliptical. The correction for the ellipticity is discussed in the following subsection.

2.4.6 Ellipticity Control

A Bessel beam produced from a phase mask with Φ^{Tilt} as described in the previous subsection normally has an elliptical profile as can be seen in Fig. 2.19. Another cause for this ellipticity is a non-normal incidence of the input laser beam to a surface normal of an optical element such as a lens, a SLM or an axicon. In the later case, an interested reader can follow the discussion in Ref. [104, 105] for more detail. In this section, we change the ellipticity of the Bessel beams along arbitrary axes by modifying the phase mask function $\Phi(r, \phi) = n\phi - k_r r$, where $r = (x^2 + y^2)^{1/2}$ and $\phi = \arctan(y/x)$. The modification starts from squeezing the mask along the x and y coordinates and follows by rotating the squeezed mask. For this modification, two coordinate transformations are used. First, the squeezing can

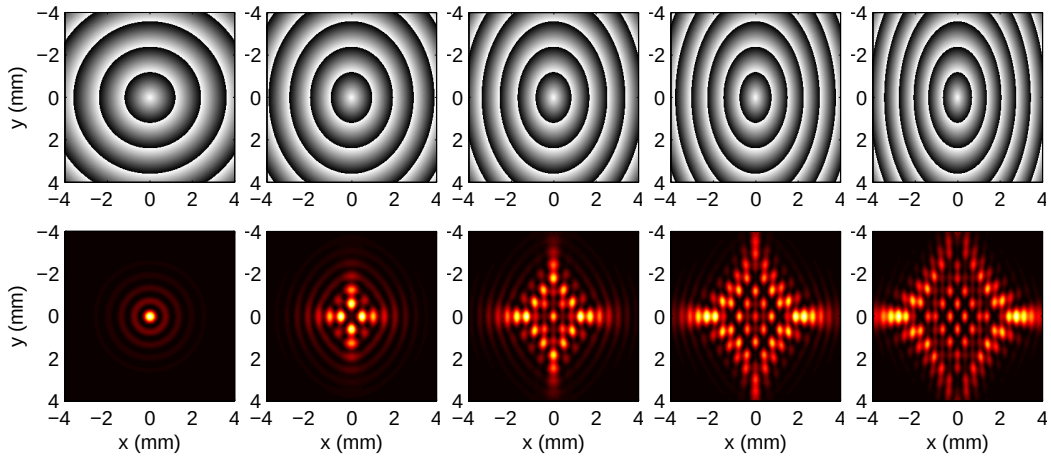

Figure 2.21: Squeezed conical phase masks (top row) and its simulated intensity profiles (bottom row). The masks are squeezed along the x axis in ascending order of the squeezing strength. Without squeezing, the mask produced a J_0 beam as shown in the leftmost column.

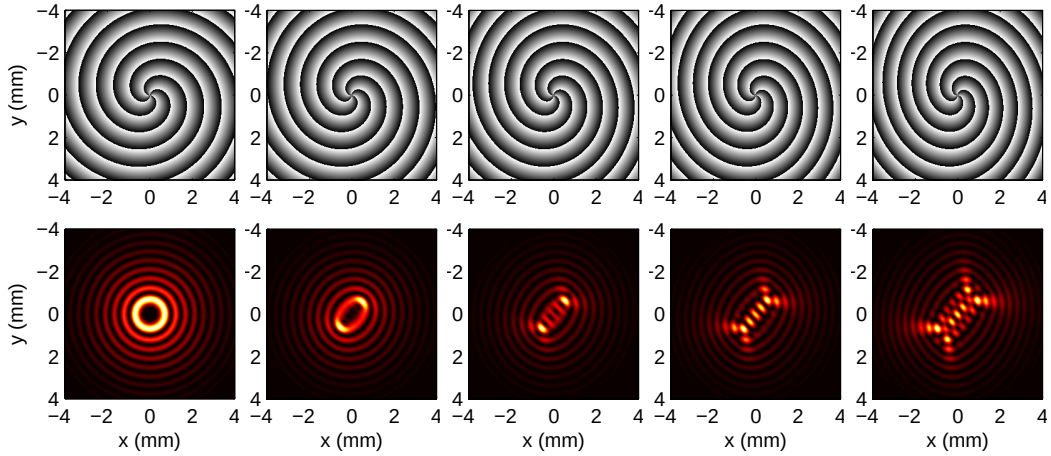

Figure 2.22: Squeezed J_4 phase masks (top row) and its simulated intensity profiles (bottom row). The masks are squeezed along the x axis in ascending order of the squeezing strength. Without squeezing, the mask produced a J_4 beam as shown in the leftmost column. Due to the cylindrical asymmetry in the squeezing, the vortex of charge 4 breaks up into four vortices of charge 1.

be achieved by scaling the coordinates $x \rightarrow x'$ and $y \rightarrow y'$, where

$$x' = \eta_x x, \tag{2.32}$$

$$y' = \eta_y y. \tag{2.33}$$

Second, a rotation through an angle ξ can be achieved by substituting $x' \rightarrow x''$ and $y' \rightarrow y''$, where

$$x'' = +x'\cos(\xi) + y'\sin(\xi), \tag{2.34}$$

$$y'' = -x'\sin(\xi) + y'\cos(\xi). \tag{2.35}$$

The double prime axes decribe the mask on the SLM. Thus, the rotated mask makes an angle of $+\xi$ (counter clock wise) with respect to the original unprime axis. The

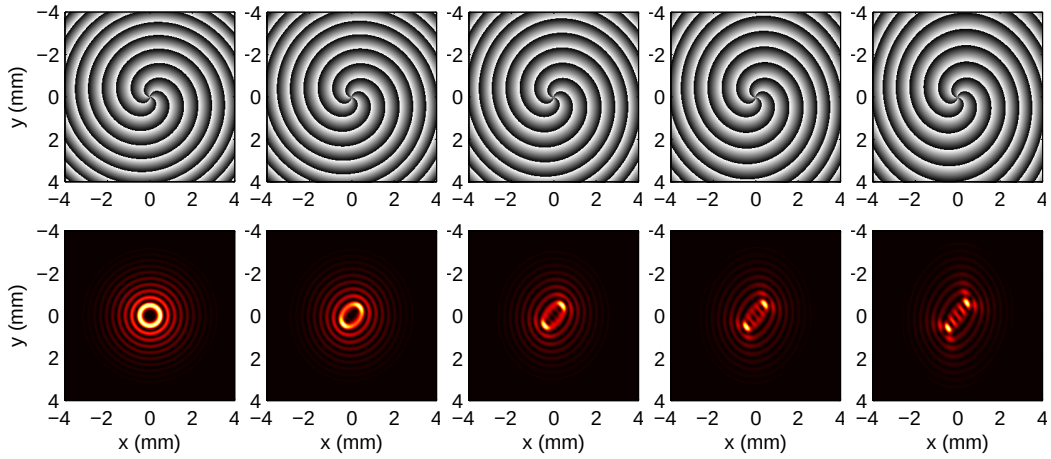

Figure 2.23: Phase profiles of a squeezed lens (top row) and the simulated intensity profiles of a J_4 Bessel beam passing through the lens (bottom row). Due to the cylindrical asymmetry in the squeezing, the vortex of charge 4 breaks up into four vortices of charge 1.

parameters η_x and η_y can be used to control the aspect ratio of the mask along the unprime axes as well as the strength of the ellipticity along the x'- and y'- axis respectively. By squeezing the mask, the phase shift of $k_r r'$ can be thought of as originating from an elliptical or a tilted axicon.

The ellipticity can also occur in the imaging system when a physical lens is used to deliver the output light to an imaging device. In this case, the radial coordinate r in the the phase function of a lens (Eq. 2.29) can be modified in the same manner by substituting the unprime with prime axes. This modification can also be thought of as a rotation of the imaging lens around an axis perpendicular to the propagation direction of the output light.

The resulting intensity profiles of a Bessel beam that passes through an elliptical axicon, picking up a squeezed conical phase shift, are shown in Fig. 2.21 and Fig. 2.22 for J_0 and J_4 respectively and that of an elliptical lens is shown in Fig. 2.23. The strengths of the ellipticity are shown in ascending order from left to right. The ellipticity only changes along the horizontal axis ($\xi = 0$, $\eta_x \neq 0$ and $\eta_y = 0$) and the simulations are based on the 2D angular spectrum method (see Appendix C.2). Notice from the intensity profiles in Fig. 2.22 and Fig. 2.23 that a vortex of $n = 4$ in the leftmost column breaks up into four smaller ($n = 1$) vortices in the column to the right as the squeezing strength increases, owing to the cylindrical asymmetry in the squeezing.

When using a Bessel beam as an atomic guide, we generated the tunnel from a Gaussian beam that made $\sim 3^\circ$ angle with respect to the normal of the SLM. The adjustment we made to our mask's aspect ratio [106] to correct for the ellipticity of the beam was $\eta_x/\eta_y = 1.03$.

2.4.7 Zeroth Diffraction Order from a Binary Grating

One of the simplest gratings to fabricate is a binary amplitude grating. By *binary* we mean that the grating has only two levels, 0 and π or open and blocked; the latter corresponds to what we mean by an *amplitude grating*. As we have seen in Fig. 2.1, the phase profile of a Bessel beam is a conical helix. If we choose to assign the area with a phase from 0 to π to transmit light and the area from π to 2π to block light, the binary mask that generates the Bessel beam will be in the form of a spiral pattern as seen in the upper left corner of Fig. 2.24 for $n = 1$. The binary mask produced in this manner is called a *Fresnel zone plate* [107]. If printed on a transparent sheet, such a mask will transform a laser beam passing through it into a Bessel beam with the intensity profile as shown in the upper right corner of Fig. 2.24. Combining the conical helix phase with the grating mask that deflects light, we get the fork pattern as we have already seen in Fig. 2.19. The zone plate of such a pattern is shown in the lower left corner of Fig. 2.24 and the resulting intensity profile is shown in the lower right corner of the same figure. We note that

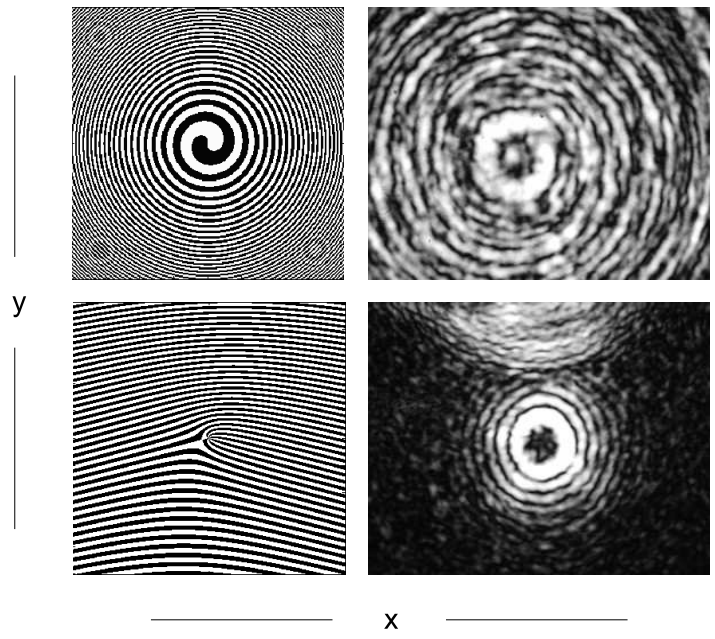

Figure 2.24: The binary amplitude masks (left column) and the resulting intensity profiles (right column). The mask in the top row is created from a conical-helix phase mask with $n = 1$ and with $\vec{k} \cdot \vec{r} = 0$. The intensity profile to its right is a combination of the specular beam and all diffraction orders generated from the mask. The mask in the bottom row is generated from a phase with $n = 6$ and $\vec{k} \cdot \vec{r} = k_y y \neq 0$. The intensity profile to its right is the J_6 beam from the first diffraction order, seen together with a fraction of specular profile above it.

the intensity profile in the upper right corner is resulted from a combination of all diffraction orders including the Gaussian specular beam, diffracted into one beam. In the lower right corner, only the first order and some part of the zeroth order are shown, all diffraction orders are separated due to the addition of a deflection grating to the spiral pattern.

We can simulate this separation numerically with our usual angular spectrum method (see Appendix C.2). For example, the resulting intensity and phase pattern diffracted from a binary amplitude fork of charge $n = 1$, as demonstrate experimentally by Vasara *et al.* [79], is shown in the left image of Fig. 2.25. The center and right images show the intensity and phase from our simulation. The calculated re-

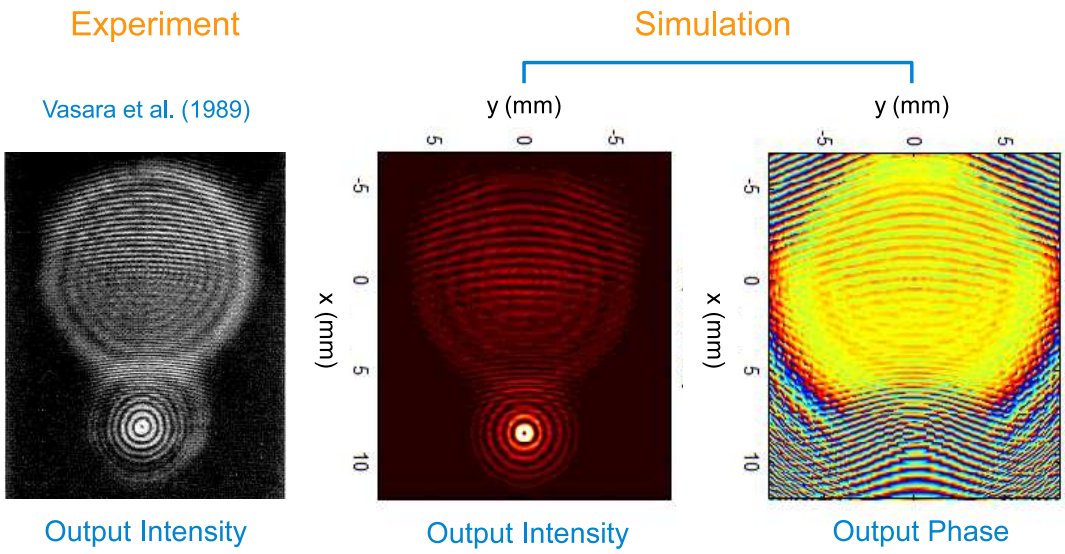

Figure 2.25: Comparison of the J_1- intensity pattern from the experiment (left image) and the numerical simulation (middle image) generated from the binary amplitude mask. The mask diffracts the J_1- Bessel beam into the first diffraction order away from the zeroth order pattern above it. The simulated phase pattern of the intensity in the middle image is shown in the right image. The simulations were performed using the 2D angular spectrum method as described in Appendix C.2. The figure in the left image is reproduced from Ref. [79].

sult in the middle image of Fig. 2.25 is in good agreement with the experiment. The simulation correctly produces the zeroth and first diffraction orders from Vasara's binary amplitude mask. For the amplitude mask, the input power delivered to the mask is not efficiently transfered to the first order. Vasara pointed out that a change from the binary amplitude mask to a binary phase mask improves the efficiency. To increase the efficiency of the binary phase mask further, the number of the allowed phase shift levels, generally known as phase quantization levels, need to be increased. From Fig. 2.26 for a Bessel beam of order 7, the efficiency of the power transfered to the first diffraction order is shown to be improved significantly when the mask is changed from the binary type (left image) to a type with 64 quantization levels (right image). In-depth measurements of the efficiency of the SLM to generate a Bessel beam are discussed in the sections that follow.

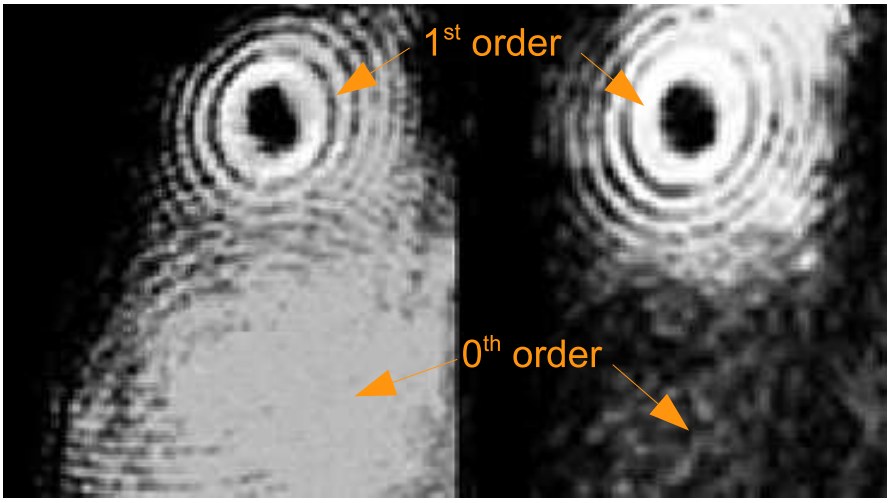

Figure 2.26: By adjusting the bias voltage across the liquid crystals, we can control the phase shift produced by the grating. On the left, the phase modulation is approaching binary phase quantization, and we get a significant amount of light in the zero order diffraction beam. On the right, phase quantization level is approaching 64, and almost all the power is in the first order diffracted beam, while only a small amount remains in the zero order.

2.5 Vortex Quality

We defined the *quality* of the vortex mode by its suitability for atom containment and transport. For best utility, the intensity of the first ring, I_{fr}, must be high and uniform. The high intensity must not only provide a confinement potential that exceeds the kinetic energy of the atoms, it must ensure a steep field gradient to maximize the dipole force and minimize the time atoms spend in the non-zero intensity region of the tunnel. This will allow long, nearly heat-free containment. Uniformity will minimize unwanted leaks and motional excitation due to holes or imperfections in the wall. For single-vortex beams, a third condition may be desirable, a pure mode. Pure modes can be focused without destruction of the axial hole, allowing funnels to be created. Funnels can be used to load atoms from a cold source into neutral atom circuits on a chip or other restricted volumes such as hollow-core fibers.

To probe the factors contributing to the quality, we performed three investigations. First, we measured the total and differential power conversion efficiency (from an input Gaussian beam) as a function of the *spatial resolution* (N)[4], the *phase quantization level* (G) and the *vortex charge* (n). This was done by measuring the power in the first ring, $P_{fr}(N, G, n)$, while N, G, and n were changed systematically. The results are shown in Fig. 2.29 - 2.31. To determine the uniformity, we measured P_{fr} as a function of angle around the ring and as a function of r across the ring. The values of N and G for these measurements were fixed at 768 and 256 respectively and the vortex charges studied were $n = 1$, 5, 10 and 15. These results are displayed in Figs. 2.32 and 2.33.

Finally, for fixed N and G, the first ring intensity ($I_{fr} = P_{fr}$/annular area) as a function of n was studied both experimentally and theoretically to determine optimum values for N, G, and n, consistent with the physical constraints of the SLM. Figures 2.34 and 2.35 summarize our findings.

2.5.1 Measuring Bessel-Beam Conversion Efficiency

In this subsection, we described how the vortex is generated in our experiment, the phase mask parameters important for the Bessel beam conversion efficiency and the procedure to measure the conversion efficiency.

Our hollow Bessel modes have been generated effectively with binary holographic phase masks [84]. As mentioned earlier, a binary phase mask has two regions that have a relative phase shift of π. Hollow Bessel modes, however, can be generated with ten times higher intensity in the first ring with a 6-bit phase mask, 128 regions between 0 and 2π, with phase steps of 0, $\pi/64$, ..., $127\pi/64$ [85]. We will refer to masks with a larger number of regions as having higher *phase quantization*. Examples of 8-bit phase masks (256 phase steps) for producing a vortex and a Bessel beam of charge 1 is displayed in Fig. 2.27, along with the corresponding transverse intensity profiles of the beams generated.

[4]We define N as the number of the effective pixels in the width of a (square) phase mask. See details in Sec. 2.5.1.

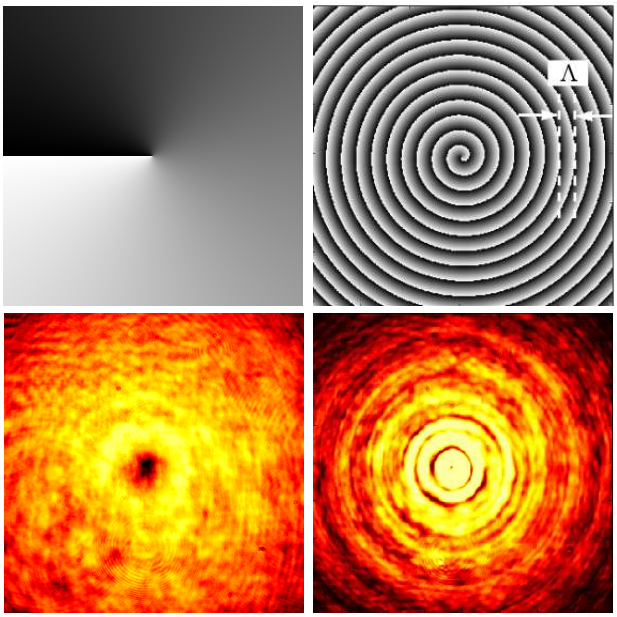

Figure 2.27: Phase masks and cross sections of the converted beams for a charge 1 vortex embedded on a Gaussian beam leading to a vortex mode (left column) and a J_1 mode (right column). The parameter Λ ($= 2\pi/k_r$) indicates the physical size of a 2π phase range on the mask (see Sec. 2.3).

The experimental arrangement employed to create the vortices is shown in Fig. 2.28 (similar to that in Ref. [85]). From the figure, the linearly polarized Gaussian 780-nm Ti-Saphire laser is expanded and collimated by a pair of lenses to have a width of 2 cm in order to cover the active area of the SLM. The SLM shifts the phase of the incident beam according to the digitized pattern received from a computer. This digitized pattern is generated to produce a desired phase mask as discussed in the previous sections. Note, that the laser is tuned near 780 nm, but a few giga-Hertz to the blue of the Rb $5S_{1/2} \rightarrow 5P_{3/2}$ resonance line. Thus, the dipole force confines the Rb atoms to the lowest intensity portion of the beam – typically the central dark core. The SLM, configured for 780 nm, was used to maximize beam conversion to allow phase shifts from 0 to 2π for VGA inputs of 0 to 255. While the SLM was used in a reflection mode, for these experiments, only non-deflected vortex beams ($\vec{k}\cdot\vec{r} = 0$) were created. Finally, the SLM had a resolution of 768×768 pixels. We denote the spatial resolution ($N \times N$) by N, with the highest resolution

given by $N = 768$. Each pixel had an 8-bit dynamic range between 0 and 2π. We label the phase quantization level by the number of shades of gray and denote it by G, with the highest resolution given by $G = 256$.

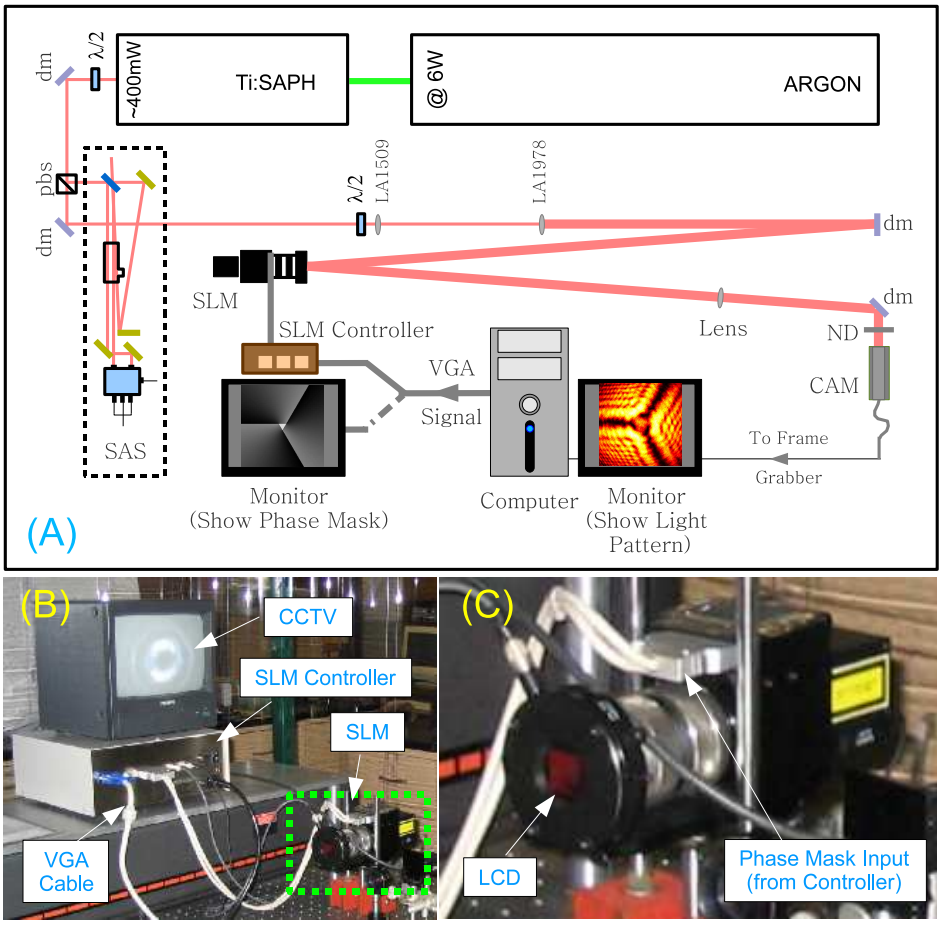

Figure 2.28: Experimental arrangement consisting of (1) a Ti-Saph laser beam, tuned near 780 nm, which is expanded and collimated by two lenses (LA1509 and LA1978) before being sent to the SLM; (2) neutral density filters (ND) to control the intensity of the modulated beam before being detected by a CCD camera and (3) a PC to process the image and control the SLM. Other optical elements in the figure are: the dielectric mirror (dm), the polarizing beamsplitter cube (pbs), the half-waveplate ($\lambda/2$), the argon laser (ARGON) used to pump the Ti:Saph laser, the CCD camera (CAM), and the saturated absorption spectrometer (SAS).

In our experiments, we studied the quality of Bessel modes as N and G were

varied. We changed N from 768 to 48 by grouping pixels together. For example, when 16 pixels are grouped (4×4), N is reduced to 192 (= 768/4). We stepped the resolution down by dividing 768 by 2, 4, 8 and 16. The value of G was changed by reducing the number of phase steps between 0 and 2π. We tested the quality for G = 2, 4, 8, 16, 32, 64, 128 and 256. For each value of N and G, the influence of the vortex charge on the quality was tested as well for n = 1, 2, 3, 4, 5, 10 and 15.

Bessel phase masks were created corresponding to Eq. 2.10 with k_r = 5.5 mm^{-1}, which corresponds to a first ring radius for n = 1 of about 330 μm. The mask matrix for each set of triple values (N, G, n) was stretched symmetrically to fill the SLM screen, which was a square that is approximately 2 cm on each side. The quality of the Bessel mode was monitored with a CCD camera, and digital images were captured with a frame grabber. The transverse intensity profile of the Bessel mode for each mask was extracted after averaging 45 frames which took about 1.4 s. To monitor the long-term laser fluctuation, a reference profile was taken with N = 768, G = 256 and n = 1, before and after each set of (N, G, n) values obtained. The laser power fluctuated by $\leq \pm 5\%$, during the runs with a period of 2 to 4 min.

The ability of the Bessel mode to confine and transport atoms was tested for selected values of N, G and n with cold (T $\sim$ 500 μK) Rb atoms released from a standard vapor-loaded magneto-optical trap (MOT) described in Sec. 3.1.

2.5.2 Total Efficiency

We estimated the conversion efficiency for generating a non-deflected Bessel mode from an TEM_{00}-mode by comparing the input and converted powers using a phase mask with N = 768, G = 256 and n = 2. The converted power was measured to be about 86% of the input power. The reflective and absorptive loss of the SLM when configured as a mirror (a constant phase across its surface) was 8%. The additional 6% loss when a Bessel mask is in place is presumably due to diffraction into other orders. Of the 86%, about 80% of the power goes into the first 3 rings, with about 30% going into the first ring, for n = 2. Thus, $\sim$ 60 mW can be diffracted into the first Bessel ring from a 200 mW input beam. While the total

efficiency changes little as N, G and n are changed, the power converted into the first ring grows as $\sqrt{n}$, as we discuss below.

2.5.3 Differential Efficiency

2.5.3.1 Fixed Spatial Resolution

Figure 2.29 shows $P_{fr}(N = 768, G, n)$ as G and n are varied. The curves exhibit two trends. First, all curves saturate at a relatively low value of G, with P_{fr} increasing by a factor of 2 or 3. The phase quantization level at which saturation sets in, however, increase monotonically with charge. The second trend we observe, is that higher charges produce more power within the first ring. For example, $P_{fr}(N = 768, G = 8, n = 1)$ is only 20% of $P_{fr}(N = 768, G = 8, n = 15)$. While P_{fr}^{sat} (the saturation power) increases with n, dP_{fr}^{sat}/dn decreases. As will become clear below, $dP_{fr}^{sat}/dn \propto 1/\sqrt{n}$ so that $dP_{fr}^{sat}/dn \to 0$ as $n \to \infty$. While the largest possible charge appears to be desirable to maximize P_{fr}, at $n = 15$ an 8-bit mask (256 phase steps) does no better than a 4-bit mask (16 steps). As we discuss in Sec. 2.5.3.3, this is due to spatial resolution.

2.5.3.2 Fixed Phase Quantization Level

Figure 2.30 shows $P_{fr}(N, G = 256, n)$ as N and n are varied. In distinction to Fig. 2.29, these curves do not saturate up to charge 15. Rather, they increase roughly as $\sqrt{n}$. At charge 1, P_{fr} is independent of N and G. However, as n increases, the curves begin to separate. At charge 10, for example, P_{fr} is 50% larger for $N = 96$ compared with $N = 48$. At the same time, P_{fr} is the same for all values of $N \geq 96$. At charge 15, $P_{fr}(N = 96)$ begins to fall below the curves for the higher values of N. We again conclude that it is desirable to have a large n. However, in contrast to P_{fr}'s dependence on G, the minimum value of N to reach the maximum P_{fr} depends on n.

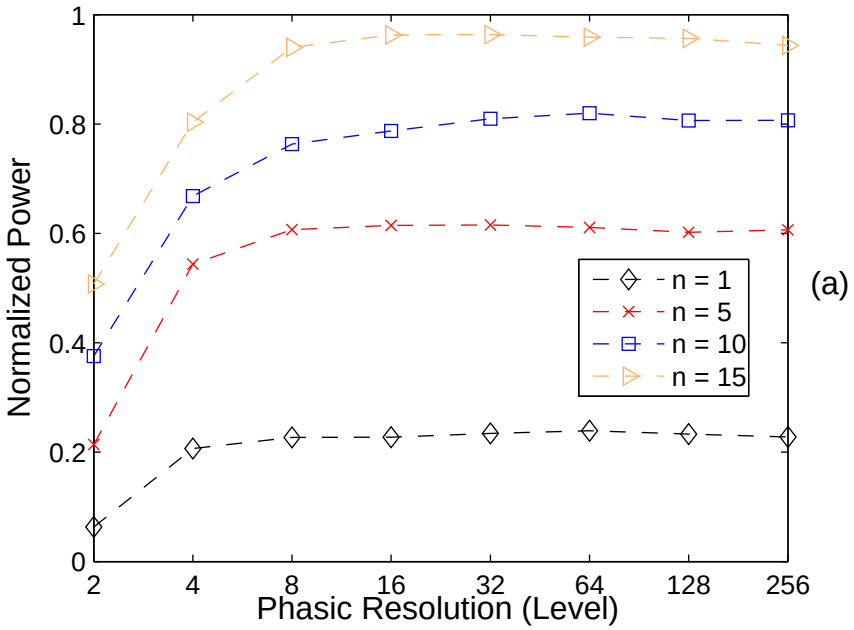

Figure 2.29: Normalized power in the first Bessel ring, $P_{fr}(N, G, n)$, for $k_r = 5.5$ mm^{-1} as N, G and n are varied: (a) fixed spatial resolution, $P_{fr}(N = 768, G, n)$.

2.5.3.3 Fixed Charge

Figure 2.31 shows $P_{fr}(N, G, n = 1)$ as N and G are varied. The curves all saturate at $N = 96$, where the intensity jumps by about a factor of 4 in going from $G = 2$ to $G = 4$. The curve for $G = 4$ is within 87% of the curves for higher G values, which all nearly coincide. This is consistent with what we learned from Fig. 2.29: G needs to be no larger than 8 or 16 to produce the maximum power in the first ring.

2.5.3.4 Discussion

The fact that saturation sets in at $N = 96$ over a wide ranges of vortex charge values allows us to estimate the minimum number of pixels (or effective pixels) required to define a 2π phase range on the mask. That is, we can determine the minimum number of pixels to define the range Λ indicated in the upper right hand image in Fig. 2.27. To make this determination, we recognize that the number of 2π phase ranges across half the mask is given by $k_r r_m/2\pi$, where r_m ($= 0.01$ m) is the

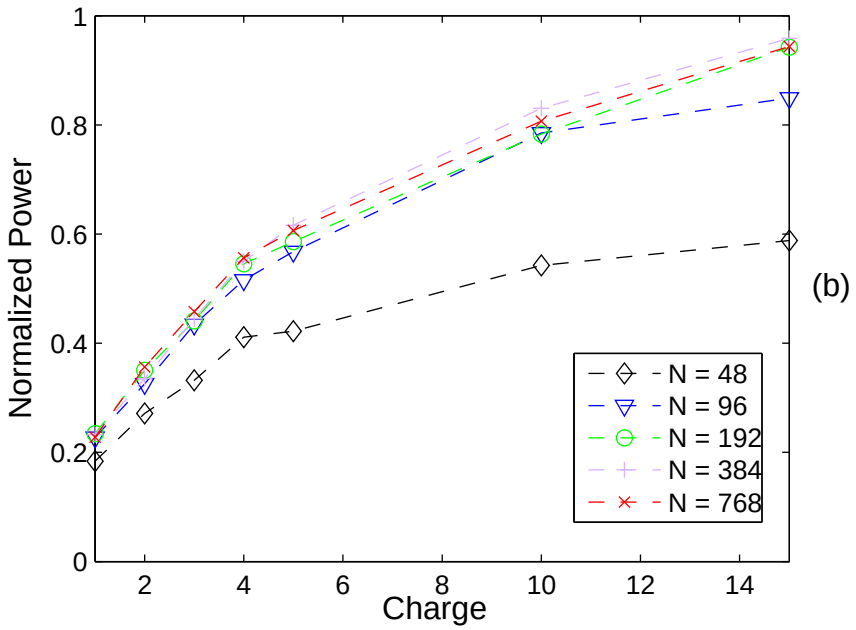

Figure 2.30: Normalized power in the first Bessel ring, $P_{fr}(N, G, n)$, for $k_r = 5.5$ mm^{-1} as N, G and n are varied: (b) fixed phase quantization levels, $P_{fr}(N, G = 256, n)$ showing an approximate $\sqrt{n}$ trend as discussed in the text.

radius of the phase mask. For $k_r = 5.5$ mm^{-1} and $n = 1$, there are 9 ranges. There are twice as many ranges, 18, across the entire mask. This implies that to create a quality vortex, ≈ 5 pixels ($\approx 96/18$) are required to define Λ. Five pixels per 2π range appears to hold for higher charge values as well. At some point, however, we would expect more resolution to be required to define more closely packed features. This may be why the $N = 96$ curve in Fig. 2.30 begins to fall away from the pack at $n = 10$, while the curves for $N = 192$ and higher continue to follow the $\sqrt{n}$ trend. More complicated vortices, as will be discussed below, could also require higher resolution. For low charge, however, 5 pixels per 2π range is a good rule of thumb.

2.5.4 Ring Uniformity

As mention above, to contain atoms without loss or heating, the first ring must be uniform and have no holes. We determined the uniformity of the first ring by

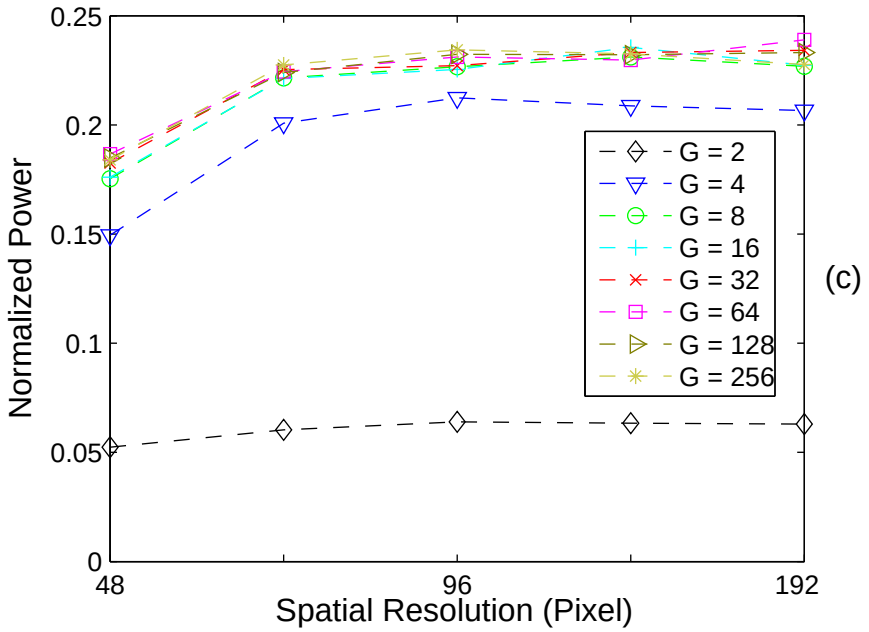

Figure 2.31: Normalized power in the first Bessel ring, $P_{fr}(N, G, n)$, for $k_r = 5.5$ mm^{-1} as N, G and n are varied: (c) fixed charge, $P_{fr}(N, G, n = 1)$.

comparing the average power per camera pixel for small areas around the ring. The area consisted of a 2° wedge bounded by the full width at half maximum of the ring determined by its front and back slopes. The results for a few values of n within the range from 1 to 15, $N = 768$, $G = 256$ and $k_r = 5.5$ mm^{-1}, are displayed in Fig. 2.32. We first notice that there are no holes in the ring; the intensity drops close to zero at no location around the ring. The resolution of this determination is 8.6 μm, the size of the camera pixel. We next notice that while there are no holes in the ring, the intensity fluctuates with angle. Except for $n = 10$, these fluctuations are 30% or less. There are at least two sources of this fluctuation. The first is a digital effect caused by the fact that the intensity within the wedged area was determined only by those pixels entirely within the wedge boundaries; pixels partially enclosed were ignored. Thus, the number of pixels included in the count varied with angle. This causes small, non-periodic, variations in the intensity that appear as noise in the curves. There is also a larger fluctuation that is periodic, with number of peaks and troughs equal to the number of charge, suggesting that the periodic fluctuation is

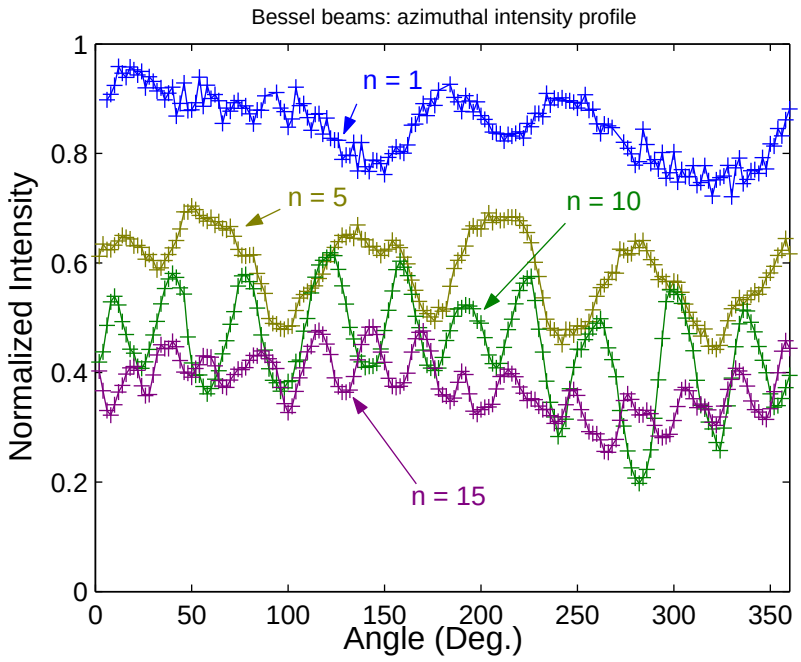

Figure 2.32: Intensity within a small wedged area for $n = 1, 5, 10$ and 15, with $N = 768$, $G = 256$ and $k_r = 5.5$ mm^{-1}, as a function of angle around the ring showing no holes in the profile. The area consisted of a 2° wedge bounded by the full width at half maximum determined by the front and back slopes of the ring. The large periodic fluctuations are due to reflection between the input and generated beams as discussed in the text.

set by the properties of the phase mask. We have confirmed this through numerical calculations, where the Bessel beam was calculated using the 2D angular spectrum method as previously discussed in Sec. 2.4.3.

Finally, we notice that the average intensity decreases with n. This is due to two complementary effects. First, for fixed k_r, the radius locating the peak of the first ring increases with n. At the same time, the width of the ring increases with n. Both of these effects can be seen in Fig. 2.33 where we plot the intensity profile over the first ring for several values of n[5]. We show in the next section that this is not a limitation.

[5]An example of MATLAB codes that can be used to generate intensity profiles is given in Appendix G.11.3 and G.11.4.

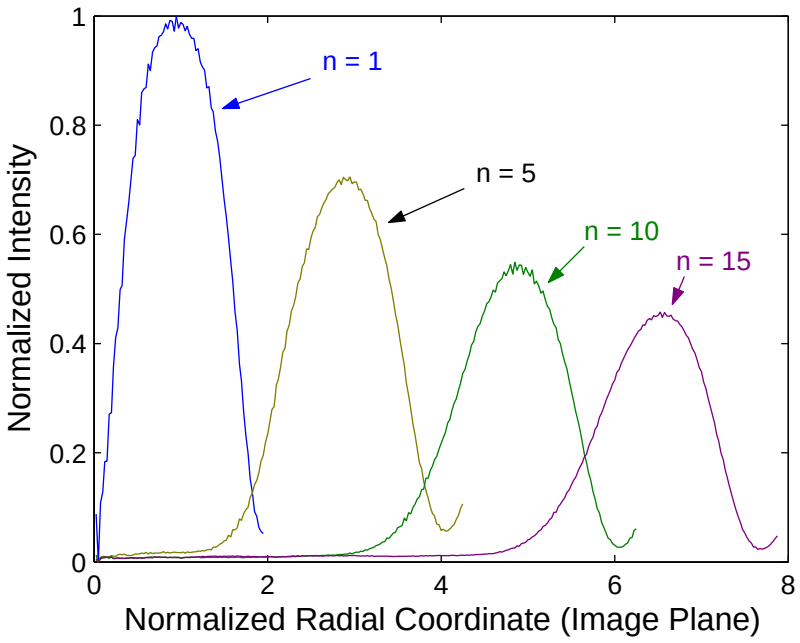

Figure 2.33: Intensity profiles of the first Bessel ring generated with $k_r = 5.5$ mm^{-1} for $n = 1, 5, 10$ and 15 as a function of normalized radial coordinate, where one unit on the axis corresponds to 330 μm, showing the peak position and the width increasing with n. These curves correspond to $N = 768$ and $G = 256$.

2.5.5 First Ring Power and Atom Confinement

As mentioned in the introduction, best confinement results from the highest intensity in the first ring. We concluded from our efficiency study that the highest power in the first ring is reached for the largest n. However, there is a technical issue that must be addressed when generating large n, i.e., the radius increases with n. Consider the rings for $n = 1$ and $n = 15$ in Fig. 2.33, which were generated with the same k_r. The radius of the $n = 15$ ring is about 8 times larger than that for $n = 1$ ring (~ 2.8 mm compared with ~ 0.35 mm). Worse, the peak intensity for the $n = 15$ ring is $\sim 60\%$ smaller than the intensity of the $n = 1$ ring. This is correctable by reducing the peak radius, r_p, using a focusing lens while maintaining the beam power. In Fig. 2.34 we compare the intensity of several rings after a lens was used to focus the rings to the same size. It is clear that as the radius shrinks, the area is compressed, as well, causing the intensity to increase with charge; the

peak intensity of the $n = 15$ ring is now about 20 times larger than that of the $n = 1$ ring. The radial profiles in Fig. 2.34 were obtained from the 2D intensity profiles of the focused Bessel beams taken at a distance such that all their peak radii are equal to 330 μm, the peak radius of the J_1-Bessel beam in Fig. 2.33.

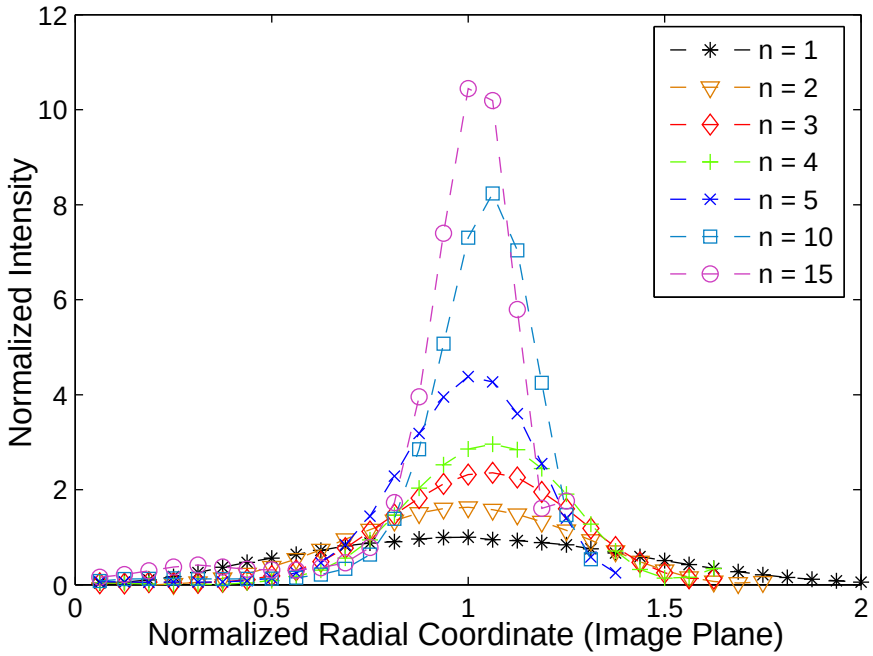

Figure 2.34: Modified intensity profiles of the profiles from Fig. 2.33. The higher charge rings are focused by a converging lens so that all peaks coincide at a normalized radius of 1, where one unit on the axis corresponds to 330 μm. Clearly, the peak intensities grow with n while the widths decrease. Compare with Fig. 2.33. The radial profiles were obtained from the 2D intensity profiles of the focused Bessel beams, captured by a CCD camera after the lens. The 2D profiles were converted to radial profiles via the same procedure as mentioned in the caption of Fig. 2.33.

It is also possible to generate Bessel modes with higher charge and smaller radii directly by increasing k_r. This is shown in Fig. 2.35. Increasing k_r leads to resolution issues as can be understood by comparing the profiles in Figs. 2.34 and 2.35. While in Fig. 2.34 the intensity increases monotonically with n, in Fig. 2.35 it increases initially but begins to decrease between $n = 4$ and 5. There are two factors that contribute to the anomalous reduction. One is the finite resolution discussed

earlier. As k_r increases, the radial spacing, $\Lambda = 2\pi/k_r$ (see Fig. 2.27), decreases. When the number of pixels used to define Λ drops below 4 or 5, the maximum power in the first ring, P_{fr}, can no longer be reached and P_{fr} stops increasing prematurely. A second aspect of this anomaly that is true for the aperture limited beam only, is also associated with the decrease of Λ. As Λ decreases, the number of Bessel rings generated by the mask increases. These additional higher order rings steal intensity from the lower orders. In addition to the resolution issue, large k_r can lead to the breakup of the vortex into smaller vortices. Typically, the smaller vortices have charge 1 so that the number of vortices generated in the breakup is equal to n. This tends to occur when there is an asymmetry in the phase of the beam at the SLM interface. This will happen, for example, when a Gaussian beam strikes the SLM at an angle other than normal. The discussion of this breakup was done at the end of Sec. 2.4.6.

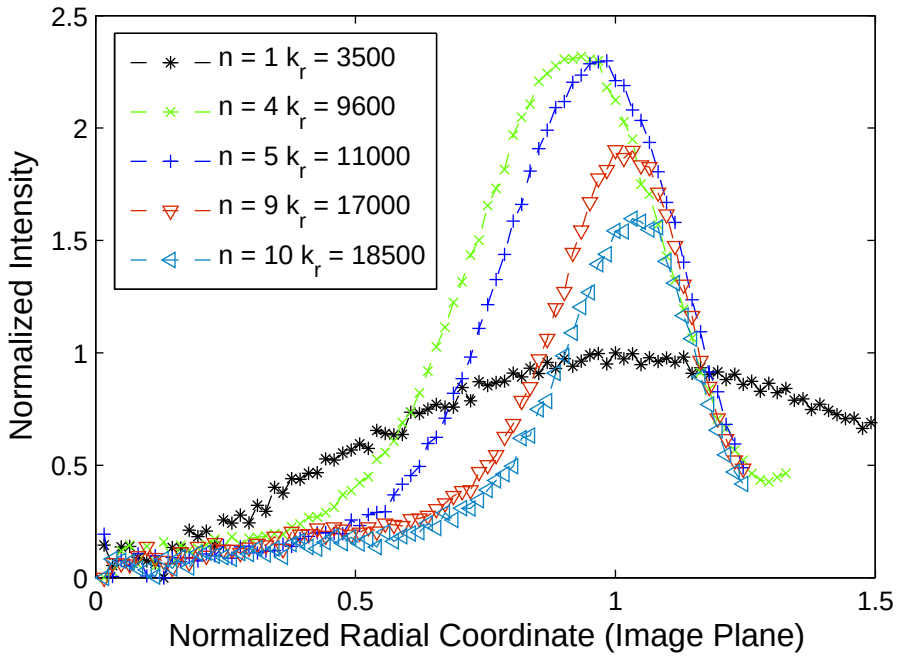

Figure 2.35: Intensity profiles of the first Bessel rings as a function of n for different k_r values such that the peaks coincide at a normalized radius of 1. One unit on the axis corresponds to 330 μm. The units of k_r are m^{-1}. Compare with Fig. 2.33 and 2.34.

We confirmed that larger n values lead to better confinement by monitoring the containment efficiency for MOT-temperature Rb atoms in tunnels created with $n = 1 - 5$. This was done for fixed ring radius and for k_r in the range of $\sim 5 - 10$ mm^{-1}. The tunnel intensities were set so that the confining potential and the temperature of the atoms were about the same for $n = 1$. Thus, the atoms could not be contained efficiently in $n = 1$ tunnels. The confinement efficiency increased dramatically[6] with increasing n. According to our observation, by looking at the column density of atoms inside the tunnel along the tunnel's cylindrical axis, the $n = 4$ and $n = 5$ tunnel can hold the atoms for longer time ($\gtrsim 80$ ms) compared to the tunnel with lower n ($\lesssim 60$ ms). Figure 2.36 shows atom confinement for $n = 4$. The arrangement used to capture the image of the atomic cloud is shown in Fig. 3.13.

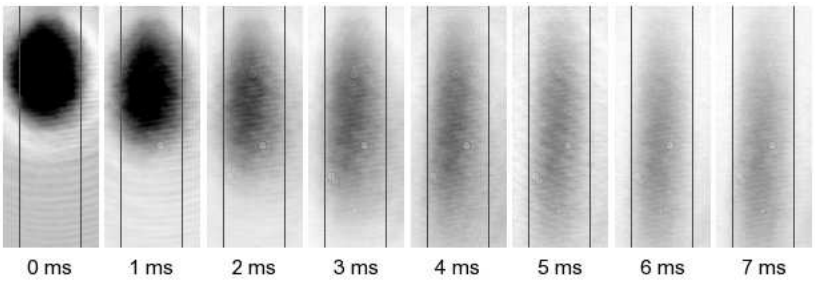

Figure 2.36: A cloud of Rb atoms is guided for at least 20 ms inside a Bessel beam with $n = 4$, $N = 768$ and $G = 256$. The cloud has a Gaussian width of 1 mm. The power of the beam in the first ring is ~ 60 mW. The Bessel beam is generated from $\Phi^{Bes-Vor}$ expressed in Eq. 2.10 with $k_r = 8.3$ mm^{-1}. Viewed perpendicularly to the propagation direction of the Bessel beam, the cold atom cloud expands and falls under gravity and takes the shape of the tunnel formed by the first ring of the Bessel beam. Times are the hold times in the tunnel. For the probe beam arrangement, see the diagram in Fig. 3.13B

[6]We note that the data that leads to this confirmation were lost in the process of data transfer among computers. However, it can be seen clearly from Fig. 2.35 that the peak intensity, which is related to the strength of the optical potential used to confine atoms, increases with increasing n up to $n = 5$.

While focusing appears to work better than increasing k_r with regards to the spatial resolution, we point out that focusing is also limited by resolution issues. As we have already shown, Bessel modes with larger n are physically larger, for fixed k_r (see Fig. 2.33). Generating larger modes that are pure, becomes increasingly more difficult as n grows because of truncation of the beam. This impurity manifests itself as a premature destruction of the mode upon focusing. At the same time, collimated beams with larger n propagate for shorter distances. This might be due the the fact that a slight cylindrical asymmetry in the collimation process after reducing the size of the beam causes the vortex of large n to break up. The asymmetry can arise from several factors, e.g., diffraction disturbances from the edge of the square aperture, the ellipticity in the Bessel beam, and the mixed phase and amplitude modulation produces by the SLM. We discussed a similar issue previously in Sec. 2.4.1. Considering all the limitations we mentioned, the optimum Bessel tunnel with a diameter of 1 mm that is suitable for confining atoms and can be generated without focusing, is generated by a mask with $n = 4$, $k_r = 8.3$ mm^{-1}, $N = 768$ and $G = 256$.

2.6 Exotic Vortices

From the quality measurement presented in the previous section, it is clear that high-quality vortices can be embedded in a laser beam with a phase mask with $N = 96$ and $G = 4$. This opens the possibility of embedding more exotic vortex structures in laser beams. For example, using the full 768×768 resolution of the SLM, it would be possible to divide the full screen into eight smaller areas and produce eight vortex beams with the maximum possible intensity. Figure 2.37 shows an example where four vortices are placed in one beam. In this section we will examine some of the possibilities for creating beams with multiple point singularities (ordinary vortices) and multiple line singularities. In order to appreciate how such structures are constructed, we will present two different methods of embedding complex vortices in a single laser beam. The first we call tiling, where the SLM is divided into several sections each containing a single-vortex phase mask as in

Fig. 2.37. In this case each section of the mask works independently. The second method, introduced by Indebetouw [108] and Rozas *et al.* [109], we refer to as nesting, which involves a composite phase mask that is not separable into individual masks. The latter method is key to creating multiple line singularities of Eq. 2.2.

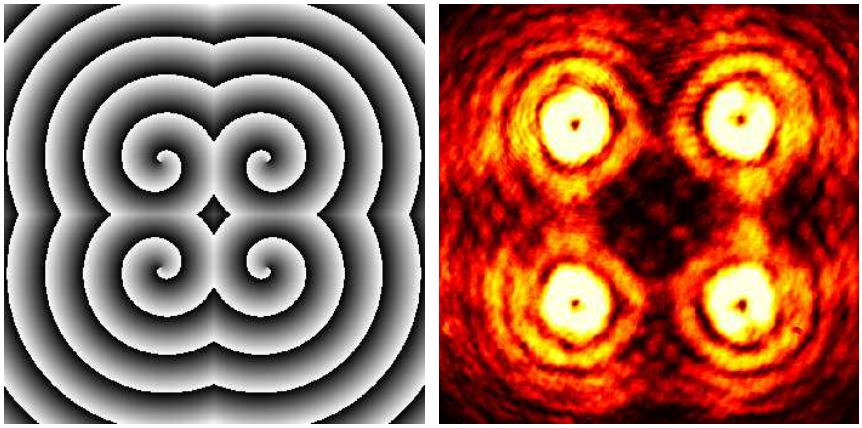

Figure 2.37: The phase mask and beam profile of tiled Bessel beams as described in the text. The mask is generated with $k_r = 1.8$ mm^{-1}, $N = 768$, $G = 256$ and $n = 1$.

2.6.1 Tiled Masks

The phase mask shown on the left in Fig. 2.37, an example of tiling, contains four different phase masks each having a phase given by Eq. 2.10. The upper left mask has the same phase structure as that used to create the Bessel beam in Fig. 2.27. The upper right, lower left, and lower right masks are the horizontal, vertical and diagonal reflections of the upper left mask respectively. A cross sectional picture of the converted mode is shown on the right in Fig. 2.37. As intimated above, the maximum number of tiles is limited by the critical values for N and G – 96 for N and 4 to 8 for G. When the number of tiles forces N below its critical value, we observe degradation of the beam. In addition to not achieving the maximum intensity, the range of propagation before the vortices fall apart also decreases.

2.6.2 Nested Masks

We nest two or more vortices by superposing their respective masks. We give two examples – multipoint singularities and multiple line singularities.

2.6.2.1 Multiple Point Singularities

A nested multipoint-singularity phase mask is different from a tiled mask as the entire mask participates in the generation of each vortex. The phase on a plane background for a nested mask producing a non-deflected beam is given by

$$\Phi^{nest} = \left[\sum_{j=1}^{M} n_j \phi_j(x,y)\right] \bmod 2\pi, \tag{2.36}$$

where n_j is the charge of j^{th} vortex. The locations of the embedded vortices can be controlled by the placement of the center of circulation. A vortex centered at (x_j, y_j), where $x_j = y_j = 0$ is the center of the beam, has a phase $\phi_j(x,y) = \arctan[(y-y_j)/(x-x_j)]$ for $y \geq 0$ and $\phi_j(x,y) = \arctan[(y-y_j)/(x-x_j)] + \pi$ for $y < 0$. To create multiple vortices on a Bessel background, we simply add $k_r r$ to Φ^{nest} as we did to Φ^{Vor} in the single vortex case,

$$\Phi^{Bes-nest} = \left[k_r r + \sum_{j=1}^{M} n_j \phi_j(x,y)\right] \bmod 2\pi. \tag{2.37}$$

Figure 2.38 is an example of seven vortices embedded in a Laguerre-Gaussian beam via nesting. An example implementation of Eq. 2.37 is shown in Fig. 2.39. Two point singularities with $n = 1$ are nested on a J_0 Bessel background. These nested singularities not only persist during propagation, they demonstrate the vortex nature (orbital angular momentum) of the entire beam in that they rotate about each other. Tiled singularities do not have this property. Nested singularities can be used to create a real-time, albeit slow (order of seconds), atom beam splitter by changing their separation. If the singularities are separated too far, however, they break up (see lower left picture in Fig. 2.39) because they interact with the neighboring ring. We can eliminate this breakup, and increase the separation, by

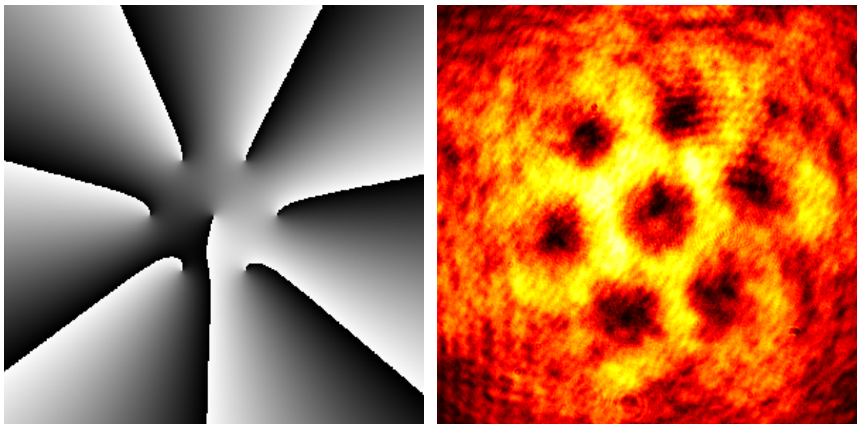

Figure 2.38: The picture on the left is the phase mask created from nesting seven vortices on a plane background. On the right is the output profile of the converted beam.

embedding the singularities in a plane background. Molina-Terriza *et al.*[110], Orlov and Stabinis [111] have studied superposing two beams with embedded vortices, and the associated arithmetic of combining multiple singularities.

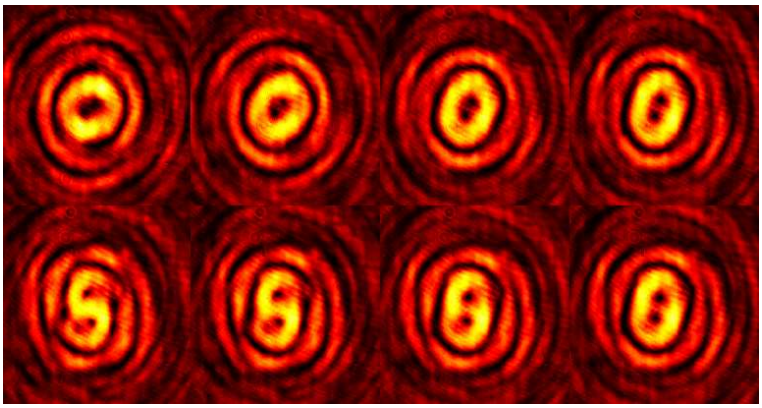

Figure 2.39: Sequence of pictures of nested pair of vortices. The separation between the singularities is increasing systematically. The two vortices have the same charge ($n = 1$) and the Bessel background has $k_r \approx 7$ mm^{-1}. The separation increases clockwise from top left with an increment of 0.6 mm. When the two vortices are separated far enough that they encounter the neighboring ring (separation equals 4.2 mm in this case), they break up as shown in the lower left picture.

2.6.2.2 Multiple Line Singularities

Nesting line singularities permits other structures to be formed. An embedded structure of potential utility for atom optics is an axial intensity void (hollow laser beam) with two or more line singularities, which can be used to channel atoms in directions that are not parallel to the laser propagation direction. The appropriate phase on a plane background for a simple half-integer charge is given by summing only the term, $\left[\frac{1}{2}\phi(x,y)\right] \bmod \pi$,

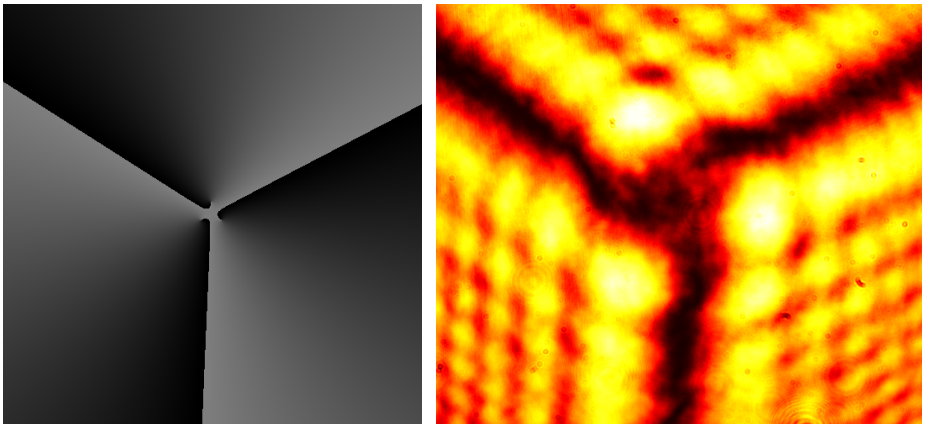

Figure 2.40: From left to right, a phase mask and a beam profile of a channel beam in a plane background. The origins of the ϕ_js, i.e. (x_j, y_j)s, are $(0, -0.40)$, $(-0.20, 0.35)$ and $(0.20, 0.35)$ mm, where $(0, 0)$ is at the center of the mask. The parameter $\vartheta = 9\pi/25$ rad.

$$\Phi^{Nest-Half} = \left\{ \sum_{j=1}^{M} \left[\frac{1}{2}\phi_j(x,y) \right] + \vartheta \right\} \bmod \pi, \tag{2.38}$$

where the charge of j^{th} vortex is $1/2$ and ϕ_j as described in Eq. 2.36. As before, ϑ is used to rotate the mask. We point out, however, that if the origins of the ϕ_js do not coincide, the discontinuity interfaces will be curves due to the phase circulation of neighboring half-integer charges. The curvatures of the discontinuities depend on the value of ϑ. For certain values of ϑ, all the dark channels in the intensity profile will be connected. An example containing three line singularities is shown in Fig. 2.40, where the origins form an equilateral triangle with sides of

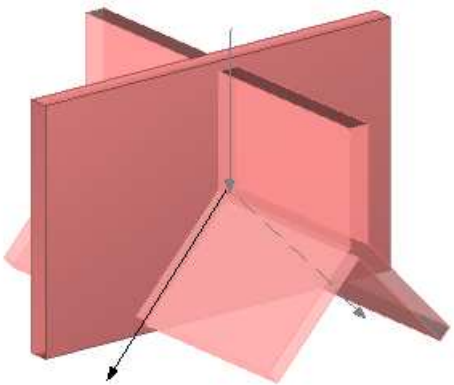

Figure 2.41: A possible beam splitter formed by intersecting two beams at right angle containing line singularities (one with three channels and the other with one channel). The intersection would create a Y-shaped rectangular channel. The vertical channel divides into two non-orthogonal paths.

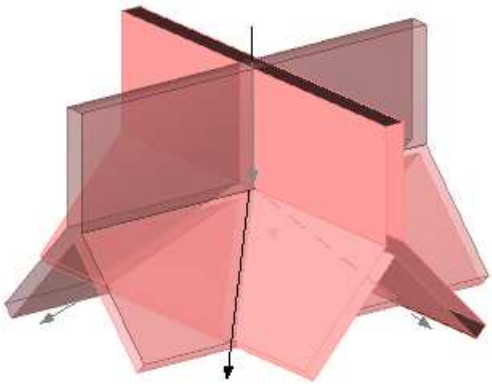

Figure 2.42: A possible beam splitter formed by intersecting two beams at right angle containing line singularities (each with three channels). In this case, the vertical channel divides into four non-orthogonal paths.

0.7 mm and $\vartheta = 9\pi/25$ rad. In general, the intersection of line singularities forms narrow channels that can be orthogonal to the laser propagation direction or in any other direction. Such channels are ideal for creating beam splitters. We show cartoon sketches of two possibilities in Fig. 2.41 and 2.42. In Fig. 2.41, two beams

cross at right angles, one with three line singularities similar to what is shown in Fig. 2.40 while the other has just one line across its diameter. Figure 2.42 shows the orthogonal crossing of two beams each with three line singularities embedded.

2.7 Cold Atoms Confined in Exotic Potentials

Before we close this chapter, it is worthwhile looking at confining atoms to a few of the more exotic optical potentials corresponding to some of the beams described in this paper. Specifically, Fig. 2.43 compares cloud of atoms freely expanding to clouds confined to the first ring of a J_0 beam with $k_r = 8.5$ mm^{-1}, the center of a J_4 beam with $k_r = 10$ mm^{-1} and a beam with two nested vortices separated by 4 mm with $k_r = 8$ mm^{-1}. The first three images were taken ~ 3 ms after the MOT beams were turned off while the right image was taken at ~ 10 ms after the MOT beams were turned off. All images were taken along the propagation direction (see Fig. 3.13C).

While all atoms enclosed within the J_4 and nested beams were confined when the MOT was turned off, only a small fraction was confined to the first ring of the J_0 beam. This is because that potential was smaller than the mean energy of the atoms so only the coldest atoms within the tail of the distribution were restrained. We point out, however, this outer ring could provide an attractive way to confine much colder atoms, such as those from a Bose-Einstein condensate. This could allow interferometers of adjustable size to be created or ring-shaped condensates to be studied. The experimental work in this chapter has been reported in Ref. [85] and Ref. [43].

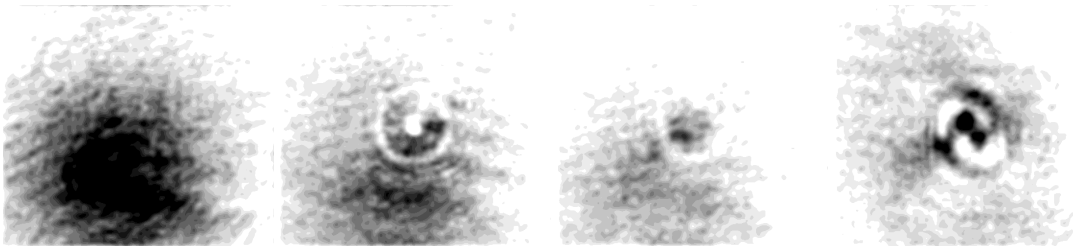

Figure 2.43: Shadow images viewed along the beam of cold Rb atoms confined to several exotic optical potentials. From the left this figure shows: (1) after a free expansion with no optical potential; (2) atoms confined to the zero between the peak at $r = 0$ and the first ring of a J_0 beam generated with $k_r = 8.5$ mm^{-1}; (3) atoms confined within a J_4 beam generated with $k_r = 10$ mm^{-1} and (4) atoms confined within the intensity voids of two nested vortices separated by 4 mm generated with $k_r = 8$ mm^{-1}. Some atoms are also seen to be trapped in between the first and the second ring. The three left images were taken ~ 3 ms after the MOT beams were turned off while the right image was taken ~ 10 ms after the MOT beams were turned off. Optical potentials produced by the SLM were on before the MOT beams were turned off.

Chapter 3

Experimental Setup and Instrumentation

This chapter is devoted to the description of the experimental setup that we divide into three main parts: (1) the setup to generate the cold-atom ensemble trapped in a magneto-optical trap (MOT) (Sec. 3.1), (2) the setup for the optical tunnel that we used to manipulate the atom distribution (Sec. 3.2), and (3) the detection system setup used to monitor the evolution of the ensemble inside the tunnel (Sec. 3.3). Figure 3.1 shows a schematic of the overall experimental setup. The aim of our experiment was to study the dynamics of the cold atoms guided

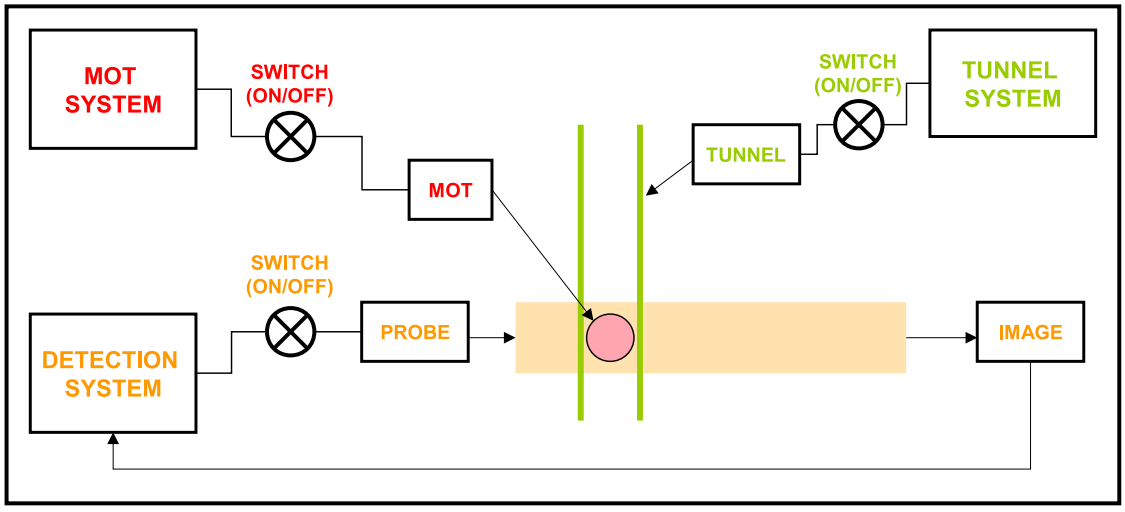

Figure 3.1: The overall experimental setup consists of a MOT cloud, the optical tunnel, and the detection system. In the diagram the MOT ensemble (red ball) falls down under the gravity inside a tunnel (green parallel lines). The probe beam (orange) is used to obtain the spatial distribution of the MOT ensemble.

vertically under gravity inside an optical tunnel. Due to the frame rate limitation of our CCD camera, we employed the following operations in order to monitor the

evolution of the cold atoms:

1. Alignment of the Bessel tunnel with the center of the MOT
2. Generation of the MOT cloud
3. Turning the MOT off at time t_{MOT} and turning the tunnel off at the time t_{tun}
4. Probing the MOT distribution (for 100 μs) with the detection system at time $t_{\mathrm{probe}} = t_{\mathrm{MOT}} + n\Delta t$, where n is an integer, Δt is a constant denoting an incremental time delay typically 1 ms. Initially we set $n = 0$.
5. Taking/Saving an image of the atom distribution collected by the detection system to the computer and labeling its name according to n.
6. Repeat from the second step with the next value of n.

The implementation of these procedures is described in more detail in Sec. 3.4. The following sections will describe the main blocks of the experiment and the computer control interfaces in more details.

In Chapter 4, we will use these sequences to capture the dynamics of a cold atomic ensemble influenced by a hollow light tunnel.

3.1 MOT Setup

Even though the general setup of the MOT is well documented elsewhere (see for example Ref. [112]), the instruments used in experiment vary from lab to lab. In this section, we will described our instruments and how they were put together to build our MOT. The setup of the MOT can be divided into three steps: (1) vacuum chamber, (2) arrangement of optical beams, (3) trap setup.

3.1.1 Vacuum Chamber

The chamber that we constructed is a playground where all the manipulations of an atomic ensemble (by laser light) take place. In order to observe the dynamics

of the rubidium cloud, we first evacuated atoms or molecules out of the chamber, especially those with large scattering cross section present at the atmospheric pressure. After the evacuation, a highly purified source of rubidium metal (99.99%) is used to supply rubidium vapor to the chamber. The rubidium solid is sealed in a glass ampule, which is then placed inside a copper tube (labeled as "Rb source" in the left panel of Fig. 3.2). Collisions of the room-temperature atoms with a cold MOT cloud destroys the latter and a low background pressure is essential for a long life time of the cloud. The life time of the cloud can be calculated from the total collision rate (γ_C), given in table I of Ref. [113] by Bali *et al.*, and the ideal gas law that relates pressure to number density. For rubidium (Rb) vapor, which is the dominant species in our vacuum chamber, the Rb-Rb total collision rate is calculated to be 6.3×10^{-9} cm^3/s, assuming warm-cold collisions. Therefore, in order to have a half life on the order of ~ 100 ms, we need the pressure to be about 10^{-8} Torr. The construction of the chamber began with a stainless steel cylinder (a UHV spherical octagon model MCF600-SO200800 from Kimball Physics Inc.), as shown in Fig. 3.2, with eight circular ports distributed evenly on the side and two big circular opening on the front and back of the cylinder. The side and front/back ports were 2 3/4" and 6" conflat flanges respectively. The height of the cylinder is 2.8". One of the side ports was attached to a 40 l/s ion pump. Two other ports are extended by a conflat tees so that two additional openings can give access to the rubidium source and a turbo pump to rough out the chamber. All the optically accessible side ports were sealed by glass windows that had anti-reflection coating for 780 nm on both sides. The 6" ports, however, were sealed with uncoated glass windows. After the chamber was sealed, we used a turbo pump (Pfeiffer TPH170) to reduce the pressure inside the chamber to $\sim 10^{-6}$ Torr. The turbo pump was connected to the chamber through a mechanical valve so that the pump could be removed from the chamber. Next, we reduced the pressure further to the desired 10^{-8} Torr with an ion pump (Varian Starcell). While we pumped the chamber using the turbo and ion pump, we baked the chamber (without baking the ion pump) to ~ 200 °C to accelerate the process and to drive out contaminants on the inner surface of the chamber. We

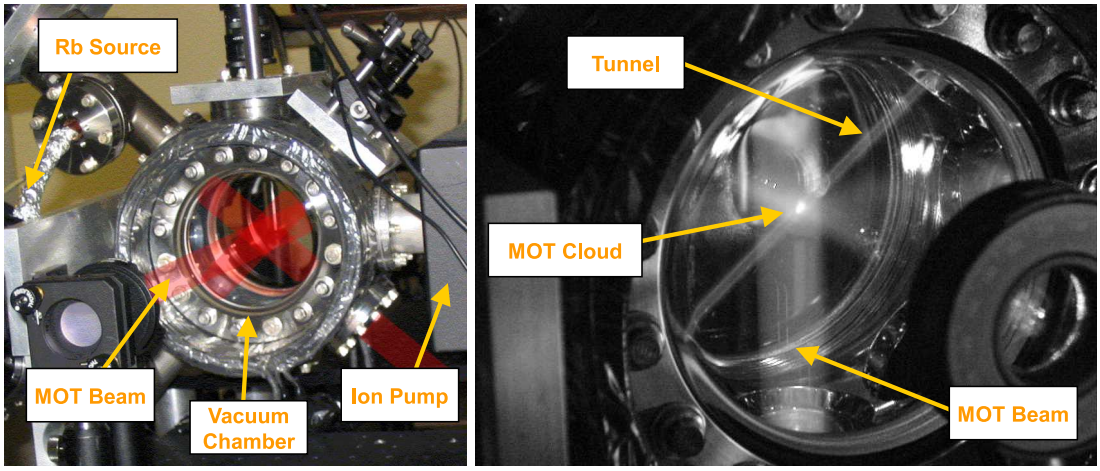

Figure 3.2: Experimental vacuum chamber. In the left panel, the figure shows the chamber with the source of rubidium atoms attached to a conflat tee and the ion pump attached to one of the 2 3/4" port on the right side of the chamber. On the right, several bright beams are shown in the chamber. The rubidium pressure inside the chamber in this figure is high enough for the laser tuned on resonance (D2 line) to be seen (via light scattering). The MOT cloud can be seen to be inside the tunnel, which is seen as two parallel lines diagonally traversing the chamber from the top right. The alignment of the tunnel is more elaborate when the rubidium pressure is low. The procedure is described at the end of Sec. 3.2.

wrapped heating strap around the chamber (excluding the ion pump) and cover it with several layers of aluminum foil for a thermal insulation. The chamber was baked for several days before we achieved the desired pressure. After the chamber cooled down to the room temperature, only the ion pump was used to maintain the pressure. The pump current was used to estimate the pressure in the chamber. Once the operating pressure was reached, we cracked the rubidium ampule inside the copper tube (see Fig. 3.2) that is connected to one of the extended conflat tees as mentioned before. We then injected rubidium vapor into the chamber by heating up the copper tube to $\sim 50^{\circ}$ for several days until the chamber was all coated up with rubidium and the pressure inside the chamber came to equilibrium at 10^{-8} Torr. The vapor pressure of heated Rb atoms can be seen in Fig. 3.3.

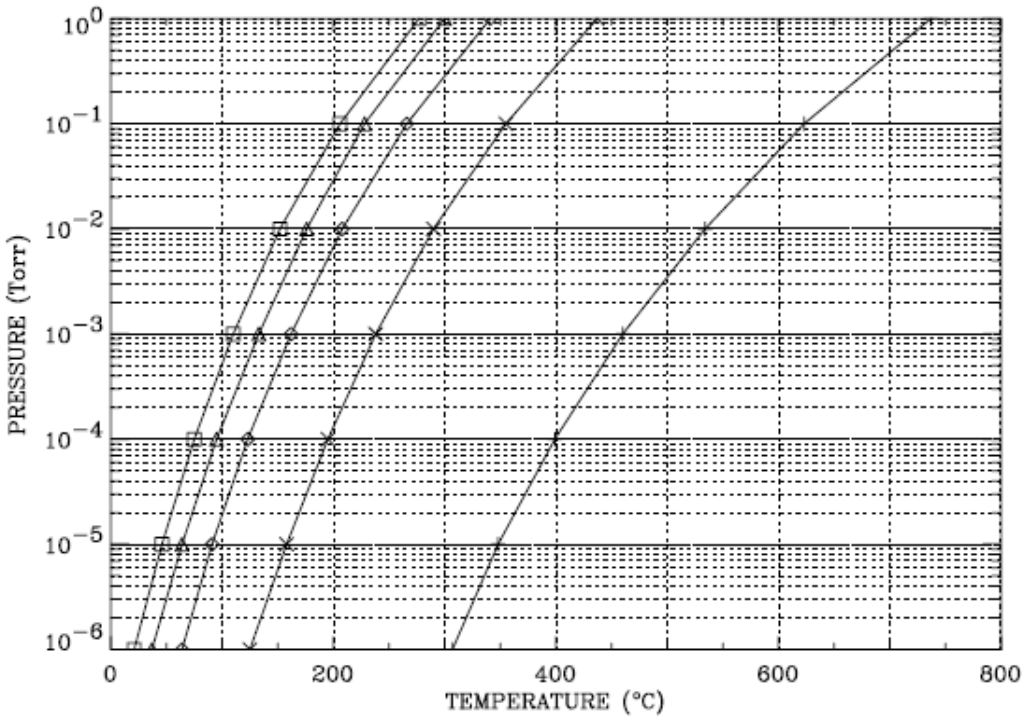

Figure 3.3: The plots shows vapor pressure versus temperature for alkali metals: Li(+), Na(×), K(◇), Rb(△), Cs(□). Reproduced from Ref. [60]

3.1.2 MOT Laser Setup

As pointed out in Sec. A.6, generation of rubidium MOT requires two lasers to excite two different transitions, one for trapping and the other for repumping. The frequencies of these transitions differ by $\sim$ 3 GHz in ^{85}Rb and $\sim$ 7 GHz in ^{87}Rb. We used a Toptica laser (model DL100) for the trapping transition and a Vortex laser (New Focus^{TM} model#6013) for the repumping transition. Before we could use these lasers to trap and cool atoms, the frequency of each laser needed to be stabilized. We note that the absorption rate (Eq. A.2) drops by half when the detuning Δ is approximately one natural linewidth, Γ. Therefore, the trap will not be efficient when the laser frequency fluctuations exceed Γ.

We used a feedback loop that enabled us to stabilize the laser at a desire frequency. An electrical circuit as shown in Fig. 3.4 was used for this task. The frequency was adjusted by a piezoelectric transducer (PZT) attached to a diffraction

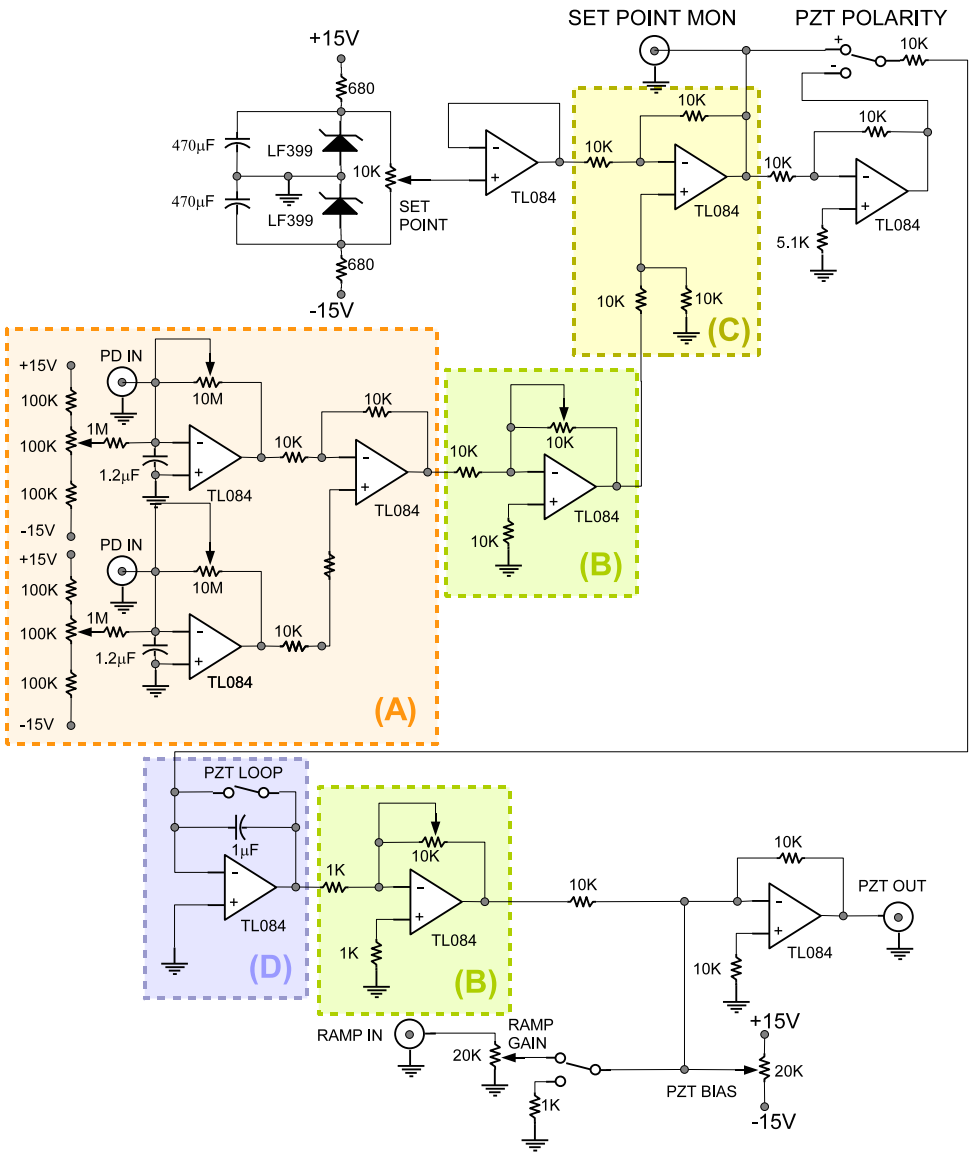

Figure 3.4: Locking circuit. (A) the photodiode signal subtractor - SAS signal, (B) amplifier, (C) set-point comparator that produces an error signal, (D) Integrator produces a time averaged signal for stability. Adapted from Ref. [60].

grating inside the laser cavity [114, 60, 115]. Adjusting the voltage across the PZT changes the alignment of the grating and, as a consequence, changes the eigen-mode of the laser cavity. In addition to the frequency sweep, the absolute frequency of the laser must be known in order to specify the locking point. This can be achieved through saturated absorption spectroscopy (SAS) [116].

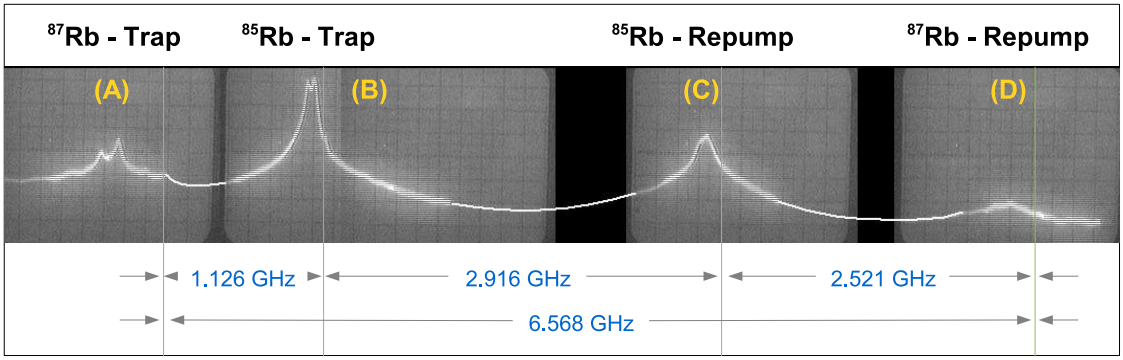

Figure 3.5: The saturated absorption spectrum (SAS) for all D2 lines of ^{85}Rb and ^{87}Rb from the Toptica laser (MOT Laser). The green vertical lines are placed roughly at the transition frequencies we used for the MOT. The spacing between these lines can be obtained from Fig. A.7 and Fig. A.8

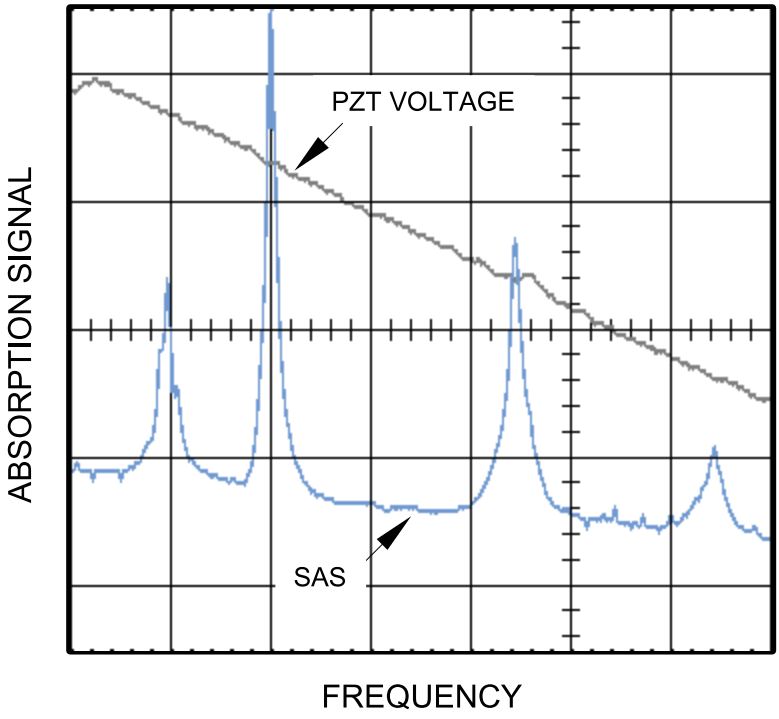

Figure 3.6: The triangular wave form (diagonal line), used to drive the PZT as described in the text, is shown together with the saturated absorption spectrum produces by a Ti-Saph Laser.

The SAS relates, as the name may suggest, the amount of laser light absorbed by the atoms of interest to the frequency of the laser light being absorbed. By

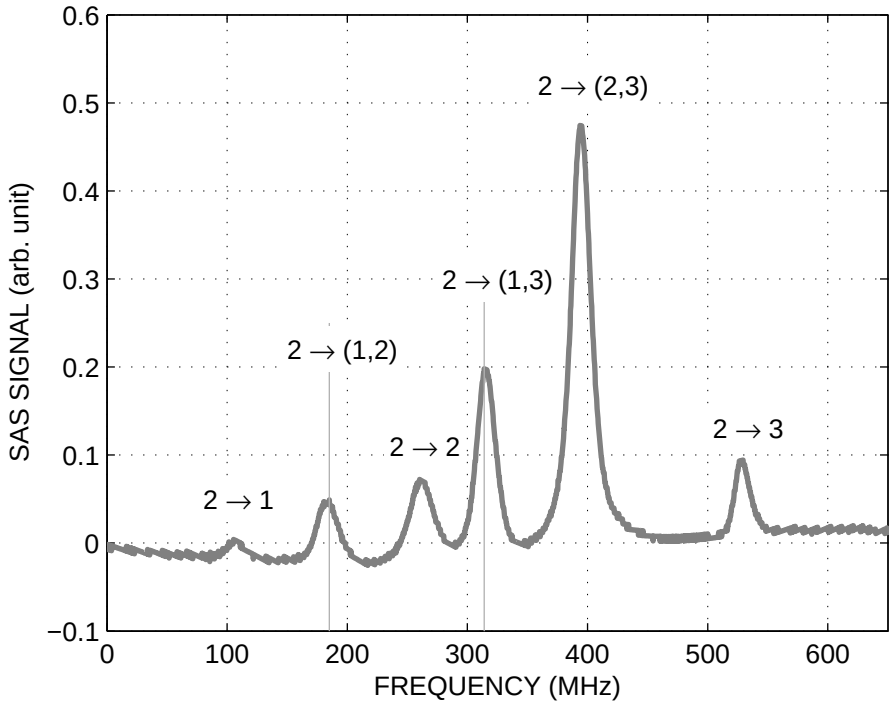

Figure 3.7: A saturated absorption spectrum (SAS) of $5^2S_{1/2}(F = 2) \rightarrow 5^2P_{3/2}(F' = 1, 2, 3)$ for ^{87}Rb trapping beams. We can associate the features in the SAS signal with the atomic transitions, $F \rightarrow F'$, and the crossover transitions, $F \rightarrow (F'_1, F'_2)$, as labeled in the figure. The crossover peaks are in the middle of the transition pairs $F \rightarrow F'_1$ and $F \rightarrow F'_2$. Right in the middle of both transitions, atoms absorb light from both the probe and the pump beams causing a peak of the probe intensity as shown. The MOT trapping beams are locked at $\sim$ 15 MHz lower than the $F = 2 \rightarrow F' = 3$ peak.

sweeping the PZT voltage, both the frequency and the absorption change, creating a one-to-one correspondence. The SAS signals from different frequency ranges are shown in Fig. 3.5 through Fig. 3.10. The peaks in the SAS signals correspond to different transitions in rubidium (Fig. A.7 and Fig. A.8). The transitions were identified by comparing the relative amplitudes of the peaks and distances between the peaks to tabulated values.

After generating the SAS peaks, we were ready to lock the laser using the frequency locking circuit provided in Fig. 3.4. From the figure, we used photodiodes

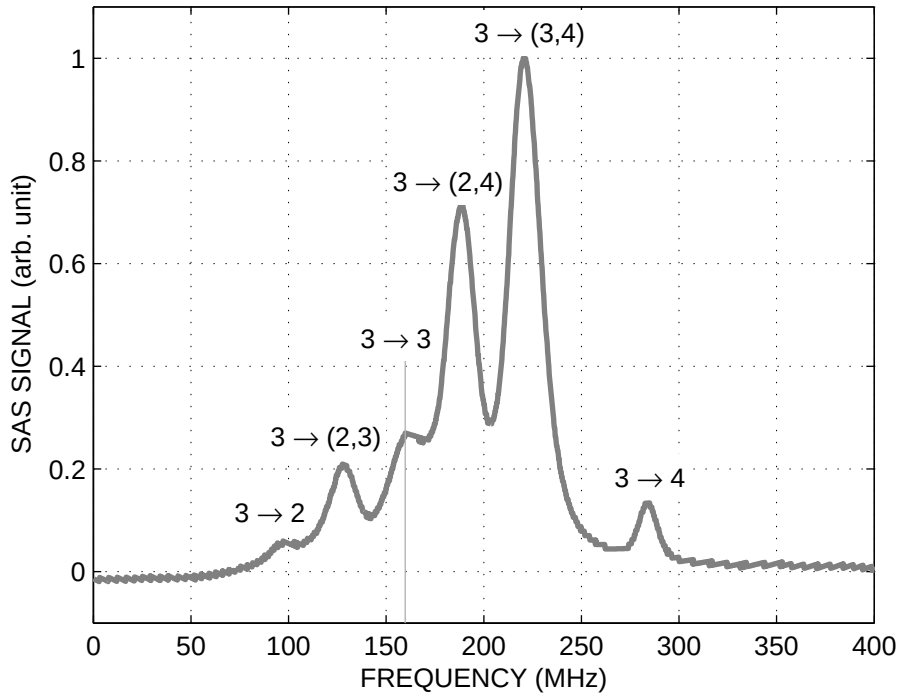

Figure 3.8: A saturated absorption spectrum (SAS) of $5^2S_{1/2}(F = 3) \rightarrow 5^2P_{3/2}(F' = 2, 3, 4)$ for ^{85}Rb trapping beam. The MOT trapping beams are locked at ~ 15 MHz lower than the $F = 3 \rightarrow F' = 4$ peak. The crossover peaks as described in Fig. 3.7 are labeled with round brackets.

(PD) to convert the intensity of the probe beams into voltage. The subtraction of the Doppler profile from the two probe beams in the SAS setup was obtained from the circuit A in Fig. 3.4. After that the signal was amplified by a circuit B. The circuit C, a differential amplifier circuit, subtracts off the a set point from the signal. This gave an error signal to be used in the next stage. Note that the set point could be manually adjusted through a variable resister and the polarity of the output from the circuit C could be changed by the PZT polarity switch. Next if the PZT LOOP switch was closed, raw error signal would by-pass the integrator in the circuit D and the laser would be in the "unlock" state. After that it would be amplified by the circuit B and added to the RAMP IN signal if it were switched on. The ramp signal had a triangular wave form (the diagonal line crossing Fig. 3.6) that was used to sweep the voltage across the PZT periodically. At this stage, the output signal

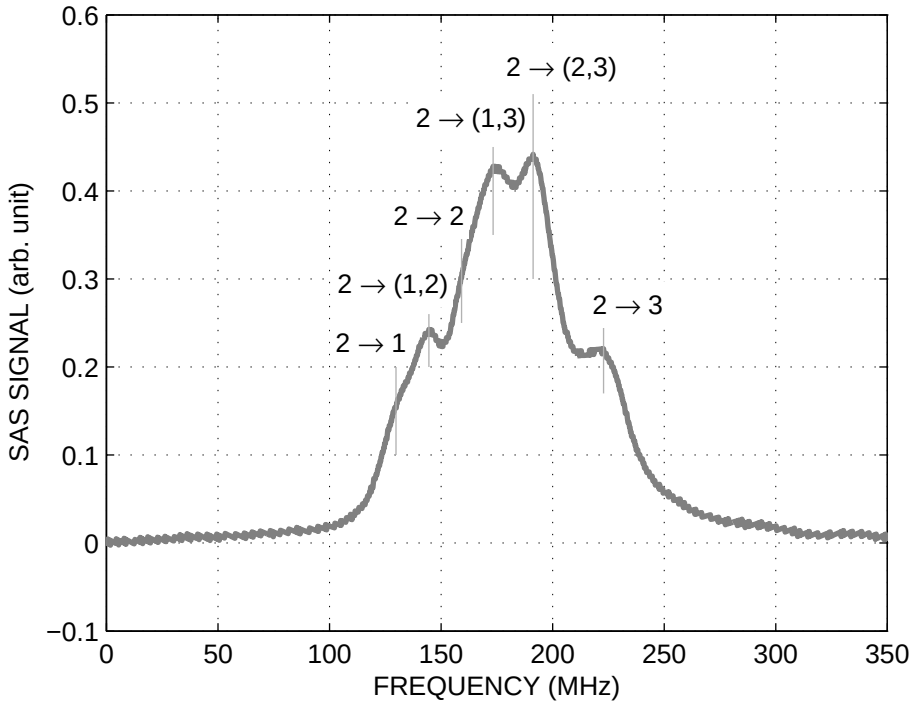

Figure 3.9: A saturated absorption spectrum (SAS) of $5^2S_{1/2}(F = 2) \rightarrow 5^2P_{3/2}(F' = 1, 2, 3)$ for ^{85}Rb repumping beam. The repumping beam is locked at ~ 5 MHz on the right side of $F = 2 \rightarrow F' = 3$ peak. The crossover peaks as described in Fig. 3.7 are labeled with round brackets.

could be used to monitor the SAS signal.

To put the laser in the "lock" state, the RAMP IN switch was turned off and the PZT LOOP switch was opened so that the error signal could be integrated by circuit D. When the laser frequency shifts from the set value, the integrator provides time averaged signal that drives the PZT in the direction opposing the change of frequency.

Note, the circuit drive the error signal toward zero only when the sign of the error signal corresponds correctly to the sign of the slope of the SAS signal where we tend to lock the laser.

Typically, as required by the MOT condition, we adjusted the set point of the locking circuit so that it corresponded to a red detuning of $\sim 2\gamma$ (~ 15 MHz) away from the SAS peak of the trapping transition. For the repumping transition, the set

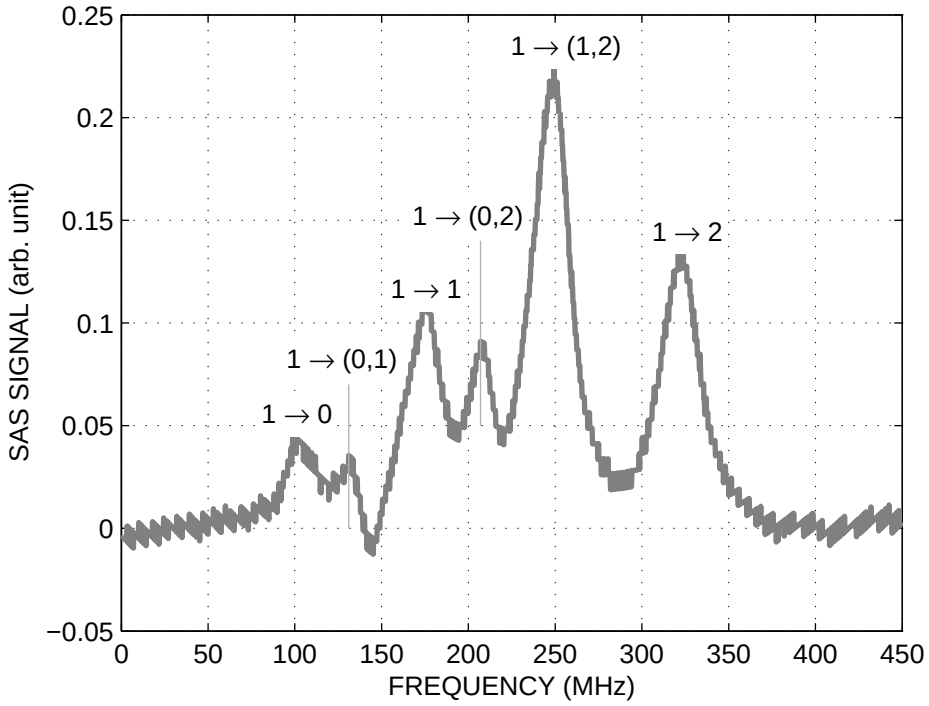

Figure 3.10: A saturated absorption spectrum (SAS) of $5^2S_{1/2}(F = 1) \rightarrow 5^2P_{3/2}(F' = 0, 1, 2)$ for ^{87}Rb repumping beam. The repumping beam is locked at ~ 5 MHz on the right side of $F = 1 \rightarrow F' = 2$ peak. The crossover peaks as described in Fig. 3.7 are labeled with round brackets.

point was adjusted as close as possible to the SAS peak of the transition (~ 5 MHz). However, if the set point is too close to the peak, fluctuation in laser frequency could get strong enough to drive the frequency over the peak and the laser would be out of lock.

3.1.3 Trap Setup

A pair of anti-Helmholtz coils is required to generate a MOT as described in Sec. A.4. The coils were constructed manually by winding an insulated copper tube around a 6"-diametered cylinder with 42 loops in each coil. The coils were connected together in such a way that electric current in the two coils runs in the opposite direction as shown by the green arrows in Fig. A.3. After this stage, the coils were placed around the vacuum chamber so that the cylindrical axes of the coils and the

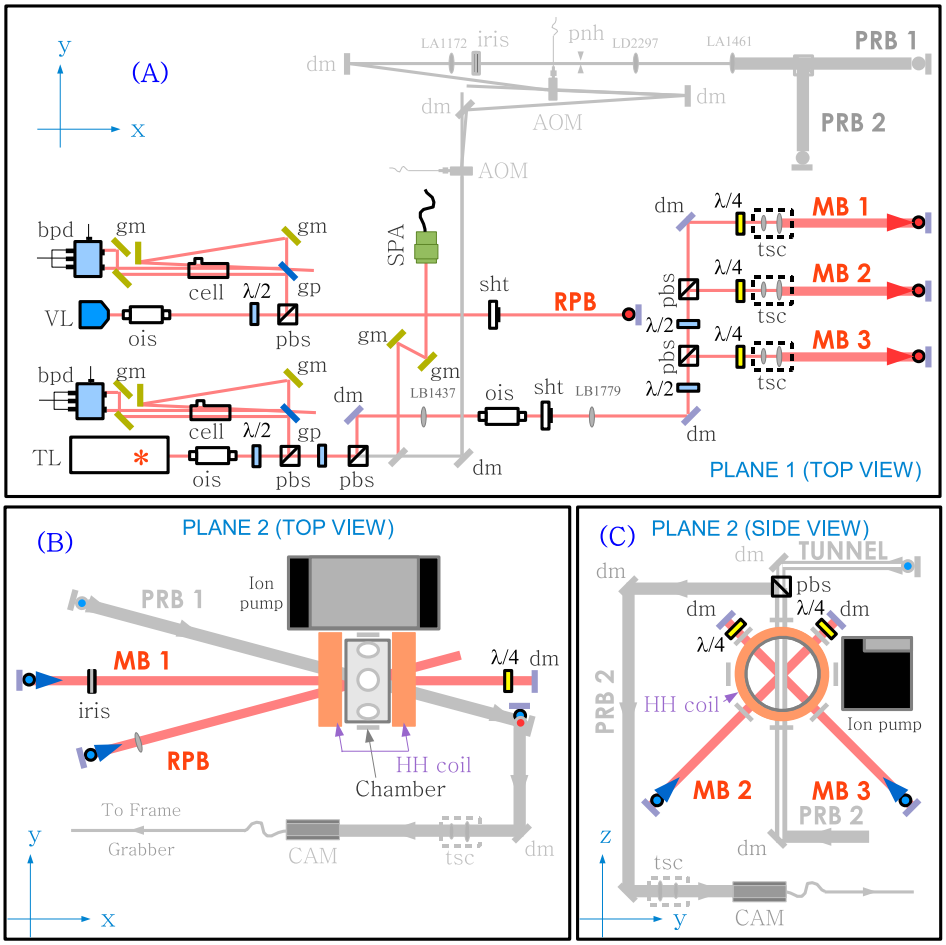

Figure 3.11: Detailed diagrams of the MOT setup as described in the text. The elements shown in the figure are: Vortex laser (VL), Toptica laser (TL), spectrum analyzer (SPA), acousto-optic modulators (AOM), photodiodes (bpd), gold mirrors (gm), dielectric mirrors (dm), Rb vapor cells (cell), half-waveplates ($\lambda/2$), quarter-waveplate ($\lambda/4$), glass plate (gp), polarizing beam splitter cubes (pbs), optical isolators (ois), mechanical shutter (sht), lenses (Lxxxxx), pinhole (pnh), telescope lens pair (tsc), camera (CAM), and Helmholtz coils (HH coil). The MOT trapping beams are labeled as MB1, MB2 and MB3. The z-axis is the vertical axis.

chamber coincided. This is shown in Fig. 3.11 and Fig. 3.2. The closest distance of separation between the coils was 2.8", the thickness of the chamber. When we ran 25 A through the coils, the magnetic field in the middle of the chamber produced a gradient of 15 G/cm as measured by a Hall probe. The magnitude of the field

created in the middle of the chamber was zero and increased approximately linearly within 5 cm radius around the magnetic zero. To dissipate the heat generated by the current, water was fed through the copper tube.

Once the coils were in place, we arranged the trapping and repumping beams to form a trap as shown in Fig. 3.11. The trapping beam (Fig. 3.11A) was provided by a 90 mW Toptica DL100 laser (TL). It was optically isolated from the back scattered light by a 32 dB optical isolator (ois) from Isowave (model I-80-T5-H). The isolation prevented the back scattered light from disturbing the laser stability or causing any damage to the laser. Several milliwatts of power was split off from the main beam by a combination of a half-waveplate ($\lambda/2$) and a polarizing beam splitter (pbs) to feed to the SAS setup. The remainder of the beam was split again so that a few milliwatts were used as a probe beam (PRB: gray path) in the imaging system as described in Sec. 3.3. If re-routed, the probe beam could also be aligned with a spectrum analyzer (SPA) to observe the longitudinal mode structure of the laser. The rest of the main beam was additionally isolated by another 32 dB optical isolator (Isowave model I-80-T5-H). The beam could be blocked/unblocked by a mechanical shutter (sht) from Uniblitz (model LS6 T2). Afterward, the main beam was again split into three independent beams (MOT Beam: MB1, MB2 and MB3). Each beam was circularly polarized by a quarter-waveplate ($\lambda/4$). The size of each beam was expanded and collimated by a pair of lens (tsc) to 2 cm in diameter. Finally, the trapping beams were aligned to form a trap as shown from different angles in Fig. 3.11 B and Fig. 3.11 C, following the description in Sec. A.5. Note that the counter-propagating beams, as required by the MOT, was created by placing quarter-waveplates and dielectric mirrors (dm) after the beams passed through the vacuum chamber as seen in the figure. A Vortex laser (VL), with the output power of ~ 5 mW, was used as the repumping beam (RPB). It was isolated by an optical isolator from Isomet (model 1205C-2-804B). A few milliwatts were fed to the SAS setup. The remainder was delivered to the trap beam overlap region inside the vacuum chamber.

3.2 Optical Tunnel Setup

Our experimental setup to create an optical tunnel is shown in Fig. 3.12 . From the Figure, a 6 W Ar^+ laser[1] (ARGON: Coherent Innova, model 400) pumped a Ti:Sapphire laser (Ti:Saph: Coherent, model 899). The output from the Ti:Saph laser was 400 mW, linearly polarized Gaussian beam at 780 nm. To tune the laser to Rb resonance lines, a small amount of light was split from the main beam to feed the SAS setup as described in Sec. 3.1.2. After the splitting, a half-waveplate was used to rotate the polarization of the laser to match a director of a 2D spatial light modulator[2] (SLM: Hamamatsu Corp.), a device used to create a tunnel from the input Gaussian beam. To cover the entire active surface on the SLM that is used to create the tunnel, the beam was expanded and collimated by a pair of lenses (focal lengths of 10 cm and 75 cm placed 85 cm apart). After the expansion, we directed the beam toward the SLM and picked up the tunnel as it reflected off the surface. The beam was incident on the SLM at an angle of 3° with the surface normal, resulting in an ellipticity of 1.03 (major axis divided by minor axis). This problem was corrected by altering the phase mask as described in Sec. 2.4.6. Note that the phase mask on the SLM could be controlled via a computer through a VGA port as shown in Fig. 3.12C.

Once the tunnel was created, we delivered it to the chamber where the MOT ensemble was formed. For the purpose of alignment, we observe the interaction between the tunnel and the MOT ensemble by looking at the spatial distribution of the ensemble on a monitor (MNT1) from the imaging system as described in Sec. 3.3. First, we overlapped the tunnel with the MOT cloud approximately by tuning the tunnel's frequency close to the trapping transition that caused the tunnel to expel atoms from the MOT. To ensure that most of the atoms in the ensemble were coupled efficiently to the tunnel, we slowly blue-detuned the tunnel frequency away

[1] Ar^+ laser was used in the atom switch/lock experiment described in the introduction. For the experiments reported in Chapter 4, the Ar^+ laser was replaced by a solid state laser (Coherent: Verdi-V18) with 8 W of pump power.

[2] The detailed description of the SLM is described in Appendix D.

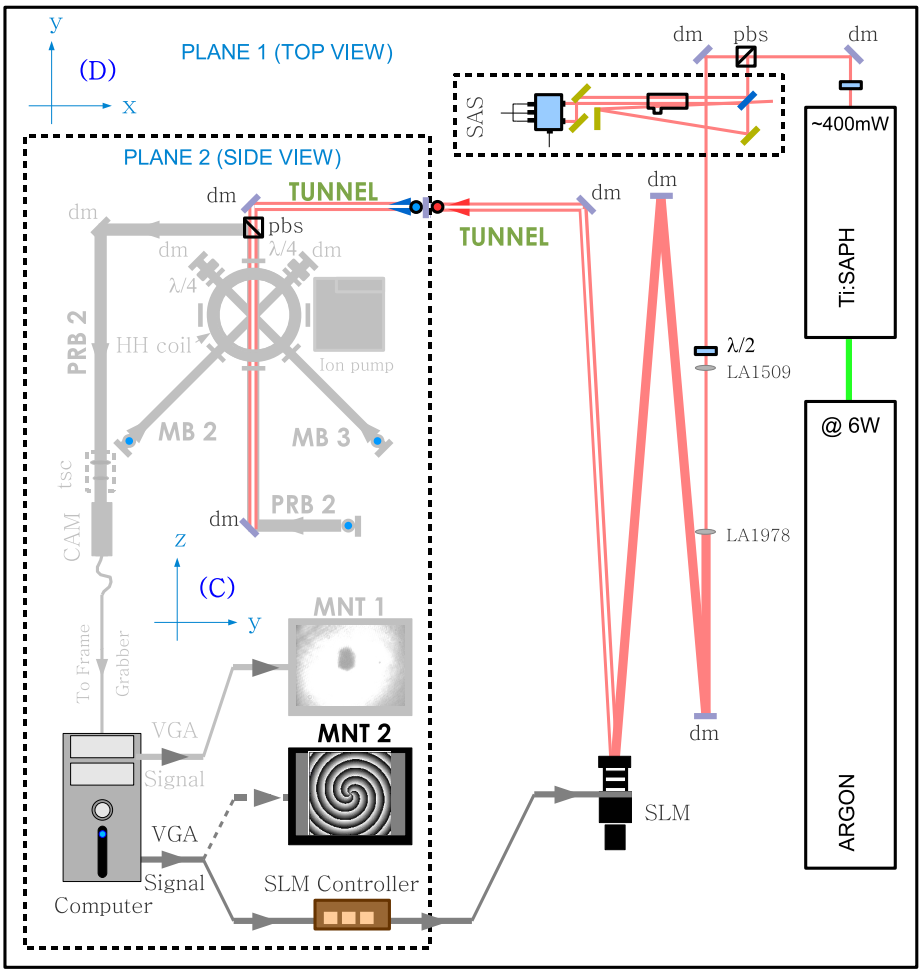

Figure 3.12: Upon reflecting from the spatial light modulator (SLM), the Gaussian beam (solid red) is converted into a hollow tunnel that we used to guide atoms as described in the text. The tunnel alignment is shown in box (C). The elements in the figure are: argon laser (ARGON), Ti:Saph laser (Ti:SAPH), shadow image monitor (MNT1), and phase mask monitor (MNT2). The rest are described in Fig. 3.11. The box labeled as SAS shows the saturated absorption spectrum setup. Note, the setup in box (C) is in a vertical plane perpendicular to the rest of the figure.

from the trapping transition (toward higher frequency). As the tunnel's influence on the MOT decreased, we were able to monitor the ensemble inside the tunnel's dark core. The majority of atoms were expelled near the peak of the tunnel. At a proper detuning[3], we could observed a dent in the spatial distribution of the ensemble

[3]For example, we detuned the laser by ~ 1 GHz for peak intensity of $\sim 10^4$ mW/cm^2 and ~ 100

that resemble the shape of the tunnel[4]. At this stage, we could finely adjusted the position of the dent so that the center of the ensemble coincide with the center of the tunnel.

3.3 Imaging System

The imaging system was shown before as a gray path in Fig. 3.11A. The alignment of the imaging laser beam with respect to the MOT ensemble is shown in Fig. 3.13. We used the shadow imaging technique as described in Ref. [60] and Ref. [117] to probe the spatial distribution of the ensemble being manipulated in the experiment. We shone a beam of light on the ensemble and capture the shadow that the ensemble cast on the beam through the absorption process. The strength of the absorption, discussed in Appendix A and given by Eq. A.2, was maximized when the beam was tuned to resonance, $\Delta = 0$. When the beam is approximately uniform and travels in the z direction, the relationship between the spatial distribution, $\rho(\vec{r})$, and the absorption shadow just after the beam passes through the ensemble, $I(\vec{r}, z = 0)$, for a low density ensemble, can be shown to be $\rho(\vec{r}) \propto I_0 - I(\vec{r}, z = 0)$, where $\vec{r}$ represents the coordinate transverse to the probe beam and I_0 is the intensity of the input beam. As an example, figure 3.14 shows pictures of I_0, I and $I_0 - I$ respectively from left to right.

For the experimental implementation, from Fig. 3.11A, we pick up about ten milliwatts from the trapping beam using a half-wave plate ($\lambda/2$) and a polarized beam splitting cube (pbs). The frequency of the beam was then shifted to that of the trapping transition by two acousto-optic modulators (AOM: Isomet, model 1205C-2-804B) to maximize the absorption strength. Recall from Sec. 3.1.2 that the Toptica laser is locked $\sim$ 15 MHz below the frequency of the trapping transition by the frequency locking circuit. To shift the frequency back to the trapping transition, we need two AOMs.[5] Our AOM has a central frequency of 80 MHz and the bandwidth

mK trap depth.

[4]Similar dents can be seen in Fig. 2.43 for an ensemble trapped in various tunnel profiles.

[5]An acousto-optic spatial light modulator is a device that diffracts light based on interaction

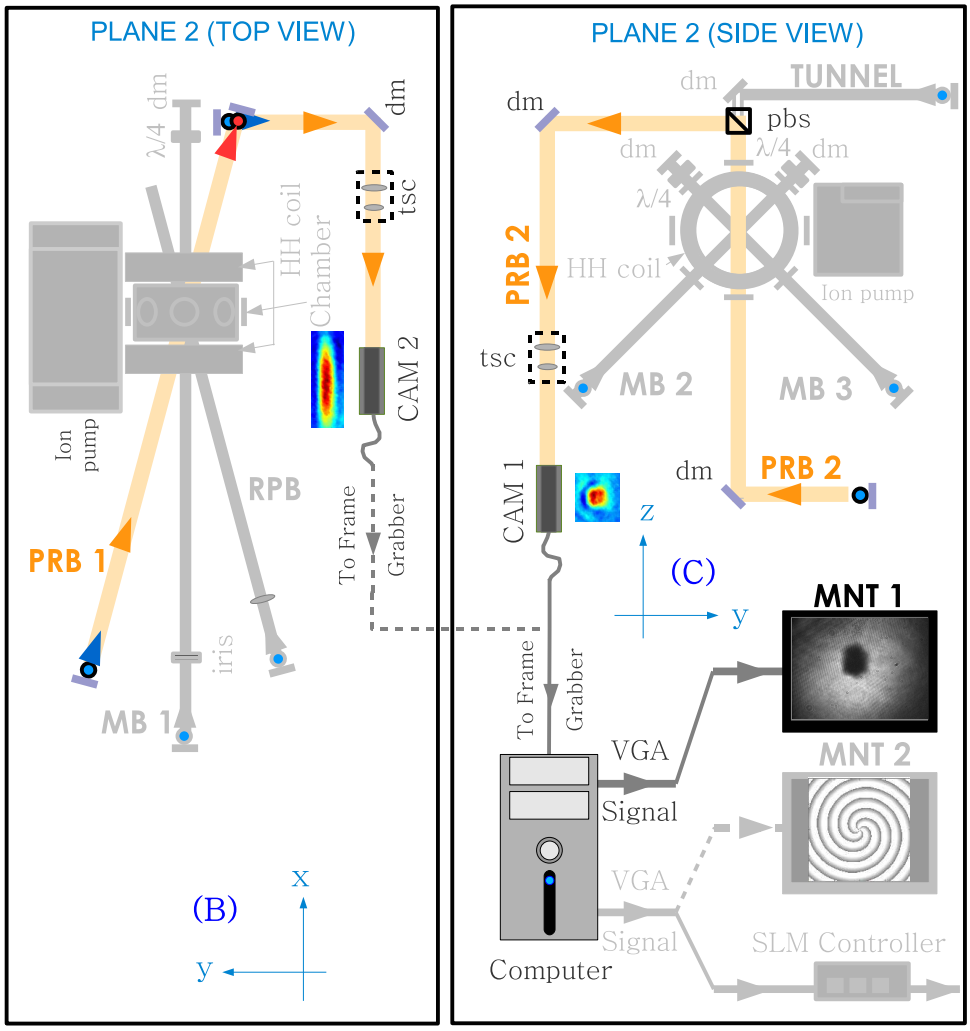

Figure 3.13: Arrangement to monitor Rb atoms confined to the optical potentials. The sub-figures (B) and (C) are the detailed version of Fig. 3.11(B) and Fig. 3.11(C) accordingly. Alignment of the probe beam for shadow imaging of the atoms across (PRB1) and along (PRB2) the tunnel. The optical potential (TUNNEL) is oriented vertically. The CCD cameras are labeled as as "CAM1" and "CAM2". A pair of lenses (tsc), not to scale, forming a 4f imaging system delivers the shadowed image to the camera.

of 30 MHz. Therefore one AOM cannot shift the frequency by 15 MHz. Shifts this small are possible with two nearly identical AOMs, by taking the difference

of light with a running sound wave inside a crystal. The diffraction with an order other than zero picks up a frequency shift due to the Doppler effect from the running sound wave [97].

between the two shifts. In the experiment, we tune AOM1(AOM2) to provides 70 MHz(90 MHz) shift. The shift can be manually adjusted through an AOM driver (IntraAction, model DE802M).

After adjusting the laser detuning, we use a spatial filter to eliminate high spatial frequency fringes by placing a pinhole at the focal point between a pair of lens, acting as a beam expander and collimator. The resulting beam after the pinhole and the collimator was nearly Gaussian with a diameter of 1". The expanded beam was then split into two, PRB1 and PRB2, which were used to probe the distribution of the ensemble from two different angles. The alignment of PRB1 and PRB2 can be seen in Fig. 3.13(B) and Fig. 3.13(C) respectively. The alignment in Fig. 3.13(B) gives the distribution of the ensemble along the tunnel (seen as an elongated ellipse besides CAM2) while the one in Fig. 3.14(C) gives the distribution transverse to the tunnel (a circular dot besides CAM1). A shadow image right after the beam passed through the ensemble was delivered to a CCD camera (CAM1 and CAM2: COHU, model 4910) using a pair of lenses (tsc) to form a 4f-system. The focal length of one lens is $f_1 = 1$ m and the other is $f_2 = 75$ cm. The first lens is placed at f_1 away from the ensemble and the other at $f_1 + f_2$ away from the first lens. Lastly, the camera is at a distance f_2 away from the second lens. An example of a shadow image is shown in Fig. 3.14 captured with CAM1.

3.4 Data Acquisitions and Softwares

As described in the beginning of the Chapter, the data acquisition of the evolution of the ensemble spatial distribution can be obtained through the sequence summarized in Fig. 3.15. Since the sequence merely concerns the on/off state of the laser beams involved in the experiment, we can use a computer to control all the switches electronically in a straightforward manner. Two electro-mechanical shutters (Uniblitz, model LS6 T2) were used as the switches by placing each of them in the path of the optical tunnel and the trapping beam (before being split). Each shutter was powered by a shutter driver (Uniblitz, model D122) which had a

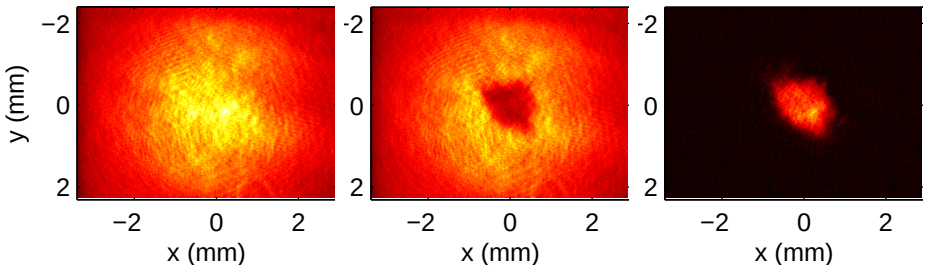

Figure 3.14: The figures show three images related to the shadow imaging technique described in the text. The image on the left shows the intensity profile of a Gaussian beam passing through the MOT chamber without the MOT ensemble. The image in the middle shows a shadow cast on the same beam after being absorbed by the ensemble. The last image on the right shows the spatial distribution of the ensemble obtained by subtracting the image in the middle from the one on the left.

BNC connector for a TTL pulse input that determined the state of the shutter. The blade of the shutter has the speed of ~ 5 mm/ms. Therefore, the beam's width of 0.5 mm at the focal spot can be shut off in 0.1 ms. We created the pulse inputs from a digital delay/pulse generator (DDG: Stanford Research System, Inc, model DG535) which was connected to the computer through a GPIB card (National Instrument, model NI-488.2) and a cable. The card allowed us to control the delay of the pulse with respect to our specified trigger time. Note that it takes the shutter 2 ms to response after it receives the trigger, therefore, in Fig. 3.15, the computerized pulse (red mark) led the real on/off state of the beams by 2 ms. In the case of the probe beam, the width of the pulse needed to be short enough to capture a still image of the ensemble spatial distribution. In the experiment, we set this width to be 100 μs, short enough that the change in the evolution of the distribution was negligible[6] and long enough that the beam intensity fit the dynamic range of the CCD camera. We switch the state of the probe beam by sending a pulse to the AOM driver. When the pulse input arrived, the driver changed the frequency of the acoustic wave in the AOM and therefore changed the diffraction angle of the probe beam. We set

[6]In 100 μs, for a 150 μK ensemble, an atom with the average velocity ($\sim 20cm/s$) moves ~ 20 μm while the size of the ensemble is in order of a few millimeters.

the probe beam so that when the pulse input was in the low state (0 V), the probe beam was blocked by an iris. However, when the pulse input was in the high state (0.5 V), the probe beam was deflected by the AOM (by $\sim 2°$) so that it passed through the iris and could be used to probed the ensemble.

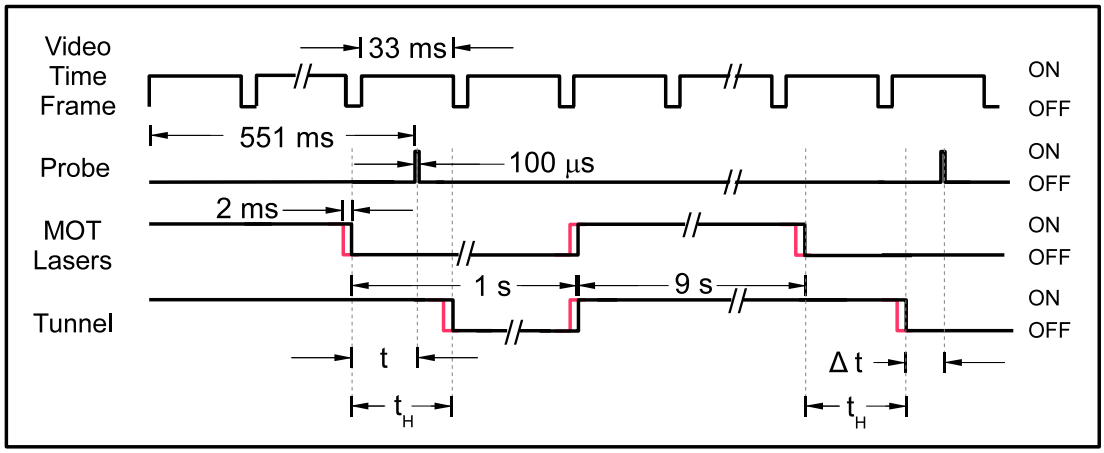

Figure 3.15: The diagram of events associated with the data acquisition process. The video time frame is a train of time intervals the CCD camera waits to capture a picture. The probe pulse is set to be triggered 551 ms after a camera frame is triggered so that it always in the middle of the video time frame. To capture the expansion of the MOT atom ensemble, the MOT lasers are turned off at time t before the probe is triggered so that the ensemble expands by the same amount of time after it is released. Of all the time mentioned, t is the only variable that we adjust in one set of experiments, others are kept fixed. Thus the camera captures the expansion of the ensemble with the tunnel on when $t < t_H$ and it captures the expansion of the ensemble with the tunnel off when $t > t_H$. The MOT lasers are left off for 1 ms before we turn them on again. After that the MOT beams are on for 9 sec. to collect the atomic cloud.

The delay times of all the pulses were based on the CCD camera's video time frame as shown in Fig. 3.15. The video time frame consists of a series of time frames each 33 ms long, when the camera captures incident light, followed by a blank interval to mark the end of the frame. The camera converted the captured light intensity into a voltage signal. We digitized and saved this signal to a hard disk

drive by using a frame grabber card (PIXCI^{TM}, model SV4) that was connected to the computer through a GPIB interface. The end mark was used as a time reference point for all other pulses controlled by the computer via the GPIB card.

The diagram in Fig. 3.15 summarizes all the control pulses mentioned in this section. We developed a computer program to implement these pulses automatically, according to the procedure we mentioned in the chapter's introduction. The source code of the program, written in C/C++, is shown in Appendix G.1.

As shown in Fig. 3.15, the computer program started from recognizing the end-of-frame mark and command all the DDGs to fire pulses. The probe pulse was always fired 551 ms after the end mark so that it was always in the middle of a given time frame. Thus we obtained an expansion of the MOT ensemble by setting the MOT laser pulse to be off at time t ms before the probe pulse was fired. To obtain the expansion of the MOT ensemble with the tunnel on, the tunnel pulse was turned off at t_H ms after the MOT pulse was off while keeping $t < t_H$. When $t > t_H$, the free expansion of the MOT ensemble was obtained after the MOT was held in the tunnel for t_H ms.

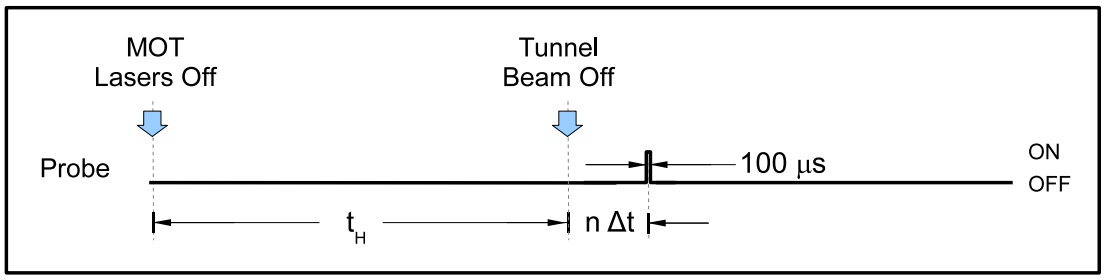

Figure 3.16: The diagram of events associated with the data acquisition process. It shows the same events occuring in Fig. 3.15 but with respect to the time the MOT lasers are turned off.

We note that the variables t_{MOT}, t_{probe}, and t_{tun} we mentioned in the chapter's introduction are related to t (expansion time) and t_H (hold time) via

$$t = t_{\mathrm{probe}} - t_{\mathrm{MOT}} = n\Delta t, \tag{3.1}$$

where n and Δt were mentioned at the beginning of this chapter, and

$$t_H = t_{\text{tun}} - t_{\text{MOT}}. \tag{3.2}$$

The diagram in Fig. 3.16 summarizes the meaning of t and t_H with respect to the time the MOT lasers are turned off. When $t_H = 0$, as an example, we get the expansion of the MOT cloud without an influence from the optical tunnel. The variables t and t_H will be used again in Chapter 4.

After we finish the data acquisition, MATLAB codes are used to analyze the data.

Chapter 4

Atoms Guided in a Single Tunnel

As mentioned in the introduction section, we will look at the dynamics of an atomic ensemble guided in a single tunnel across a plane perpendicular to the tunnel's propagation direction. We observe the evolution of the atomic distribution using shadow imaging technique described in Chapter 3. The ensemble's dynamics can be divided into two cases: (1) when the average kinetic energy of the atoms is much lower than the potential height of the tunnel and (2) when they are comparable to each other.

For the first case the ensemble's dynamics can be calculated analytically. It was discussed in detail in Song's thesis [60]. The characteristic of the tunnel guide was summarized through a single factor, the shape factor, related to the shape of the tunnel. In the first section of this chapter, we will follow Song's analysis and roughly approximate the shape factor of several tunnels using geometrical functions. From our approximations, the reader can quickly obtain and compare different shape factor values.

For the second case where the ensemble's average kinetic energy is comparable to the height of the tunnel, the dynamics has to be calculated numerically. In the second section, the evolution of the ensemble inside a Bessel tunnel in phase-space will be followed. A transverse temperature [1], which is a representation of the velocity distribution in a plane transverse to the tunnel's propagation direction, will be extracted from the experimental measurements and numerical simulations at different

[1]The term called "transverse temperature" is not proper terminology because temperature is a scalar entity as has been pointed out by Song [60]. It is used for our convenience to associate the velocity distribution in a plane perpendicular to the propagation direction of the tunnel with a temperature related to a Maxwellian velocity distribution on the plane in 2D.

times to track the evolution. Comparisons between the experimental measurements and the results of the simulations will help provide a better understanding of the dynamics and allow the total energy of the ensemble propagating inside the tunnel to be approximated.

4.1 Time-Averaged Absorption Rate and Longitudinal Acceleration

An experiment carried out by Song [36, 60] demonstrated that an atom ensemble can be guided for a very long distance ($\sim$ 20 cm) in a single blue-detuned hollow tunnel, 1 mm in diameter. The guide was shown to accelerate or decelerate the ensemble in addition to the acceleration by the Earth's gravity. By adjusting the frequency of the tunnel, the ensemble acceleration could be changed. In Fig. 4.1, plots of vertical positions of the center of mass of a ^{133}Cs ensemble against time are shown for different values of detuning. To account for this acceleration, Song [60] considered a single atom traversing only radially inside his near-cylindrical symmetric tunnel and calculate the acceleration a_{asp} from the time-averaged photon-absorption-rate $\langle R \rangle$, which was written as

$$a_{asp} = v_{rec} \cdot \langle R \rangle = \frac{v_{rec}}{\tau} \int_0^\tau R(t)\ dt, \tag{4.1}$$

where v_{rec} is the atom recoil velocity, $R(t)$ is the absorption rate at time t and τ is the round trip travel time for the atom to make one round trip. The value of $R(t)$ and τ depends on the intensity $I(r)$, which is a function of radius, r. For a detuning of Δ, $R(r(t))$ can be written as

$$R(r) = \frac{\Gamma^3}{8\Delta^2} \frac{I(r)}{I_s}, \tag{4.2}$$

assuming a large detuning $(\Delta/\Gamma)^2 \gg I(r)/I_s \gg 1$, where Γ is the natural linewidth of the atom and I_s is the saturation intensity.[2] Using the conservation of energy $m(dr/dt)^2 + 2U(r) = 2E$ and the fact that $I(r)$ is proportional to the potential $U(r)$,

[2] see Appendix B for the derivation of the absorption rate.

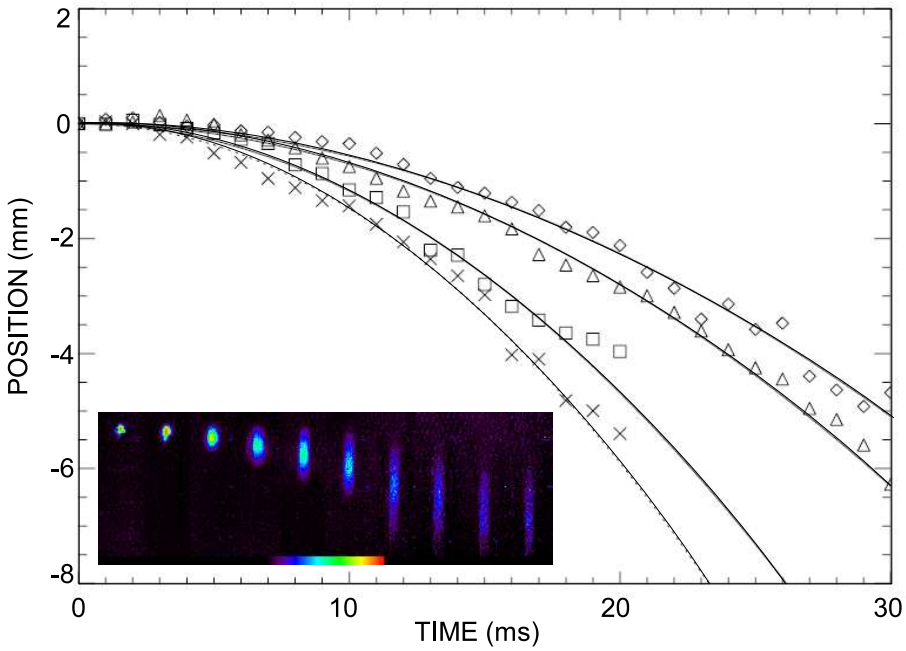

Figure 4.1: Vertical positions of the center of mass of a Cs ensemble vs. time for different values of frequency detuning. For the ensemble with initial temperature of $T = 80$ μK, the values of the detuning are 0.25 GHz ($\square$), 1 GHz ($\triangle$), and 2 GHz ($\diamond$). For initial $T = 140$ μK, the value of the detuning is 1 GHz ($\times$). The solid curves represent the predictions as described in Ref. [60]. The accelerations, $g+a_{asp}$, extracted from the solid curves are 11.3 ($\diamond$), 14.0 ($\triangle$), 23.4 ($\square$) and 29.5 ($\times$) m/s^2 accordingly. The inset shows shadow images of the ensemble viewed perpendicular to the propagation direction of the tunnel. Reproduced from Ref. [60, 118].

the integral in Eq. 4.1 can be written as

$$\langle R\rangle = \Gamma_E \cdot \frac{\displaystyle\int_0^{r_t} \frac{U(r)/E}{[1-U(r)/E]^{1/2}}\, dr}{\displaystyle\int_0^{r_t} \frac{1}{[1-U(r)/E]^{1/2}}\, dr} = \Gamma_E \cdot SF, \tag{4.3}$$

where $\Gamma_E = \Gamma E/\hbar\Delta$ and SF denotes the shape factor related to the shape of the potential.

To quickly evaluate the SF, we first consider a geometrical potential [118] $U(r) = kr^s/2$ and $E = kr_t^s/2$, where r_t is the radius at the turning point and s a

positive real number. The SF can be written as

$$SF_{(geo,hollow)} = \frac{\int_0^1 \frac{\zeta^s}{[1-\zeta^s]^{1/2}}\, d\zeta}{\int_0^1 \frac{1}{[1-\zeta^s]^{1/2}}\, d\zeta} = \frac{2}{s+2}, \tag{4.4}$$

where $\zeta = r/r_t$ and the subscript $(geo, hollow)$ denotes that the tunnel is geometric and hollow. This equation shows that the SF of the geometrical tunnels does not depend on r_t and decreases as the bottom of the potential get flatter for higher power s. Now, instead of the hollow tunnel, if we use a red-detuned bright tunnel with the geometrical shape to trap the atom, we will have.

$$SF_{(geo,bright)} = 1 - SF_{(geo,hollow)} = \frac{s}{s+2}. \tag{4.5}$$

For a special case when $s = 2$, the potential is harmonic, an atom in the hollow and the bright beam absorb photons at the same rate at $\Gamma_E/2$. With higher s, the atom in the bright beam has higher rate of absorption than its counterpart, i.e. $SF_{(geo,bright)}/SF_{(geo,hollow)} = s/2$.

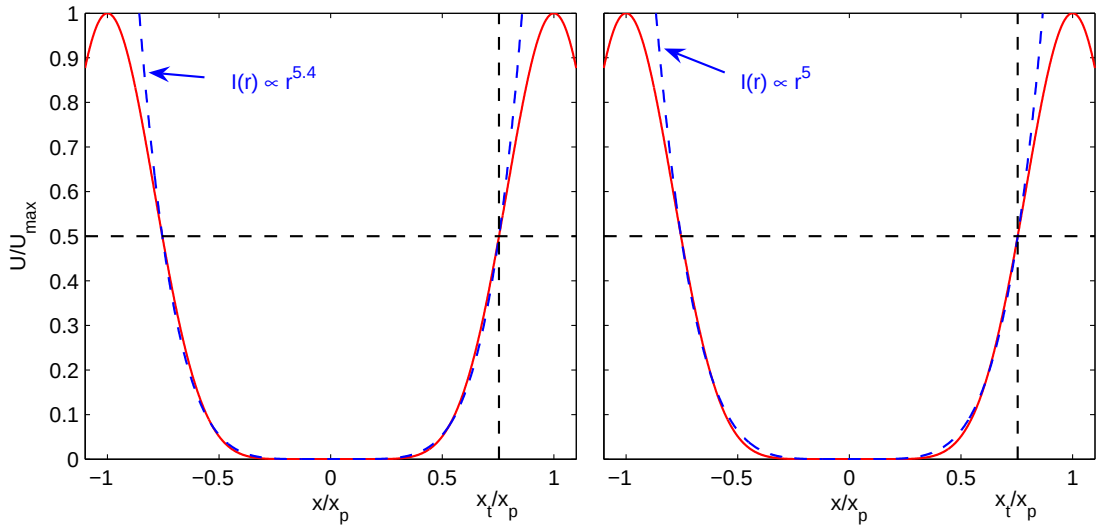

Figure 4.2: The intensity profile of J_4-Bessel tunnel as represented by $I(r) \propto r^{5.4}$ (left) and $I(r) \propto r^5$ (right) for r_t such that $U(r_t) = 0.5\, U_{max}$. The profile is plotted along an x-axis that passes through the center of the tunnel and $x_p = r_p$.

It can be seen that once the power s of the geometrical function is known, the SF can be calculated easily. However, unlike a geometrical function with a specific s value, a summation of geometrical functions of different powers (e.g. a Taylor expansion of a function) does not make the evaluation of Eq. 4.3 easy. The ratio $U(r)/E$ of the summation cannot be reduced to a form that depends only on a single variable. Following this fact, we can roughly approximate the value of SF for a tunnel only with a shape similar to r^s. We choose s that best represents the shape of the tunnel of interest, providing that the values of r_t are the same for both the tunnel of interest and the geometrical tunnel. For example, the intensity of a

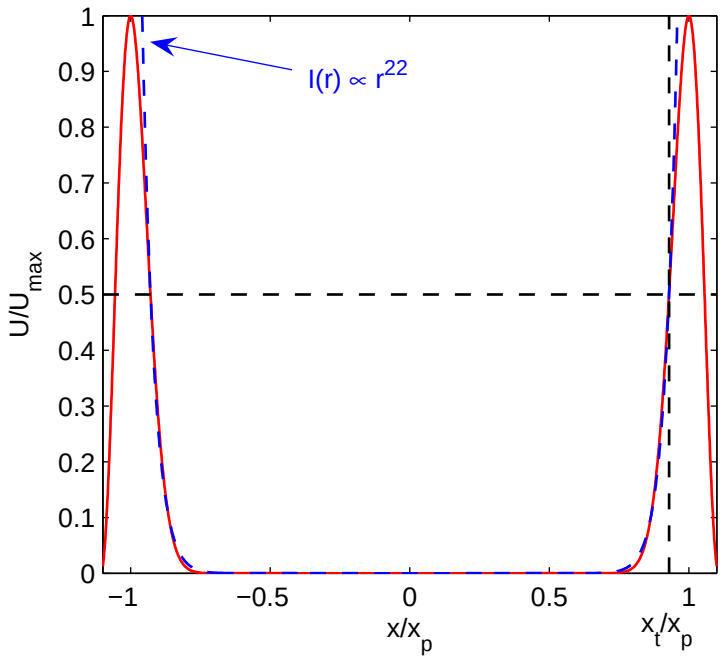

Figure 4.3: The intensity profile of J_{31}-Bessel tunnel is represented by $I(r) \propto r^{22}$ for r_t such that $U(r_t) = 0.5\,U_{max}$. The profile is plotted along an x-axis that passes through the center of the tunnel and $x_p = r_p$.

blue-detuned J_4-Bessel tunnel can be approximated by $I(r) \propto r^{5.4}$ when the turning point r_t is chosen such that $U(r_t)$ is half the tunnel's peak potential U_{max} as shown in Fig. 4.2. The value of the SF is $2/(2+5.4) = 0.27$. Therefore, the atom absorbs $\sim 1/3$ times the absorption when it is in the red-detuned bright tunnel with $s = 6$,

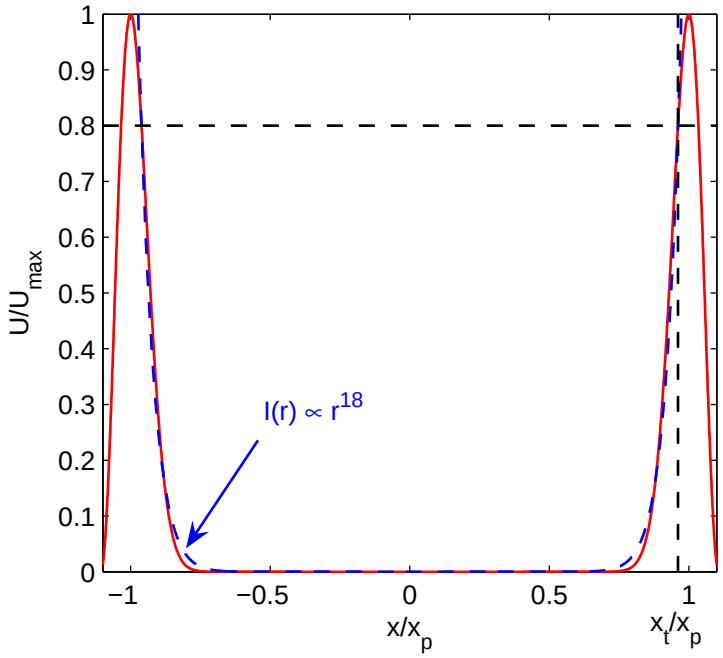

Figure 4.4: The intensity profile of J_{31}-Bessel tunnel represented by $I(r) \propto r^{18}$ for r_t such that $U(r_t) = 0.8\,U_{max}$. For this large r_t, the geometrical profile deviated from the Bessel profile as indicated by the arrow. The x-axis passes through the center of the tunnel on the transverse plane and $x_p = r_p$.

and $\sim 1/2$ times when it is in the red-detuned tunnel with $s = 2$ for the same r_t.

For the case of a blue-detuned J_{31}-Bessel tunnel, which is approximately the same as Song's potential, the intensity profile up to r_t such that $U(r_t) = 0.5\,U_{max}$ can be represented by $I(r) \propto r^{22}$, as shown in Fig. 4.3. The geometrical profile gives $SF \sim 0.08$. For r_t such that $U(r_t) = 0.1\,U_{max}$, $I(r) \propto r^{31}$ best represents the intensity profile and $SF \sim 0.06$. The values of SF calculated here are roughly what Song has provided[3] in Fig. 5.6 in his thesis [60]. Note that the geometrical approximation is not justified for all the range of r_t. As shown in Fig. 4.4, to match the profile near the peak, the geometrical profile deviated from the J_{31}-Bessel profile near the end of the flat bottom as indicated by the arrow. For a Bessel tunnel, the

[3]In Song's thesis, the intensity profile of his potential is approximated by that of a modified harmonic potential. He extends the intensity zero point to a finite length in the middle of the potential[60].

range of r_t that is suitable for the geometrical approximation depends on the order of the Bessel function. The range is larger for a higher order Bessel function.

From this single atom model, the acceleration from the tunnel is velocity dependent. To estimated the acceleration of the ensemble in the experiment, the most probable value of r_t calculated from the averaged velocity of atoms in the ensemble is chosen. Note that this method is useful for the condition in Song's experiment which has the peak potential much higher ($\sim 10\times$) than the ensemble's initial temperature. In the case where the potential height is comparable to the ensemble temperature, there are leaks of atoms from the potential and the dynamics of the whole ensemble must be considered. In the next section, we consider this dynamics from various point of views, instead of considering just one atom.

4.2 Transverse Temperature Extractions and Ensemble Dynamics

By guiding an atom ensemble in a tunnel with a maximum potential U_{max} comparable to the mean kinetic energy of the ensemble, some fraction of atoms with high kinetic energy can leak out of the tunnel, leaving the colder ensemble inside. The tunnel thus has an additional function being an atom gating device, other than just being a guide. Raising or lowering U_{max} around this temperature significantly changes the content of energy allowed to be guided. For a single blue-detuned tunnel, this leak mechanism has been witnessed. A sharp reduction in the total number of atoms in the tunnel, within the first 5 ms after the atoms are released from the MOT, has been reported[4] [118].

By contrast, the population is relatively stable during transit at later times. This behavior can be understood as follows. The tunnel is loaded with atoms from a MOT. When the trap lasers are turned off ($t = 0$), most of the cold ensemble is inside the tunnel. An atom near the tunnel wall with sufficient kinetic energy (and properly oriented momentum) to make it through the wall will be accelerated away from the tunnel core by the tunnel after making it past the peak of the tunnel poten-

[4]We also see this in the next chapter from a plot (red square) in Fig. 5.5.

tial. There are substantially fewer atoms outside the tunnel initially with energies sufficient to penetrate the wall so the number of energetic MOT atoms entering the tunnel will be smaller than the number leaving, leading to the net outward flux of warmer atoms. The energetic tail of the Maxwellian distribution in the transverse direction was missing, leaving an ensemble that is effectively colder than the initial load. Along with this reduction in the number of atoms in the ensemble and reduction in the transverse temperature there was a decoupling between the "transverse" temperature ($T_{\perp}$) and the "longitudinal" temperature ($T_{||}$). The values of $T_{\perp}$ and $T_{||}$ were observed to be very different. Experimentally, while $T_{||}$ was essentially observed to be the same as the initial load temperature, $T_{\perp}$ dropped precipitously within $\sim$ 5 ms to an estimated $T_{\rm tun}/5$, where $T_{\rm tun} = U_{max}/k_{\rm B}$ denotes the tunnel potential height in terms of Kelvin and $k_{\rm B}$ denotes the Boltzmann constant [118].

The mechanical restriction from the tunnel allows the separation of variables of the Liouville Equation (LE) in 3D into equations evolving transverse coordinates and a longitudinal one along the tunnel's propagation axis. The separation can be done assuming that the shape and size of the tunnel is spatially invariant upon propagation.

In this section we will investigate the connection between the leak mechanism and the reduction in the ensemble temperature via experiments and simulations. Ideally, we would like to know the evolution of the velocity distribution exactly and calculate temperature that is associated with it. However, tracking the velocity of all particles ($\sim 10^8$ atoms) is challenging. One way to map the velocity distribution could be to monitor the spatial profile of the frequency-dependent absorption spectrum (Doppler profile) at various angles in the ensemble. Another way, which we employed is to compare simulations with experimental results of the tunnel guide. Specifically, we used the Liouville equation (LE) (the collision-free Boltzmann equation). In Cartesian coordinates, in the six dimensional phase-space of distribution function, $\zeta(\vec{r}, \vec{v}_r, t)$, of the ensemble is given by

$$\frac{d}{dt}\zeta(\vec{r}, \vec{v}, t) = \frac{\partial}{\partial t}\zeta(\vec{r}, \vec{v}, t) + \vec{v} \cdot \nabla_{\vec{r}}\zeta(\vec{r}, \vec{v}, t) - \frac{\nabla_{\vec{r}}U(r)}{m} \cdot \nabla_{\vec{v}}\zeta(\vec{r}, \vec{v}, t) = 0, \qquad (4.6)$$

where m is the atomic mass, $\nabla_{\vec{r}}$ and $\nabla_{\vec{v}}$ denote the gradients with respect to $\vec{r}$ (position) and $\vec{v}$ (velocity) respectively, and $U(r)$ the potential. The spatial distribution $g(\vec{r})$ and the velocity distributions $h(\vec{v})$ are found by integrating $\zeta(\vec{r},\vec{v},t)$ over all velocities and positions, respectively, i.e.

$$g(\vec{r}) = \int_{-\infty}^{\infty} \zeta(\vec{r},\vec{v}) d\vec{v}, \tag{4.7}$$

and

$$h(\vec{v}) = \int_{-\infty}^{\infty} \zeta(\vec{r},\vec{v}) d\vec{r}. \tag{4.8}$$

The Liouville equation is suitable for describing our system because the mean-free path at MOT densities exceeds 1 m while the relevant dimension of the confined atoms is $\sim$ 2 mm. While collisions between atoms can be ignored, the atoms do collide with the tunnel wall and scatter photons.

In the following subsections, two special solutions of the LE, the steady-state ($\partial\zeta/\partial t = 0$) and the free-expansion solution ($\nabla_{\vec{r}} U(r) = 0$), will be used to track the phase-space distribution and the transverse temperature at different times. We will provide (1) a description of the experiments and simulations that exploit these solutions, (2) ways to extract velocity distribution and the transverse temperature from these solutions, and (3) the results and discussions. From these studies, it will become clear that the ensemble in the tunnel is not in thermal equilibrium and the velocity distribution of the ensemble can no longer be described by a Maxwellian distribution. However, the transverse velocity distribution will be seen to be best described by a truncated Maxwellian with velocity components corresponding to $v \gtrsim (2k_{\mathrm{B}}T_{\mathrm{tun}}/m)^{1/2}$ missing, where k_{B} and T_{tun} denotes the Boltzmann constant and tunnel potential height in terms of Kelvin. Furthermore, we will show that the velocity distribution is not spatially uniform. We will end this section with a proposal to exploit the inherent leak of blue-detuned tunnels for evaporative cooling, which may be possible to implement during cloud transit.

4.2.1 Holding and Releasing Scheme

For the experiments and simulations in this section, a hollow J_4-Bessel beam is used to confine the ensemble in its dark core. We monitor two categories of spatial distributions: (1) a series of images of spatial distributions taken from the evolution of the ensemble in the tunnel after times t_H (hold time) subsequent to the cloud being released from the MOT, and (2) a series of images of the spatial distribution at times t (expansion time) taken after the cloud is released from the tunnel (tunnel turned off). These processes are described in detail in Sec. 3.4. We use profiles of the first category to extract the transverse temperature from the steady-state analysis (Eq. 4.6 with $\partial\zeta/\partial t = 0$). The other category is used to extract the transverse temperature from the free expansion or time-of-flight (TOF) analysis. The range of t_H used in the experiment and simulations was from 0 up to 20 ms. On the other hand, the free expansion series is only obtained after three particular hold times i.e. $t_H = 10$, 15, and 20 ms. We chose these values of hold times because the atom distribution inside the tunnel could be distinguished from the background distribution of hot atoms leaking out of the tunnel. For $t_H > 20$ms, however, the number of the in-tunnel atoms became obscured by the background for the observation of the free expansion after the tunnel was turned off.

From the experiments, the initial spatial distribution of the ensemble in the MOT is assumed to be Gaussian (Maxwellian velocity distribution). This assumption was confirmed by measurements discussed in the next chapter.

For the simulations, we performed (1) a classical trajectory Monte Carlo (MC) simulation and (2) an integration of Liouville Equation (LE) to simulate the time dependent behavior of the transverse temperature and compared it to the temperature we extracted from both experiments described in the beginning of this section. We performed both MC and LE simulations in order to provide consistency checks in our calculations. The simulations will be explained in the following sections. Our two numerical simulations provided theoretical estimates of the phase-space distribution out of which the density and velocity distributions could be projected for

different values for t_H. While the tunnel's orbital angular momentum is reported to influence the atomic motion, even for thermal atoms [119, 90], its contribution was not included in our simulations.

The simulations were performed on a grid that represented a physical space larger than the tunnel and the MOT, allowing atoms inside and outside the tunnel to be modeled.[5] Thus, the simulations included atoms in the hot tail of the velocity distribution that traversed the tunnel wall. Both the spatial and velocity distributions are modeled with Gaussian functions at $t = 0$ to reflect the atom source (i.e, a MOT) from the experiments. At the end of the hold period, $t = t_H$, modified spatial and velocity distributions were obtained from the atoms within the spatial boundary of the tunnel.

4.2.1.1 Experimental Conditions

The procedure of obtaining the distribution was the same as that described in Chapter 3. We monitored the distribution projected on a plane transverse to the tunnel's propagation direction, using probe PRB2 as shown in Fig. 3.13. The probe makes a slight angle of 20 mrad with the tunnel which causes $\sim 3\%$ error in the width of the spatial distribution. The error was estimated from a calculation based on free expansion in 1D of the Gaussian distributed ensemble projected on a frame rotated by 20 mrad. The expansion time used in this estimation is 20ms. All experiments were performed on thermal ensembles of ^{87}Rb prepared in a MOT. As described earlier, our experiments consisted of monitoring the time-dependence of the spatial distribution while the tunnel was on (profile measurements) and after it was extinguished (TOF measurements) as shown in Fig. 4.5 and Fig. 4.6 respectively. The atoms were initially trapped in a near-spherical volume with a radius ~ 1 mm by a vapor loaded MOT at a temperature of ~ 150 μK. The tunnel diverged with a half angle of ~ 0.2 mrad; the tunnel radius increased by ~ 20 μm over the 10 cm experimental region, which was smaller than our uncertainty in determining $r_{\rm p}$

[5] At $t = 0$, when the MOT is turned off, $\sim 10\%$ of the atoms are outside the tunnel.

($= 0.89 \pm 0.03$ mm, corresponding to $k_r \sim 5975$ m^{-1} at the MOT). A beam power of ~ 370 mW (60 mW in the first ring) lead to $T_{\rm tun} = 57$ μK ($= U_{\rm max}/k_{\rm B}$), which was stable to within $\pm$ 5% during the course of the experiments. The tunnel was oriented vertically and aligned to overlapped with the central portion of the MOT cloud while the trap beams were still on and included $\sim 90\%$ of the MOT ensemble. The tunnel was loaded by turning off the trap (MOT) beams. We detuned the tunnel's frequency 4 GHz away from the ^{87}Rb $5S_{1/2}(F = 2) \rightarrow 5P_{3/2}(F' = 3)$ transition.

4.2.1.2 Numerical Simulation: Liouville Equation

The evolution of an ensemble distribution in the phase-space can be described by the Liouville equation (LE). We simplified our analysis by treating only the radial motion, in which case Eq. 4.6 reduced to

$$\frac{\partial}{\partial t}\zeta(r, v_\perp, t) + v_\perp \frac{\partial}{\partial r}\zeta(r, v_\perp, t) - \frac{1}{m}\frac{\partial}{\partial r}U(r)\frac{\partial}{\partial v_\perp}\zeta(r, v_\perp, t) = 0, \tag{4.9}$$

where $v_\perp = (v_x^2 + v_y^2)^{1/2}$ denotes the radial speed. We determined the evolution of the $\zeta(r, v_\perp, t)$ from t_0 to t_1 in the standard way by applying the appropriate propagator[6],

$$\zeta(r, v_\perp, t_1) = \exp\left[(t_1 - t_0)\left(-v_\perp \frac{\partial}{\partial r} + a_\perp \frac{\partial}{\partial v_\perp}\right)\right]\zeta(r, v_\perp, t_0), \tag{4.10}$$

where $a_\perp$ is the radial acceleration defined through $ma_\perp = -\partial U(r)/\partial r$. Equation 4.10 can be solved iteratively for time steps Δt. Employing the split-operator method [120], Eq. 4.10 can be transformed into

$$\zeta(r, v_\perp, \Delta t) = \exp\left(-\frac{\Delta t}{2} v_\perp \frac{\partial}{\partial r}\right)\exp\left(\Delta t\ a_\perp \frac{\partial}{\partial v_\perp}\right)\exp\left(-\frac{\Delta t}{2} v_\perp \frac{\partial}{\partial r}\right)\zeta(r, v_\perp, t_0 = 0). \tag{4.11}$$

Solutions for Eq. 4.11 are found by applying the three operators sequentially (from right to left). When $\zeta(r, v_\perp, \Delta t)$ is well behaved, the solutions are good to second order in Δt [121].

Figure 4.7 shows ζ for a confinement duration of ($t_H =$) 10 ms, where $t_0 = 0$ corresponds to when the atoms were loaded into the tunnel from the MOT (trap

[6]see details in Appendix E.5

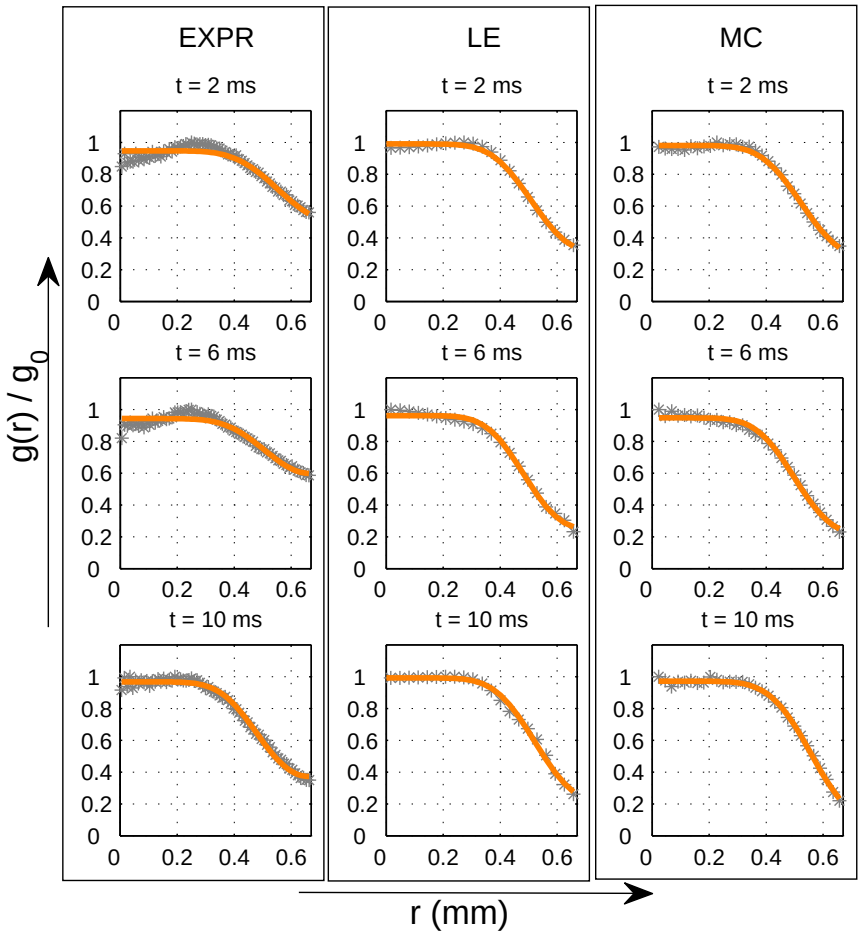

Figure 4.5: Experimental (left column) and simulated radial profiles obtained for tunnel hold times of $t_H = 2$ (top row), 6 and 10 ms (bottom row) along with numerical fits based on Eq. 4.15 (solid curves) for the LE (middle column) and MC calculations. On the vertical axis, g_0 denotes the normalization constant.

lasers turned off). The corresponding spatial, $g(r)$, and velocity, $h(v_\perp)$, distributions are shown as well. The distribution $g(r)$ and $h(v_\perp)$ were calculated from $\zeta(r, v_\perp, t)$ using Eq. 4.7 and Eq. 4.8 respectively. The spatial profiles for $t_H = 2, 6$ and 10 ms are also displayed in Fig. 4.5 in the middle column. Clearly, ζ is not spatially uniform inside the tunnel (see Fig. 4.7). Thus, $g(r)$ and $h(v_\perp)$ represent the average behaviors inside the tunnel. After the tunnel is turned off, $g(r, t)$ gives the free expansion profile at t.

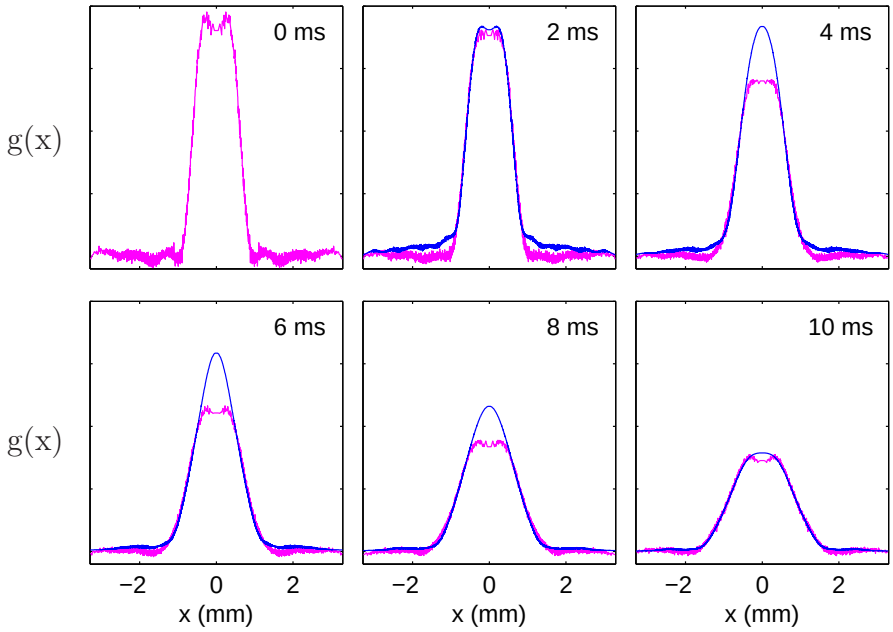

Figure 4.6: Measured free-expansion profiles (purple) along the x-axis ($y = 0$) after $t_H = 10$ ms along with the fit profiles, $\langle g(x - v_x t)\rangle$ (blue) of Eq. 4.17 as described in the text. For this particular example, $T_{\rm MOT} = 150$ μK and the integral was truncated at $v_{\rm m}$ corresponding to $T_{\rm tun}$ ($= 57$ μK).

4.2.1.3 Numerical Simulation: Classical trajectories

Our classical-trajectory Monte Carlo (MC) calculations (also known as molecular dynamics calculation) included 2×10^6 trajectories and was performed with the aid of a 2D Cartesian array of cells upon which the tunnel potential was superimposed. Each cell was assigned a specific acceleration value[7], $\vec{a} = -\vec{\nabla}U/m$, which allowed an evolution of the cloud to be followed numerically via Newton's equations by taking small time steps, Δt. Time steps were chosen to be small enough that the final results changed by less than 1% when the steps were cut in half. Simulations for the evolution in the tunnel were initiated at $t = 0$ and terminated at $t = t_H$. Simulated profiles $g(r)/g_0$, where g_0 is the normalization constant, for $t_H = 2, 6$ and 10 ms are shown in Fig. 4.5. This simulation also lead to a numerical estimate of the velocity distribution, $h(v_x, v_y)$, from which we were able to estimate the transverse

[7] A la particle-in-cell approach, see Appendix E.6 for more detail

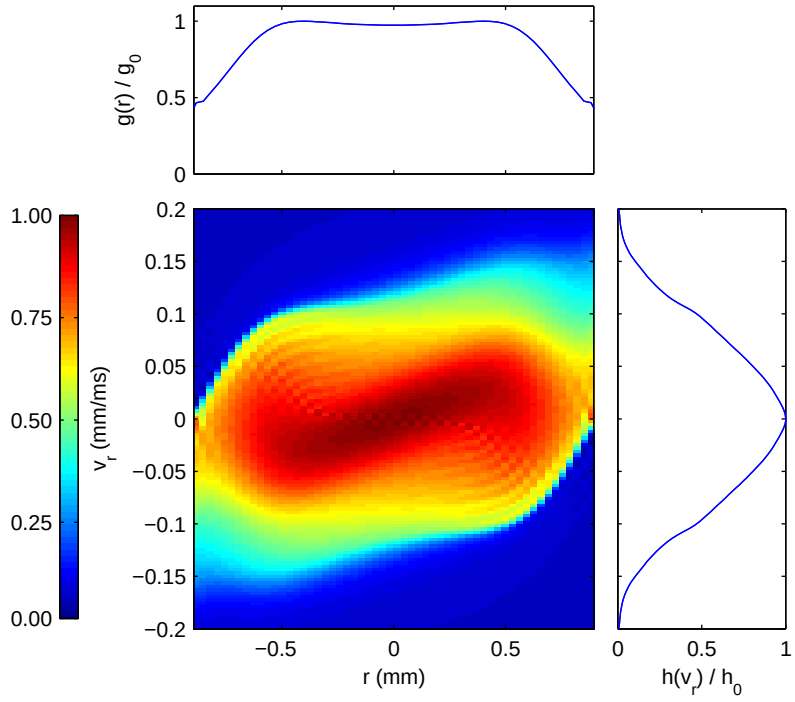

Figure 4.7: Phase space atomic distribution (ζ) based on the LE simulation (main figure) for $t_H = 10$ ms in a Bessel tunnel matching the conditions of our experiment. The upper (right) line plot is the spatial (velocity) distribution projected out ζ (as described in the text) normalized to 1 at its peak, where g_0 and h_0 denote the normalization constants.

temperature as described in the next subsection. The detail of the MC calculation is provided in Appendix E.6.

4.2.2 Temperature Extraction

We estimated the transverse temperature $T_\perp$ in three distinct ways yielding the following estimates: (1) $T_{\perp,0}$ from fits to the spatial distribution profiles $g(r)$ at t_H in Fig. 4.5; (2) $T_{\perp,1}$ from the measured cloud expansion at time t after the tunnel is turned off, and (3) $T_{\perp,2}$ from the LE and MC simulations of the velocity distributions $h(v_\perp)$ inside the tunnel. The results are summarized in Table 4.1.

4.2.2.1 Steady State Profile Fit: $T_{\perp,0}$

Steady state demands $\partial\zeta/\partial t = 0$, in which case the radial Liouville equation, Eq. 4.9, is separable, $\zeta(r, v_\perp) = g(r)h(v_\perp)$. The solution can be written as (see Appendix E.3)

$$\zeta(r, v_\perp) = \zeta_0 \exp\left[-\frac{U(r)}{k_B T_\perp}\right] \exp\left(-v_\perp^2/2\sigma_v^2\right), \tag{4.12}$$

where ζ_0 is the normalization factor and $\sigma_v = (k_B T_\perp/m)^{1/2}$. For a J_n-Bessel tunnel with a large detuning $(\Delta/\Gamma)^2 \gg I(r)/I_s \gg 1$,

$$U(r) = \frac{\hbar\Gamma^2}{8\Delta}\frac{I(r)}{I_s} = \alpha k_B T_\perp J_n^2(k_r r), \tag{4.13}$$

where

$$\alpha \equiv \frac{1}{J_n^2(k_r r_\mathrm{p})}\frac{U_\mathrm{max}}{k_\mathrm{B} T_\perp} = \frac{1}{J_n^2(k_r r_\mathrm{p})}\frac{T_\mathrm{tun}}{T_\perp}, \tag{4.14}$$

r_p is the position of the peak value of the first Bessel ring, and $T_\mathrm{tun} = U_\mathrm{max}/k_\mathrm{B}$. Therefore by integrating Eq. 4.12 over all velocities, $g(r)$ is given by

$$g(r) = g_0 \exp[-\alpha J_n^2(k_r r)], \tag{4.15}$$

with

$$g_0^{-1} = 2\pi \int_0^{r_\mathrm{p}} \exp[-\alpha J_n^2(k_r r)] r dr, \tag{4.16}$$

Theoretical plots of the spatial distribution function $g(r)$ inside a J_4-Bessel tunnel are shown in Fig. 4.8 for different values of α. The distribution depends on the size of the tunnel (controlled by k_r) and the ratio of the potential height of the tunnel wall, U_max, and the transverse kinetic energy of the atoms, $k_\mathrm{B} T_\perp$, through the parameter α. It is clear from Fig. 4.8 that when $T_\perp$ is well above $T_\mathrm{tun}/5$ (α well below 30), there is an appreciable number of atoms that can penetrate the tunnel wall (i.e., those with relatively large transverse velocities). Clearly, when $g(r_\mathrm{p})$ is significantly larger than zero, population can flow in and out of the tunnel in this steady-state model. When $\alpha \gtrsim 30$ motion of atoms in and out of the tunnel is greatly suppressed. We note that $g(r_\mathrm{p})$ is ~ 44 times larger and there are roughly four times as many atoms in the wall (10% to peak) when $T_\perp \sim T_\mathrm{tun}$ as compared to when $T_\perp \sim T_\mathrm{tun}/5$.

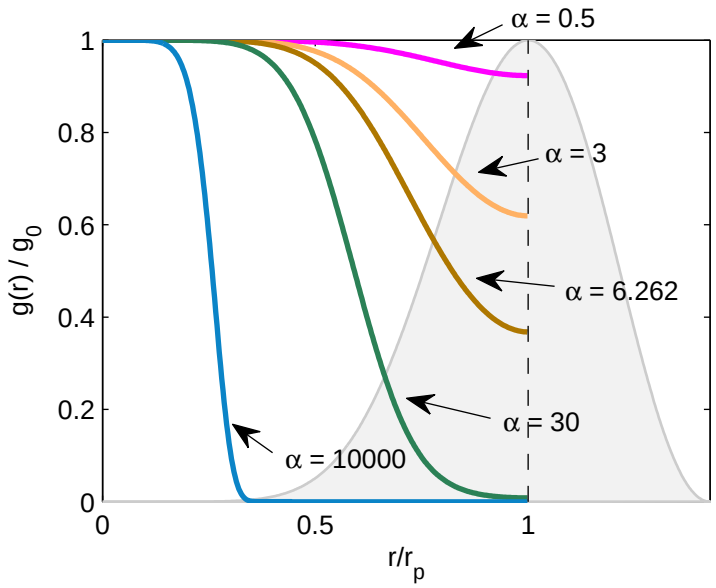

Figure 4.8: Radial profiles (Eq. 4.15) of a thermal ensemble in a J_4-Bessel mode tunnel (shaded area) for different values for α (Eq. 4.14). For the conditions of this experiment, $\alpha = 6.262$ corresponds to $T_\perp = T_{\rm tun}$. As discussed in the text, small values of α allow the warmer atoms to leak out of the tunnel, as indicated by a substantial number of the atoms existing at $r_{\rm p}$. When $\alpha \gtrsim 30$ ($T_\perp \sim T_{\rm tun}/5$) the leak is nearly negligible.

In our experiments and simulations, we used a Bessel mode of $n = 4$ and at the peak of the first ring, $J_4^{-2}(k_r r_{\rm p}) \approx 6.262$, thus, $\alpha \approx 6.262\ T_{\rm tun}/T_\perp$. Values for α and thus $T_\perp$ were extracted from the nonlinear fit to the spatial density profiles of an assumed steady-state spatial distribution across the tunnel at time t_H. The numerical fits were run from $t_H = 0$ to 20 ms; some selected results are shown in Fig. 4.5 as solid lines. The extracted temperatures are sensitive to the background density associated with the hot atoms that ultimately leave the tunnel. This population is difficult to isolate in the steady-state density profiles. Depending on how we estimate its magnitude, the resulting $T_{\perp,0}$ can vary from 3 nK (with the background removed in the largest case) to 50 μK (with no background population removed)[8]. What we

[8]The sensitivity of this approach to the "proper" removal of the background makes this approach to estimating the temperature problematic.

report in Table 4.1 is $T_{\perp,0}$ without the background removed. The errors for $T_{\perp,0}$ in the table correspond to the 95% fit-confidence interval.

4.2.2.2 Ensemble Free Expansion: $T_{\perp,1}$

Temperature extraction via TOF measurements is very straightforward when the spatial and velocity distributions are both Gaussian; the cloud spread can be shown to be characterized by any point (other than the peak) on the Gaussian, such as the $1/e$ point. This can also be done for non-Gaussian distributions at long times compared with the inverse trap frequency. In our case, however, neither the spatial (see Fig. 4.8 and Eq. 4.15) nor the velocity (see Fig. 4.7 and discussion below) distributions were Gaussian nor were we able to reach the long-time regime. However, given a closed form of the velocity distribution, it is possible to predict how an initial arbitrary spatial profile, $g(\vec{r}) = g(x, y)$, will evolve if we recognize that the solution to Eq. 4.6 with $\nabla_{\vec{r}} U(r) = 0$ has the functional form $\zeta(\vec{r} - \vec{v}t, T)$. Here, we explicitly put in a temperature dependence, which only applies to motion in the transverse plane. When the tunnel is turned off, the velocity distribution appears to be locked in so the spatial and velocity functions are again separable, $\zeta(\vec{r} - \vec{v}t, T) \rightarrow g(\vec{r} - \vec{v}t)h(\vec{v}, T)$, at least for the short times of our experiments. The transverse spatial components in g (and hence ζ) are not separable in general. Thus, the spatial profile at a time t after turning off the tunnel will be given by a 2D integration of ζ over all velocities, i.e. in Cartesian coordinates,

$$g_c(\vec{r}, t, T) = \int_{-\infty}^{\infty}\int_{-\infty}^{\infty} g(\vec{r} - \vec{v}t)h(\vec{v}, T)\, dv_x\, dv_y \tag{4.17}$$

$$= \int_{-\infty}^{\infty}\int_{-\infty}^{\infty} g(x - v_x t, y - v_y t)\, h(v_x, v_y, T)\, dv_x\, dv_y. \tag{4.18}$$

It can be shown that a numerical evaluation of Eq. 4.17 can be obtained using the convolution theorem for the Fourier transforms (see Appendix E.4 for more detail), i.e.,

$$g_c(\vec{r}, t, T) = \frac{g_0}{t^2}\, \tilde{\mathfrak{F}}\left\{ \mathfrak{F}\{g(x, y)\}\, \mathfrak{F}\left\{ h\left(\frac{x}{t}, \frac{y}{t}\right)\right\}\right\}, \tag{4.19}$$

where $\mathfrak{F}\{\Box\}$ and $\tilde{\mathfrak{F}}\{\Box\}$ are the Fourier and inverse Fourier transform of function $\Box$ respectively.

To match $g_c(r,t,T)$ to our series of measured (or simulated) TOF profiles, we take one of two approaches. In the first, we assume that $h(\vec{v},T)$ is a Gaussian function with the width $\sigma_v = (k_{\rm B}T/m)^{1/2}$ and T is adjusted; $T_{\perp,1}$ is taken to be the value of T that gives the best fit. In the second, we assume that $h(\vec{v},T)$ is a truncated Gaussian function described by

$$h(v_x,v_y,T) = \begin{cases} h_0 \exp(-v_\perp^2/2\sigma_v^2); & 0 \le v_\perp \le v_m, \\ \\ 0; & v_\perp > v_m, \end{cases} \tag{4.20}$$

where in this case $\sigma_v = (k_{\rm B}T_{\rm MOT}/m)^{1/2}$, $v_m = (2k_{\rm B}T/m)^{1/2}$ and $v_\perp^2 = v_x^2 + v_y^2$. We adjust v_m until $g_c(r,t,T)$ matches the measured (or simulated) TOF profiles. We let $T_{\perp,1}$ be given by $\langle v^2\rangle$-temperature, calculated with the truncated distribution, i.e.,

$$\left\langle v^2 \right\rangle_{2D} = \int_{-\infty}^{\infty}\int_{-\infty}^{\infty} (v_x^2+v_y^2)\, h(v_x,v_y,T)\, dv_x\, dv_y = 2\pi \int_0^{\infty} v_\perp^2 h(v_\perp)\, v_\perp\, dv_\perp, \tag{4.21}$$

where $T_{\perp,1} = m\left\langle v^2\right\rangle_{2D}/2k_{\rm B}$ and in the last expression on the right we assume that $h(v_\perp)$ is a cylindrically symmetric function of $v_\perp$. For the numerical implementation of Eq. 4.21, the upper limit of the integration is not infinity but rather a finite value v_m, large enough to cover the whole ensemble. This will be described explicitly in Sec. 4.2.2.3 below. We point out that an alternative fitting approach based on the diffusion equation is described in Ref. [122].

The values of $T_{\perp,1}$ from both the Gaussian and truncated Gaussian $h(v_\perp)$ for the measured and simulated TOF profiles are reported in Table 4.1. We note that an effective $T_{\perp,1}$ depends on $h(v_\perp)$, the transverse velocity distribution used. Three forms of $h(v_\perp)$ that were tried: (1) Maxwellians, (2) super Gaussians with functional dependence of v^4 and (3) Maxwellians truncated near $v_{\rm e}$ (the tunnel escape velocity). Each produced convolution profiles (Eq. 4.17) that nearly matched the measured expansion, but with a different effective $T_{\perp,1}$. The uncertainties in $T_{\perp,1}$ reported in the fourth to the ninth rows of Table 4.1 are equal to $\Delta T_{\perp,1}$ and are meant to indicate

its sensitivity to changes in the squared residuals $S = \sum_i [g(r_i) - g_c(r_i)]^2$. In all three cases, the values in parenthesis for $T_{\perp,1}$ caused a 10% change in S. For the calculations of S and the reduced χ^2, r_i starts from 0.4 mm to avoid the anomaly in the atomic distribution profile near the center of the beam (see Fig. 4.6). We note that the values for $T_\perp$ obtained via TOF measurements were less sensitive to the magnitude of the background than the profile fit of Sec. 4.2.2.1. However, removing the background helps to find where to truncate v "correctly". The background in this case, was removed by fitting the hot atoms, which could easily be identified as a wide pedestal in the atomic distribution, to a Gaussian function (representing one component of the Maxwellian velocity distribution for these atoms). This distribution was then subtracted from the total distribution leaving a distribution representing the colder atoms primarily.

4.2.2.3 Phase-Space Calculation: $T_{\perp,2}$

The evolution of $\zeta(\vec{r}, \vec{v})$ in phase space can be followed with either LE (Sec. 4.2.1.2) or MC (Sec. 4.2.1.3) numerical simulations. We obtained the velocity distribution from the integration as shown in Eq. 4.8, over the spatial coordinate $\vec{r}$ that is terminated at $|\vec{r}| = r_\mathrm{p}$. The temperature, $T_{\perp,2}$, is proportionial to the second moment of v in this velocity distribution,

$$\left\langle v^2 \right\rangle_{2D} = 2\pi \int_0^{v_\mathrm{m}} v^2 h(v)\, v\, dv, \tag{4.22}$$

where $v_\mathrm{m} = 3v_\mathrm{e}$ and $v_\mathrm{e} = (2k_\mathrm{B}T_\mathrm{tun}/m)^{1/2}$ is the tunnel escape velocity, which includes $> 99\%$ of the atoms. That is, $T_{\perp,2} \equiv \langle v^2 \rangle$-temperature $= m \langle v^2 \rangle / 2k_\mathrm{B}$.

The velocity distribution of the two phase-space calculations produced values for $T_{\perp,2}$ for a series of t_H values from 0 to 20 ms. These values, which nearly coincide, are plotted as solid (dashed) curves in Fig. 4.11 for the LE (MC) simulation.

4.2.3 Discussions

We will begin our discussion by noting that the total number of atoms in the tunnel was observed to drop sharply initially and then was relatively stable as the

Table 4.1: Summary of the transverse temperature estimates ($T_{\perp,0,1,2}$) made at $t_H = 10$, 15 and 20 ms. See text for description of the various approaches.

Label	Temperature (μK) @ t_H			Approach	
	10 ms	15 ms	20 ms		
$T_{\perp,0}^{(\mathrm{exp})}$	59 ± 3	51 ± 3	50 ± 4	PF[a]	$T_\perp = 6.262 T_{\mathrm{tun}}/\alpha$
$T_{\perp,0}^{(\mathrm{LE})}$	44 ± 6	31 ± 9	35 ± 2	PF[a]	$T_\perp = 6.262 T_{\mathrm{tun}}/\alpha$
$T_{\perp,0}^{(\mathrm{MC})}$	28 ± 14	13 ± 15	20 ± 5	PF[a]	$T_\perp = 6.262 T_{\mathrm{tun}}/\alpha$
$T_{\perp,1}^{(\mathrm{exp})}$	30 (3)	25 (6)	18 (2)	TOF:TM[b]	$T_\perp = m\langle v^2\rangle/2k_{\mathrm{B}}$
$T_{\perp,1}^{(\mathrm{LE})}$	21 (5)	13 (2)	17 (2)	TOF:TM[b]	$T_\perp = m\langle v^2\rangle/2k_{\mathrm{B}}$
$T_{\perp,1}^{(\mathrm{MC})}$	40	27	27	TOF:TM[b]	$T_\perp = m\langle v^2\rangle/2k_{\mathrm{B}}$
$T_{\perp,1}^{(\mathrm{exp})}$	33 (3)	22 (3)	17 (5)	TOF:G[c]	$T_\perp$ from fit
$T_{\perp,1}^{(\mathrm{LE})}$	25 (5)	15 (2)	20 (2)	TOF:G[c]	$T_\perp$ from fit
$T_{\perp,1}^{(\mathrm{MC})}$	60	35	35	TOF:G[c]	$T_\perp$ from fit
$T_{\perp,2}^{(\mathrm{LE})}$	51 (1)	30 (1)	26 (2)	NVD[d]	$T_\perp = m\langle v^2\rangle/2k_{\mathrm{B}}$
$T_{\perp,2}^{(\mathrm{MC})}$	51 (1)	32 (2)	27 (2)	NVD[d]	$T_\perp = m\langle v^2\rangle/2k_{\mathrm{B}}$

(a) PF: Profile fit using Eq. 4.15. The uncertainties correspond to the 95% fit-confidence interval. *(b)* TM: Truncated Maxwellian fit using $T = T_{\mathrm{MOT}}$ and $v_{\mathrm{m}} = 1.06v_{\mathrm{e}}, 0.85v_{\mathrm{e}}$ and $0.83v_{\mathrm{e}}$ in Eq. 4.17 respectively for $t_{\mathrm{H}} = 10$, 15 and 20 ms; $\langle v^2\rangle$ calculated with Eq. 4.22. The values inside the parentheses are meant to indicate the sensitivity of the $\langle v^2\rangle$ temperature to changes in the squared residuals $S = \sum_i [g(r_i) - g_c(r_i)]^2$. In all cases, S changed by 10% when $T_{\perp,1}$ was changed by the amount indicated in parenthesis. The reduced χ^2 ranges from 0.3 to 0.8. *(c)* G: Full Maxwellian fit using $T = T_\perp$ and $v_{\mathrm{m}} = 3v_{\mathrm{e}}$ in Eq. 4.17. The values inside the parentheses have the same meaning as in (b). The values of reduced χ^2 for all cases range from 0.3 to 1. *(d)* NVD: Numerical velocity distribution determined by integrating ζ; $\langle v^2\rangle$ calculated with the 2D Cartesian equivalent to Eq. 4.22. The values inside the parentheses are meant to indicate the sensitivity of the $\langle v^2\rangle$ temperature to 10% changes in the tunnel temperature. *(b-c)* For the calculations of S and the reduced χ^2 in all cases, r_i starts from 0.4 mm to avoid the anomaly in the atomic distribution profile near the center of the beam (see Fig. 4.6).

hold time t_H increased as shown in Fig. 4.9. Clearly when the population is declining, the assumption of steady state is questionable at best because of the appreciable number of atoms leaving the tunnel. This is exacerbated by the fact that the profile

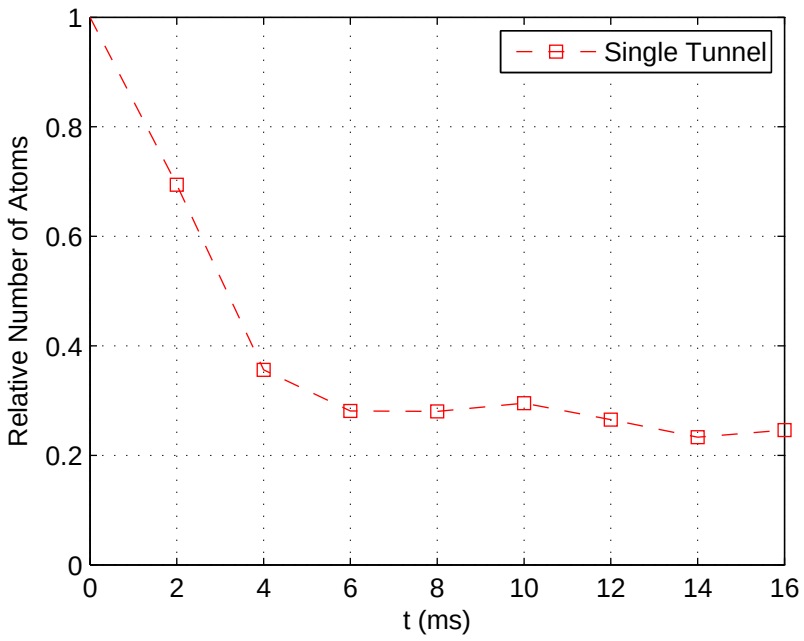

Figure 4.9: Number of atoms in a tunnel vs. time. The number drops sharply within the first 5 ms and maintains a relatively stable value for the next 10 ms.

of the spatial distribution changes with time as atoms leaves the tunnel. This is clear from Fig. 4.5 where we show $g(r)/g_0$ for the ensemble after being held in the tunnel for different lengths of time t_H at 2, 6 and 10 ms. We also observed that as t_H increases $g(r_{\rm p})$ (the magnitude of the distribution at the wall) decreases, indicating less leakage and colder temperatures. We assume that during the time when the population is relatively stable, the ensemble reaches steady state from which we use to extract the $T_{\perp,0}$. The values of $T_{\perp,0}$ as shown in the first row of Table 4.1 indicate that the mean energy is stable after 15 ms for both the experimental and simulated ensemble, hinting that the steady state is reached. However, at the same t_H, the values of $T_{\perp,0}$ from the experiment, LE and MC simulation are not the same. This may be due in part to $T_{\perp,0}$ being sensitive to the background of hot atoms as discussed at the end of Sec. 4.2.2.1. Note that the background seen in the LE simulation is not the same as that in the MC simulation because the former relies upon a numerical solution to Eq. 4.9, which only included radial motion, while the latter is based on integrating the equations of motion and includes radial and

non-radial trajectories.

The trend of the rapid drop followed by stabilization in temperature can be seen in all the rows in the table albeit with small differences compared with the initial temperature of the ensemble, ~ 150 μK. We note that for the LE simulation the temperature at $t = 20$ ms is higher than it is at $t = 15$ ms. While this is not observed experimentally, such a behavior might be caused by atoms flowing in and out of the tunnel wall. Specifically, the initial spatial and velocity distributions are Gaussian. It can be shown that the maximum number of atoms in a ring roughly the thickness of the tunnel wall occurs at a radius $\sim r_p/2$. The atoms with kinetic energy less that ~ 60 μK that are moving outward, have a speed of ~ 0.1 mm/ms. These atoms reach the wall and come to rest before being reflected back into the low potential region of the tunnel, at a time that corresponds to the minimum in the LE temperature. Being in the wall, these atoms are not counted by the LE simulation at this time. Consequently, the LE behavior is probably an artifact of the simulation and the way atoms were counted. The TOF measurements from the experiments (rows four and seven) are shown to be in good agreement with the LE simulation (rows five and eight) but differ significantly from the MC one (rows six and nine). This is true regardless of which velocity distribution considered. We believe the agreement with the LE simulation suggests that the initial MOT ensemble contains a large fraction of atoms traversing radially because this is also the the case considered in the LE calculations and the only difference from the MC calculations. Despite these agreements, we notice that the values of $T_{\perp,1}$ obtained from the experiment and the LE simulation (row four and five) are lower than the values of $T_{\perp,2}$ calculated directly from the simulated phase-space distribution (row ten). One reason the values of $T_{\perp,1}$ maybe suppressed is that the background of the hot atoms is removed from the free expansion profiles. The magnitude of the suppression, in the case of the MC simulation, depends on the velocity distribution considered (compare row six, nine and eleven).

To investigate other possible sources that cause the suppression, we look at two ways we can force the simulation to approach the TOF results. First, we lower

the effective height of the tunnel and calculate $T_{\perp,2}$ from the LE simulation as a function of t_H. In Fig. 4.10, the comparison of $T_{\perp,1}^{(\mathrm{exp})}$ (dot) with $T_{\perp,2}^{\mathrm{LE}}$ (lines) for three different values of U_{max} is shown. We found that the suppression cannot be lifted at $t_H = 10$ ms even for the case of the free expansion where $U_{max} = 0$. Clearly, the imperfections in the tunnel potential is unlikely to be the primary reason for the suppression. Moreover, because the tunnel with $U_{max} = 0$ gives the limiting value of $T_{\perp,2}$, we can argue that the suppression of $T_{\perp,1}^{(\mathrm{exp})}$ is likely unrealistic. The reduction of the effective hight is based on the fact that there are dips in the first ring of the Bessel tunnel. We observed that, for the real tunnel used in the experiment, the lowest observable dip corresponds to $\sim$ 35 μK, which is $\sim$ 50% lower than the averaged value, allowing atoms with lower energies to escape at some points around the tunnel. Note that the values of $T_{\perp,1}^{(\mathrm{exp})}$ at larger hold times approach the limiting value of $T_{\perp,2}$, indicating that the suppression is less as the ensemble approaches steady state where the background of hot atoms is negligible. Second, we include in the simulation the spatially dependent loss of atoms in the ensemble due to atoms scattering into a wrong hyperfine state. The temperature can be forced to match the TOF ones (see the dotted-dash curved in Fig. 4.11). However, the probability of scattering into the wrong hyperfine state would have to be 1 in 20 for every time the atom absorbs a photon. The true probability is $\sim$ 1 in 1000 and the re-simulated temperature based on this probability varies negligibly from that without including the loss. The calculation of the photon scattering did not take into account the obliqueness of the tunnel with respect to the direction of gravity. To the extent any of the tunnel's orbital angular momentum gets transferred to the atoms, the trajectories of the atoms would become more non-radial, giving warmer atoms a little extra boost sufficient to escape. In this case, the MC simulation may have done a better job of estimating $T_\perp$ (visa vis the TOF $T_\perp$) because it included non-radial trajectories.

At the first glance, it is reasonable that the initial Maxwellian velocity distribution is truncated at a velocity commensurate with the effective tunnel potential because the hot atoms leaves the tunnel as mentioned previously. In more detial, we

first observe that the paucity of collisions inhibits re-thermalization on the timescale of our experiments leading to a velocity distribution that is spatially nonuniform (see Fig. 4.7). All entries of Table 4.1 show that the ensemble is clearly out of equilibrium at early times. A consequence of the system not being in equilibrium is an inability to define an actual ensemble temperature. The $\langle v^2 \rangle$ temperature calculated with the truncated Maxwellian (fourth entries) is very compelling as it is an estimate of the energy contained in the transverse velocity components. The temperature used in the truncated Maxwellian was taken to be that of the MOT, which was measured (150 μK). After 10 ms the best fit (Fig. 4.6) corresponded to $v_{\rm m} = 1.05\, v_{\rm e}$, which is associated with truncating at $T_{\rm tun} \sim 64$ μK, close to a measured quantity that depends on the intensity, size and order of the Bessel mode. The ensemble loses additional energy as it stays in the tunnel longer, due to the defect in the tunnel as pointed out above, so the integral had to be cut off at lower and lower velocities. After 20 ms the truncation corresponded to an effective $T_{\rm tun} \sim 40$ μK that was ~ 0.7 times as large. From Fig. 4.6, we note that the non-equilibrium population distribution most likely contributes to the measured and simulated TOF profiles not fitting well near the axis of the tunnel. Another contribution to the suppression of atoms on the axis comes from imperfections in the tunnel; specifically, the axis was not completely dark. We estimate the power of the light distributed evenly around the axis was $\sim 1\%$ of the power in the ring.

Matching the series of profiles generated with Eq. 4.17 to the experimental series was not very sensitive to the precise functional form of the velocity distribution. Except for the portion of the profile near the axis, the truncated Maxwellian, full Maxwellian and even a functional form based on a super Gaussian all gave reasonable matches, albeit with significantly different values for $T_\perp$. At the same time, additional energy loss and an apparent re-thermalization of the ensemble evidently occurs when the cloud remains in the tunnel longer. In the LE simulation, it is observed that the longer the ensemble stays inside the tunnel, the more the velocity becomes spatially uniform. This comes from the fact that the tunnel mixes and glazes the phase-space of the ensemble inside the tunnel. For spatially uniform veloc-

ity distributions with the same amount of total energy, the $T_\perp$ from the truncated velocity distribution serves as a lower bound compare to that from the Gaussian and super Gaussian distribution because, in the last two, they include a contribution from the high velocity component in their tails. As a side note, the apparent re-thermalization might be aided by light scattering with tunnel photons. Although, at our detuning, light intensity and tunnel geometry the photon-scattering rate is $\sim 1\ \mathrm{ms}^{-1}$, which would lead to a very slow redistribution of the velocity components and a longitudinal heating of $< 0.2\ \mu$K/ms.

For our next remark, we first observed that the removal of atoms with transverse velocity components sufficient to make it over the tunnel barrier is very efficient at reducing the effective transverse temperature of the confined ensemble. It is important to note that while $T_{\perp,1}$ does not represent the measured ensemble temperature, it does correspond to the equilibrium temperature the ensemble would reach if it were purely 2D. Clearly the temperature of the full 3D ensemble, if brought into equilibrium, would be higher because the longitudinal velocity components would still have an appreciable amount of their initial energy gained from the MOT. Nevertheless, if we were able to induce equilibrium the ensemble would be colder than the original MOT and we would have a means of cooling the atoms. The tunnel, only offering 2D confinement, would required end caps and perhaps some reduction in its radius to induce equilibrium. As hot atoms leave, the intensity and/or frequency of the tunnel and end caps, along with the tunnel radius, could be changed in real time to reach lower and lower temperatures. This might be an alternative evaporative cooling approach. It might also be possible to carry out the cooling while the atoms are in transit by moving the end caps at the same time. If the tunnel were vertical, it might even be possible to use a single end cap, a modification of the Gravito-optical atom trap [123], to move atoms from the collection point (the MOT) to the experimentation point consistent with maintaining an ensemble in a degenerate phase, such as a Bose Einstein condensate.

Finally, we note that an apparent disadvantage of blue detuning is that atoms are not confined absolutely to the axial core; quantum mechanically there are no

bound states. For red detuning, bound states exist for axially confined atoms for the lowest-order mode as well as annular confining for high-order modes. However, the leak for axial confinement in the blue-detuned case can be controlled[118]. The leak can be made arbitrarily small by setting the ratio between the potential barrier of the tunnel, $k_{\mathrm{B}}T_{\mathrm{tun}}$, and the kinetic energy of the atoms in the transverse plane, $k_{\mathrm{B}}T_a$ sufficiently high, where T_a the temperature of the atoms. The tunneling rate in the quantum case is also reduced when $T_{\mathrm{tun}} \gg T_a$.

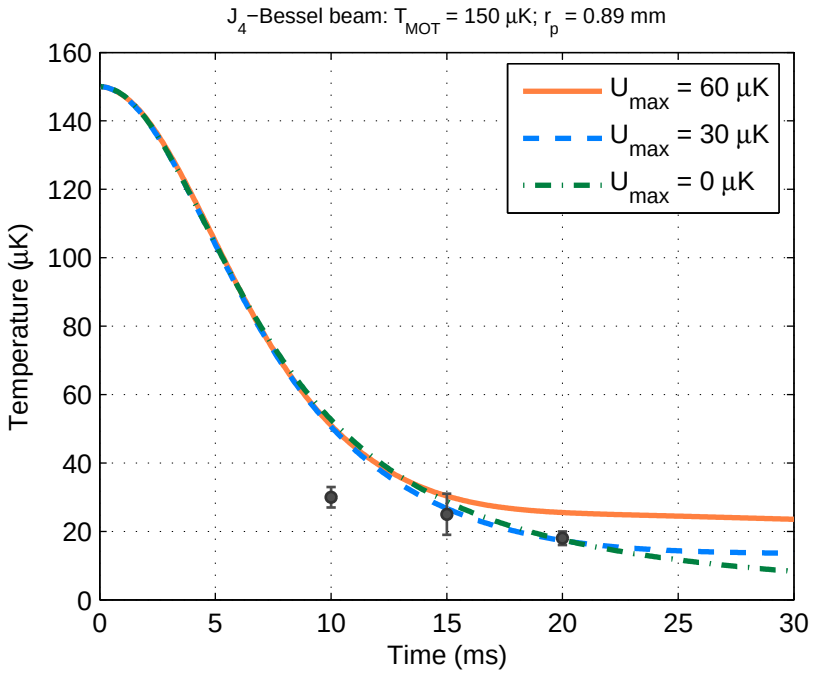

Figure 4.10: Effective transverse temperature vs hold time for different U_{max} values. The line $U_{max} = 0$ serves roughly as a lower bound for the $\langle v^2 \rangle$ temperature of ensemble inside the tunnel.

4.3 Conclusions

In conclusion, we have shown that (1) acceleration along the Bessel tunnels (or the likes) can be conveniently estimated from a geometrical potential, (2) the rapid transverse cooling followed by a stabilization in transverse temperature is verified theoretically, (3) the effective transverse TOF profile can be estimated from an

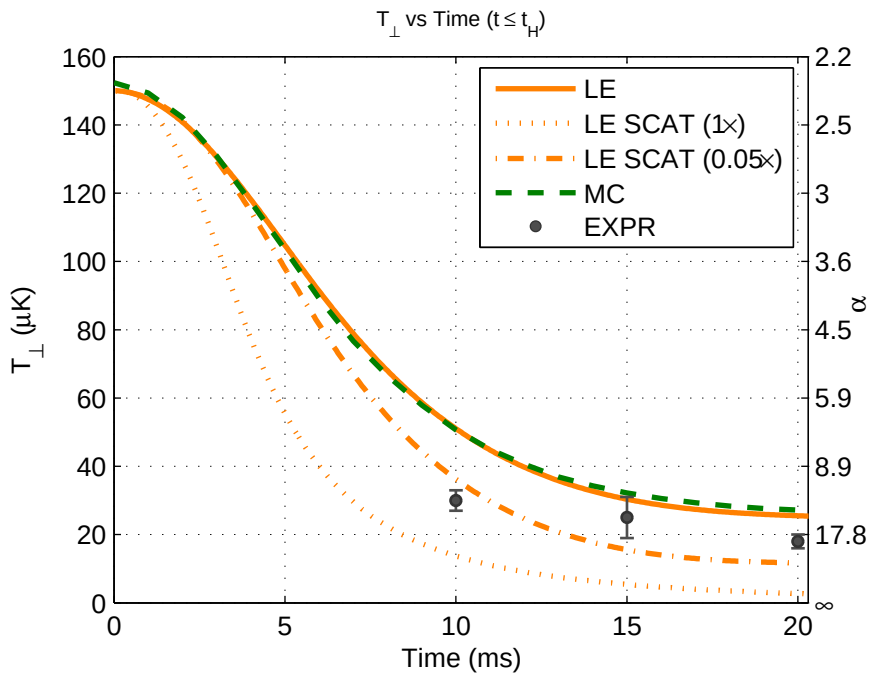

Figure 4.11: Effective transverse temperature vs hold time. The symbols represent $T_{\perp,1}^{\mathrm{exp}}$ at $t_H = 10$, 15 and 20 ms obtained from the truncated Maxwellian as described in the text. The solid (dashed) curve represents $T_{\perp,2}^{(\mathrm{LE})}$ ($T_{\perp,2}^{(\mathrm{MC})}$) for t_H between 0 and 20 ms. The dotted-dash (dotted) curve represents $T_{\perp,2}^{(\mathrm{LE})}$ of the LE simulation with $1\times(0.05\times)$ chance of loss into a wrong hyperfine state for every photon scattering event.

ensemble truncated at a velocity commensurate with the effective tunnel potential, (4) the TOF method can be used to point to a more reliable temperature calculated from the simulated phase-space distribution, and (5) the tunnels can be exploited as a tool not only to confine atoms as has already been shown, but to enhance pre-cooling thermal clouds at arbitrary low temperatures (i.e. a 2D atom gate).

Specifically, the hollow light tunnels are very efficient at removing atoms with transverse velocity components that exceed a well-defined potential barrier of the tunnel; the effective transverse temperature (considering $T_{\perp,2}$) is approximately 50% of the effective tunnel temperature providing a scalpel to remove hot atoms. We observed this truncation to saturate within 20 ms, however, this timescale is temperature and geometry dependent. For the open tunnel, the resulting ensemble is

out of equilibrium with effective temperatures in the longitudinal and transverse directions being nearly decoupled and potentially very different. Our LE model, which included only radial trajectories and ignore any angular moment transferred to the atoms by the tunnel, seem to capture most of the dynamics which reflect in the trend of $T_{\perp}(t)$. Evidently, orbital angular momentum exchange between the atoms and the tunnel is small under our conditions. Finally we discussed how a combination of restricting the ensemble flow, modifying the tunnel geometry and size and changing the potential height of the tunnel could allow the tunnel to be used for evaporative cooling of the ensemble while in transit.

Chapter 5

Preliminary Test of Bessel Tunnels

One of the building blocks for an atom network, as we have mentioned in the introduction, is a single tunnel, which can be used to move atoms. A combination of several single tunnels creates a structure that can be used to realize the network. Examples for these structures have been reported with Gaussian modes [124, 34] as have more sophisticated interferometer structures [23, 125, 126]. These structures rely on the dipole force, a result of interaction between an external electric field of the laser light and the induced dipole moment of an atom.[1] The sign of the interaction depends on the wavelength of light, which can be either red or blue detuned from the atomic resonance. While a red detuned tunnel draws atoms into the brightest part of the beam, a blue detuned tunnel pushes atoms into the region where the intensity is lowest.

As discussed in the introduction, we intend to use light patterns generated from a SLM to manipulate the spatial distribution of an atomic ensemble. We have shown in Chapter 2 that by changing locations of vortices embedded in a laser beam, we can create various patterns, e.g., connected or disconnected channels between vortices, which can be useful for an atom network. We can change intensity patterns in real time by controlling the phase mask of the SLM. At the end of Chapter 2, we used tunnels with some of these patterns to guide atoms.

In this chapter, however, we employ a single-vortex Bessel tunnel as a building block to make a "tunnel lock", a device used to divide and delay an atomic ensemble, or to switch the ensemble's propagation direction, which can be useful in an atom network.

[1] see Appendix A for a detailed discussion of the dipole force.

5.1 Tunnel lock

In general, the development of elements built upon hollow (donut-type) laser modes [127, 128, 56, 36, 129, 130, 40] detuned blue of resonance would be particularly useful for a variety of reasons. Specifically, they can be produced with relatively low intensity (< 1 W) cw laser beams tuned only a few gigahertz to the blue of an atomic resonance. A reasonable scattering rate is maintained because the atoms spend most of their time in the dark [36]. As an example, for a J_4-Bessel tunnel tuned 4 GHz blue of resonance, with the first peak radius of 0.5 mm and 100 mW of power in the first ring, an atom with half the energy of the peak potential scatters ~ 8 photons per millisecond. For a Gaussian tunnel tuned red by the same amount, with the spot size of 0.5 mm and with the same power of 100 mW, an atom with half the energy of the peak potential scatters ~ 45 photons per millisecond. Far-blue detuned operation would essentially eliminate absorption and would be possible at condensate temperatures with a frequency-doubled Nd:YVO_4 laser. At high intensities, hollow beams can be generated with axicons [36] or fabricated optical elements embedded with appropriate phase masks. For near-resonance operation, detuning can be used as a knob to accelerate or slow the ensemble [36].

While free-space splitters and dividers based on crossing two red-detuned Gaussian (filled) tunnels have been demonstrated in the past decade [124, 34], we have reported recently that similar elements based on crossing blue-detuned hollow tunnels [35, 117] can be achieved. This is due in part to the fact that transferring atoms between two crossed blue-detuned hollow tunnels cannot be done passively; a modulation of both tunnel intensities is required. The modulation – gating the intensities on and off – produces the tunnel lock, where the barrier caused by the intensity of the second or crossed tunnel is momentarily lowered (entrance gate opened) to allow the cloud to be positioned in both tunnels simultaneously. When the intensity of the second tunnel is raised (entrance gate closed), a portion of the cloud will be trapped in three dimensions. When the intensity of the first tunnel is reduced (exit gate opened), the confined portion of the cloud will be free to travel

within the second tunnel with a different momentum (i.e., with a different direction and perhaps speed). The schematic of our tunnel lock is demonstrated in Fig. 5.1. Intensity gating of both tunnels in the figure can be made on or off by using two independent mechanical shutters placing on the path of the tunnels before they cross.

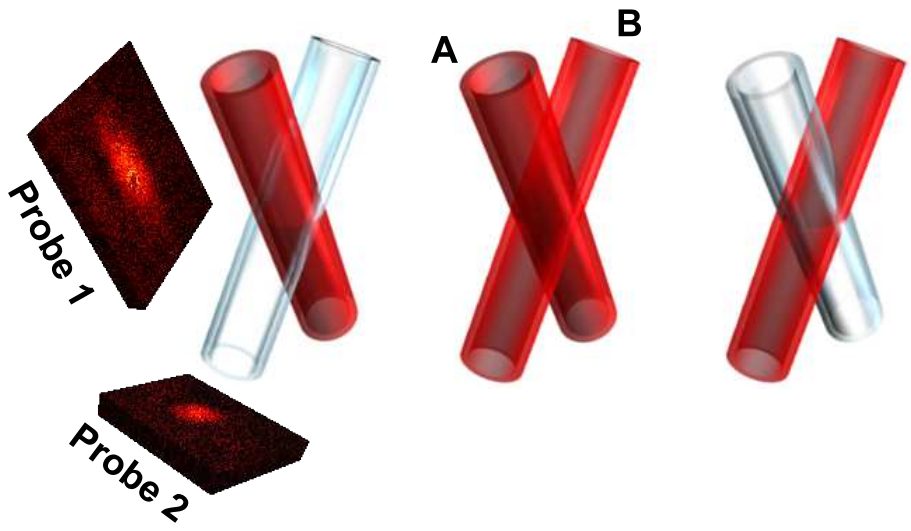

Figure 5.1: Schematic of the tunnel lock formed by crossing two tunnels, labeled as A and B, and the planes of observation, probe 1 and 2. Red (clear) cylinders indicate tunnels being on (off). From left to right: entrance gate open (atoms enter overlap volume), both gates closed (atoms trapped), exit gate open (atoms leave overlap volume). Appropriate timing of the gates generates a beam splitter, delay line or beam switch. Reproduced from Ref. [35].

To demonstrate a prototype version of the tunnel lock, we created a J_4-Bessel tunnel using the SLM, as described in Chapter 2. The tunnel was blue-detuned with respect to the trapping transition of both rubidium isotopes. We trapped both ^{85}Rb and ^{87}Rb atoms. However, ^{85}Rb atoms were contained in the tunnel better, providing shadow images with more contrast. This was becuase the frequency separation between the trapping and repumping transitions was ~ 3 GHz for ^{85}Rb but ~ 7 GHz for ^{87}Rb. Therefore, the tunnel was tuned to the repumping frequency for ^{85}Rb atoms [117]. The tunnel was split equally into two beams with a polarizing

beam splitter cube. Each tunnel has a diameter of $\sim$ 1 mm with a power of 80 mW in the first ring. In Fig. 5.2, we can see the experimental result of one basic operation of the tunnel lock when both tunnels are on at the same time, creating an enclosed volume that can trap atoms. The operation causes the ensemble to be

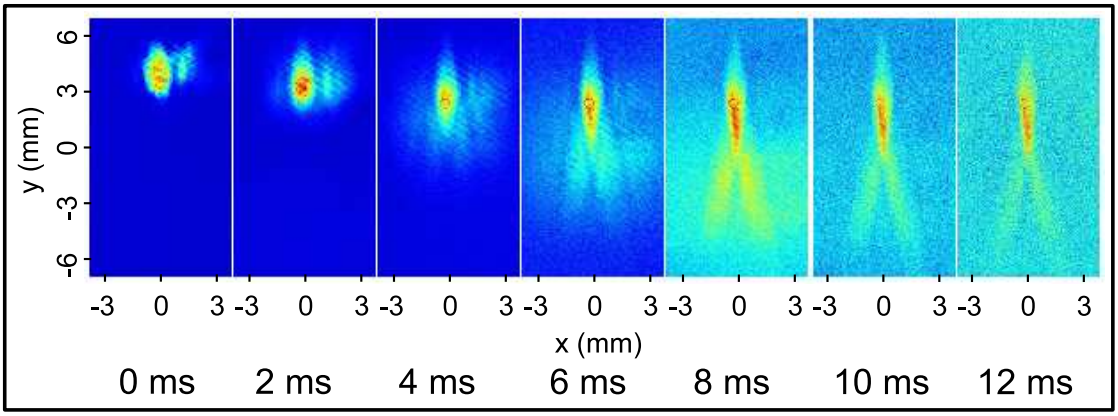

Figure 5.2: Beam splitter and delay line created with two crossed tunnels. Both tunnels were on when loaded with the ^{85}Rb ensemble. Three different momentum groups were generated corresponding to ensemble moving downward to the left, to the right, or trapped in the overlap volume. Adapted from Ref. [35].

separated into three distinct groups each with different velocity distribution. From the figure, the group that are enclosed and trapped in the crossed volume contains the majority of the atoms while the other two groups contain atoms that travel along, in the same direction as, the tunnels. This tunnel lock operation can be used as (1) a delayed line for the atom that is trapped and becomes delayed with respect to the other two groups, and (2) a beam splitter for the atoms that travels along the tunnels. With a proper alignment, the crossed volume can be adjusted, allowing more atoms to be split and fewer atoms to be delayed. Before finishing of the tunnel lock, we note that one concerns was there can be leaks of atoms from the lock caused by the interference fringes from the intersecting tunnels. However, we observed that the density of the background atoms around the intersection and those away from the intersection (i.e. around each tunnel), as can be seen from Fig. 5.2, are comparable. It is not obvious that the interference fringes contributes

to the leaks.

Another basic operation of the tunnel lock is to switch an atomic beam by turning on and off gates as described earlier. Recall from Fig. 5.1 that when tunnel A is on and tunnel B is off, the ensemble will propagate and freely expand along A.[2] The observation of the atomic density distribution, projected on the plane of both tunnels, reflects the elongated distribution as seen on a plane labeled as probe 1 in the figure. The projection of the distribution on a plane transverse to tunnel B, on the other hand, is labeled as probe 2 in the figure. A series of pictures capturing

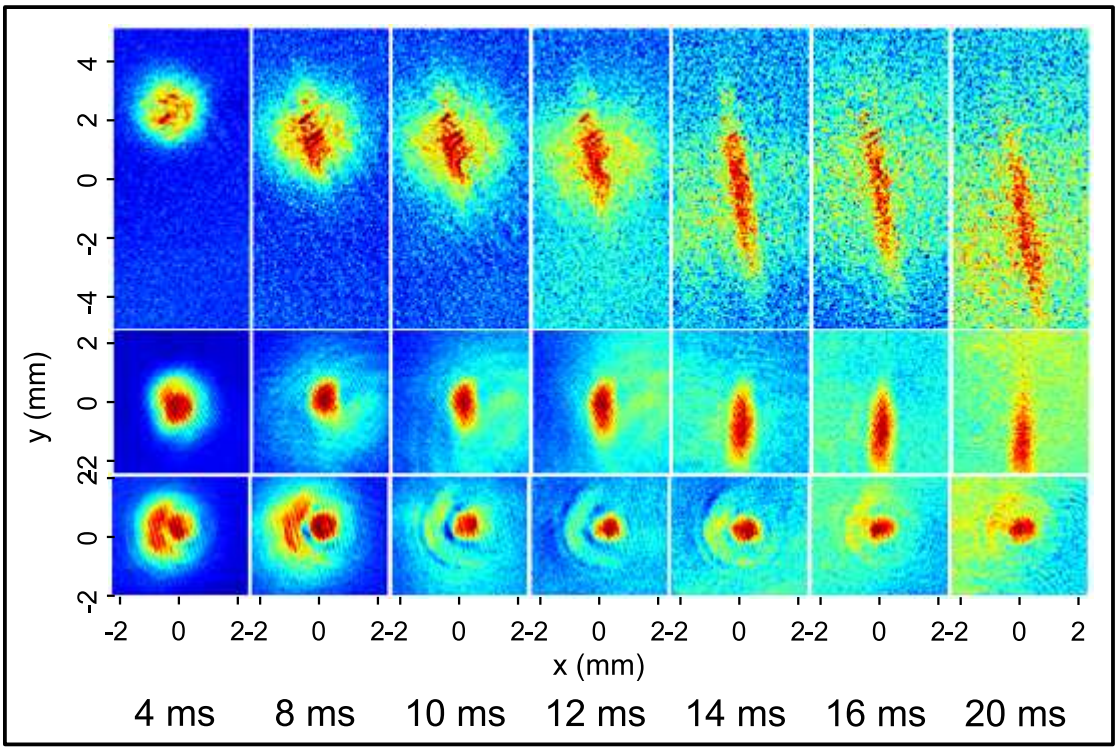

Figure 5.3: Shadow images of ^{87}Rb ensemble at selected times falling under gravity in a single 1-mm-diameter tunnel (tunnels A), starting at 4 ms after the tunnel was loaded. The top row represents the ensemble evolution as seen by probe 1. The middle (bottom) rows correspond to the evolution of the ensemble projected on a plane transverse to tunnel B (tunnel A). See Fig. 5.1 for the label of the tunnels and the probes. Reproduced from Ref. [35].

[2]There is no obstacle to restrict the propagation of the atoms along the tunnel axis. Therefore the atoms expand freely based on their velocities along the direction of the tunnel alone.

the evolution of the ensemble in the top row of Fig. 5.3 shows an experimental observation of an ensemble propagating in tunnel A, taken at 4 ms to 20 ms after the magnetic field is turned off, with probe 1. In the middle row of the same figure, the observation with probe 2 along tunnel B gives slightly elongated distribution because the ensemble expands along tunnel A. In the bottom row, the probe is coaxial with tunnel A, therefore, the distribution is not elongated as time evolves but rather takes a round shape resembling the transverse profile of the tunnel. To switch the ensemble from tunnel A to tunnel B, tunnel A is turned off and tunnel B is turned on at the same time. The experimental result is shown in Fig. 5.4 as a series of pictures taken at times 4 ms to 20 ms after the trap lasers are turned off. The series is interrupted at 10 ms when the switch is engaged. The projections on probe 1 (2) are seen in the top (bottom) row of the figure. The switch operation can be clearly seen when comparing the top row of Fig. 5.4 to that of Fig. 5.3. From the figures, we can see that it takes approximately 4 ms from the third to the fourth column for the ensemble to completely switch from tunnel A to tunnel B. Note that for Fig. 5.3 and Fig. 5.4, the frequency of all tunnels is tuned ~ 6 GHz to the blue of the resonance frequency of ^{87}Rb atoms, corresponding to a peak potential of ~ 150 μK.

5.2 Atom Switch Properties

Propagation from one tunnel to the other in the atom switch causes some of the atoms that are not in the crossed volume to be lost. The efficiency of the switch can be characterized by the ratio of the number of atoms remaining in the tunnel after the switch to the number in the tunnel without the switch. The efficiency of our switch is shown in Fig. 5.5. From the figure, we see that the efficiency has a tendency to stabilize; with the value of the averaged efficiency, after $t \geq 12$, to be 42%. Besides the switching efficiency that characterizes the atom switch, we point out that the operations of the switch changes the spatial distribution of the ensemble greatly. Apart from the change in the spatial distribution, the velocity

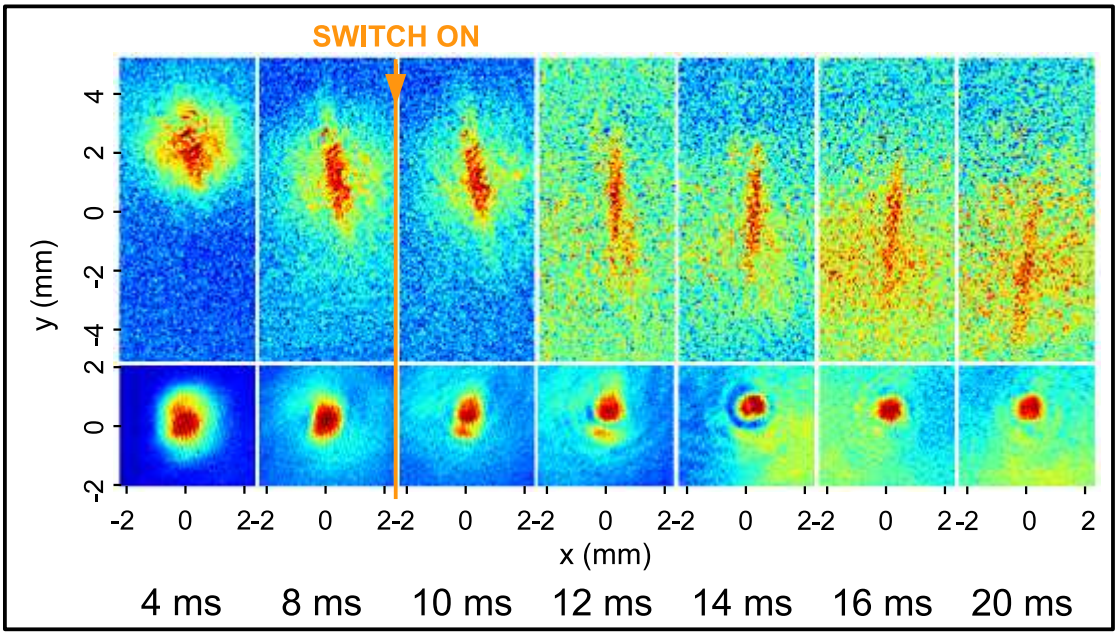

Figure 5.4: Shadow images of ^{87}Rb atoms at selected times passing through the tunnel lock and being switched between tunnels. The upper (lower) series is the evolution of the cloud for 20 ms after it was launched as seen by probe 1 (2). The upper row shows the cloud redirection upon switching from the first tunnel, in which the cloud moves downward and to the right, to the second tunnel, in which the cloud moves downward and to the left. The lower row shows the same transition in terms of the cloud shape change. Reproduced from Ref. [35].

distribution also changes because the ensemble evolves in time. This can be seen in the graph in Fig. 5.6 where we investigated the temperature along the tunnel before and after the switch operation. Along the tunnel, the ensemble expands freely without any constraint from the tunnel. The evolution of the ensemble, can be obtained by convolving[3] the initial spatial distribution, which is a Gaussian, with the velocity distribution, a Maxwellian in our case. The convolution among Gaussian functions also results in another Gaussian function[4] that has a time dependent width described by $\sigma^2(t) = \sigma_0^2 + \sigma_v^2 t^2$, where σ_0 is the initial width of the distribution, and σ_v the average speed of the atoms along the tunnel. The temperature can

[3]As described briefly in Chapter 4 or in detail in Appendix E.4

[4]see Appendix E.4.2 for the derivation of a Gaussian expansion from the convolution.

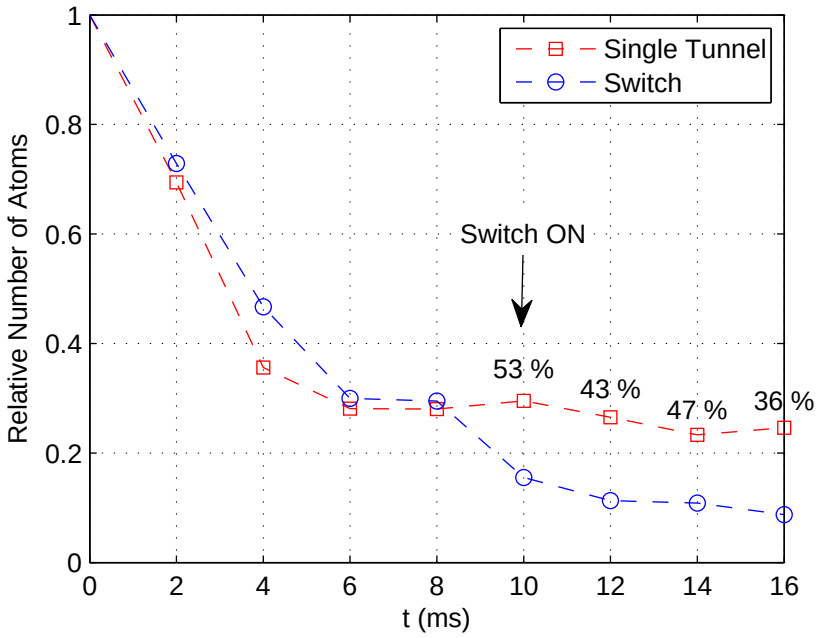

Figure 5.5: Efficiency of atom switch. The graphs show relative number of Rb atoms guided in a single tunnel (square) and an atom switch (circle).

be related through σ_v by $T = m\sigma_v^2/k_B$. In Fig. 5.6, $\sigma^2(t)$ of the ensemble in the tunnel without any switch operation (blue triangle) is plotted against that with the switch operation (red circle). The temperature of the ensemble before the switch is activated at $t = 8$ ms is 150 ± 7 μK identical to that of the single tunnel. After the switch is activated, the width of the cloud drops by $\sim 25\%$ because the size of the tunnel at the intersection of the switch is smaller than the size of the expanded ensemble. Hot atoms, which travel faster than the cold ones, move further outside the intersection. Thus only a cold portion of the ensemble is recaptured by the second tunnel. During 8 and 10 ms, the width of the cloud does not change much unlike that from the Gaussian expansion. After that period, the velocity distribution re-adjusts and the ensemble begins to expand, in a similar fashion as the Gaussian expansion, with a temperature of 118 ± 29 μK.

Guiding atoms through networks of well-defined channels is an essential requirement for realizing future applications not only in the areas of atom interferometry or atom circuit, but also in the area of atom lithography [131, 132] as well. For

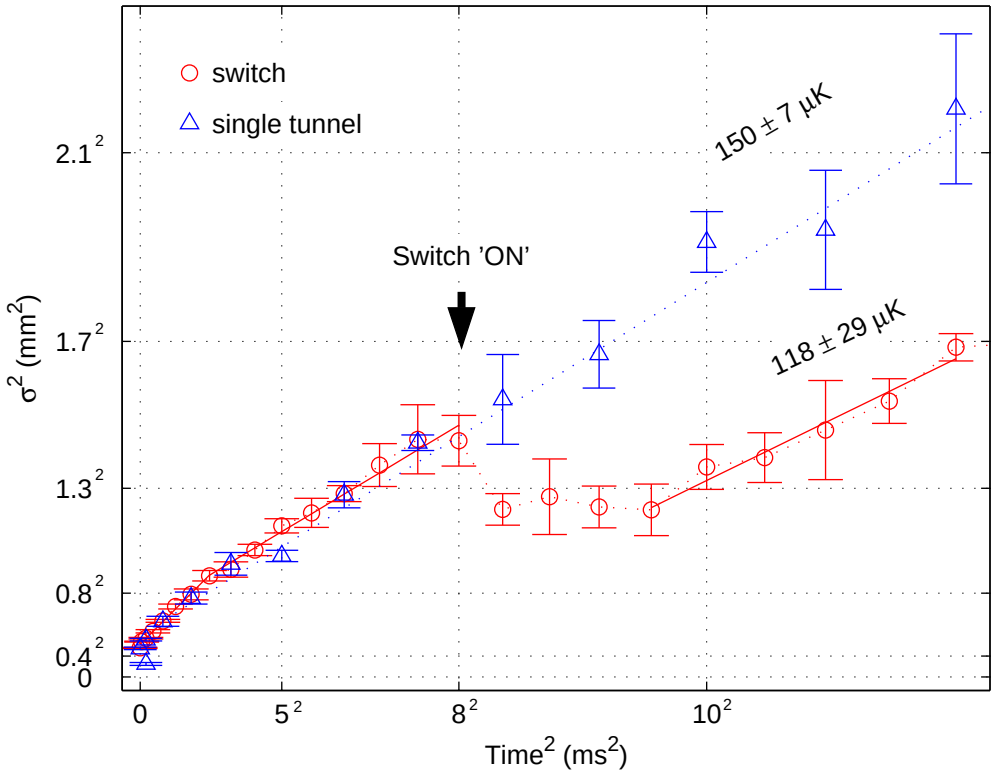

Figure 5.6: Evolution of an ensemble in a single tunnel and through the switch where the time axis denotes the time after the cloud is released from the trap and σ is the width of a Gaussian fit of the ensemble density distribution along either tunnel. The error bars represent the standard deviation in the mean of five runs. Reproduced from Ref. [35].

atom lithography, understanding dynamics of the ensemble is important to achieve precision of desired patterns.

Lastly, while an atom ensemble is contained inside the blue detuned tunnel, it is possible that we couple light orbital angular momentum (OAM) of the tunnel to the atom ensemble through photon absorption [88, 133, 89, 134, 90] when it is in contact with the wall. For a red detuned beam, the tunnel forms a ring potential where atoms reside and move around the axis. Therefore, most of the atoms inside the potential can be forced to rotate by the OAM. For a BEC, persistent flow induced by a light vortex has been demonstrated [89, 135]. Through the coupling to OAM, the atom interferometer or the atom network can be made much more complex and

can be used as a part of additional operations done on the ensemble to encode more information into the system [133, 136, 137, 138]. The work in this chapter has been reported in Ref. [35, 117].

Chapter 6

Single Mode Propagation in a Hollow Tunnel

In the previous chapter we considered a cold atom ensemble trapped in a J_4-Bessel tunnel in 2D. In the classical regime, the evolution of the cloud can be described by the Liouville equation (LE), Eq. 4.6, where the partial derivative with respect to time is zero ($\partial/\partial t = 0$) in steady state. The steady state solution gives the flat spatial atom-distribution profile at and around the center of the tunnel as confirmed by the experiments. In addition, by raising or lowering the tunnels potential barrier, the hot tail of the atom clouds velocity distribution can be removed, leaving us with a transversely colder ensemble. As a result, the tunnel acts as a low-pass velocity filter, compatible with evaporative cooling where collision exists. Moreover, when the diameter of the tunnel is comparable to the de Broglie wavelength[139] $\lambda_T = h/(2\pi m_a k_B T)^{1/2}$ of the atoms, quantum issues start to reveal themselves. For rubidium, λ_T is in the order of a micrometer when $T \sim 100$ nK. It is interesting to investigate the probability distribution of an atom in the quantum regime inside the Bessel tunnel, realizing that the Bessel tunnel provides a flat spatial distribution in the classical regime as mentioned earlier.

In particular, we would like to create single-mode channels for matter waves i.e. a matter-wave fiber. We are interested in a condition where only one eigen-mode is allowed to exist within the tunnel, analogous to a single-mode propagation of light in a single-mode optical fiber. For a single atom inside the tunnel, a single-mode state has an advantage that it is a solution of the time-independent Schrödinger equation and its structure is well localized especially for the ground state. Together with highly stable laser pointing stability, the single mode can be used for precision alignment or atom lithography [131]. Provided that (probabilistic) entangled atom

ensembles are realized [133, 137], the single mode (or a set of known multi-mode) atom distribution might also be used as a basis for quantum communication in analogous to that performed by photons [136]. Recently a quasi-monomode atom laser was demonstrated with a far red detuned bright tunnel [140, 141, 142].

Concerning the feasibility of creating a single-mode channel experimentally, by exploiting a hollow Bessel beam in particular, a few features need to be addressed:

- The energy of the state in the potential must be accessible by the experiment and the potential height and the size of the tunnel must be within values that can be realized experimentally.

- The energy gap between the ground state and the first excited state must be large enough to avoid excitations to higher energy states.

In this chapter, we will focus on eigen-functions and eigen-energies for a single atom by solving the time dependent Schrödinger equation numerically. We first look at the analytic solution of a time-dependent Schrödinger equation with a cylindrical infinite square well (i.e., impenetrable wall). Next we will calculate the eigen-energies and eigen-functions of the atoms inside the hollow blue detuned Bessel tunnel. The single-mode and multi-mode configurations will be discussed. Our results show that the single-mode guide should be possible at condensate temperatures for tunnels diameters ~ 1 μm. At the same time, the degeneracy between energy levels could provide a platform for generating interesting spatial superpositions, which can be controlled by the Bessel order, the size of the tunnel, and the potential height. Lastly, we will show a single-mode condition for a red detuned ring trap that has by default topological restriction on the wave function. Note that, for a BEC, more work would be involved in solving the Gross-Pitaevskii equation as discussed briefly at the end of the chapter.

6.1 Hard Wall Cylindrical Potentials

Time independent Schrödinger equation for a cylindrical symmetric potential $U(r)$ (ignoring gravitational potential) can be written as

$$\nabla^2\Psi + \frac{2m_a}{\hbar^2}\left[E - U(r)\right]\Psi = 0, \tag{6.1}$$

where Ψ is the wave function, E is the energy and m_a is the mass of the atom. In cylindrical coordinates, Eq. 6.1 can be written as

$$\frac{1}{r}\frac{\partial}{\partial r}r\frac{\partial}{\partial r}\Psi + \frac{1}{r^2}\frac{\partial^2}{\partial\theta^2}\Psi + k^2\Psi = 0, \tag{6.2}$$

where $k^2 = 2m_a\left[E - U(r)\right]/\hbar^2$.

For a hard wall, $U(r < a) = 0$ and $U(r \geq a) = \infty$, where a is the radius of the well. The boundary conditions require $\Psi(r = 0)$ be finite and $\Psi(r = a) = 0$. The solution that satisfies the boundary condition at $r = 0$ is

$$\Psi(r, \theta) = \mu J_l(k_{ol}r)\exp(\pm il\theta), \tag{6.3}$$

where l is an integer denoting the vortex index of the wave function. k_{ol} is chosen so that at $r = a$, $J_l(k_{ol}a) = 0$. Thus we have $k_{ol}a = z_{ol}$, where z_{ol} is the zero of the Bessel function, J_l. Inside the well, $U(r < a) = 0$, therefore

$$k_{ol}^2 = 2m_aE_{ol}/\hbar^2, \tag{6.4}$$

and the energy is quantized to

$$E_{ol} = \frac{\hbar^2k_{ol}^2}{2m_a} = \frac{\hbar^2z_{ol}^2}{2m_aa^2}. \tag{6.5}$$

The squared amplitude and the phase of the first sixteen wave functions inside an infinite cylindrical well with $a = 1$ μm are shown in Fig. 6.1 and Fig. 6.2 respectively. The wave functions are distinguished by the radial index o and the azimuthal index l. The radial index counts the number of radial lobes that Ψ or $|\Psi|^2$ has. The azimuthal index counts 2π phase windings in the phase of Ψ around the center of the well. A list of the first 20 eigen-energies are provided in Fig. 6.3 for the well with different a values. Note that the Bessel function of the first kind

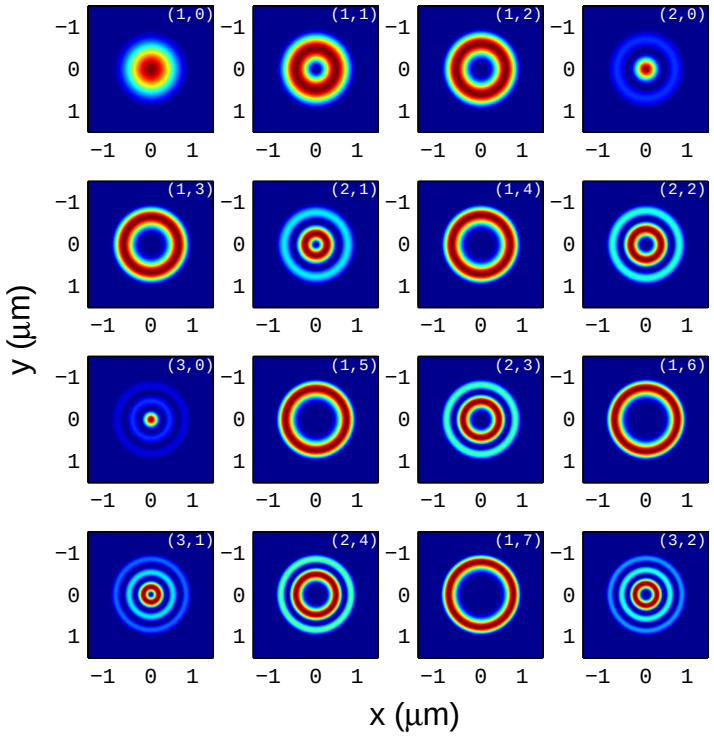

Figure 6.1: Transverse profiles of squared amplitude of the eigen-functions in an infinite cylindrical well with a radius of 1 μm. The eigen-functions are listed in ascending value of energy starting from the left to right and from top to bottom. Each eigen-function is labeled by the tuple, (o, l), on the upper right corner where o denotes the number of radial lobes and l denotes the azimuthal quantum number.

J_l is a function with a definite value of z_{ol} for each distinct value of index o and l. Therefore, according to Eq. 6.5, the order of the eigen-energies depends only on the index o and l and it is independent of a as shown in Fig. 6.3.

6.2 Modeled Bessel Potentials

In this section, we use a time dependent Schrödinger equation to calculates the corresponding eigen-energies and eigen-functions. The equation can be solved numerically using the split-operator method [121, 120]. The results are verified with the Runge-Kutta method [143] by comparing the eigen-energies and eigenfunctions

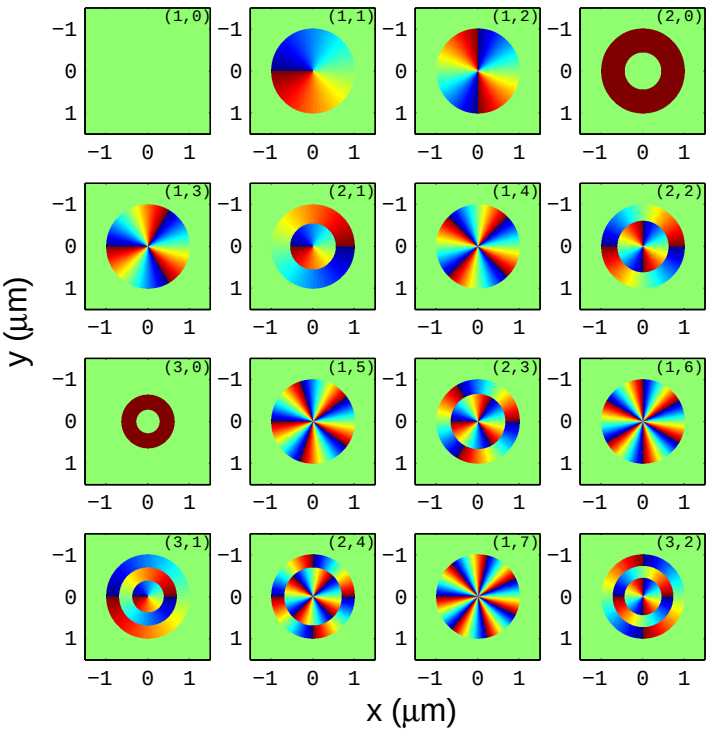

Figure 6.2: Phase profiles of the eigen-functions in an infinite well corresponding to the squared amplitudes provided in Fig. 6.1. The (o, l) labels on the top right corner of each phase profile are described in Fig. 6.1. The azimuthal quantum number, l, can be quantified by counting the number of 2π phase winding around the center of the well.

obtained from the same potential. The detailed description of the numerical implementation is provided in Appendix F. Our simulations are done with a model potential that prevented us from exploring tunneling issues. They are performed in 2D for ^{85}Rb with the potential,

$$U(r) = \begin{cases} U_{max} J_n^2(k_r r)/J_n^2(k_r r_p); & r < r_p, \\ \\ U_{max}; & r \geq r_p, \end{cases} \tag{6.6}$$

where U_{max} is the potential height, $r = (x^2 + y^2)^{1/2} \equiv$ the radial coordinate, (x, y) denotes the Cartesian coordinates, r_p is the peak radius, the radius of first Bessel

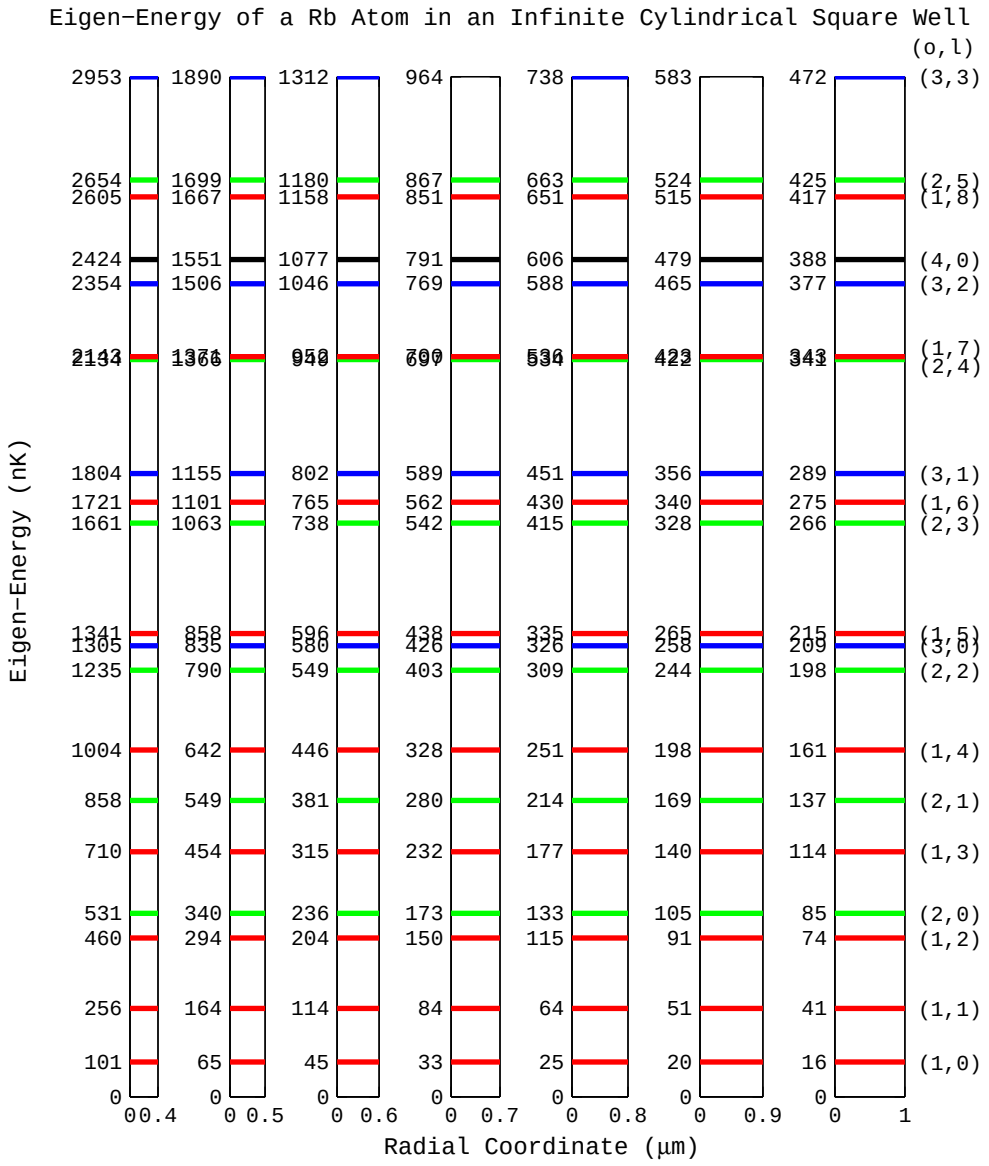

Figure 6.3: Energy levels of infinite wells with different radii. From left to right, the wells' radii are 0.4, 0.5, 0.6, 0.7, 0.8, 0.9, and 1.0 μm respectively. The order of energy levels and the ratio between any two neighboring energy gaps in each well never change with the well's radius. The eigen-states are labeled by tuples (o, l) as described in Fig. 6.1 in the right hand column of the figure. The numbers on the left of each well are the energy eigen-values in nanoKelvin.

max, n is the Bessel order, and k_r is the radial scale factor.

In the following text, we will briefly mention a physical description of this method. First we note that the solution of the time-dependant Schrödinger equation,

$$i\hbar\frac{\partial\Psi(\vec{r})}{\partial t} = -\frac{\hbar^2}{2m_a}\nabla^2\Psi(\vec{r}) + U(x,y)\Psi(\vec{r}), \tag{6.7}$$

can be approximated as

$$\Psi(\vec{r}, t=\Delta t) = e^{-i\hbar\nabla^2\Delta t/2m_a}e^{U(x,y)\Delta t/2i\hbar}e^{-i\hbar\nabla^2\Delta t/2m_a}\Psi(\vec{r}, t=0) + O(\Delta t^3), \tag{6.8}$$

where $\Psi(\vec{r}, t=\Delta t)$ is the updated wave function after the initial wave function $\Psi(\vec{r}, t=0)$ evolves for time Δt, and $O(\Delta t^3)$ denotes the big O notation for the calculation error on the order of Δt^3. The advantage of this approximation is that now the terms that involve spatial derivatives are separated from the term that involves only spatial coordinates. Equation 6.8 can be evaluated by operating each exponential term on $\Psi(\vec{r}, 0)$ over a short time increment Δt one by one from right to left. The terms that involve spatial derivatives can be evaluated in Fourier space using the Fourier integral transforms. On the other hand, the term that involves spatial coordinates can be evaluated directly through multiplication. The value of $\Psi(\vec{r}, t)$ as a function of time (discrete) can be obtained by iteratively applying the operators in Eq. 6.8 many times to the initial wave function that is newly updated for every time increment. The eigen-energies can be calculated from a correlation function, $P(t)$, defined as an overlap (inner product) of the initial wave function and a wave function at time t, i.e.

$$P(t) = \langle\, \Psi(\vec{r}, t=0) \,|\, \Psi(\vec{r}, t) \,\rangle\,. \tag{6.9}$$

The plot of $P(t)$ against t contains oscillations at various frequencies as shown in the top row of Fig. 6.4. The origin of the oscillations can be understood by noticing that the time-dependent wave function of each eigen-state of $\Psi(\vec{r}, t)$ fluctuates in time at a single frequency associated with its eigen-energy. As an example, if the initial wave function is only associated with two eigen-functions, $P(t)$ will oscillate at only two frequencies specific to the two eigen-energies of those eigen-functions.

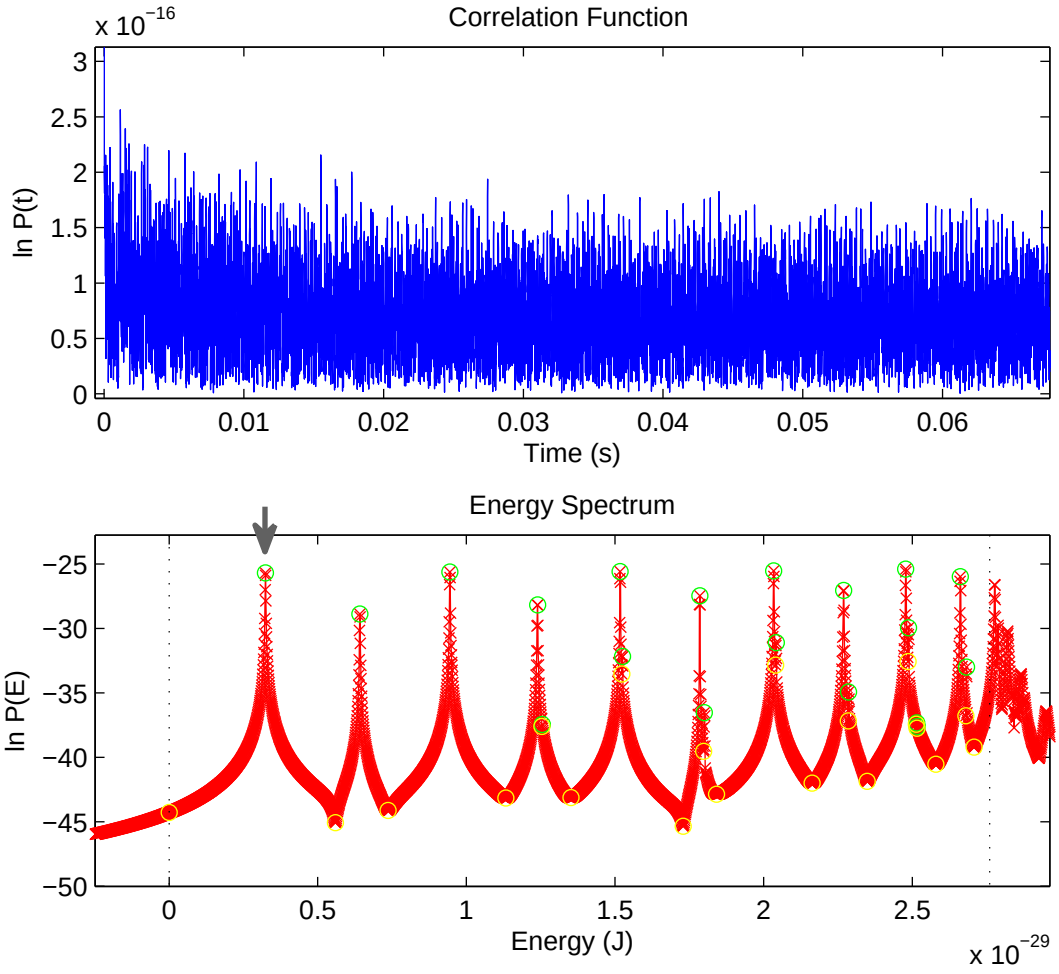

Figure 6.4: The plot of the natural logarithm of the correlation function, $P(t)$ and the natural logarithm of its Fourier transform, $P(E)$, that gives the spectrum of eigen-energies of a single atom inside an optical tunnel. The arrow indicates the peak that corresponds to the ground state. The simulation was done for a tunnel with $r_p = 1$ μm and $U_{max} = 2.76 \times 10^{-29}$ J $= k_B \times 2$ μK in a model J_1-Bessel potential as described by Eq. 6.6. There are ten noticeable peaks between 0 and U_{max} corresponding to the $m = 0$ states. The locations of 0 and U_{max} are indicated by the dash lines.

A Fourier transform of $P(t)$ therefore contains spikes revealing the eigen-energies as shown in the bottom row of Fig. 6.4. Once an eigen-energy, E_n, is known, the eigen-function can be calculated by filtering out the other eigen-functions (with different frequencies) from $\Psi(\vec{r},t)$. The filtering can be achieved by first multiplying $\Psi(\vec{r},t)$ with an oscillating function, $w(t)$, that is in phase with the eigen-function of interest, e.g. $w(t)=\exp(iE_nt)$ or $w(t)=\cos(E_nt)$, and summing up all the past history of $\Psi(\vec{r},t)w(t)$ starting from $t=0$.[1] By doing such, the contribution from other eigen-functions are washed out as time increases. At the same time, $w(t)$ strengthens (suppresses) the contribution from the eigen-function of interest (not of interest) when the amplitude of the eigen-function is maximum (not maximum). From this fact, the ground state needs to be accumulated the longest time because its oscillation frequency is the slowest.

We calculate our simulation by using a Gaussian wavepacket, comparable in size to the tunnel, as our initial wave function, i.e. $\Psi(\vec{r},0)=\exp\left(-0.1\,r^2\right)$. We use 256 pixels to define our grid in x and y spatial coordinates. The size of the simulation is 5 μm whereas the maximum size of r_p is 1 μm. The time increment Δt is chosen such that the entire spectrum of the bound states is covered [120], i.e., $\Delta t<\pi\hbar/U_{\max}$. According to Feit *et al.* [120] the best result is obtained when $\Delta t<\pi\hbar/3U_{\max}$. To be able to resolve the ground state from the first excited state, the total time of the simulation Δt_{tot} has to be such that $\Delta t_{tot}=\pi\hbar/\Delta E_{\min}$, where $\Delta E_{\min}$ is the energy separation we want to resolve. However, the energy separation is not known a priori. Thus to implement the simulation, once we know Δt, we iterate the evolution of Ψ over Δt for as long as needed until the ground state is resolved. For our case, $\Delta t\sim 4$ μs and $\Delta t_{tot}\sim 70$ ms so that $\Delta E_{\min}\sim 0.4$ nK. An example of the plot of $\ln P(t)$ versus t and the plot of the natural logarithm of a Fourier transform of $P(t)$ versus the energy are shown in Fig. 6.4. The plots are based on $r_p=1$ μm and $U_{max}=2$ μK for a J_1-potential. The ground state eigen-energy in this case is found to be 235 nK. The tunnel can support at least 16 bound states. The pictures of the squared amplitude and the phase of sixteen

[1] see Eq. F.23 for a numerical implementation in a discrete form

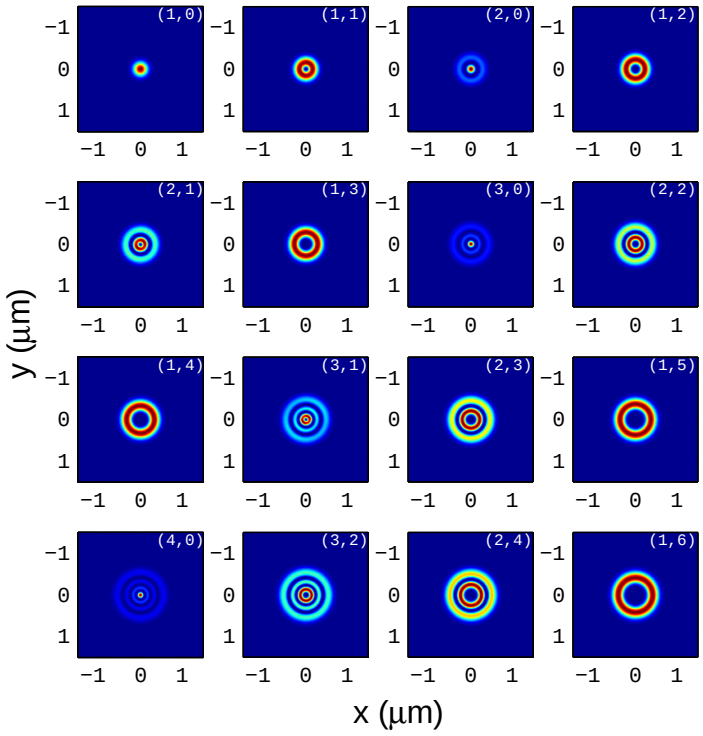

Figure 6.5: Transverse profiles of squared amplitude of the eigen-functions in a Bessel tunnel described in Fig. 6.4. The eigen-functions are listed in ascending value of energy starting from the left to right and from top to bottom. The notation (o, l) for the eigen-function is the same as that described in Fig. 6.1. Note the influence from the potential wall that pushes the wavefunctions toward the center, resulting in smaller size wavefunctions compared to those in Fig. 6.1.

lowest-energy wave functions are shown in Fig. 6.5 and Fig. 6.6 respectively.

To find a single mode tunnel that supports only the ground state, we decrease U_{max} so that the excited states are forced to leave the tunnel until there is only one bound state left in the tunnel. The largest U_{max} occurs when the first excited state just leaves the tunnel. For a J_1-tunnel with $r = 0.5$ μm, the largest U_{max} is 280 nK and the value of the ground state energy is 164 nK. The spectrum of this single mode is displayed in Fig. 6.7, where in the figure the dash lines on the left (right) indicates the zero (U_{max}) potential. The radial profile of the squared amplitude of

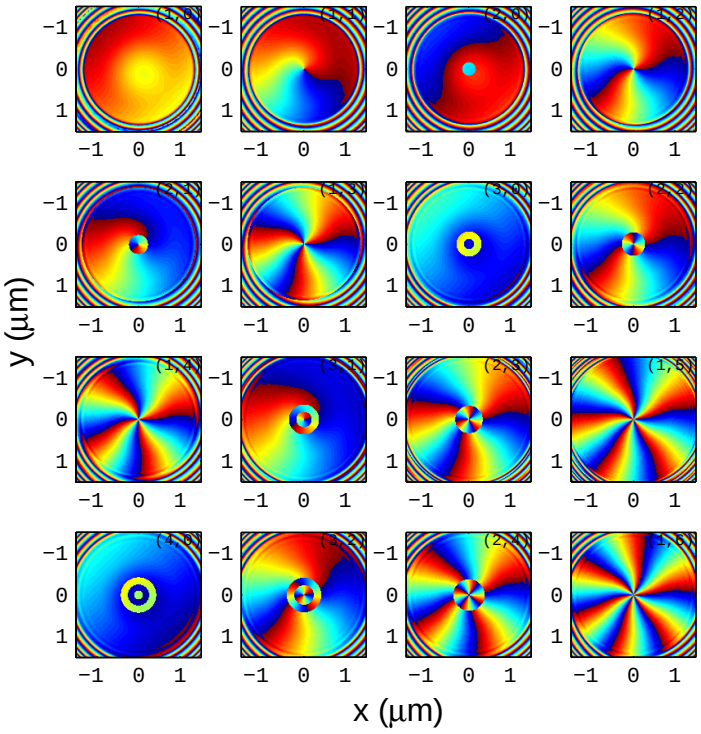

Figure 6.6: Phase profiles of the eigen-functions corresponding to the squared amplitudes shown in Fig. 6.5. The azimuthan index l can be counted in the same way as described in Fig. 6.2.

this single-mode ground state is shown together with the potential in Fig. 6.8. The 2D amplitude and phase of this state are also shown in Fig.6.9.

In the example above the potential height U_{max} is used to control the energy levels inside the Bessel tunnel. There are two other important variables that affect the energy levels as well, i.e., the peak radius, r_p, and the index n of the J_n-Bessel tunnel. Three sets of simulations are done to reflect the effects from changes in these variables.

For the first set of simulations, we vary U_{max} from 1 μK to 10 μK by an increment of 1 μK while keeping $r_p = 0.5$ μm and $n = 1$ fixed. We then calculate the energy levels of the bound states inside the tunnel. The result is shown in Fig. 6.10. Each eigen-energy is labeled by a tuple (o, l) where o and l are the radial

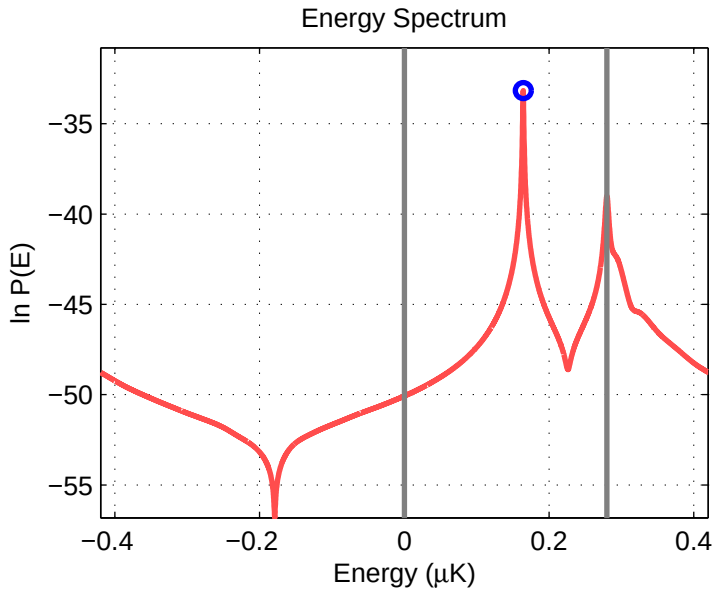

Figure 6.7: Energy spectrum inside a single mode J_1-Bessel tunnel with the peak radius of 0.5 μm. The ground state energy occurs at 164 nK when the first excited state is leaving the tunnel at $U_{\max} = 280$ nK toward higher energy.

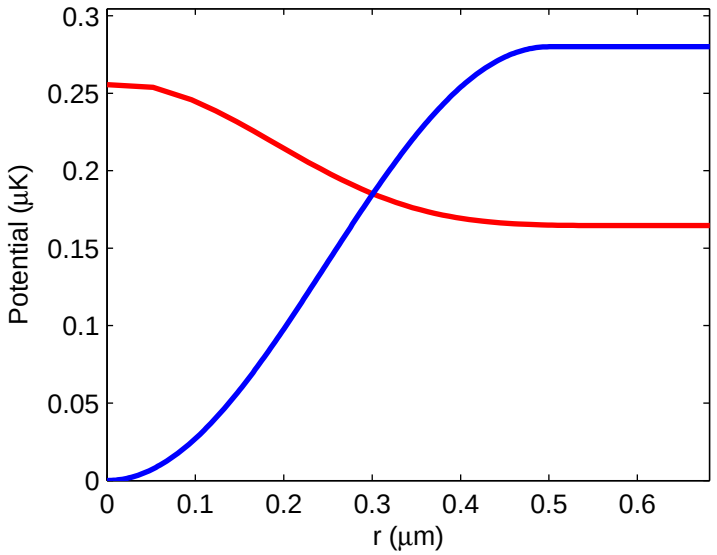

Figure 6.8: Ground state wave functions of a single mode tunnel (red), which correspond to the ground state energy in Fig. 6.7. Also shown in the picture is the model potential (blue), $U(r)$ as described by Eq. 6.6.

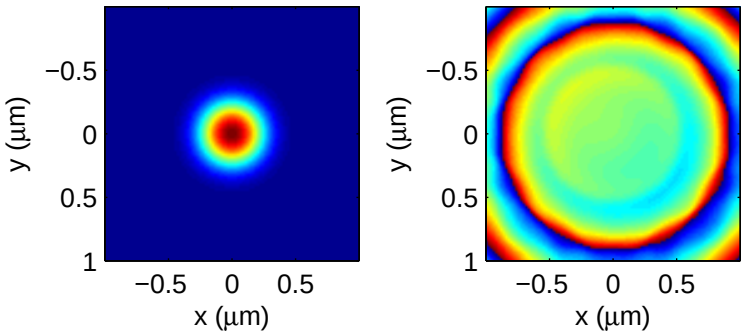

Figure 6.9: 2D profile of the squared amplitude (left) and phase (right) of the ground state shown in Fig. 6.8.

and azimuthal index as described in the previous section. Some labels are shown at the right of the figure. The plots of each o are also associated with a specific color as shown in the legend. For example, all the red plots are associated with $o = 1$. Moreover, for each o value, the higher the value of l, the higher the value of the corresponding eigen-energy and l always increases by an integer increment of 1. The circles shown in the figure indicates crossings between levels, which will be further discussed in Sec. 6.4.

The second set of simulations is performed by varying r_p from 0.4 μm to 1 μm by an increment of 0.1 μm. We keep the value of U_{max} fixed at 1 μK and the index n is fixed at 1 to produce a J_1-Bessel potential. The resulting energy levels of the bound states are shown in Fig. 6.11. The tuple labels and the color coding scheme have the same meaning as that shown in Fig. 6.10 and described in the previous paragraph.

Lastly, for the third set of simulations, we vary the value of n from 1 to 10 by an increment of 1. The index n is not varied continuously because a fraction in n can produce a leak in the tunnel as discussed in Sec. 2.1. The resulting energy levels from the simulation are shown in Fig. 6.12. The tuple labels and the color coding scheme also have the same meaning as that shown in Fig. 6.10 and described in the previous paragraph.

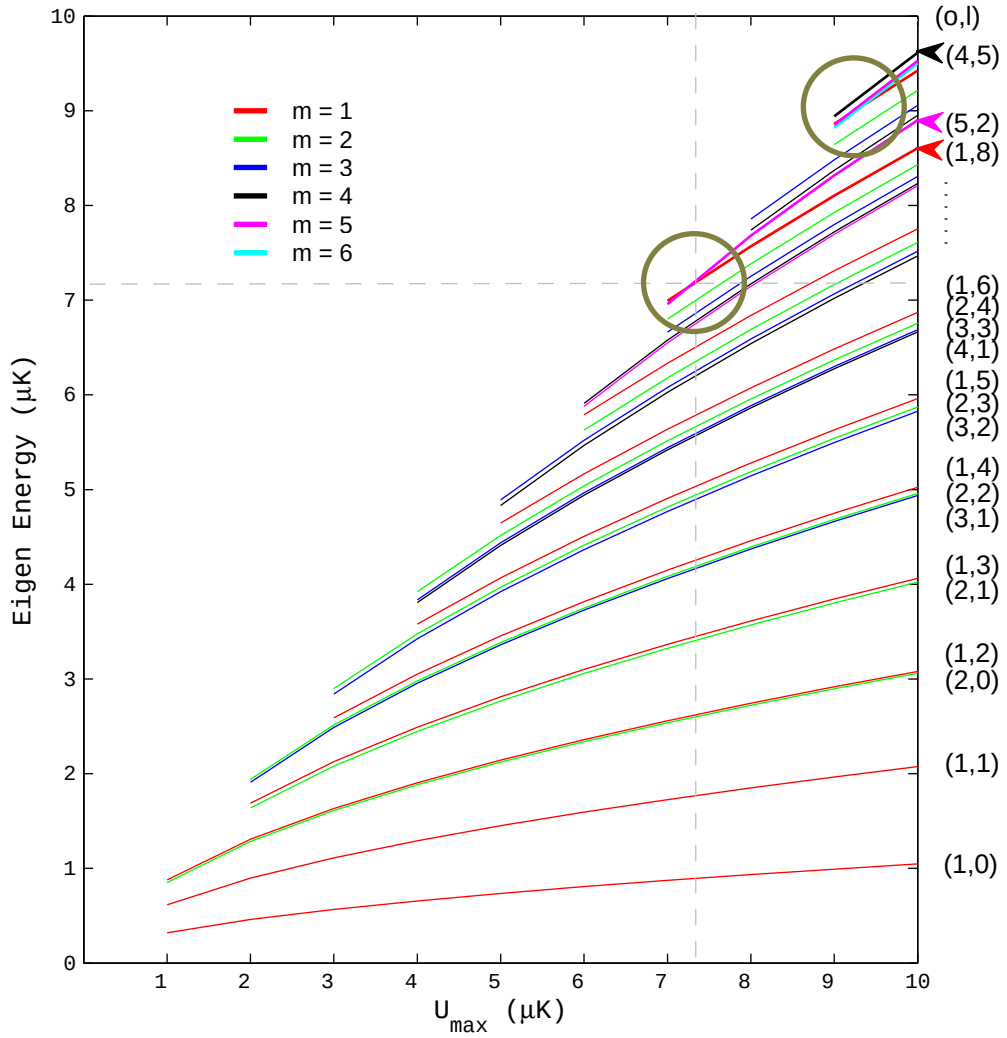

Figure 6.10: Energy eigen-value vs. potential height, $U_{\max}$. When comparing the energy-sorted list of the mode (o, l) between those in the infinite well and the Bessel tunnel, the lists are not the same. When the potential changes from the infinite well to the Bessel tunnel, there are intermediate configurations where different states are degenerate. These degenerate levels can be used as a channel to launch superposition of modes (o, l) in the tunnel.

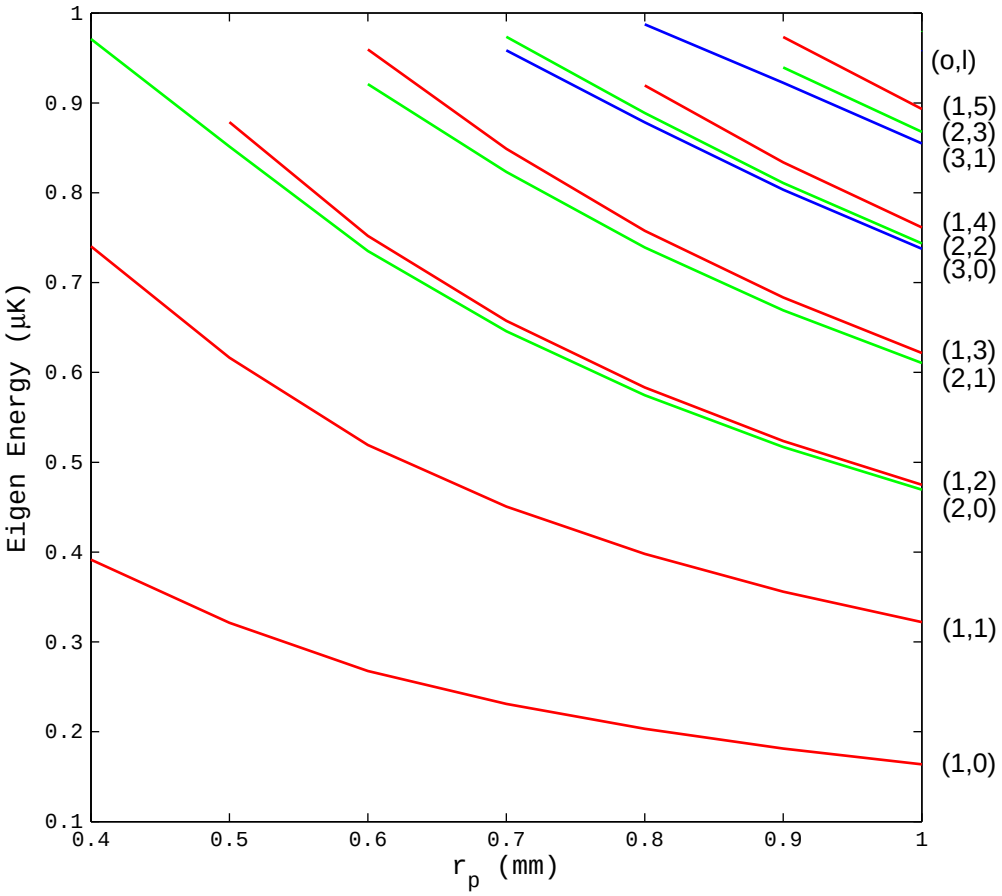

Figure 6.11: Eigen-energy vs. peak radius of J_1- Bessel beam. The value of $U_{\max}$ is fixed at 1 μK.

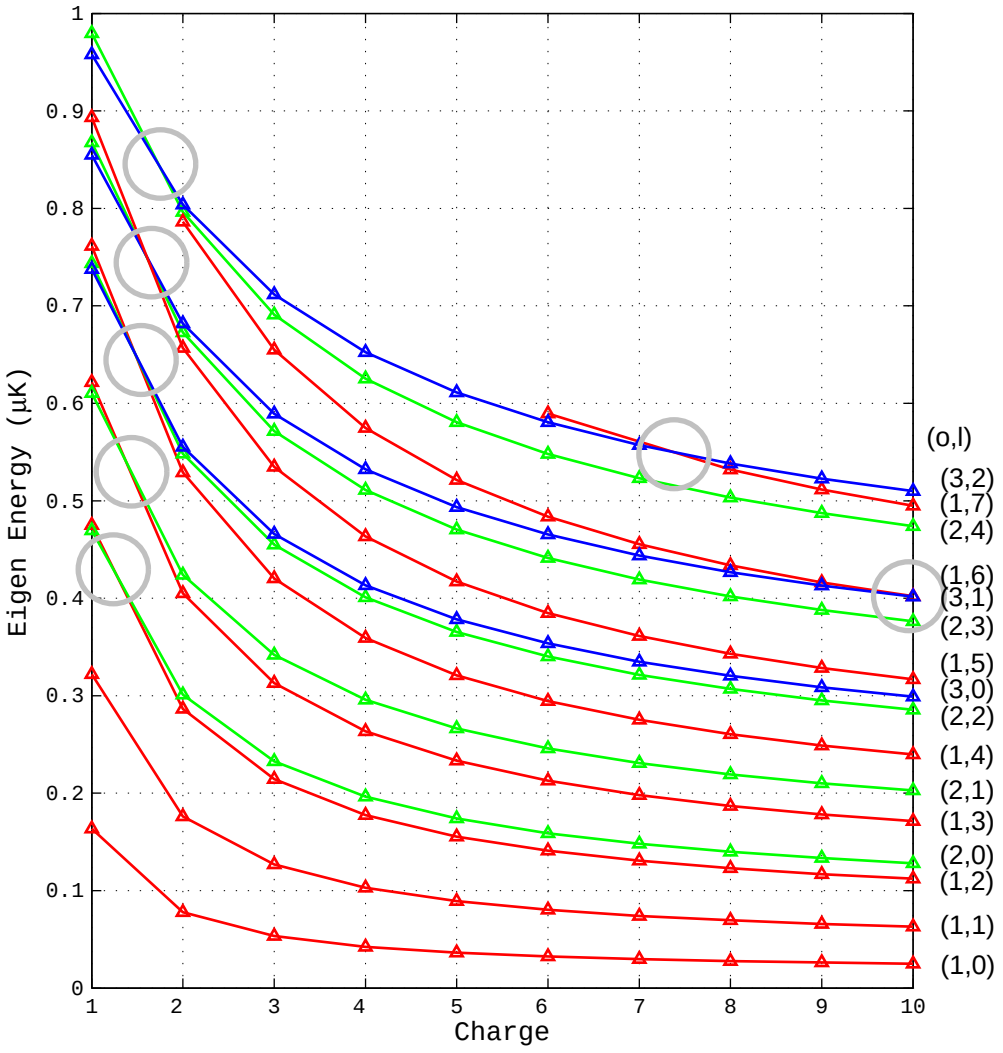

Figure 6.12: Eigen-energy vs. charge n in J_n- Bessel beam. There are crossings of energy levels located by the grey circular marks. As the value of n becomes larger, the order of the energy levels in the tunnel becomes more similar to the order in an infinite well.

6.3 Single Mode in a Red Detuned Ring

In the previous section, our simulation is based on a model blue-detuned beam that traps atoms in the dark core of the beam. However, for the experimentally realizable blue-detuned beam where the wall has a finite thickness, the beam cannot support real bound states because the probability for the atom tunneling through the wall is not zero. In this section, we look at red-detuned Bessel potentials that have true bound states. For a high order Bessel beam, a red-detuned laser provides a ring-shaped potential well in place of the wall barrier as encountered in the case of the blue-detuned beam. Ring-shaped potentials have a closed loop geometry that has attracted a lot of attention in physics communities for several reasons associated with its circular or cylindrical symmetry. For instance, a ring trap can be used to study Sagnac atom interferometry that is useful in sensing rotation and acceleration [144, 145], or persistent current in Josephson junctions and their applications [146, 147]. Red-detuned ring traps with embedded optical lattices can be used to study a one dimensional system with periodic boundary conditions [148, 149, 150, 90] which can be useful to realize a Feynman quantum simulator [151]. Multi-ring structures can also be used to make an atomic-phase inference device analogous to a SQUID [17, 18, 19].

In our simulation, the red-detuned ring potential can be described by

$$U(r) = \begin{cases} -U_{max} J_n^2(k_r r)/J_n^2(k_r r_p); & r < r_z, \\ \\ 0; & r \geq r_z, \end{cases} \tag{6.10}$$

where U_{max}, r, r_p, n and k_r have the same meanings as in Eq. 6.6, and r_z is the radius of the first Bessel zero. The eigen-energies and eigen-functions are calculated by following the same procedure as describe in the previous section. The simulations are based on the red detuned J_1-Bessel potential with $r_p = 0.5$ μm and $U_{max} = 250$ nK. The ground state has an energy of -163 nK and the first excited state is at the brim at -24 nK, which indicates that it almost exits the potential. Their spectrum and radial profiles are shown in Fig. 6.13 and Fig. 6.14 respectively. The 2D squared

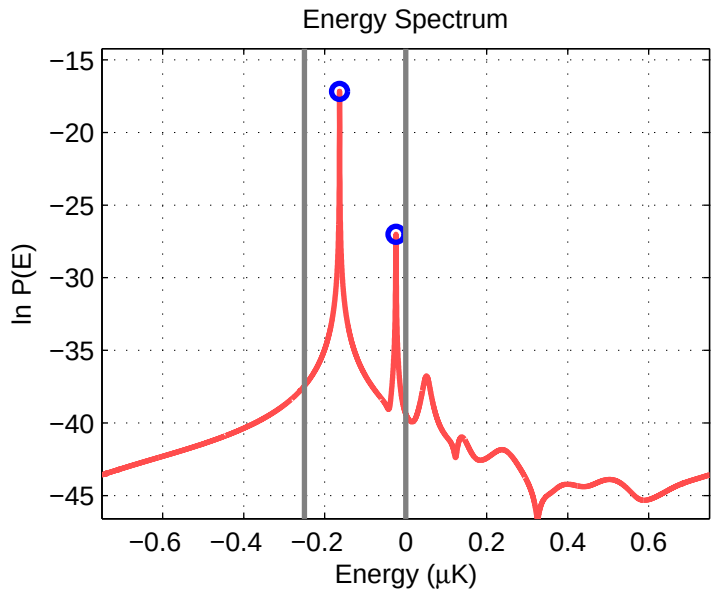

Figure 6.13: Energy spectrum of a single mode inside the first ring of a red-detuned J_1-Bessel tunnel with the first peak radius of 0.5 μm. The ground state energy occurs at -163 nK when the first excited state is leaving the tunnel at $U_{\max} = 0$ nK toward higher energy. The depth of the well is at $-U_{\max} = -250$ nK.

amplitude and phase profiles of both states are provided in Fig. 6.15.

6.4 Discussion

We begin the discussion with our main interest, i.e., the condition for single mode propagation. For a blue-detuned J_1-Bessel potential with $r_p = 0.5$ μm, the maximum eigen-energy of the single-mode ground state is 164 nK which has approximately the same magnitude as the ground state energy inside the single-mode red-detuned J_1-Bessel potential of the same r_p. However, due to the geometry of the red-detuned potential, only the states with $l \neq 0$ are supported. The ground state of the red-detuned potential is the mode $(o, l) = (1, 1)$ while that of the blue-detuned potential is the mode $(o, l) = (1, 0)$. The values of U_{max} in both cases, are similar i.e., $U_{max} = 280(250)$ nK for the blue (red)-detuned potential. Note that J_1-Bessel potential gives the highest ground state energy. For higher order Bessel potentials

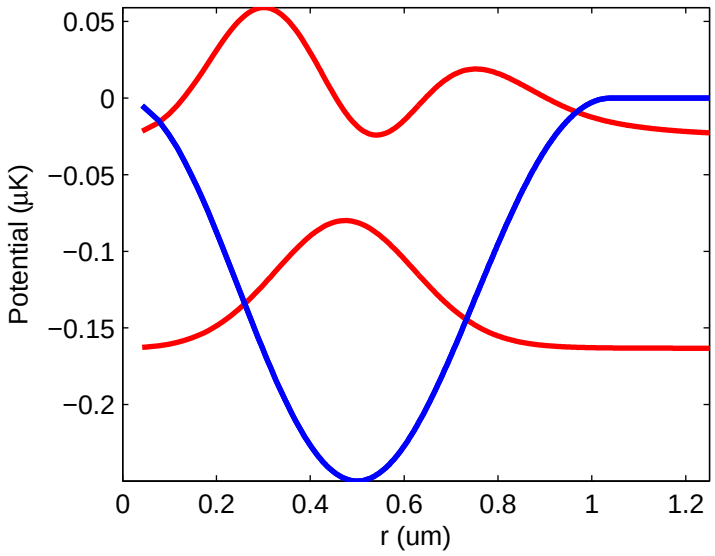

Figure 6.14: Ground and the first excited state wave functions (red) of a single-mode ring potential, which corresponds to the ground and the first excited state energy in Fig. 6.13. Also shown in the picture is the potential (blue), $U(r)$, as described by Eq. 6.10.

with the same r_p, the ground state energy is lower as can be seen in Fig. 6.12 where the Bessel order (or charge) is changed from 1 to 10. This is because the lower the Bessel order is, the further the potential extends into the center dark core region and the more it pushes the atoms. For the infinite well with $r_p = 0.5$ μm, we see from Fig. 6.3 that the ground state has the energy of 65 nK, which is a lower bound for all hollow potentials with the same r_p. In all cases, the Bessel potentials with the peak radius $r_p \sim 0.5$ μm is promising for realizing a single mode guide. The ground state energy is in the neighborhood of the Bose-Einstein condensates temperature. The gap between the first excited state and the ground state is around two times the ground state energy. For rubidium, the hollow beam of this size is larger than the diffraction limited size and can be created with an axicon with a base angle of around 10° to 60° (see Appendix 2.3). Although the range where the Bessel beam exists for this setup is rather short[2], a careful alignment, e.g. with a computer controlled mirror to steer beams, can still be achievable. The atom loading can be

[2] $\sim$ 9 mm for a glass axicon, 2.5 cm in diameter with 10° based angle

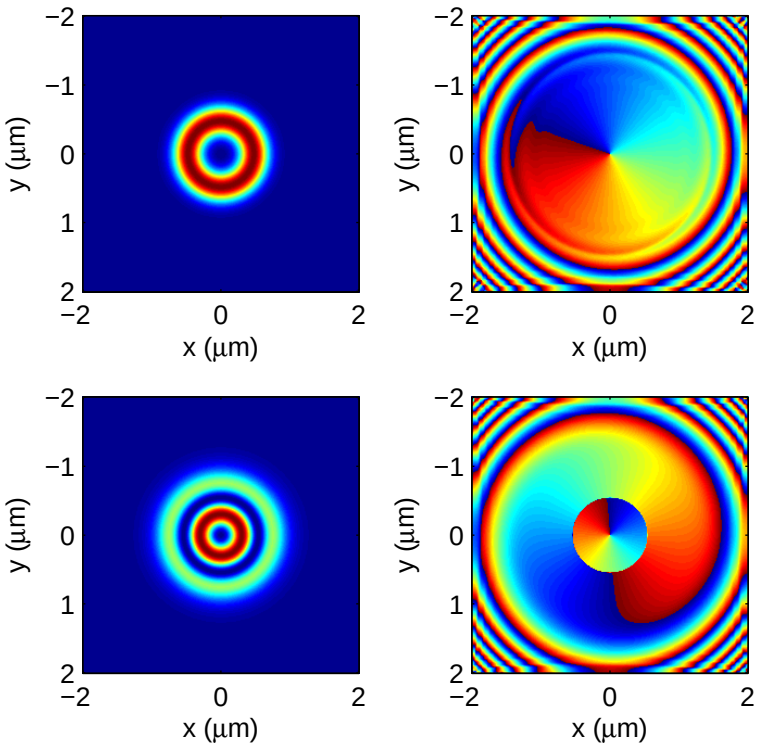

Figure 6.15: 2D profiles of the squared amplitude (left column) and phase (right column) of the ground and the first excited state shown in Fig. 6.14. The ground state wave function is restricted by the shape of the potential. It is a degenerate state that always contained an azimuthal index (vortex) of either +1 or −1.

achieved by gating the tunnel on/off as we have already seen in Chapter 4.

As mentioned earlier, in the case of the blue-detuned hollow potential well, the potential setup in the simulation is unphysical. The thickness of its wall is infinite and cannot be realized experimentally. If the thickness is finite, tunneling occurs and in that case we will no longer have bound states. However, the tunneling can be suppressed by either increasing the thickness of the wall or by increasing U_{max} so that the time it takes for atom to tunnel out of the potential is longer than other time scales in the experiment. For a more realistic multi-mode potential where the potential is truncated at the second peak of $J_1^2(k_r r)$, the preliminary results asserts that the tunneling is negligible [143]. The tunneling from the potential is not always a disadvantage. An atom-phase interference device or a scanning tunneling

microscope, for examples, exploits this effect to operate. For our purpose, tunneling can be studied by using various initial wavepackets in the split-operator simulation and measuring the loss of the population inside the tunnel. One suitable wavepacket to be used as a initial trial function is a thermal wavepacket [152] described as

$$\Psi(r, t=0) = \left(\frac{1}{\pi\sigma^2}\right)^{1/4} \exp\left[-\frac{r^2}{2\sigma^2}\right] \exp\left[-\frac{i}{\hbar} p_0 r\right], \tag{6.11}$$

where σ and p_0 are the width and the momentum of the wavepacket respectively. The magnitude of the tunneling probability can be observed by integrating the probability inside the potential at a particular time because the operation in the split-operator method is unitary. The plot of the tunneling probability versus time can give the tunneling rate for the thermal state. This calculation will not be presented in this thesis.

Next, we will discuss about the multi-mode states inside the blue-detuned tunnel as shown in Fig. 6.10, Fig. 6.11, and Fig. 6.12. We notice that the energy-levels inside the Bessel tunnel changes as we change U_{max}, r_p, and n. In Fig. 6.10, the number of multi-mode states and the values of the eigen energies increase when U_{max} increases. The order of the mode (o, l) which corresponds to an ascending order of energy in the J_1-Bessel potential is different from the mode order in the infinite well. There are some crossings between energy-levels, for example, at $U_{max} \sim 7.3$ μK and 9.1 μK. This is expected because J_1-Bessel potential approaches an infinite well as U_{max} approaches infinity. Note, however, that the order in the low energy-levels is not sensitive to the change in U_{max}, i.e. those below $E(o, l) = E(1, 8)$. In Fig. 6.11, the energy-levels decrease as we increase r_p. This is what we have also seen in the infinite well where the energy is inversely proportional to the size of the well as described by Eq. 6.5. The order of the energy-levels is not affected in the range of r_p we have covered in our simulation. Although, we have observed that the rates of change in the eigen-energies are different. For example, the rate of the mode $(2, 0)$ is different from the rate of $(1, 2)$. Thus it is expected that at a certain r_p these two modes might become degenerate. In Fig. 6.12, the change in n affects the order of the energy-levels greatly. It is apparent that the potential wall get steeper with

higher n and resembling more of the wall of the infinite well. For our simulation where $U_{max} = 1$ μK and $r_p = 1$ μm, the order of the energy-levels at $n = 10$ is the same as that of the infinite well. At $n = 1$ the order is different. Thus the change from $n = 1$ to $n = 10$ results in level crossing. However, as we can see from the figure, the crossings do not occur at the exact value of n, therefore they cannot be realized in the experiment simply by using one Bessel beam since n always has to have an integral value for the potential to contain atoms. The continuous change of the wall shape among different n values, however, might be achieved by laying two beams on top of one another. The polarization of the beams can be made to be othogonal to one another to avoid destructive interferences. Other than the degeneracy that arises from the level crossings, there is also degeneracy in the $\pm l$ states.

The atom that is excited to the degenerate energies can be in a superposition of the degenerate states. Therefore by changing the configuration of the potential as we have mentioned earlier, we can break the degeneracy at will. The ability to control the degeneracy can be useful in identifying entangled states in the tunnels. For example, by coupling and guiding atoms from two different ensembles located at different locations to two entangled tunnels, the change of tunnel in one beam breaks the degeneracy of the atoms guided in one ensemble and thus identifies the entangled state in the other ensemble. This scheme might be achieved with the probabilistic entanglement as describe in Ref. [133, 137].

So far we have the ability to create hollow optical tunnels that can guide cold atoms. To date, we have applied the technique to thermal atoms. We are planning to use it to guide degenerate ensembles. To extend the simulation of this single-atom guide to the degenerate ensembles such as the BECs, we consider the Gross-Pitaevskii equation [153]. The equation with a cylindrically symmetric potential $V(r)$ can be written as

$$i\hbar\frac{\partial}{\partial t}\Psi(\vec{r}) = \left[-\frac{\hbar^2}{2m}\nabla_\perp^2 + V(r) + g|\Psi(\vec{r})|^2\right]\Psi(\vec{r}), \tag{6.12}$$

where m is the mass of the atom, $g = 4\pi\hbar^2\xi/m$ is the coupling constant and ξ is the

scattering length. For ^{87}Rb, the triplet scattering length $\xi \sim 100\xi_0$, and for ^{85}Rb, $\xi \sim -350\xi_0$, where ξ_0 is the Bohr radius [154].

Javanainen *et al.* [155] found that the Gross-Pitaevskii equation can also be solved using split-operator method, for a certain accuracy, provided that the nonlinear term in the equation is updated with the most recent wave function, i.e., Eq. 6.12 can be split to

$$\Psi_{t+\Delta t}(\vec{r}) = \exp\left[\frac{i\hbar}{4m}\nabla^2\Delta t\right]\exp\left[\frac{V(r)+g|\Psi(\vec{r})|^2}{i\hbar}\Delta t\right]\exp\left[\frac{i\hbar}{4m}\nabla^2\Delta t\right]\Psi_t(\vec{r}), \tag{6.13}$$

and we evaluate Eq. 6.13 in three steps, i.e.

$$\Psi_K = \exp\left[\frac{i\hbar}{4m}\nabla^2\Delta t\right]\Psi_t(\vec{r}) \tag{6.14}$$

$$\Psi_{UK} = \exp\left[\frac{V(r)+g|\Psi_K|^2}{i\hbar}\Delta t\right]\Psi_K \tag{6.15}$$

$$\Psi_{t+\Delta t}(\vec{r}) = \exp\left[\frac{i\hbar}{4m}\nabla^2\Delta t\right]\Psi_{UK}. \tag{6.16}$$

The catch is in the second step when $|\Psi(\vec{r})|^2$ is replaced with $|\Psi_K|^2$. With this substitution the calculation error becomes $O(\Delta t^3)$ as normally does without the nonlinear term. The work in this chapter has been reported in Ref. [118]

Chapter 7

Summary and Future Plans

In the thesis, we observed dynamics of atoms transported inside a Bessel tunnel that preserved its size while propagating. There were three main topics covered. One main interest is the generation of the tunnels suitable for the experiment carried out in later chapters. This was described in Chapter 2. Two other main interests that characterized the transport in classical and quantum regimes were described in Chapter 4 and Chapter 6 respectively.

In summary, we have shown in Chapter 2 that ideal phase patterns displayed on two-dimensional spatial light modulators can be used to embed a variety of vortices and intensity-void patterns that propagate along with laser beams. While these ideal patterns assume input beams that are plane waves of infinite extent, high-quality, nearly pure modes can be generated as long as the number of phase steps for each 2π range exceeds 4. Since currently available SLMs have limited spatial resolution, there is an upper bound to the maximum charge state that can be generated before truncation degrades the beam quality. To raise this limit, it will be necessary to modify the phase pattern to account for truncation. Such modification requires further investigations in the future. For our SLM, the Bessel tunnel that is suitable for us to use in Chapter 4 and 5, considering the size of the tunnel, was the J_4-Bessel beam. Finally, while SLMs can be used for direct generation of exotic modes, they could find wider application as tools for the design and prototype development of static optical elements, imprinted with the desired phase mask. Such static elements could be fabricated with much higher resolution and spatial area than will be possible with SLMs in the near future. This will allow the generation of high-quality vortex beams with higher charge states to be

converted from standard laser beam profiles over a wide range of input diameters.

In Chapter 4, we have shown that hollow light tunnels are very efficient at removing atoms with transverse velocity components that exceed a well-defined potential barrier of the tunnel; the effective transverse temperature is approximately 50% of the effective tunnel temperature. Thus the tunnel provides a scalpel to remove hot atoms. We observed this truncation to saturate within 20 ms, however, this timescale is temperature and geometry dependent. For the open tunnel, the resulting ensemble is out of equilibrium with effective temperatures in the longitudinal and transverse directions being nearly decoupled and potentially very different at time relevant to our experiment. Our LE model, which included radial trajectories and ignored any angular momentum transferred to the atoms by the tunnel, seem to capture most of the dynamics. Evidently, orbital angular momentum exchange between the atoms and the tunnel is small under our conditions. Finally, we discussed how a combination of restricting the ensemble flow, modifying the tunnel geometry and changing the potential height of the tunnel could allow the tunnel to enable evaporative cooling of the ensemble while in transit. These ideas are currently under further investigation in the lab. In the future, it might be possible to exploit the thermal leak of atoms out of tunnels to study particle exchange between adjacent atom guides. Moreover, based on a Feshbach resonance, a study of correlated gas [156, 157] in or around a tunnel or array of tunnels is also an interesting topic.

In Chapter 6, we looked at the quantized energy level structure in the tunnels. We found that a ground-state single-mode tunnel can be achieved for a tunnel with 1 μm diameter at a condensate temperature $\sim$ 150 nK for both red- and blue-detuned beams; at typical condensate temperatures, diameters up to $\sim$ 10 μm could be used. This temperature is about half the value of the potential height. We found that multi-mode transport in the tunnel can be controlled by changing the peak radius, potential height and/or the charge of the Bessel beam. Adjusting these parameters could enable pairs of eigenstates to be tuned through degeneracy. We suggested that such degeneracy might be used to create a superposition of states. This and other quantum properties remain to be investigated.

Appendix A

Atom-Photon Interactions and Magneto-Optical Traps

In this appendix we describe a simple model of the interaction between atoms and the light field. The force of light on atoms involves momentum exchange between photons and atoms upon absorption and emission. Because the emitted photons can be either spontaneous or stimulated, the resulting forces fall into two categories (1) a radiative force, sometimes called the scattering force, which is dissipative or inelastic (loss of energy) and related to spontaneous emission [158, 159] and (2) a dipole force, which is conservative or elastic (energy conserved) and related to stimulated emission [159, 160]. The descriptions of these forces, along with their uses in the experiments, will be reviewed in this appendix. The radiative force is employed to cool (Zeeman slower for example) and trap atoms (a magneto-optical trap (MOT) for example) while the dipole force generates the potential also suitable to trap atoms as in the case of our atom guides.

A.1 Scattering force

A time average of the radiative force results in a net force in the direction of absorbed photon. When the atom absorbs or emits a photon, its momentum changes by an amount $\hbar k$, where k is the wavenumber and $\hbar$ is the Plank constant divided by 2π. Given an absorption or emission rate, R, the averaged scattering force, $\langle F_{sp} \rangle$, can be written as

$$\langle F_{sp} \rangle = \hbar k R. \tag{A.1}$$

Based on a two-level atom model, R can be written as

$$R = \Gamma \rho_{ee} = \Gamma \cdot \frac{I/2I_s}{1 + I/I_s + 4(\Delta/\Gamma)^2}, \tag{A.2}$$

where Γ is the natural linewidth or the decay rate of the excited state, ρ_{ee} is the steady state population in the excited state, $I_s \equiv 2\pi^2\hbar c/3\lambda^3\tau$ is the saturation intensity, λ is the wavelength of the absorbed light, c is the speed of light, $\tau = 1/\Gamma$ is the lifetime of the excited state, and Δ is the detuning of the incident light beam. A derivation of Eq. A.1 and Eq. A.2 can be found in Appendix B. The magnitude of $\langle F_{sp} \rangle$ depends on the detuning. In our atom guide experiment, $(\Delta/\Gamma)^2 \gg I/I_s \gg 1$ so the absorption rate can be approximated as

$$R = \frac{\Gamma^3}{8\Delta^2} \cdot \frac{I}{I_s}. \tag{A.3}$$

Now let us look at an example of the absorption rate for a ^{87}Rb atom inside a 60 mW

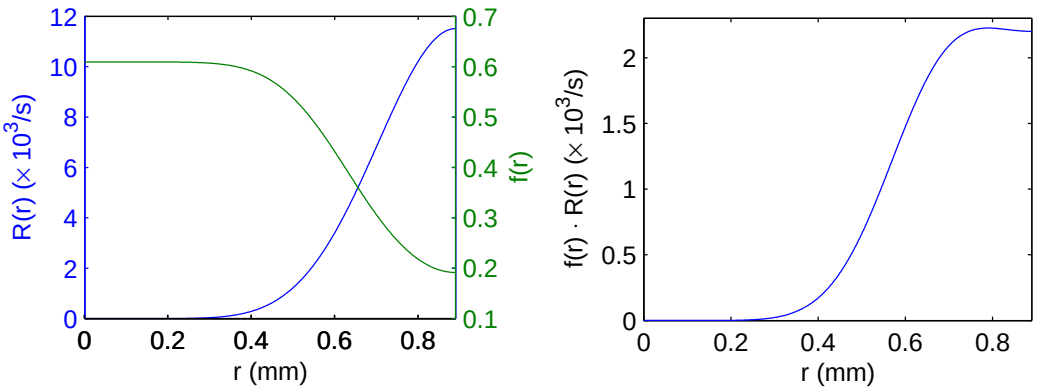

Figure A.1: Left: The blue trace shows the absorption rate, $R(r)$, as described in Eq. A.3, and follows the laser intensity. The green trace shows the probability of finding an atom, $f(r)$, inside a 1-mm Bessel tunnel. Right: the plot represents the product of $R(r)$ and $f(r)$, which is the weighted absorption rate or the absorption probability per a unit time in the range shown in the figure.

Bessel beam with an intensity distribution $I(r) = I_0 J_4^2(kr)$ as used in Chapter 2.2. For this choice of intensity pattern, the absorption rate in Eq. A.3, which depends on the intensity I, also depends on the radius r. The absorption rate is the blue trace in the left plot of Fig. A.1. If the probability of finding an atom, $f(r)$, in the Bessel beam is not uniform, which is the case for our experiments, the absorption rate is modified according to $R_{\text{mod}} = f(r)R(r)$, the weighted absorption rate or the absorption probability per a unit time in the range shown in the right column of

Fig. A.1. Integrating the area under R_{mod} gives the weighted average absorption rate for the whole ensemble.

A.2 Dipole Force and Potential

The dipole force can be understood in many contexts. One easy explanation is to look at the atom system as a harmonic oscillator: an electron attached to the atom by a spring driven by an external force. The driven harmonic oscillator is characterized by its natural frequency. We denote the frequency of the external force as "blue detuned" when it is higher than the resonance frequency and "red detuned" when it is lower. For the blue detuned light field, the motion of the electron tends to be out of phase with respect to the external force. For the red detuned case, the motion of the electron has a tendency to be in phase with the external force. Note that the in-phase condition is reached when the frequency of the driving force is much smaller than the resonance frequency and vice versa in the case of the out-of-phase condition. This in and out of phase motion can be demonstrated easily with a pendulum such as a pencil or a ruler [160]. One simply holds one end of the pendulum loosely with the finger tips so that the pendulum can swing freely. The driving force can be given to the pendulum by rocking the hand holding the pendulum back and forth. When the frequency of the driving force is much smaller than the pendulum's natural frequency, the pendulum will swing in phase with the hand motion. On the contrary, when the frequency of the driving force is much larger, the pendulum cannot keep up and it will swing 180° out of phase with respect to the hand motion. Out of these two conditions, the in-phase motion is the system's preferable state because the energy of the system is lower [1]. If the atoms is placed in the spatially inhomogeneous light field, the energy of the system varies spatially as well. Since the system seeks the lower energy state, for the blue

[1]The energy (E) of the system can be calculated from $E = -\mu \cdot \mathbf{E}$, where μ is the dipole moment and $\mathbf{E}$ is the electric field. When the motion of the electron is out of phase with respect to the driving force, the dipole moment is anti-aligned with the electric field. As a result, the energy of the system is positive, opposite to the in-phase motion.

detuned light field, the atom prefers to be in the place with lower intensity. On the other hand, if light field is red detuned, the atom prefers to be in the place with higher intensity.

The dipole force can be calculated from the density matrix approach. The detailed derivation can be found in Appendix B based on a two-level model (for a three-level model see Ref. [57]). The formula is shown below.

$$\langle F_{dp} \rangle = -\frac{\hbar\Delta}{2} \nabla \ln \left[1 + \frac{I/I_s}{1 + 4(\Delta/\Gamma)^2} \right], \tag{A.4}$$

corresponding to the potential

$$\langle U_{dp} \rangle = \frac{\hbar\Delta}{2} \ln \left[1 + \frac{I/I_s}{1 + 4(\Delta/\Gamma)^2} \right], \tag{A.5}$$

where Δ, Γ and I_s are previously defined in Eq. A.2. For the condition that we usually encounter in the experiment, for a large detuning and high intensity beam, $(\Delta/\Gamma)^2 \gg I/I_s \gg 1$, Eq. A.5 can be approximated to be

$$\langle U_{dp} \rangle = \frac{\hbar\Gamma^2}{8\Delta} \cdot \frac{I}{I_s}. \tag{A.6}$$

A.3 Doppler Effect on Light Force

Due to the Doppler effect in 1D, atoms moving with the speed v toward (away from) a light beam, with a wave number k, will see frequency shifted up (down) by the amount of kv. The sign of k and v determine the direction of propagation of the beam and the atoms respectively. Thus the formulas for the forces or potential we derived earlier for the stationary atoms must be changed by substituting the detuning[2], Δ, with an effective detuning, $\Delta - kv$.

In this case, $\langle F_{sp} \rangle$ from Eq. A.1 and Eq. A.2 will be changed to

$$\langle F_{sp}(v) \rangle = \hbar k \, \Gamma \frac{s_0/2}{1 + s_0 + 4\left[(\Delta - kv)/\Gamma\right]^2}, \tag{A.7}$$

where $s_0 = I/I_{sat}$. For a small Doppler shift, Eq. A.7 can be approximated to first

[2] A more ellaborate approach to this modification can be found in [158].

order in v as

$$\langle F_{sp}(v)\rangle \approx \hbar k\ \Gamma \frac{s_0/2}{1+s_0+4(\Delta^2-2kv\Delta)/\Gamma^2} \tag{A.8}$$

$$\approx \hbar k\ \Gamma \left(\frac{s_0/2}{1+s_0+4\Delta^2/\Gamma^2}\right)\left(\frac{1}{1-\dfrac{8kv\Delta/\Gamma^2}{1+s_0+4\Delta^2/\Gamma^2}}\right) \tag{A.9}$$

$$\approx \hbar k\ \Gamma \left(\frac{s_0/2}{1+s_0+4\Delta^2/\Gamma^2}\right)\left(1+\frac{8kv\Delta/\Gamma^2}{1+s_0+4\Delta^2/\Gamma^2}\right) \tag{A.10}$$

$$\langle F_{sp}(v)\rangle \approx \langle F_{sp}\rangle + \beta v, \tag{A.11}$$

where

$$\beta = \hbar k^2 \frac{4(\Delta/\Gamma)s_0}{\left[1+s_0+4(\Delta/\Gamma)^2\right]^2}. \tag{A.12}$$

Thus moving toward a red detune beam (β is negative), say in x-direction, the atom experiences opposing damping force that can be described by the classical equation of motion as $m\ddot{x} = -|\langle F_{sp}\rangle| - |\beta|\dot{x}$.

Note that if we shine the on-resonance light ($\Delta = 0$) on the thermal atomic ensemble at room temperature (rms speed is ~ 140 m/s), only a fraction of the atoms can be decelerated i.e. the atoms that move toward the light and have Doppler shift within the Lorenzian linewidth of the frequency dependent profile of $\langle F_{sp}\rangle$. Normally the captured velocity is defined to be $v_c \equiv \Gamma/k$, which for the Rb atoms the value[3] is ~ 5 m/s.

A.4 Magneto-Optical Trap (MOT)

The MOT is well known and extensively explained in detail in many books and theses [1, 159, 60, 115, 117]. A detailed explanation is provided here for a convenience of interested readers.

In this section we will show that by combining near resonance laser beams and magnetic field in an appropriate configuration, an atom trap can be created. Let us look at one of the configurations that is commonly used and first demonstrated by Raab *et al.* [1]. The setup consists of three pairs of counter propagating beams

[3]Based on the value of Γ and λ obtained from [161, 162]

and a pair of anti-Helmholtz coil. This setup is shown later in Sec. A.5 in Fig. A.3 and Fig. A.4 and in Chapter 3 in Fig. 3.2. Notice that the three pairs of beams are othogonal to one another. Following the explanation of the trap's machanism by Raab *et al.*[1], we consider a simple model where the atoms has spin $S = 0$ ($m_s = 0$) for the ground state and spin $S = 1$ ($m_s = -1, 0, +1$) for the excited state[4]. If we look only at one of the beam pair and the magnetic field along the beams, e.g. along the z-axis, we can see that the magnetic field in the middle of the anti-Helmholtz coils, at $z = 0$, is zero and changes roughly linearly up to a finite distance away from it (see Fig. A.6 and Fig. A.5). We can write $B = bz$, where b is a constant representing the gradient of the field. With this field, the energy levels of the atoms split apart linearly among different magnetic sublevels (m_s) according to the Zeeman shift, $\Delta E = \mu m_s B = \mu m_s bz$, as shown in Fig. A.2. For light frequency red detuned relative to the resonance frequency at $B = 0$, if we shine the beam with negative helicity (σ^- beam) from the right side and positive one (σ^+ beam) from the left side, the atoms in the $+z$ region will absorb σ^- beam more than the σ^+ beam. This is because the light frequency is closer to the transition from the ground to $m_s = -1$ level. The opposite is true for the atoms on the $-z$ region, i.e. the atoms will absorb the σ^+ beam more than the σ^- beam. Thus the atoms will experience a net force toward $z = 0$ where $B = 0$. The force due to $\sigma^{\pm}$-beams can be derived, similar to Eq. A.7, by substituting Δ with $\Delta - k_{\pm}v_z - \eta_{\pm}z$, where $k_{\pm} = \pm k$ and $\eta_{\pm} = \pm\eta = \pm\mu b/\hbar$, i.e.

$$\left\langle F_{sp}^{\sigma^{\pm}}(z, v_z)\right\rangle = \hbar k_{\pm}\ \Gamma\frac{s_0/2}{1 + s_0 + 4(\Delta - k_{\pm}v_z - \eta_{\pm}z)^2/\Gamma^2}. \tag{A.13}$$

For a small Doppler and Zeeman shift, the force can be approximated to the first order in v and z similar to Eq. A.11 as

$$\left\langle F_{sp}^{\sigma^{\pm}}(z, v_z)\right\rangle \approx \left\langle F_{sp}^{\pm}\right\rangle + \beta_{\pm}v_z + \kappa_{\pm}z, \tag{A.14}$$

where $\left\langle F_{sp}^{\pm}\right\rangle = \pm\left\langle F_{sp}^{trvl}\right\rangle$, $\beta_{\pm} = \beta$ and $\kappa_{\pm} = \beta\eta_{\pm}/k_{\pm} = \beta\eta/k = \kappa$. Thus the net

[4]This can be generalized to our case for the Rb atoms where we have $m_F = 0,\pm1,\pm2,\pm3$ for the excited state and $m_F = 0,\pm1,\pm2$ for the ground state. The spliting of the energy levels in the Zeeman regime can be seen in Fig.4 and Fig.6 in [161, 162]

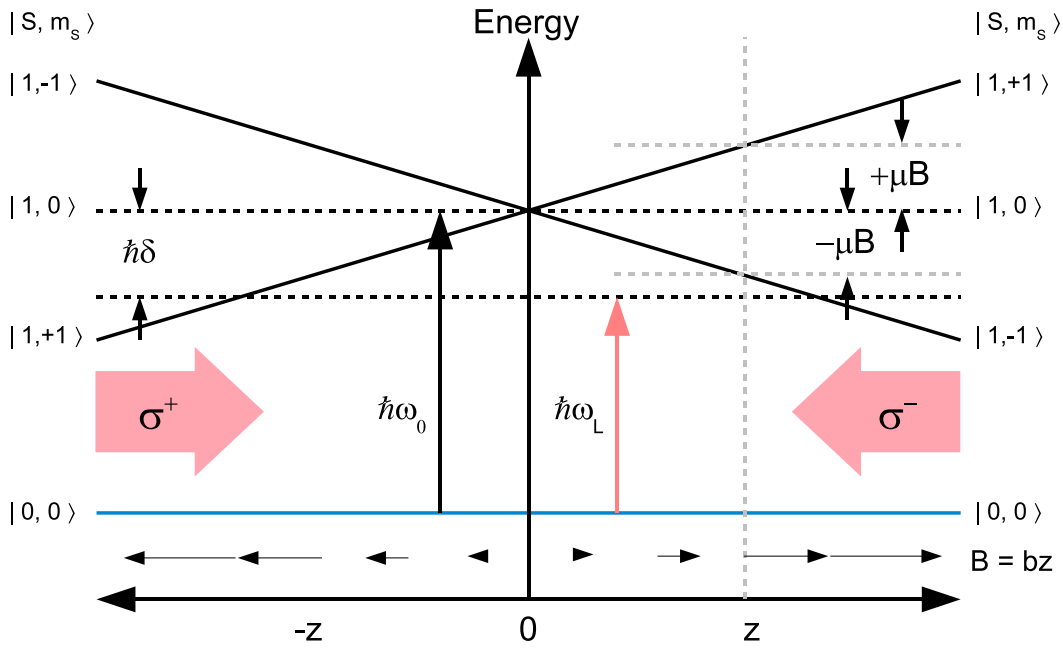

Figure A.2: The 1D model of the MOT shows the ground state energy-level of the atom with $S = 0$ and the Zeemann energy-level splitting among different magnetic sublevels, $m_s = -1$, 0 and 1 in the $S = 1$ excited state. The value of the magnetic field, B, is a linear function of the distance, z, which causes the energy-level splitting to be linear as shown. An $m = +1$ ($m = -1$) atom that travels to the left (right) absorbs the σ^+ (σ^-) light as described in the text. The light is detuned $\hbar\Delta$ below the $m_s = 0$ level. The value of Δ is the difference between the laser frequency (ω_L) and the resonance frequency (ω_0).

force due to both red detuned $\sigma^{\pm}$-beams will be

$$\left\langle F_{sp}^{\mathrm{MOT}}(z, v_z)\right\rangle \approx \left\langle F_{sp}^{\sigma^+}(z, v_z)\right\rangle + \left\langle F_{sp}^{\sigma^-}(z, v_z)\right\rangle = -2|\beta|v_z - 2|\kappa|z. \qquad \text{(A.15)}$$

The associated classical equation of motion is $m\ddot{z} + 2|\beta|\dot{z} + 2|\kappa|z = 0$, which is the same as the equation for a damped harmonic oscillator whose spring constant $K = 2|\kappa|$ and a constant of proportionality $C = 2|\beta|$. For our typical magnetic field gradient of 15 G/cm, $(C/2m)^2 - K/m > 0$ and our oscillator is overdamped [160].

A.5 Magneto-Optical Trap: Symmetry Consideration

In this section, I will only describe the aspect involving geometrical symmetry that helps to setup the MOT experimentally.

The basic setting of a MOT is done by using three sets of counter propagating beams, arranged so that they are mutually perpendicular to one another. The importance lies in the arrangement of the beams with respect to magnetic Helmholtz coils.

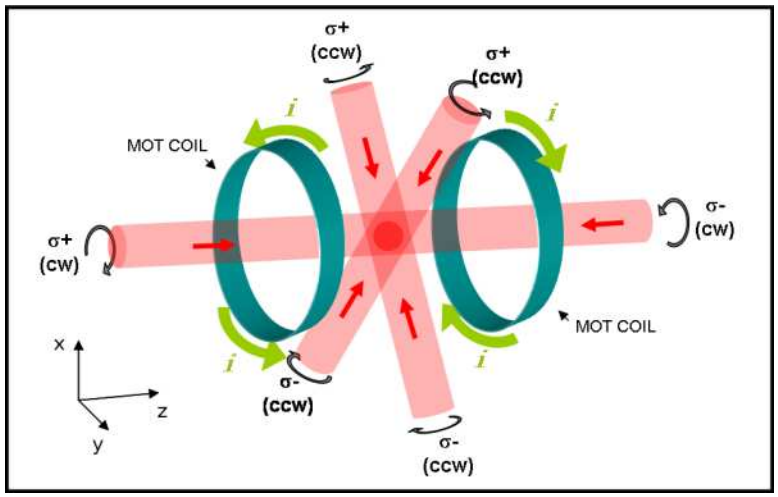

Figure A.3: Beam alignment, configuration one, for the MOT setup. The six red beams represent the main laser beams used to trap atoms in the MOT. The small black circular arrows shows sense of rotation or helicity of a beam with circular polarization with respect to the beam's direction of propagation represented by the red arrows. The σ^+ and σ^- represents the helicity of the laser beam as felt by the atoms. The big green circles represent the Helmholtz coils. The directions of current runs in the coils are represented by the green arrows. The atoms are trapped in the overlapping region of all six laser beams.

The Helmholtz coils, as shown in Fig. A.3 and Fig. A.4, consists of a pair of coaxial electrical conducting wire loops. The current in the loops flows in opposite directions with respect to one another (green arrows). Thus, looking toward the loop pair along the cylindrical axis, which will be denoted as the z-axis, from either

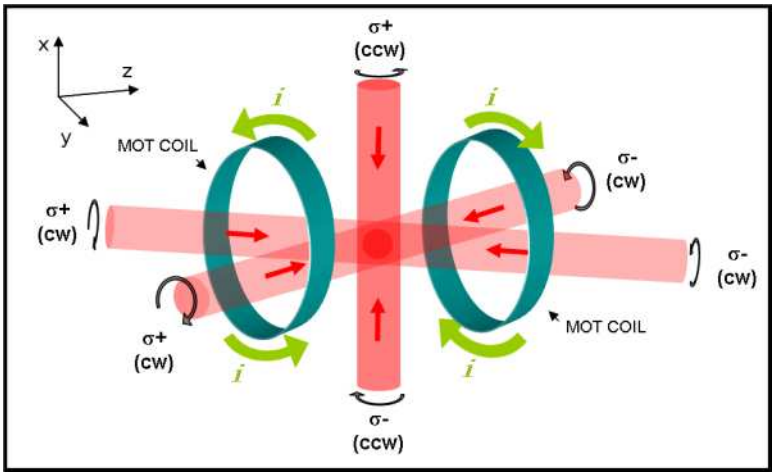

Figure A.4: Beam alignment, configuration two, for the MOT setup. The alignment of the two trap beams in the horizontal plane exploits the symmetry around the cylindrical axis as described in the text. All the labels are the same as described in Fig. A.3 above.

side gives the same picture. As a result, the magnetic field produced from this loop pair can have two symmetries: (1) the circular symmetry around the z-axis, and (2) the symmetry about a plane perpendicular to the z-axis in the middle between the loop pair. If we bisect the loop pair with a plane along this z-axis, we will have a field configuration as shown in Fig. A.5. Another bisection along the z-axis and perpendicular to the previous plane will give the same configuration because of the circular symmetry. The plots of the strength of the field and its gradients are shown in Fig. A.6. Note that the field shown in the figures is based on a premise that the distance between the loop pair is smaller than the diameter of the loops so that the change in the magnetic field is approximately linear near the center of the loop pair (see the right column of Fig. A.6).

Now, since we know the field configuration, arranging the trapping beams will be straight forward. Based on the two distinct symmetries mention earlier, we can have two configurations that we can exploit to trap atoms. We have already seen these two possible arrangements in Fig. A.3 and Fig. A.4. They are also experimentally verified to be able to trap atoms.

For a typical configuration in Fig. A.3, the π-rotational symmetry of the field in Fig. A.5 (around an axis pointing out toward the reader at the center of the figure), dictates that the beams that enter from $\pm z$ need to have the same polarization. All four beams that enter through $\pm x$ (or $\pm y$) (on a plane perpendicular to the z-axis) need to have the same polarization by circular symmetry. However, the beams will have to have different polarization from the beam that enter through $\pm z$ since the directions of the magnetic field are opposite. To be more specific on the polarization of the beam, according to Fig. A.3, the beam enter through the $-z$ should be σ^+ and the beam enter through $+z$ should be σ^-. These plus and minus sign on the σ indicates the sense of rotation of the polarization or helicity as felt by the atoms. The helicity with respect to the beam's direction of propagation, however, is the same. Note that the polarization of the beam traveling along the z-axis should have the same helicity as that of the electric current flow in the loop that it first enters as indicates by the thick green arrows in Fig. A.3. The same argument can be applied to the rest of the beams that enter through the x- and y-axis.

Similar to the configuration in Fig. A.3, a non-typical configuration in Fig. A.4 needs all four beams that enter the circular faces of the loop pair to have the same helicity. A different helicity is needed for the rest of the beams that enter the side of the loop pair. The trap from this configuration is much weaker than the previous one because the beams that enter through the circular face of the loop make and angle with the magnetic field lines. To improve the trap strength, the polarization of the beams needs to be adjusted. It is experimentally verified that the trap strength is improved when the polarization of the beams is elliptical and the degree of ellipticity depends on the angle that the beams make with the z-axis. Another drawback of this configuration is that there can be a geometrical constraint on the angle between the beam pairs that enter the circular faces of the loop, depending on the size of and distance between the loops. Despite all the disvantages, this configuration exploit the space on the circular faces efficiently. It can be useful when more space on the side between the loop pair is needed.

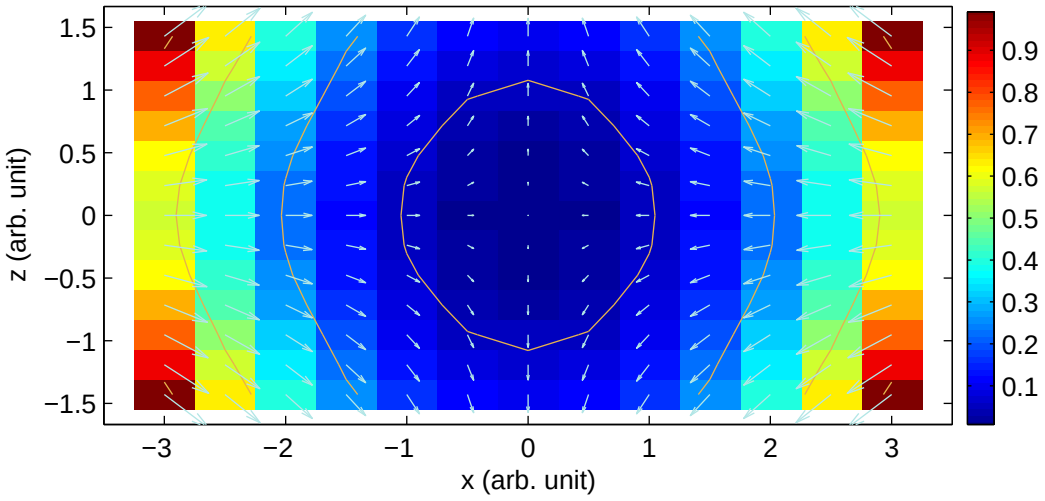

Figure A.5: Magnetic field between a pair of the MOT coils in an anti-Helmholtz configuration presented in 2D on an xz-plane. The z-axis is the axis along the anti-Helmholtz coil pair (cylindrical symmetry axis). The solid lines represent the contour of equal field value.

A.6 Electronic Structure of Rubidium Atom

In the previous section, we consider a simple two-level atom model. The real atom however has multiple levels as is shown in Fig. A.7 and Fig. A.8. These levels are results of several energy splittings. In the diagrams we see the fine structure energy spliting [163] that results from spin-orbit coupling. The excited level, $5^2P_{1/2}$ and $5^2P_{3/2}$ are results from $S = 1/2$ and $L = 1$. Light emitted from these two excited levels and the ground constitutes the so called D2 lines. Typically, we choose one of the D2 lines that corresponds to the transition between $5^2S_{1/2}$ and $5^2P_{3/2}$ in trapping and cooling atoms. The second splitting is called the hyperfine splitting [163], due to the coupling between a nuclear spin (I) and the total angular momentum (J). The nuclear spins of ^{85}Rb and ^{87}Rb are 5/2 and 3/2 respectively. The coupling between I and J further splits the fine structure into even finer structures, denoted by F in the diagrams.

For ^{87}Rb, we exploit the transition $F = 2 \rightarrow F' = 3$ to trap and cool atoms,

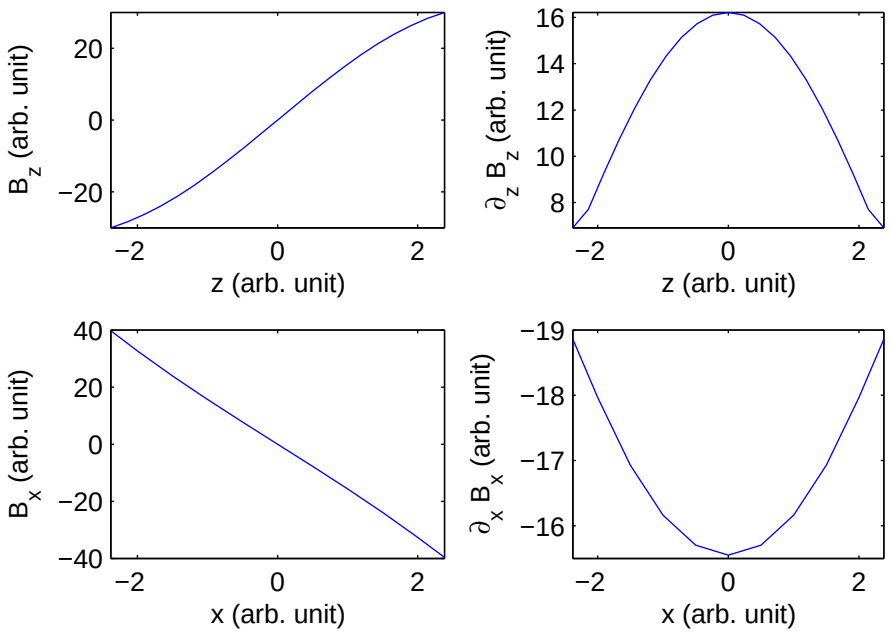

Figure A.6: One dimensional plot of the value of magnetic field (left column) and its gradient (right column) as shown in Fig. A.5. The top row shows the values along the z-axis at $x = 0$ whereas the bottom row shows the values along the x-axis at $z = 0$.

where the prime in F' indicates the excited state. However, there is a significant probability for the electron to be excited from the ground level $F = 2$ into $F' = 2$ and decay into $F = 1$ level. Thus light responsible for the transition $F = 1 \rightarrow F' = 2$ is required to pump the population back to the main trapping transition. The trapping and repumping transition is shown in Fig. A.8 as red and orange arrows respectively. In the case of ^{85}Rb, similar arguments apply. We exploit $F = 3 \rightarrow F' = 4$ for the trapping and $F = 2 \rightarrow F' = 3$ for the repumping atoms as shown in Fig. A.7.

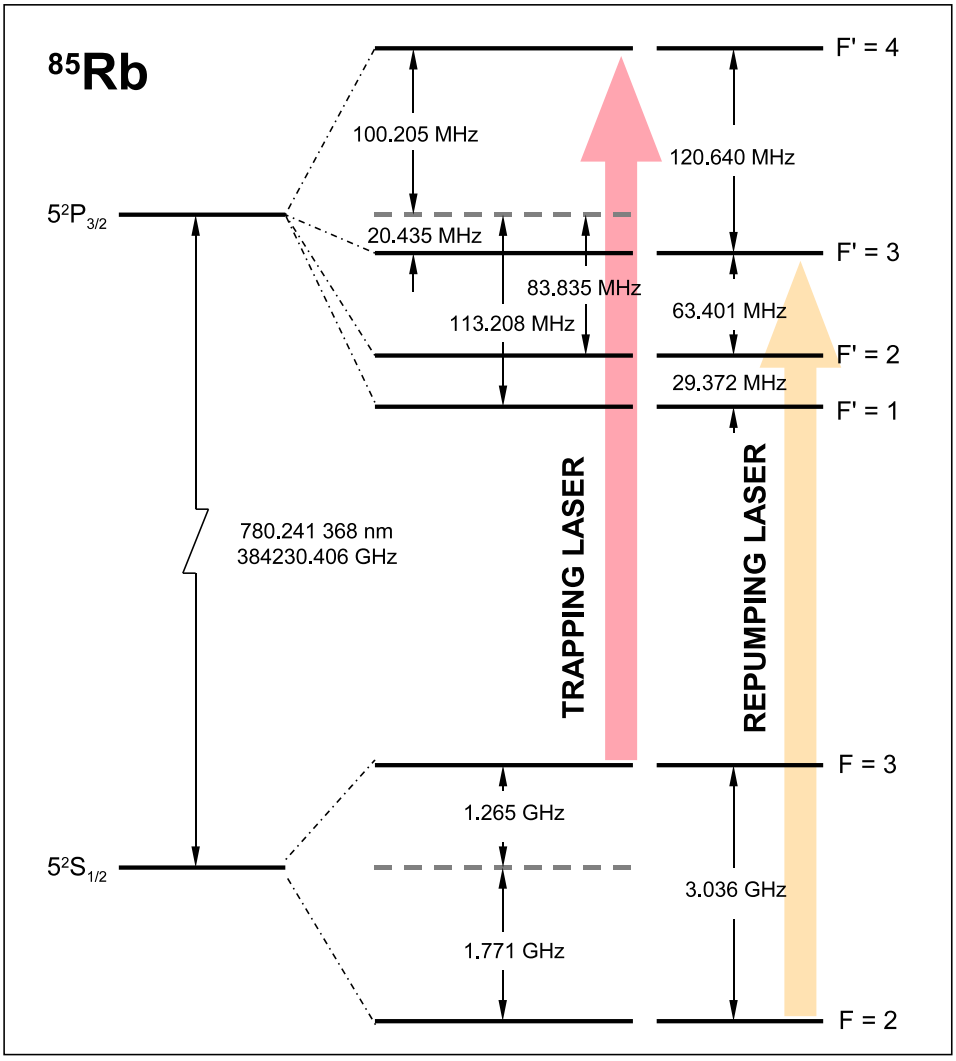

Figure A.7: Energy-level diagram of Rb^{85} (D2 lines). The hyperfine levels are distinguished by the value of the total angular momentum F, which is the vector sum of the electron's total angular momentum ($J = 1/2$ and $3/2$) and the nuclear spin ($I = 5/2$). The trapping and repumping transition are labeled with big red and orange arrows respectively. Adopted from Ref. [161].

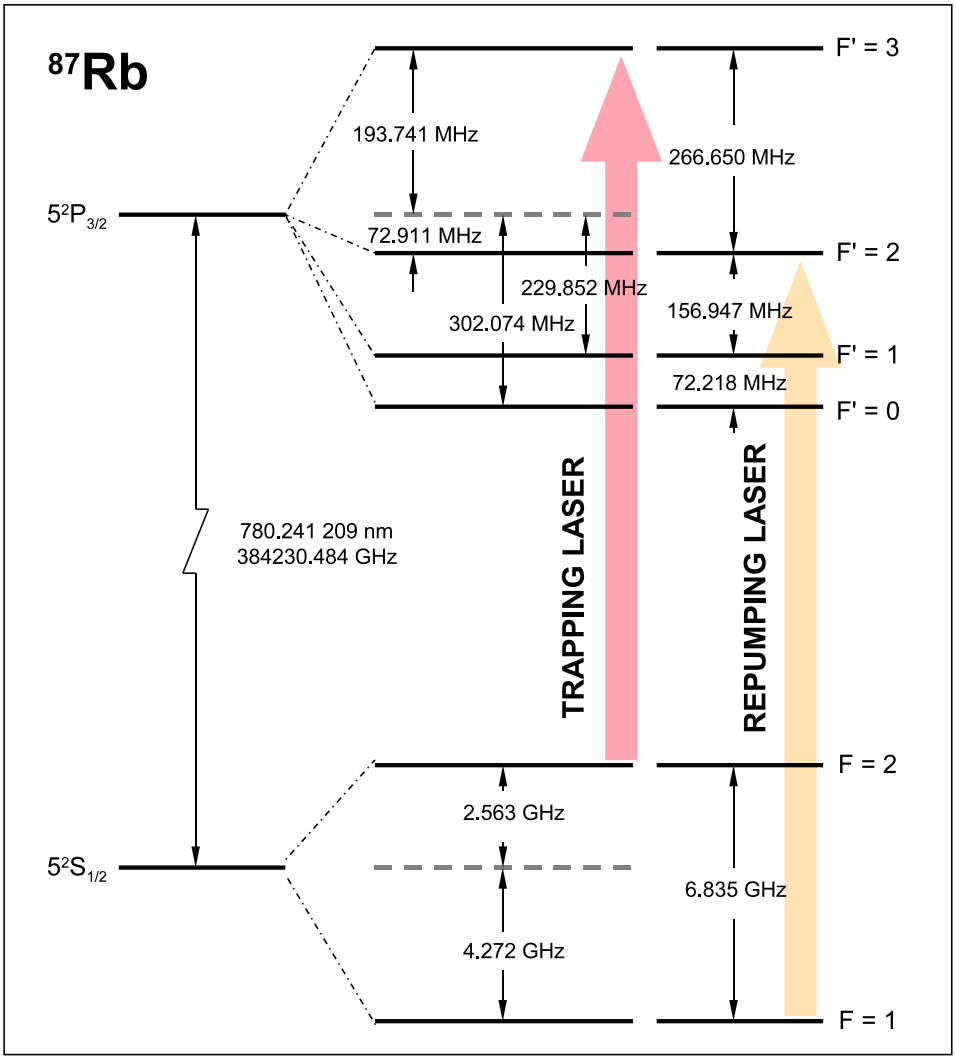

Figure A.8: Energy-level diagram of Rb^{87} (D2 lines). The hyperfine levels are distinguished by the value of the total angular momentum F, which is the vector sum of the electron's total angular momentum ($J = 1/2$ and $3/2$) and the nuclear spin ($I = 3/2$). The trapping and repumping transition are labeled with big red and orange arrows respectively. Adopted from Ref. [162].

Appendix B

Scattering and Dipole Forces: Density Matrix Approach

In this Appendix, the derivations of scattering and dipole forces are written out explicitly using the density matrix approach. These derivations are adapted from Ref.[163, 119, 164, 87].

B.1 Time-Dependent Potentials and the Interaction Picture

We start by writting the time-dependent Schrödinger equation for an atom evolving under the total Hamiltonian, $H = H_0 + V(t)$, i.e.,

$$H \,|\, \alpha, t_0; t \,\rangle_S = i\hbar \frac{\partial}{\partial t} \,|\, \alpha, t_0; t \,\rangle_S \,, \tag{B.1}$$

where H_0 is the time-independent Hamiltonian, $V(t)$ the time-dependent potential, and the subscript S denotes that the ket is in Schrödinger's picture.

It is more convenient to look at Eq. B.1 in the interaction picture by defining

$$|\, \alpha, t_0; t \,\rangle_I = T_I^\dagger \,|\, \alpha, t_0; t \,\rangle_S \,, \tag{B.2}$$

$$A_I = T_I^\dagger A_S T_I, \tag{B.3}$$

where the time operator $T_I(t) = \exp(-iH_0 t/\hbar)$, A denotes an observable, and the subscript I denotes the interaction picture. Combining Eq. B.1 with Eq. B.2 and Eq. B.3, the time derivative of $|\, \alpha, t_0; t \,\rangle_I$ can be shown to be

$$\frac{\partial}{\partial t} \,|\, \alpha, t_0; t \,\rangle_I = -\frac{1}{i\hbar}\, T_I^\dagger H_0 \,|\, \alpha, t_0; t \,\rangle_S + \frac{1}{i\hbar}\, T_I^\dagger \,(H_0 + V_S) \,|\, \alpha, t_0; t \,\rangle_S \,, \tag{B.4}$$

$$= \frac{1}{i\hbar}\, V_I \,|\, \alpha, t_0; t \,\rangle_I \,. \tag{B.5}$$

If we decompose $|\, \alpha, t_0; t \,\rangle_I$ in terms of $|\, n \,\rangle$ as

$$|\, \alpha, t_0; t \,\rangle_I = \sum_n c_n(t) \,|\, n \,\rangle \,, \tag{B.6}$$

where $|\, n \,\rangle$ is the eigenket of H_0, i.e. $H_0 \,|\, n \,\rangle = E_n \,|\, n \,\rangle$, we have

$$c_n(t) = \langle\, n \,|\, \alpha, t_0; t \,\rangle_I \,, \tag{B.7}$$

the probability amplitude to find $|\, \alpha, t_0; t \,\rangle_I$ to be in $|\, n \,\rangle$. Multiplying both sides of Eq. B.5 with $\langle\, n \,|$ from the left, we will have

$$\frac{\partial}{\partial t} \langle\, n \,|\, \alpha, t_0; t \,\rangle_I = \frac{1}{i\hbar} \sum_m \langle\, n \,|\, V_I \,|\, m \,\rangle \langle\, m \,|\, \alpha, t_0; t \,\rangle_I \,, \tag{B.8}$$

$$\frac{\partial}{\partial t} c_n(t) = \frac{1}{i\hbar} \sum_m \langle\, n \,|\, V_I \,|\, m \,\rangle \, c_m(t). \tag{B.9}$$

B.2 Time-Dependent Potential: Oscillating Field

For an oscillating field $\mathbf{E} = \hat{\epsilon} E_0 \cos(\omega_l t)$, $V_S = -e\mathbf{E} \cdot \mathbf{r}$. The expression of $\langle\, n \,|\, V_I \,|\, m \,\rangle$ in Eq. B.9 can be written as

$$\langle\, n \,|\, V_I \,|\, m \,\rangle = \langle\, n \,|\, T_I^\dagger V_S T_I \,|\, m \,\rangle \,, \tag{B.10}$$

$$= -eE_0 \cos(\omega_l t) \; \hat{\epsilon} \cdot \langle\, n \,|\, T_I^\dagger \; \mathbf{r} \; T_I \,|\, m \,\rangle \,, \tag{B.11}$$

$$= -\frac{eE_0}{2} \left(e^{-i\omega_l t} + e^{i\omega_l t} \right) \hat{\epsilon} \cdot \langle\, n \,|\, T_I^\dagger \; \mathbf{r} \; T_I \,|\, m \,\rangle \,, \tag{B.12}$$

$$= -\frac{eE_0}{2} \left(e^{-i(\omega_l - \omega_{nm})t} + e^{i(\omega_l + \omega_{nm})t} \right) \hat{\epsilon} \cdot \langle\, n \,|\, \mathbf{r} \,|\, m \,\rangle \,. \tag{B.13}$$

where $\omega_{nm} = (E_n - E_m)/\hbar$ and in Eq. B.11 we pull out E_0 from the braket assuming that the electric field varies much slower spatially than that of the eigenstates. The rotating wave approximation is done upon neglecting the term with $\omega_l + \omega_{eg}$ and keeping the term with $\omega_l - \omega_{eg}$ where g and e donote the ground and the excited states respectively. Thus, for a two-level system, Eq. B.13 above gives

$$\langle\, g \,|\, V_I \,|\, g \,\rangle = 0, \tag{B.14}$$

$$\langle\, e \,|\, V_I \,|\, e \,\rangle = 0, \tag{B.15}$$

$$\langle\, g \,|\, V_I \,|\, e \,\rangle = \frac{\hbar}{2} \Omega e^{+i\Delta t}, \tag{B.16}$$

$$\langle\, e \,|\, V_I \,|\, g \,\rangle = \frac{\hbar}{2} \Omega^* e^{-i\Delta t}. \tag{B.17}$$

where $\Delta = \omega_l - \omega_{eg}$ and the Rabi frequency

$$\Omega = -\frac{eE_0}{\hbar} \hat{\epsilon} \cdot \langle\, g \,|\, \mathbf{r} \,|\, e \,\rangle \,. \tag{B.18}$$

Thus the two-level model of Eq. B.9 can be written as

$$i\hbar\frac{\partial}{\partial t}c_g(t) = \frac{\hbar}{2}c_e(t)\Omega e^{i\Delta t}, \tag{B.19}$$

$$i\hbar\frac{\partial}{\partial t}c_e(t) = \frac{\hbar}{2}c_g(t)\Omega^* e^{-i\Delta t}. \tag{B.20}$$

Multiplying both equations by $i\hbar\,\partial/\partial t$ gives

$$-\hbar^2\frac{\partial^2}{\partial t^2}c_g(t) = i\frac{\hbar^2}{2}\Omega\ \frac{\partial}{\partial t}c_e(t)e^{i\Delta t} + i\frac{\hbar^2}{2}\Omega\ c_e(t)\ i\Delta\ e^{i\Delta t}, \tag{B.21}$$

$$-\hbar^2\frac{\partial^2}{\partial t^2}c_e(t) = i\frac{\hbar^2}{2}\Omega^*\ \frac{\partial}{\partial t}c_g(t)e^{-i\Delta t} - i\frac{\hbar^2}{2}\Omega^*\ c_g(t)\ i\Delta\ e^{-i\Delta t}. \tag{B.22}$$

Substituting Eq. B.19 and Eq. B.20 in Eq. B.21 and Eq. B.22, we will have

$$\frac{\partial^2}{\partial t^2}c_g(t) - i\Delta\frac{\partial}{\partial t}c_g(t) + \frac{\Omega^2}{4}c_g(t) = 0, \tag{B.23}$$

$$\frac{\partial^2}{\partial t^2}c_e(t) + i\Delta\frac{\partial}{\partial t}c_e(t) + \frac{\Omega^2}{4}c_e(t) = 0. \tag{B.24}$$

B.3 Density Matrix and Light Forces

Previously we described the state of the system through $|\,\alpha, t_0; t\,\rangle$. The correlation among eigenkets can be described through the coherence $\rho_{nm} = c_n c_m^*$, which is also the interference term that we would get when we interfere the state ket with itself. In the system where the spontaneous emission takes place, the coherence suffers the exponential loss. Thus to describe this system, we define a new entity called the "density matrix" that contains the coherence terms explicitly (instead of using $|\,\alpha, t_0; t\,\rangle$ as before), i.e. $\rho = |\,\alpha, t_0; t\,\rangle\langle\,\alpha, t_0; t\,|$. Therefore the element $\rho_{nm} = \langle\, n\,|\,\rho\,|\, m\,\rangle = c_n c_m^*$. With the use of the Schrödinger equation, the evolution of ρ can be written as shown below.

$$\frac{d\rho}{dt} = \frac{d}{dt}\left(|\,\alpha\,\rangle\langle\,\alpha\,|\right) = \left(\frac{d}{dt}|\,\alpha\,\rangle\right)\langle\,\alpha\,| + |\,\alpha\,\rangle\left(\frac{d}{dt}\langle\,\alpha\,|\right) \tag{B.25}$$

$$= -\frac{iH}{\hbar}|\,\alpha\,\rangle\langle\,\alpha\,| + |\,\alpha\,\rangle\frac{i}{\hbar}\langle\,\alpha\,|H \tag{B.26}$$

$$= -\frac{i}{\hbar}(H\rho - \rho H) = -\frac{i}{\hbar}\,[\,H, \rho\,] = -\frac{1}{i\hbar}\,[\,\rho, H\,] \tag{B.27}$$

For the two-level atom, ρ can be written as

$$\rho = \begin{pmatrix}\rho_{gg} & \rho_{ge}\\ \rho_{eg} & \rho_{ee}\end{pmatrix} = \begin{pmatrix}c_g c_g^* & c_g c_e^*\\ c_e c_g^* & c_e c_e^*\end{pmatrix}. \tag{B.28}$$

Using Eq. B.19 and Eq. B.20, the evolution of each element of ρ can be written, to what is known as the optical Bloch equation (OBE), as shown below.

$$\begin{aligned}
\frac{d\rho_{gg}}{dt} &= \frac{dc_g}{dt}c_g^* + c_g\frac{dc_g^*}{dt} = -\frac{i}{2}c_e\Omega e^{i\Delta t}c_g^* + c_g\frac{i}{2}c_e^*\Omega^* e^{-i\Delta t} && \text{(B.29)}\\
&= -\frac{i}{2}\Omega\rho_{eg}e^{i\Delta t} + \frac{i}{2}\Omega^*\rho_{ge}e^{-i\Delta t} && \text{(B.30)}\\
\frac{d\rho_{ge}}{dt} &= \frac{dc_g}{dt}c_e^* + c_g\frac{dc_e^*}{dt} = -\frac{i}{2}c_e\Omega e^{i\Delta t}c_e^* + c_g\frac{i}{2}c_g^*\Omega e^{i\Delta t} && \text{(B.31)}\\
&= -\frac{i}{2}\Omega\rho_{ee}e^{i\Delta t} + \frac{i}{2}\Omega\rho_{gg}e^{i\Delta t} && \text{(B.32)}\\
\frac{d\rho_{eg}}{dt} &= \frac{dc_e}{dt}c_g^* + c_e\frac{dc_g^*}{dt} = -\frac{i}{2}c_g\Omega^* e^{-i\Delta t}c_g^* + c_e\frac{i}{2}c_e^*\Omega^* e^{-i\Delta t} && \text{(B.33)}\\
&= -\frac{i}{2}\Omega^*\rho_{gg}e^{-i\Delta t} + \frac{i}{2}\Omega^*\rho_{ee}e^{-i\Delta t} && \text{(B.34)}\\
\frac{d\rho_{ee}}{dt} &= \frac{dc_e}{dt}c_e^* + c_e\frac{dc_e^*}{dt} = -\frac{i}{2}c_g\Omega^* e^{-i\Delta t}c_e^* + c_e\frac{i}{2}c_g^*\Omega e^{i\Delta t} && \text{(B.35)}\\
&= -\frac{i}{2}\Omega^*\rho_{ge}e^{-i\Delta t} + \frac{i}{2}\Omega\rho_{eg}e^{i\Delta t}. && \text{(B.36)}
\end{aligned}$$

Note that Eq. B.30, Eq. B.32, Eq. B.34 and Eq. B.36 can also be derived directly from Eq. B.27, i.e.,

$$\begin{aligned}
\frac{d\rho}{dt} &= -\frac{1}{i\hbar}\left[\,\rho, H\,\right]\\
&= \frac{i}{\hbar}\begin{pmatrix}\rho_{gg} & \rho_{ge}\\ \rho_{eg} & \rho_{ee}\end{pmatrix}\frac{\hbar}{2}\begin{pmatrix}0 & \Omega e^{i\Delta t}\\ \Omega^* e^{-i\Delta t} & 0\end{pmatrix} - \frac{\hbar}{2}\begin{pmatrix}0 & \Omega e^{i\Delta t}\\ \Omega^* e^{-i\Delta t} & 0\end{pmatrix}\frac{i}{\hbar}\begin{pmatrix}\rho_{gg} & \rho_{ge}\\ \rho_{eg} & \rho_{ee}\end{pmatrix}\\
&= \frac{i}{2}\left[\begin{pmatrix}\rho_{ge}\Omega^* e^{-i\Delta t} - \rho_{eg}\Omega e^{i\Delta t} & \rho_{gg}\Omega e^{i\Delta t} - \rho_{ee}\Omega e^{i\Delta t}\\ \rho_{ee}\Omega^* e^{-i\Delta t} - \rho_{gg}\Omega^* e^{-i\Delta t} & \rho_{eg}\Omega e^{i\Delta t} - \rho_{ge}\Omega^* e^{-i\Delta t}\end{pmatrix}\right]. && \text{(B.37)}
\end{aligned}$$

To include the effect due to the spontaneous emission, we note that the population of the ground and the excited state decay at a rate $+\Gamma\rho_{ee}$ and $-\Gamma\rho_{ee}$ respectively, i.e.

$$\left(\frac{d\rho_{gg}}{dt}\right)_{\text{sp}} = +\Gamma\rho_{ee} \qquad \text{(B.38)}$$

$$\left(\frac{d\rho_{ee}}{dt}\right)_{\text{sp}} = -\Gamma\rho_{ee} \qquad \text{(B.39)}$$

where Γ is the decay rate of a single excited state whose lifetime $\tau \equiv 1/\Gamma$. We note also that the coherences ρ_{ge} and ρ_{eg} decay exponentially at rates $-\Gamma\rho_{ge}/2$ and

$-\Gamma\rho_{eg}/2$ respectively, i.e.

$$\left(\frac{d\rho_{ge}}{dt}\right)_{\rm sp} = -\frac{\Gamma}{2}\rho_{ge} \tag{B.40}$$

$$\left(\frac{d\rho_{eg}}{dt}\right)_{\rm sp} = -\frac{\Gamma}{2}\rho_{eg} \tag{B.41}$$

Combining Eq. B.30,Eq. B.32,Eq. B.34 and Eq. B.36 with Eq. B.38,Eq. B.39,Eq. B.40 and Eq. B.41, we will have

$$\frac{d\rho_{gg}}{dt} = +\Gamma\rho_{ee} + \frac{i}{2}\left(\Omega^*\rho_{ge}e^{-i\Delta t} - \Omega\ \rho_{eg}e^{+i\Delta t}\right) \tag{B.42}$$

$$\frac{d\rho_{ee}}{dt} = -\Gamma\rho_{ee} + \frac{i}{2}\left(\Omega\ \rho_{eg}e^{+i\Delta t} - \Omega^*\rho_{ge}e^{-i\Delta t}\right) \tag{B.43}$$

$$\frac{d\rho_{ge}}{dt} = -\frac{\Gamma}{2}\rho_{ge} + \frac{i}{2}\Omega\ \left(\rho_{gg} - \rho_{ee}\right)e^{+i\Delta t} \tag{B.44}$$

$$\frac{d\rho_{eg}}{dt} = -\frac{\Gamma}{2}\rho_{eg} + \frac{i}{2}\Omega^*\left(\rho_{ee} - \rho_{gg}\right)e^{-i\Delta t}. \tag{B.45}$$

If we define $\tilde{\rho}_{ge} = \rho_{ge}e^{-i\Delta t}$ and $\tilde{\rho}_{eg} = \rho_{eg}e^{+i\Delta t}$, we will have that

$$\frac{d\tilde{\rho}_{ge}}{dt} = \frac{d\rho_{ge}}{dt}e^{-i\Delta t} - i\Delta\rho_{ge}e^{-i\Delta t} = \frac{d\rho_{ge}}{dt}e^{-i\Delta t} - i\Delta\tilde{\rho}_{ge} \tag{B.46}$$

$$\frac{d\tilde{\rho}_{eg}}{dt} = \frac{d\rho_{eg}}{dt}e^{+i\Delta t} + i\Delta\rho_{eg}e^{+i\Delta t} = \frac{d\rho_{eg}}{dt}e^{+i\Delta t} + i\Delta\tilde{\rho}_{eg}. \tag{B.47}$$

Thus Eq. B.42, Eq. B.43, Eq. B.44 and Eq. B.45 can be rewritten as

$$\frac{d\rho_{gg}}{dt} = +\Gamma\rho_{ee} + \frac{i}{2}\left(\Omega^*\tilde{\rho}_{ge} - \Omega\ \tilde{\rho}_{eg}\right) \tag{B.48}$$

$$\frac{d\rho_{ee}}{dt} = -\Gamma\rho_{ee} + \frac{i}{2}\left(\Omega\ \tilde{\rho}_{eg} - \Omega^*\tilde{\rho}_{ge}\right) \tag{B.49}$$

$$\frac{d\tilde{\rho}_{ge}}{dt} = -\left(\frac{\Gamma}{2} + i\Delta\right)\tilde{\rho}_{ge} + \frac{i}{2}\Omega\ \left(\rho_{gg} - \rho_{ee}\right) \tag{B.50}$$

$$\frac{d\tilde{\rho}_{eg}}{dt} = -\left(\frac{\Gamma}{2} - i\Delta\right)\tilde{\rho}_{eg} + \frac{i}{2}\Omega^*\left(\rho_{ee} - \rho_{gg}\right). \tag{B.51}$$

In steady state, the terms on the left hand side of Eq. B.48, Eq. B.49, Eq. B.50 and Eq. B.51 are zero. The steady state solution can be obtained from the following procedures.

$$\frac{dw}{dt} \equiv \frac{d\rho_{gg}}{dt} - \frac{d\rho_{ee}}{dt} = 2\Gamma\rho_{ee} + i\left(\Omega^*\tilde{\rho}_{ge} - \Omega\ \tilde{\rho}_{eg}\right) \tag{B.52}$$

$$0 = 2\Gamma\rho_{ee} + i\left(\Omega^*\tilde{\rho}_{ge} - \Omega\ \tilde{\rho}_{eg}\right) \tag{B.53}$$

$$0 = \Gamma - \Gamma w + i\left(\Omega^*\tilde{\rho}_{ge} - \Omega\ \tilde{\rho}_{eg}\right), \tag{B.54}$$

where we have used $w = \rho_{gg} - \rho_{ee}$ and $\rho_{gg} + \rho_{ee} = 1$, i.e., $2\rho_{ee} = 1 - w$. Moreover from Eq. B.51 we have

$$\frac{d\tilde{\rho}_{eg}}{dt} = -\left(\frac{\Gamma}{2} - i\Delta\right)\tilde{\rho}_{eg} + \frac{i}{2}\Omega^*\left(\rho_{ee} - \rho_{gg}\right) \tag{B.55}$$

$$0 = -\left(\frac{\Gamma}{2} - i\Delta\right)\tilde{\rho}_{eg} - \frac{i}{2}\Omega^* w \tag{B.56}$$

$$\tilde{\rho}_{eg} = -\frac{iw\Omega^*}{\Gamma - i2\Delta} \tag{B.57}$$

$$\tilde{\rho}_{ge} = +\frac{iw\Omega}{\Gamma + i2\Delta}\,, \tag{B.58}$$

where in the last step we have used $\tilde{\rho}_{ge} = \tilde{\rho}^*_{eg}$ (It can also be obtained directly from Eq. B.50). Substituting Eq. B.57 and Eq. B.58 in Eq. B.54 we will have

$$0 = \Gamma - \Gamma w + i\Omega^*\left(\frac{+iw\Omega}{\Gamma + i2\Delta}\right) - i\Omega\,\left(\frac{-iw\Omega^*}{\Gamma - i2\Delta}\right), \tag{B.59}$$

$$0 = \Gamma - \left(\Gamma + \frac{|\Omega|^2}{\Gamma + i2\Delta} + \frac{|\Omega|^2}{\Gamma - i2\Delta}\right)w, \tag{B.60}$$

$$w = \Gamma \Bigg/ \left(\Gamma + \frac{|\Omega|^2}{\Gamma + i2\Delta} + \frac{|\Omega|^2}{\Gamma - i2\Delta}\right), \tag{B.61}$$

$$w = \Gamma \Bigg/ \left[\Gamma + \frac{2\Gamma|\Omega|^2}{(\Gamma + i2\Delta)(\Gamma - i2\Delta)}\right], \tag{B.62}$$

$$w = 1 \Bigg/ \left(1 + \frac{2|\Omega|^2}{\Gamma^2 + 4\Delta^2}\right), \tag{B.63}$$

$$w = \frac{1}{1+s}, \tag{B.64}$$

and therefore

$$\rho_{ee} \equiv \frac{1-w}{2} = \frac{1}{2}\left(1 - \frac{1}{1+s}\right) = \frac{s}{2(1+s)}, \tag{B.65}$$

where

$$s = 2|\Omega|^2/(\Gamma^2 + 4\Delta^2) \tag{B.66}$$

$$= s_0/[1 + 4(\Delta/\Gamma)^2], \tag{B.67}$$

$$s_0 \equiv 2|\Omega|^2/\Gamma^2 \equiv I/I_s, \tag{B.68}$$

$$\text{and} \quad I_s \equiv \pi hc/3\lambda^3\tau \tag{B.69}$$

The parameter I_s is called the saturation intensity. From the definition just men-

tioned, ρ_{ee} can also be rewritten, in terms of s_0, as

$$\rho_{ee} = \frac{s/2}{(1+s)} = \frac{s_0/2[1+4(\Delta/\Gamma)^2]}{1+s_0/[1+4(\Delta/\Gamma)^2]} \tag{B.70}$$

$$= \frac{s_0/2}{1+s_0+4(\Delta/\Gamma)^2}. \tag{B.71}$$

The elements of the density matrix, ρ, obtained from steady state of the OBE can be used to obtain the optical force from the Ehrenfest theorem,

$$\frac{d^2}{dt^2}\langle \mathbf{x} \rangle = -\frac{1}{m}\ \langle \nabla V(\mathbf{x}) \rangle\,, \tag{B.72}$$

and the fact that $\langle A \rangle = Tr(\rho A)$. Thus, we will have for the two-level atom,

$$\langle F \rangle = -\langle \nabla V(\mathbf{x}) \rangle = -Tr(\rho\ \nabla V(\mathbf{x})) \tag{B.73}$$

$$= -Tr\left[\begin{pmatrix} \rho_{gg} & \rho_{ge} \\ \rho_{eg} & \rho_{ee} \end{pmatrix} \frac{\hbar}{2} \begin{pmatrix} 0 & \nabla\Omega e^{i\Delta t} \\ \nabla\Omega^* e^{-i\Delta t} & 0 \end{pmatrix} \right] \tag{B.74}$$

$$= -\frac{\hbar}{2}\left(\rho_{ge}\nabla\Omega^* e^{-i\Delta t} + \rho_{eg}\nabla\Omega e^{i\Delta t}\right) \tag{B.75}$$

$$= -\frac{\hbar}{2}\left(\tilde{\rho}_{ge}\nabla\Omega^* + \tilde{\rho}_{eg}\nabla\Omega\right) \tag{B.76}$$

For a wave with a spatial phase, we have $\mathbf{E} = \hat{\epsilon}E_0\cos[\omega_l t + \Phi(\mathbf{x})]$, thus the Rabi frequency Ω in Eq. B.18 need to be changed to $\tilde{\Omega} = \Omega e^{i\Phi}$ (i.e., after the rotating wave approximation we keep the term $\Delta = \omega_l - \omega_{eg}$). Consequently, we will have

$$\nabla\tilde{\Omega} = e^{+i\Phi}\nabla\Omega + i\Omega e^{+i\Phi}\nabla\Phi \tag{B.77}$$

$$= \left(\frac{\nabla\Omega}{\Omega} + i\nabla\Phi\right)\tilde{\Omega} \tag{B.78}$$

$$= (q_r + iq_i)\tilde{\Omega}, \tag{B.79}$$

where $q_r = \nabla\Omega/\Omega$ and $q_i = \nabla\Phi$. Therefore when we substitute $\Omega \to \tilde{\Omega}$ in Eq. B.76 we will have

$$\langle F \rangle = -\frac{\hbar}{2}\left(\tilde{\rho}_{ge}\nabla\tilde{\Omega}^* + \tilde{\rho}_{eg}\nabla\tilde{\Omega}\right) \tag{B.80}$$

$$= -\frac{\hbar}{2}\left[\tilde{\rho}_{ge}(q_r - iq_i)\tilde{\Omega}^* + \tilde{\rho}_{eg}(q_r + iq_i)\tilde{\Omega}\right] \tag{B.81}$$

$$= -\frac{\hbar}{2}\left(\tilde{\rho}_{ge}\tilde{\Omega}^* + \tilde{\rho}_{eg}\tilde{\Omega}\right)q_r + i\ \frac{\hbar}{2}\left(\tilde{\rho}_{ge}\tilde{\Omega}^* - \tilde{\rho}_{eg}\tilde{\Omega}\right)q_i \tag{B.82}$$

$$= \langle F_{dp} \rangle + \langle F_{sp} \rangle\,, \tag{B.83}$$

where

$$\boxed{\langle F_{dp}\rangle = -\frac{\hbar}{2}\left(\tilde{\rho}_{ge}\tilde{\Omega}^{*} + \tilde{\rho}_{eg}\tilde{\Omega}\right) q_r,} \tag{B.84}$$

and

$$\boxed{\langle F_{sp}\rangle = +i\,\frac{\hbar}{2}\left(\tilde{\rho}_{ge}\tilde{\Omega}^{*} - \tilde{\rho}_{eg}\tilde{\Omega}\right) q_i.} \tag{B.85}$$

Next we again substitute $\Omega \rightarrow \tilde{\Omega}$ in the expressions for $\tilde{\rho}_{eg}$ (Eq. B.57) and $\tilde{\rho}_{ge}$ (Eq. B.58). After that we substitute the results in Eq. B.84 and Eq. B.85. Thus the expression for $\langle F_{sp}\rangle$ and $\langle F_{dp}\rangle$ can be written as shown below, i.e.,

$$\begin{aligned}
\langle F_{sp}\rangle &= +i\frac{\hbar}{2}\left(\tilde{\rho}_{ge}\tilde{\Omega}^{*} - \tilde{\rho}_{eg}\tilde{\Omega}\right) q_i && \text{(B.86)}\\
&= +i\frac{\hbar}{2}\left(\frac{iw\tilde{\Omega}}{\Gamma + i2\Delta}\tilde{\Omega}^{*} - \frac{-iw\tilde{\Omega}^{*}}{\Gamma - i2\Delta}\tilde{\Omega}\right) q_i && \text{(B.87)}\\
&= +i\frac{\hbar}{2}\cdot iw|\tilde{\Omega}|^{2}\cdot\left(\frac{2\Gamma}{\Gamma^{2}+4\Delta^{2}}\right) q_i && \text{(B.88)}\\
&= -\frac{\hbar}{2}\cdot\Gamma q_i\left(\frac{s}{1+s}\right) = -\hbar\,\Gamma\nabla\Phi\rho_{ee}. && \text{(B.89)}
\end{aligned}$$

and

$$\begin{aligned}
\langle F_{dp}\rangle &= -\frac{\hbar}{2}\left(\tilde{\rho}_{ge}\tilde{\Omega}^{*} + \tilde{\rho}_{eg}\tilde{\Omega}\right) q_r && \text{(B.90)}\\
&= -\frac{\hbar}{2}\left(\frac{iw\tilde{\Omega}}{\Gamma + i2\Delta}\tilde{\Omega}^{*} + \frac{-iw\tilde{\Omega}^{*}}{\Gamma - i2\Delta}\tilde{\Omega}\right) q_r && \text{(B.91)}\\
&= -\frac{\hbar}{2}\cdot iw|\tilde{\Omega}|^{2}\cdot\left(\frac{-i4\Delta}{\Gamma^{2}+4\Delta^{2}}\right) q_r && \text{(B.92)}\\
&= -\frac{\hbar}{2}\cdot iw|\Omega|^{2}\cdot\left(\frac{-i4\Delta}{\Gamma^{2}+4\Delta^{2}}\right)\frac{\nabla\Omega}{\Omega} && \text{(B.93)}\\
&= -\frac{\hbar}{2}\cdot iw\cdot\left(\frac{-i4\Delta}{\Gamma^{2}+4\Delta^{2}}\right)\frac{\nabla|\Omega|^{2}}{2} && \text{(B.94)}\\
&= -\frac{\hbar\Delta}{2}\cdot w\cdot\nabla\left(\frac{2|\Omega|^{2}}{\Gamma^{2}+4\Delta^{2}}\right) && \text{(B.95)}\\
&= -\frac{\hbar\Delta}{2}\cdot\frac{1}{1+s}\nabla s && \text{(B.96)}\\
&= -\frac{\hbar\Delta}{2}\cdot\nabla\ln(1+s) && \text{(B.97)}\\
\therefore\quad \langle U_{dp}\rangle &= \frac{\hbar\Delta}{2}\cdot\ln(1+s), && \text{(B.98)}
\end{aligned}$$

where we have used the definition of s in Eq. B.67. Instead of writing $\langle F_{dp}\rangle$ in terms

of s, Eq. B.93 can also be rewritten as

$$\langle F_{dp}\rangle = -\frac{\hbar}{2}\,\Omega\nabla\Omega\cdot\left(\frac{1}{1+s}\right)\left(\frac{4\Delta}{\Gamma^2+4\Delta^2}\right) \tag{B.99}$$

$$= -\frac{\hbar}{2}\,\Omega\nabla\Omega\cdot\left(\frac{4\Delta}{\Gamma^2+4\Delta^2+s(\Gamma^2+4\Delta^2)}\right) \tag{B.100}$$

$$= -\frac{\hbar}{2}\,\Omega\nabla\Omega\cdot\left(\frac{4\Delta}{\Gamma^2+4\Delta^2+2|\Omega|^2}\right), \tag{B.101}$$

which is the same as Eq. 10.31 given in Ref. [165]. The force $\langle F_{dp}\rangle$ is conservative and normally called the dipole force; while the term $\langle U_{dp}\rangle$ is called the dipole potential. On the other hand, the force $\langle F_{sp}\rangle$ is obtained from absorption and spontaneous emission of photons and is normally called the radiation pressure force, scattering force or dissipative force [158]. The dissipative nature of $\langle F_{sp}\rangle$ can be viewed considering force from wave travelling in free space. For example, for a wave traveling along the z-axis, we have $\Phi = -kz$, $\nabla\Phi = -k$ and therefore the force $\langle F_{sp}\rangle$ can be written as

$$\left\langle F_{sp}^{trvl}\right\rangle = \hbar k\;\Gamma\rho_{ee} \tag{B.102}$$

$$= \hbar k\;\Gamma\frac{s_0/2}{1+s_0+4(\Delta/\Gamma)^2}, \tag{B.103}$$

which is the momentum transfer of a photon ($\hbar k$) times the spontaneous decay rate of the excited population ($\Gamma\rho_{ee}$).

A few conditions that we normally have in our experiments are:

[1] low intensity laser beam, $s \ll 1$,

$$\langle U_{dp}\rangle \approx \frac{\hbar\Delta s}{2} = \frac{\hbar\Delta}{2}\cdot\frac{I/I_s}{1+4\Delta^2/\Gamma^2} \tag{B.104}$$

[2] large detuning laser beam, $\Delta \gg (I/I_s)^{1/2}\Gamma/2$,

$$\left\langle F_{sp}^{trvl}\right\rangle \approx \frac{\hbar k\Gamma}{2}\cdot\frac{I/I_s}{4\Delta^2/\Gamma^2} = \frac{\hbar k\,\Gamma^3}{8\Delta^2}\cdot\frac{I}{I_s} \tag{B.105}$$

$$\langle U_{dp}\rangle \approx \frac{\hbar\Delta}{2}\cdot\frac{I/I_s}{1+4\Delta^2/\Gamma^2} \approx \frac{\hbar\Delta}{2}\cdot\frac{I}{I_s}\cdot\frac{\Gamma^2}{4\Delta^2} = \frac{\hbar\,\Gamma^2}{8\Delta}\cdot\frac{I}{I_s} \tag{B.106}$$

Appendix C

Optics Miscellaneous

In this Appendix, several optics formula, mentioned in the thesis, and their descriptions are provided for the convenience of the reader.

C.1 Scalar Wave Equation

The propagation of laser beam or the electromagnetic field in free space can be derived from Maxwell's equation as can be shown in Ref. [97]. Begining with the Maxwell's equation without charge, we have

$$\nabla \times \mathbf{E} = -\mu \frac{\partial}{\partial t}\mathbf{H} \tag{C.1}$$

$$\nabla \times \mathbf{H} = \epsilon \frac{\partial}{\partial t}\mathbf{E} \tag{C.2}$$

$$\nabla \cdot \epsilon\mathbf{E} = 0 \tag{C.3}$$

$$\nabla \cdot \mu\mathbf{H} = 0, \tag{C.4}$$

where $\mathbf{E}$ and $\mathbf{H}$ are the electric and magnetic field vectors respectively, and ϵ and μ are the permittivity and the permeability of the medium. We assume that our medium, e.g. air, is:
(1) isotropic i.e. the medium's properties are independent of polarization of the field. The value of ϵ and μ remain the same for all components of the vector fields.
(2) homogenious (the electric permittivity is a constant of position) i.e.

$$\nabla \cdot \epsilon\mathbf{E} = \epsilon\nabla \cdot \mathbf{E} \tag{C.5}$$

$$\nabla \times \epsilon \frac{\partial}{\partial t}\mathbf{E} = \epsilon\nabla \times \frac{\partial}{\partial t}\mathbf{E}, \tag{C.6}$$

(3) nonmagnetic, i.e. $\mu = \mu_0$, the magnetic permeability is equal to the vacuum

permeability. Thus,

$$\nabla \cdot \mu \mathbf{H} = \mu_0 \nabla \cdot \mathbf{H} \tag{C.7}$$

$$\nabla \times \mu \frac{\partial}{\partial t} \mathbf{H} = \mu_0 \nabla \times \frac{\partial}{\partial t} \mathbf{H} \tag{C.8}$$

Considering all assumption and operating curl on both side of Eq. C.1, the equation becomes

$$\nabla \times (\nabla \times \mathbf{E}) = -\mu_0 \frac{\partial}{\partial t} \nabla \times \mathbf{H} \tag{C.9}$$

$$\nabla(\nabla \cdot \mathbf{E}) - \nabla^2 \mathbf{E} = -\mu_0 \epsilon \frac{\partial^2}{\partial t^2} \mathbf{E} \tag{C.10}$$

$$\nabla^2 \mathbf{E} = \frac{n^2}{c^2} \frac{\partial^2}{\partial t^2} \mathbf{E} \tag{C.11}$$

where in the last step we have used $n^2 = \epsilon/\epsilon_0$ and $\mu_0 \epsilon_0 = 1/c^2$

By operating curl on both side of Eq. C.2, we can also arrive at the same equation for $\mathbf{H}$ i.e.

$$\nabla^2 \mathbf{H} = \frac{n^2}{c^2} \frac{\partial^2}{\partial t^2} \mathbf{H} \tag{C.12}$$

Since all the components of both $\mathbf{E}$ and $\mathbf{H}$ satisfy the same equation, we can reduce the vector equations to only one scalar equation i.e.

$$\nabla^2 Q = \frac{n^2}{c^2} \frac{\partial^2}{\partial t^2} Q \tag{C.13}$$

where Q is a scalar field.

C.2 Angular Spectrum Method

By substituting $Q = Q(x, y, z)e^{-i\omega t}$ into the scalar wave equation Eq. C.13, the time independent field $Q(x, y, z)$ must satisty the Helmholtz equation

$$(\nabla^2 + k^2)Q = \left(\nabla_\perp^2 + \frac{\partial^2}{\partial z^2} + k^2 \right) Q = 0, \tag{C.14}$$

where $k = n\omega/c$ is the wavenumber, and $\nabla_\perp^2$ denotes the Laplacian in the transverse coodinates, (x, y). The angular spectrum method [97] requires the equation to be

solved by considering a source field $Q(x, y, z)$ decomposed into a sum of elementary functions via an inverse Fourier Transform, i.e.

$$Q(x, y, z) = \int_u \int_v P(u, v, z) \exp[+i2\pi(ux + vy)]\, du\, dv, \tag{C.15}$$

where u and v are the spatial frequency complimentary to the x and y coordinates respectively. By substituting Eq. C.15 into Eq. C.14, $P(u, v, z)$ must be restricted to

$$\frac{\partial^2}{\partial z^2} P(u, v, z) + (1 - \lambda^2 u^2 - \lambda^2 v^2) k^2 P(u, v, z) = 0, \tag{C.16}$$

where a solution can be written as

$$P(u, v, z) = \exp\left[ikz(1 - \lambda^2 u^2 - \lambda^2 v^2)^{1/2}\right] P(u, v, 0), \tag{C.17}$$

and $P(u, v, 0)$ can be calculated from the Fourier transform of $Q(x, y, 0)$. The solution oscilates when the value under the square root is positive, i.e., u and v must satisfy

$$u^2 + v^2 < 1/\lambda^2. \tag{C.18}$$

To get the solution back in the spatial coordinates, we substitute Eq. C.17 into Eq. C.15.

In cylindrical coordinate, the solution in Eq. C.17 can be written as

$$P(\rho, \phi, z) = \exp\left[ikz(1 - \lambda^2 \rho^2)^{1/2}\right] P(\rho, \phi, 0), \tag{C.19}$$

where $\rho^2 = u^2 + v^2$, $\tan(\phi) = v/u$, and $P(\rho, \phi, 0)$ can be calculated from $Q(r, \theta, 0)$ via the weighted Hankel transform [97]. If $Q(r, \theta, z = 0)$ is separable into the radial and azimuthal part, i.e.,

$$Q(r, \theta, z = 0) = Q_R(r, z = 0) Q_\Theta(\theta),$$

then the transformation can be written as

$$P(\rho, \phi, 0) = \sum_{m=-\infty}^{\infty} (-i)^m c_m \exp(im\phi) \mathcal{H}_m\{Q_R(r, 0)\}, \tag{C.20}$$

where

$$c_m = \frac{1}{2\pi} \int_0^{2\pi} Q_\Theta(\theta) \exp(-im\theta)\, d\theta \tag{C.21}$$

and $\mathcal{H}_m\{Q_R(r,0)\}$ is the Hankel transform or the Fourier-Bessel transform of order m of $Q_R(r,0)$, which can be written as

$$\mathcal{H}_m\{Q_R(r,0)\} = 2\pi \int_0^\infty r Q_R(r,0) J_m(2\pi r\rho)\, dr. \tag{C.22}$$

Normally for our analysis in the main thesis, $Q_\Theta(\theta)$ is simply a single component function, $Q_\Theta(\theta) = \exp(in\theta)$. Therefore, Eq. C.20 can be reduced to

$$P(\rho,\phi,0) = (-i)^n \exp(in\phi)\mathcal{H}_n\{Q_R(r,0)\}. \tag{C.23}$$

Once $P(\rho,\phi,z)$ is known by substituting Eq. C.23 into Eq. C.19, $Q(r,\theta,z)$ can be obtained by performing the inverse weighted Hankel transform on $P(\rho,\phi,z) = P_\rho(\rho,z)P_\Phi(\phi)$, i.e.,

$$\begin{aligned} Q(r,\theta,z) &= \sum_{m'=-\infty}^{\infty} (i)^{m'} c_{m'} \exp(im'\theta)\mathcal{H}_{m'}\{P_\rho(\rho,z)\} && \text{(C.24)} \\ &= \exp(in\theta)\mathcal{H}_n\left\{\exp\left[ikz(1-\lambda^2\rho^2)\right]\mathcal{H}_n\{Q_R(r,0)\}\right\}, && \text{(C.25)} \end{aligned}$$

where

$$c_{m'} = \frac{1}{2\pi}\int_0^{2\pi} P_\Phi(\phi)\exp(-im'\phi)d\phi \tag{C.26}$$

and

$$\mathcal{H}_{m'}\{P_\rho(\rho,z)\} = 2\pi \int_0^\infty \rho P_\rho(\rho,z) J_{m'}(2\pi r\rho)\, d\rho. \tag{C.27}$$

The numerical evaluation of Eq. C.25 and the Hankel transform can be done by the quasi-discrete Hankel transform in Ref. [103].

C.3 Paraxial Equation

Upon the substitution of $Q(x,y,z) = q(x,y,z)e^{-ikz}$ into Eq. C.14, $q(x,y,z)$ must satisfy,

$$\begin{aligned} (\nabla_\perp^2 + \frac{\partial^2}{\partial z^2} + k^2)q(x,y,z)e^{-ikz} &= 0 && \text{(C.28)} \\ \exp(-ikz)\nabla_\perp^2 q - 2ik\exp(-ikz)\frac{\partial}{\partial z}q + \exp(-ikz)\frac{\partial^2}{\partial z^2}q &= 0 && \text{(C.29)} \\ \nabla_\perp^2 q - 2ik\frac{\partial}{\partial z}q &= 0, && \text{(C.30)} \end{aligned}$$

where in the last step we assume that the second derivative of q with respect to z can be disregarded. Equation C.30 is called the paraxial equation.

We can solve the paraxial equation by substituting a 2D Fourier transform integral of $q(x, y)$ into Eq. C.30. The equation and solution in the Fourier space of the spatial frequencies (u, v) will be

$$\frac{\partial}{\partial z}p(u,v) = \frac{-i}{2k}\left[(-i2\pi u)^2 + (-i2\pi v)^2\right] p(u,v) \quad \text{(C.31)}$$

$$p(u,v) = \exp\left[i\pi\lambda\left(u^2+v^2\right)\Delta z\right] p_0(u,v), \quad \text{(C.32)}$$

where $p(u, v)$ and $p_0(u, v)$ is the 2D Fourier transform of $q(x, y)$ and $q_0(x, y)$ respectively. $q_0(x, y)$ is the initial field [1]. Note that the paraxial equation becomes the Schrödinger equation in 2D for a free particle when t is substituted for z and we let $k = m/\hbar$.

C.4 Fresnel Diffraction Integral

It turns out that the solutions of the Helmholtz equation can be separated into two classes as suggested by Teague [166] by rearranging Eq. C.28 to the form below

$$\left[\left(\partial_z^2\right) + \left(\nabla_\perp^2 + k^2\right)\right] Q = 0 \quad \text{(C.33)}$$

$$\left[\partial_z - ik\left(1+\frac{\nabla_\perp^2}{k^2}\right)^{1/2}\right]\left[\partial_z + ik\left(1+\frac{\nabla_\perp^2}{k^2}\right)^{1/2}\right] Q = 0. \quad \text{(C.34)}$$

The two classes are

$$\left[\partial_z - ik\left(1+\frac{\nabla_\perp^2}{k^2}\right)^{1/2}\right] Q^+ = 0 \quad \text{(C.35)}$$

$$\left[\partial_z + ik\left(1+\frac{\nabla_\perp^2}{k^2}\right)^{1/2}\right] Q^- = 0. \quad \text{(C.36)}$$

Eq. C.35 gives the wave that oscillates in $+z$ region (i.e. $z > 0$). The solution can be written as

$$Q^+ = \exp\left[ikz\left(1+\frac{\nabla_\perp^2}{k^2}\right)^{1/2}\right] Q_0^+, \quad \text{(C.37)}$$

[1] In Matlab, we can get p from the command $p = \text{fft2c}(q)$, where the function fft2c() is shown in Appendix G.11.1. The Matlab code for solving the 2D paraxial equation can be seen in Appendix G.5.3

where Q_0^+ is the source field. Normally $Q^+ = Q^+(x, y, z)$, but for our purpose we restrict that $Q^+ = Q^+(x, y)$, a function of the transverse coordinates only. The solution in the form without the operator can be obtained through the use of the 2D Fourier Integral, by substituting $Q^+(x, y) = \tilde{\mathfrak{F}}\{P^+(u, v)\}$ and $Q_0^+(x, y) = \tilde{\mathfrak{F}}\{P_0^+(u, v)\}$ into Eq. C.37, where $\tilde{\mathfrak{F}}\{Q\}$ denotes the inverse Fourier transform of the field Q, and u and v are the spatial frequency complimentary to the x and y coordinates respectively. The solution $P^+(u, v)$ corresponding to Eq. C.37 can be written as

$$P^+ = \exp\left[ikz\left(1 - 4\pi^2\,\frac{u^2 + v^2}{k^2}\right)^{1/2}\right] P_0^+. \tag{C.38}$$

If we try to make an estimation of Eq. C.38 by expanding the quantity under the square root to the lowest order, we will have

$$\begin{aligned} P^+ &= \exp\left[ikz\left(1 - \lambda^2\,\frac{u^2 + v^2}{2}\right)\right] P_0^+ \\ &= \exp(ikz)\exp\left[-i\pi\lambda z(u^2 + v^2)\right] P_0^+. \end{aligned} \tag{C.39}$$

However, Teague pointed out that

$$\tilde{\mathfrak{F}}\left\{\exp\left[-i\pi\lambda z\left(u^2 + v^2\right)\right]\right\} = \frac{\exp(i\pi r^2/\lambda z)}{i\lambda z}, \tag{C.40}$$

where $r^2 = x^2 + y^2$. Therefore, by substituting the Fourier transform of Eq. C.40, $P^+ = \mathfrak{F}\{Q^+\}$, and $P_0^+ = \mathfrak{F}\left\{Q_0^+\right\}$ back into Eq. C.39, where $\mathfrak{F}\{Q\}$ denotes the Fourier transform of Q, we can have that

$$\mathfrak{F}\left\{Q^+\right\} = \exp(ikz)\mathfrak{F}\left\{\frac{\exp(i\pi r^2/\lambda z)}{i\lambda z}\right\} \cdot \mathfrak{F}\left\{Q_0^+\right\}, \tag{C.41}$$

and with the help of the convolution theorem, $\mathfrak{F}\{f * g\} = \mathfrak{F}\{f\} \cdot \mathfrak{F}\{g\}$, we have

$$Q^+(r, \phi, z) = \exp(ikz)\left(\frac{\exp(i\pi r^2/\lambda z)}{i\lambda z} * Q_0^+(r, \phi, z)\right), \tag{C.42}$$

which is known as the Fresnel diffraction formula, where the symbol $*$ denotes a convolution operation. In the cylindrical coordinates, Eq. C.42 can be expressed as

$$Q^+(r, \phi, z) = \frac{\exp(ikz)}{i\lambda z}\int_{r'=0}^{\infty}\int_{\phi'=0}^{2\pi} r' Q_0^+(r', \phi', z)\exp\left[i\pi\frac{(r - r')^2}{\lambda z}\right] d\phi'\, dr' \tag{C.43}$$

Appendix D

SLM Detail

The SLM is a device that shifts the phase of the input light spatially by the amount the user specifies. Upon picking up the phase shift, the output light diffracts to produce a desired diffraction pattern. The input is usually a coherent Gaussian beam with quadratic phase-front. The phase shift pattern that is responsible for the desire diffraction pattern is called the "phase mask".

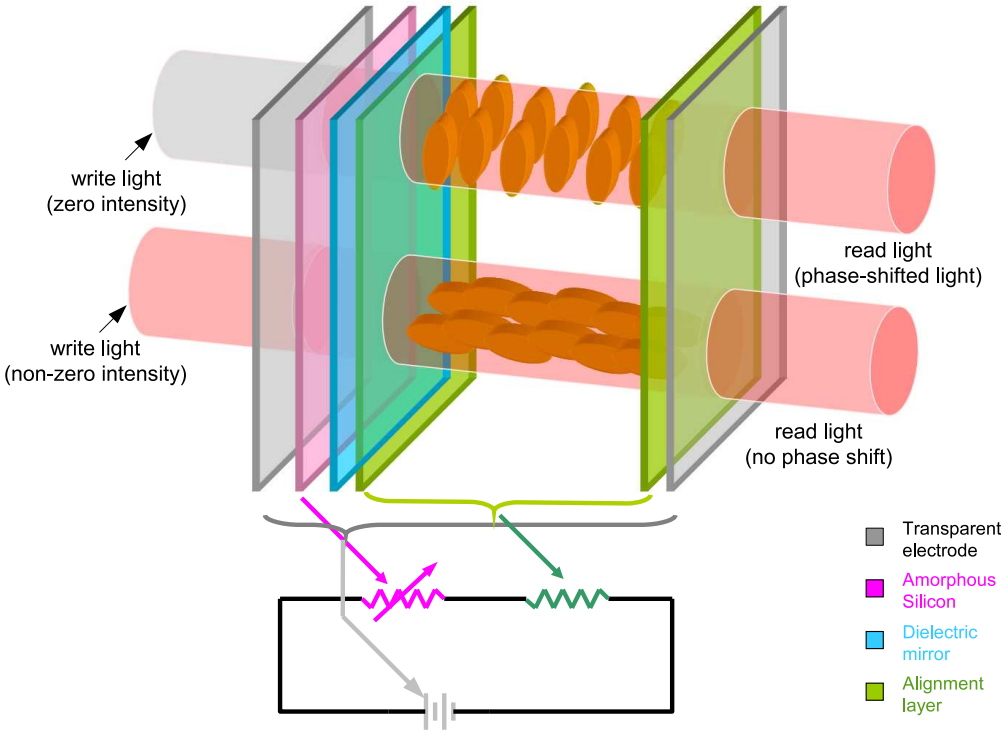

Figure D.1: SLM Schematics. See the main text for a detailed description.

The SLM normally consists of a few basic components as shown in Fig. D.1. This simplified model is explained in Ref. [97]. The most important part is the medium that modifies the phase front of the light passing through it. The medium

is liquid crystal consisting of elongated molecules. To control the medium effectively, two alignment layers are used to align the molecules in a certain direction. These layers contain surface engravings with parellel grooves through out the entire surface. When in contact with the surface, the elongated molecules align themselves in parellel along the grooves. The molecules not in contact with the plate align themselves in the same direction as the aligned ones. The direction of the molecular alignment is called the "director".

From Fig. D.1, the outermost pair of transparent electrode layer supplies electrical voltage across the liquid crystal, the amorphous silicon layer acts as a variable resister, and the dielectric mirror reflects a beam of light that interacts with the medium. There are two beams of coherent light labeled as "write light" and "read light". The read light first passes through a transparent electrode, the alignemnt layer pair, the medium, and the dielectric mirror. The mirror reflects the read light back through the same path toward the incoming read light. This reflection is the SLM's output that contains the patterns that we can use in the experiment. On the other side of the mirror, the write light passes through a transparent electrode and the amorphous silicon. When the write light hits the amorphous silicon layer, the resistance of the silicon changes. The more intense the write light, the less resistive the silicon. In the off state (write light with zero intensity), the resistance is large and the voltage drop across the alignment layer is negligible. Therefore the alignment of the molecules is unaffected and the read light obtained the maximum phase shift. However when the intensity of the write light is not zero, there is voltage drop across the alignment layer and the molecules rotate toward the alignment plate. The read light in this case has zero phase shift.

Inside the real SLM, there are Cartesian arrays of these beams of write light of which intensity can be varied in 256 steps from 0 to its maximum value. We generate the desired phase mask on a computer, and the SLM takes the value of the green part of the red-green-blue output of the videographics array (VGA) port of the computer. The VGA output from the computer can send 8-bit voltage levels for each color; therefore the SLM can apply 256 different phase shifts to the read light.

The SLM also has a bias control for adjusting the amount of voltage drop across the medium. The bias voltage ranges from 0 to 4 V, allowing the maximun phase shift to vary narrowly around 2π. For a proper alignment, the polarization of the read light has to point in the same direction as the director of the medium. A misalignment of the polarization will result in a fraction of the output to be unmodulated.

Appendix E

Liouville Equation

The objective of this appendix is to gather formulations for solving the Liouville equation (LE). The formulation of free expansion below is adapted from Song's unpublished calculations for his thesis [36]. The formulation of steady state solution is from Arakelyan's private note on calculation for his paper [35]. The LE in cylindrical coordinates is adopted from Bauer's note [167]. The numerical method to solve time dependent LE is from Cheng *et al.* [168] Fujiwara [169] and Manfredi *et al.* [170].

E.1 Liouville Equation in Cartesian Coordinates

From classical mechanics, a distribution function $f(\vec{r}, \vec{v})$ of particles flowing in the six-dimensional space of Cartesian coordinates $\vec{r}$ and velocity $\vec{v}$ is conserved, in the absence of collisions [171, 158], i.e.

$$\frac{d}{dt}f = \frac{\partial}{\partial t}f + \vec{v} \cdot \nabla_{\vec{r}} f + \vec{a} \cdot \nabla_{\vec{v}} f = 0, \tag{E.1}$$

where $\vec{a} = d\vec{v}/dt$ is the acceleration, and $\nabla_{\vec{r}}$ and $\nabla_{\vec{v}}$ denote the gradient with respect to $\vec{r}$ and $\vec{v}$ respectively. Equation E.1 is called the "Liouville theorem" or the "Liouville equation" (LE).

For our concerns in the thesis, if we denote (x, y) as the transverse coordinates and z the longitudinal coordinate, and we have $\partial f/\partial z = 0$ and $a_z = d^2z/dt^2 = 0$, the LE reduces to

$$\frac{\partial}{\partial t}f + v_x\frac{\partial}{\partial x}f + v_y\frac{\partial}{\partial y}f + a_x\frac{\partial}{\partial v_x}f + a_y\frac{\partial}{\partial v_y}f = 0. \tag{E.2}$$

In one-dimensional case of Cartesian coordinate x and one-dimensional velocity v,

the LE can be written as

$$\frac{\partial}{\partial t}f + v\frac{\partial}{\partial x}f + a\frac{\partial}{\partial v}f = 0, \tag{E.3}$$

E.2 2D-LE in Cylindrical Coordinates

From classical mechanics, we know that, in cylindrical coordinates, the acceleration can be written as

$$\vec{a} \;=\; a_r\hat{\mathbf{e}}_r + a_\phi\hat{\mathbf{e}}_\phi = \left(\ddot{r} - r\dot{\phi}^2\right)\hat{\mathbf{e}}_r + \left(2\dot{r}\dot{\phi} + r\ddot{\phi}\right)\hat{\mathbf{e}}_\phi \tag{E.4}$$

The acceleration can be derived from the force $\vec{\mathbf{F}}$ or the potential U, i.e.

$$\vec{a} \;=\; \frac{\vec{\mathbf{F}}}{m} = -\frac{\nabla_{\vec{r}}U}{m} = -\frac{1}{m}\frac{\partial U}{\partial r}\hat{\mathbf{e}}_r - \frac{1}{mr}\frac{\partial U}{\partial \phi}\hat{\mathbf{e}}_\phi \tag{E.5}$$

By comparing Eq. E.4 and Eq. E.5, we will have

$$\ddot{r} = r\dot{\phi}^2 - \frac{1}{m}\frac{\partial U}{\partial r} \quad \text{and} \quad \ddot{\phi} = -\frac{2}{r}\dot{r}\dot{\phi} - \frac{1}{mr^2}\frac{\partial U}{\partial \phi} \tag{E.6}$$

If we defined, the radial velocity $v_r = \dot{r}$ and the azimuthal velocity $v_\phi = r\dot{\phi}$, we can have that $\dot{v_r} = \ddot{r}$ and $\dot{v_\phi} = \dot{r}\dot{\phi} + r\ddot{\phi}$. With these newly defined variables, a new total derivative for the collisionless case similar to Eq. E.2 can be written as

$$\frac{\partial}{\partial t}f + v_r\frac{\partial}{\partial r}f + \frac{v_\phi}{r}\frac{\partial}{\partial \phi}f + \dot{v_r}\frac{\partial}{\partial v_r}f + \dot{v_\phi}\frac{\partial}{\partial v_\phi}f = 0 \tag{E.7}$$

By substituting Eq. E.6 into the definition of $\dot{v_r}$ and $\dot{v_\phi}$, Eq. E.7 can be rewritten as

$$\frac{\partial f}{\partial t} + v_r\frac{\partial f}{\partial r} + \frac{v_\phi}{r}\frac{\partial f}{\partial \phi} + \left(\frac{v_\phi^2}{r} - \frac{1}{m}\frac{\partial U}{\partial r}\right)\frac{\partial f}{\partial v_r} - \left(\frac{v_r v_\phi}{r} + \frac{1}{mr}\frac{\partial U}{\partial \phi}\right)\frac{\partial f}{\partial v_\phi} = 0. \tag{E.8}$$

E.3 Steady State Distribution

E.3.1 One Dimensional Distribution

The Boltzmann equation for a distribution of particles at equilibrium, for the collisionless case, is

$$v\frac{\partial}{\partial x}f + a\frac{\partial}{\partial v}f = 0 \tag{E.9}$$

We can solve this equation using separation of variables. By substituting $f = A(x)B(v)$ in Eq. E.9, we will have

$$\begin{aligned} vB(v)\frac{\partial}{\partial x}A(x) + \frac{F(x)}{m}A(x)\frac{\partial}{\partial v}B(v) &= 0 \\ \frac{1}{F(x)}\frac{1}{A(x)}\frac{\partial}{\partial x}A(x) + \frac{1}{mv}\frac{1}{B(v)}\frac{\partial}{\partial v}B(v) &= 0 \end{aligned} \tag{E.10}$$

where we have substituted $a = F(x)/m$ in Eq. E.9. From Eq. E.10, we can relate each term to a constant β as shown below

$$\frac{1}{F(x)}\frac{1}{A(x)}\frac{\partial}{\partial x}A(x) = \beta \tag{E.11}$$

$$\frac{1}{mv}\frac{1}{B(v)}\frac{\partial}{\partial v}B(v) = -\beta \tag{E.12}$$

The solutions are

$$A(x) = A_0 \exp\left(\beta \int F(x)\,dx\right) = A_0 \exp\left[-\beta U(x)\right], \tag{E.13}$$

$$B(v) = B_0 \exp\left(-\beta m \int v\,dv\right) = B_0 \exp\left(-\beta m v^2/2\right), \tag{E.14}$$

where we define the force as $F(x) \equiv -\partial U(x)/\partial x$ in Eq. E.13. In summary,

$$\begin{aligned} f(x,v) &= f_0 \exp\left[-\beta U(x)\right] \exp\left(-\beta m v^2/2\right) \\ &= f_0 \exp\left[-\frac{U(x)}{k_B T_\perp}\right] \exp\left(-v^2/2\sigma_v^2\right), \end{aligned} \tag{E.15}$$

where

$$\beta \equiv \frac{1}{k_B T_\perp} \quad \text{and} \quad \sigma_v \equiv \left(\frac{k_B T_\perp}{m}\right)^{1/2}. \tag{E.16}$$

Furthermore, the normalization factor f_0 can be evaluated by demanding that the total probability be one i.e.

$$\begin{aligned} 1 &= \int_{x=-\infty}^{+\infty}\int_{v=-\infty}^{+\infty} f(x,v,t)\,dx\,dv \\ &= f_0 \int_{x=-\infty}^{+\infty} \exp\left[-\frac{U(x)}{k_B T_\perp}\right] dx \int_{v=-\infty}^{+\infty} \exp\left(-v^2/2\sigma_v^2\right)\, dv \\ &= f_0 \cdot Q_{1D} \cdot (2\pi)^{1/2}\sigma_v. \end{aligned} \tag{E.17}$$

$$\therefore \quad f_0 = \frac{1}{Q_{1D} \cdot (2\pi)^{1/2}\sigma_v}, \quad \text{where} \quad Q_{1D} = \int_{x=-\infty}^{+\infty} \exp\left[-\frac{U(x)}{k_B T_\perp}\right] dx \tag{E.18}$$

Note that the condition $\partial f/\partial t = 0$ already demands that the velocity distribution be a Gaussian. In other words, the steady state only occurs when the velocity distribution is Gaussian.

E.3.2 Radial Distribution

If we assume that in the steady state, the distribution has no prefered direction in ϕ (i.e. $v_\phi = 0$) and the force is radial ($\partial U/\partial\phi = 0$), Eq. E.8 can be reduced to

$$v_r \frac{\partial}{\partial r} f + a_r \frac{\partial}{\partial v_r} f = 0, \quad \text{where} \quad a_r = -\frac{1}{m}\frac{\partial}{\partial r} U \tag{E.19}$$

The solution is the same as Eq. E.15, i.e.

$$f(r, v_r) = f_0 \exp\left[-\frac{U(r)}{k_B T_\perp}\right] \exp\left(-v_r^2/2\sigma_v^2\right), \tag{E.20}$$

where $\sigma_v = (k_B T_\perp/m)^{1/2}$ and the normalization factor, f_0, can be obtained from the following procedures,

$$\begin{aligned} 1 &= \int_{\theta_v=0}^{2\pi}\int_{\theta=0}^{2\pi}\int_{r=0}^{+\infty}\int_{vr=0}^{+\infty} f(r, v_r, t)\, r\, dr\, d\theta\, v_r\, dv_r\, d\theta_v \\ &= f_0 \cdot 2\pi \int_{r=0}^{+\infty} \exp\left[-\frac{U(r)}{k_B T_\perp}\right] r\, dr \;\cdot\; 2\pi \int_{vr=0}^{+\infty} \exp\left(-v_r^2/2\sigma_{vr}^2\right)\, v_r\, dv_r \\ &= f_0 \cdot Q_{2D} \cdot (2\pi)\sigma_{vr}^2, \end{aligned} \tag{E.21}$$

where

$$f_0 = \frac{1}{Q_{2D} \cdot (2\pi)\sigma_{vr}^2} \quad \text{and} \quad Q_{2D} = 2\pi \int_{r=0}^{+\infty} \exp\left[-\frac{U(r)}{k_B T_\perp}\right] r\, dr \tag{E.22}$$

E.4 Generalized Free-Expansion

The solution of the force-free LE or the so called "free-expansion solution" can be derived for the atomic cloud with an arbitrary spatial distribution and an arbitrary velocity distribution as shown below.

E.4.1 One Dimensional Free Expansion

For a free expansion, external force that acts on the particles in the system is zero (i.e. $a = 0$). Furthermore, in the collisionless case, $df/dt = 0$ and thus our equation becomes

$$\frac{\partial}{\partial t} f + v \frac{\partial}{\partial x} f = 0 \tag{E.23}$$

which has the solution in a wave form. The solution can be written as

$$f(x, v, t) = \alpha\, h(v)\, g(x - vt) \tag{E.24}$$

where α is a constant with respect to x , v and t. Equation E.23 is linear because a superposition

$$f(x, v, t) = \alpha_1 f_1(x, v, t) + \alpha_2 f_2(x, v, t) \tag{E.25}$$

is also a solution, where $f_i = \alpha_i\, h_i(v)\, g_i(x - vt)$ and $i = 1, 2$. Thus we can decompose $h(v)$ and $g(x - vt)$ into a combination of elementary functions [97]. For our purpose, we will rewrite $h(v)$ and $g(x - vt)$ using a *sifting* property of the δ function as

$$h(v) = \int_{-\infty}^{+\infty} h(v')\delta(v' - v)dv' \tag{E.26}$$

and

$$g(x - vt) = \int_{-\infty}^{+\infty} g(x')\delta(x' - (x - vt))dx' \tag{E.27}$$

The function $f(x, t)$ can be evaluated as a projection of $f(x, v, t)$ on the spatial coordinate as

$$\begin{aligned}
f(x,t) &= \int_{-\infty}^{+\infty} f(x, v, t)dv && \text{(E.28)}\\
&= \int_{-\infty}^{+\infty}\int_{-\infty}^{+\infty} \alpha h(v)g(x')\delta(x' - (x - vt))dx'dv && \text{(E.29)}\\
&= \int_{-\infty}^{+\infty}\int_{-\infty}^{+\infty} \alpha g(x')h(v)\delta(vt - (x - x'))dvdx' && \text{(E.30)}\\
&= \int_{-\infty}^{+\infty} \tilde{\alpha} g(x')h\left(v \rightarrow \frac{x - x'}{t}\right)dx', && \text{(E.31)}
\end{aligned}$$

where $\tilde{\alpha} = \alpha/t$ is a normalization constant that makes $\int f(x, t)\, dx = 1$, evaluating from $x = -\infty$ to $+\infty$, and $v \rightarrow (x - x')/t$ means we substitute v with $(x - x')/t$. The calculation of Eq. E.31 can be done numerically with a help of a convolution theorem for Fourier transforms as shown below

$$\begin{aligned}
f(x,t) &= \tilde{\mathfrak{F}}\{\mathfrak{F}\{f(x,t)\}\} && \text{(E.32)}\\
&= \tilde{\mathfrak{F}}\left\{\mathfrak{F}\left\{\tilde{\alpha}\int_{-\infty}^{+\infty} g(x')h\left(x - x'\right)dx'\right\}\right\} && \text{(E.33)}\\
&= \tilde{\alpha}\,\tilde{\mathfrak{F}}\big\{\mathfrak{F}\{g(x)\}\cdot\mathfrak{F}\{h(x)\}\big\}, && \text{(E.34)}
\end{aligned}$$

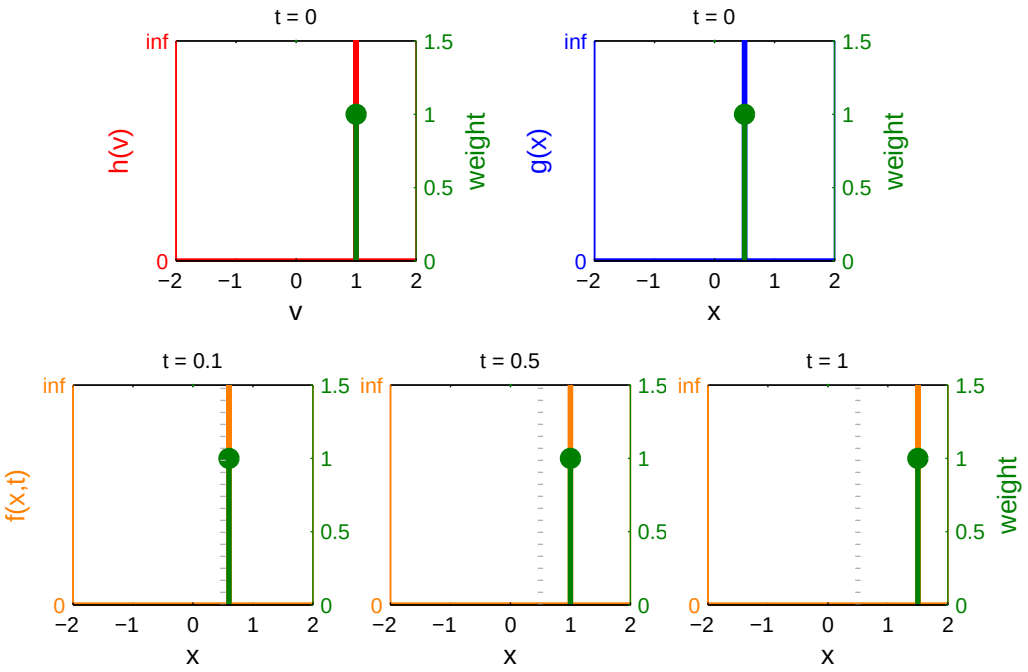

Figure E.1: Dynamics of a delta distribution function that satisfies the free expansion LE in Eq. E.23. From the top row, at $t = 0$, $h(v)$ is located at $v = 1$ and $g(x)$ is located at $x = 0.5$. The results of the evolution is shown in the bottom row by $f(x, t)$ at different values of t as labeled on the top of each subfigure. The evolution resembles the motion of a single particle moving at a constant speed $v = 1$.

where $\mathfrak{F}$ and $\tilde{\mathfrak{F}}$ denote a Fourier transform and its inverse respectively. To understand how this decomposition works we can look at a few simple examples. One simplest distributions of $h(v)$ and $g(x - vt)$ in Eq. E.24 are

$$h(v) = \delta(v - v') \quad \text{and} \quad g(x - vt) = \delta(x - x' - vt)$$

which gives $f(x, v, t) = \delta(v - v')\delta(x - x' - vt)$. Obtaining $f(x, t)$ via Eq. E.28, we have $f(x, t) = \delta(x - x' - v't)$, a delta function that moves with velocity $v = v'$ starting at $x = x'$. In other words, the probability to find a particle is 100% at $x = x' + v't$ at time t. This distribution is shown in Fig. E.1. Consider a more complicated velocity distribution

$$h(v) = \frac{1}{2}\left[\delta(v - v') + \delta(v + v')\right].$$

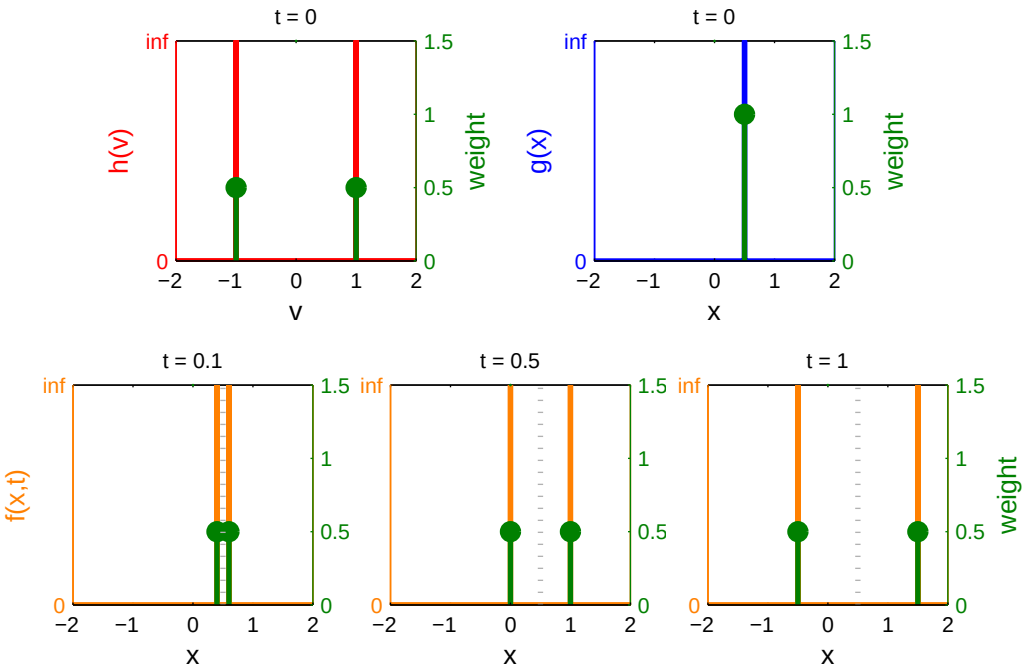

Figure E.2: This figure is similar to Fig. E.1 except that there are two delta functions with equal weight in the velocity space at $v = \pm 1$. At $t > 0$, the distribution, originally at $x = 0.5$, is divided equally into two groups moving away from each other with the speed of $|v| = 1$.

With the same $g(x - vt)$ as before the resulting $f(x, t)$ can be seen as two delta functions moving in opposite directions as shown in Fig. E.2. The probability of finding the particle is now 50% for each velocity and location. Up to this point, we can keep adding δ function to $h(v)$ with appropriate weights (i.e. the weights that make the total probability one) to reflect our desired velocity distribution. For example, the resulting $f(x, t)$ for a combination of δ-functions that reflects a Gaussian velocity distribution can be seen in the bottom row of Fig. E.3. So far the weights in front of the δ-functions are discrete depending on v'. However we can have the weight to be a continuous function $h(v')$ as we have already seen in the decomposition in Eq. E.26. For instance, if $h(v')$ is a Gaussian function, $f(x, t)$ is also a Gaussian as shown in Fig. E.4. Note that the total probability is conserved through time i.e. once $f(x, v, t)$ is normalized it stays normalized for all later time.

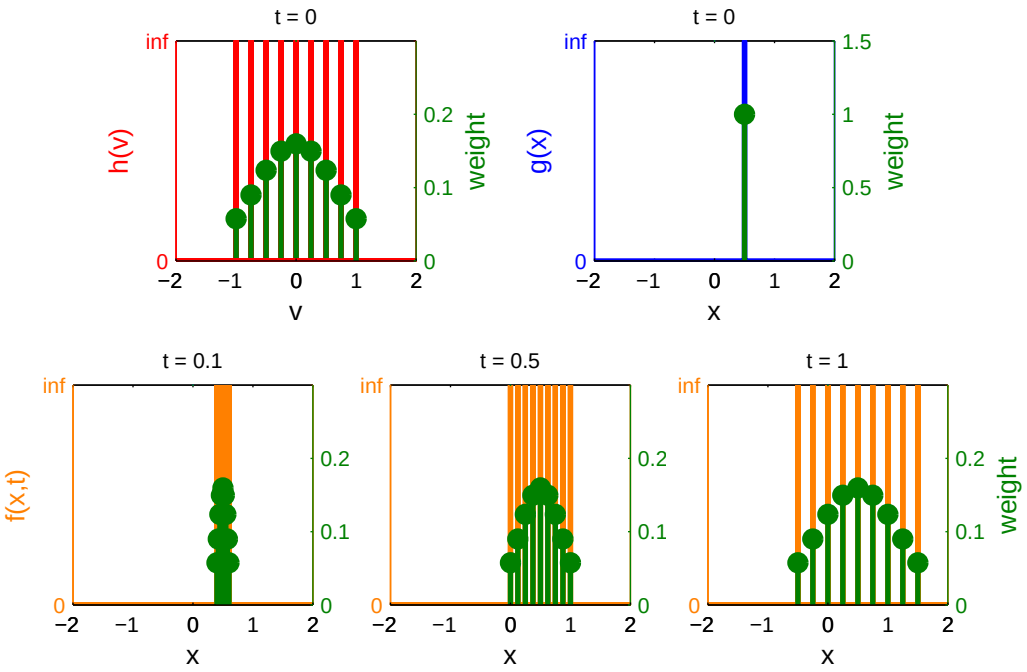

Figure E.3: By adding more delta functions to $h(v)$ with proper weighting, one can construct a desired distribution as shown in the top left corner. In this case the weights of $h(v)$ resembles a Gaussian function. The description of the free expansion in the bottom row follow the same logic as the one in Fig. E.2.

Up until now, we consider only one simple spatial distribution. We can do the same trick as what we have done with the velocity distribution by adding more δ-functions with appropriate weights to $g(x - vt)$. Let us consider a Gaussian $h(v)$ and let

$$g(x - vt) = 0.3\ \delta(x + 0.3 - vt) + 0.5\ \delta(x - vt) + 0.2\ \delta(x - 0.5 - vt).$$

The resulting $f(x, t)$ can be seen in Fig. E.5 and it is what we can already guess from the previous knowledge. It is a sum of expanding Gaussian functions peaked at three different locations. As before, we can keep adding the δ-function with proper weights at other locations or we can arrive at the continuous spatial distribution as we have seen in the decomposition in Eq. E.27. For a free expansion of a continuous (or piecewise) spatial distribution, we employ a convolution as described in Eq. E.34.

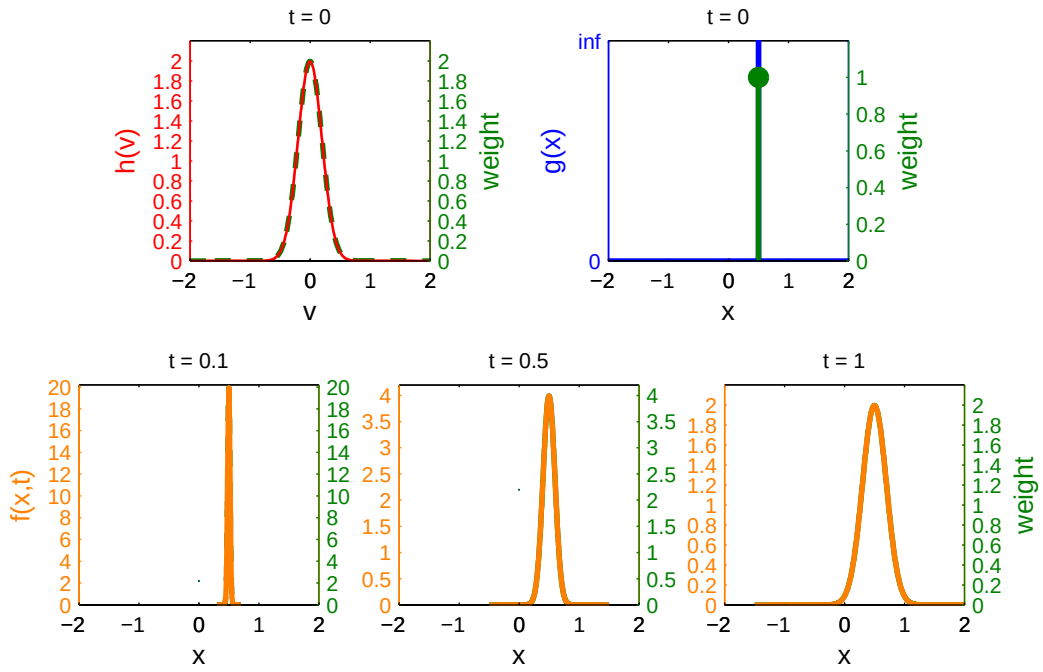

Figure E.4: Instead of a discrete $h(v)$ as shown in Fig. E.3, the Gaussian $h(v)$ can be used to convolve with $g(x)$ to get the free expansion as shown in the bottom row.

A free expansion of a square spatial distribution is shown in Fig. E.6 and Fig. E.7 for a discrete and continuous representation respectively.

There are a few remarks to be made. First, the total probability is conserved i.e.

$$\begin{aligned}
\int_x \int_v f(x,v,t)dvdx &= \alpha \int_x \int_v h(v)g(x-vt)dvdx && \text{(E.35)}\\
&= \alpha \int_x \int_v \int_{v'} h(v')\delta(v-v')dv' \\
&\quad \times \int_{x'} g(x')\delta(x'-x+vt)dx'\ dvdx && \text{(E.36)}\\
&= \alpha \int_{x'} \int_{v'} h(v')g(x')dv'dx' && \text{(E.37)}\\
&= \int_x \int_v f(x,v,t=0)dvdx, && \text{(E.38)}
\end{aligned}$$

where in going from Eq. E.36 to Eq. E.36 we interchange the integrals[1] over x' and

[1]The interchange of integral can be done properly by defining the delta functions as the limit of a continuous function such as a Gaussian function.

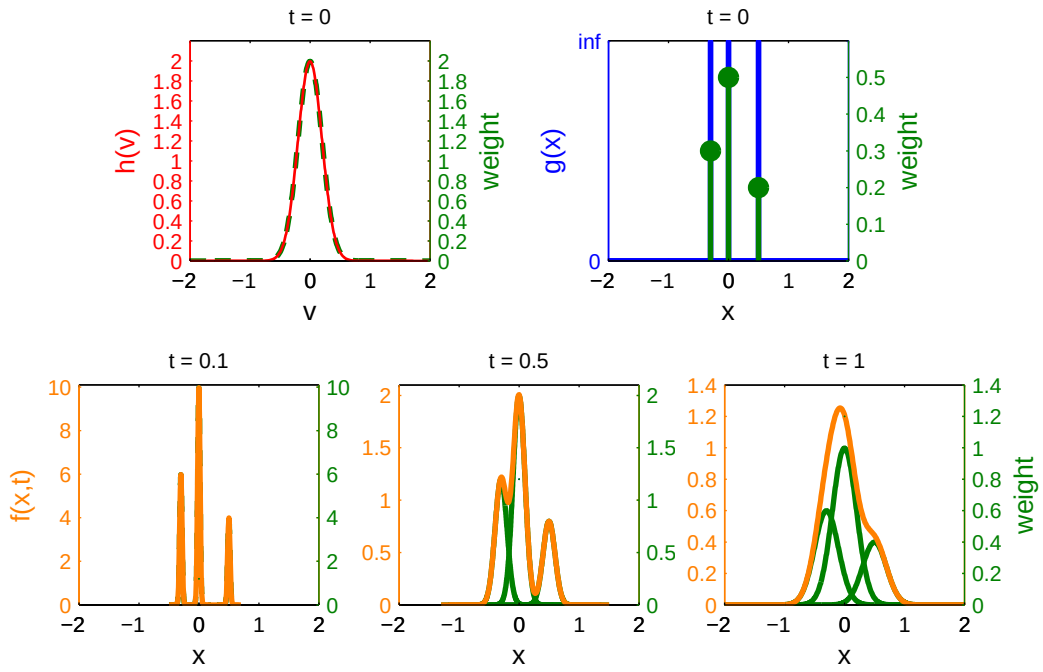

Figure E.5: Free expansion of three delta spatial distributions with a Gaussian velocity distribution. The expansion is similar to the one in Fig. E.4 except that there are three weighted delta functions located at different places in the coordinate space. The overall expansion is the sum of the expansion from each individual delta distribution.

v' with those of x and v. Second, recognizing that the total probability is one, the value of α can be written as

$$\alpha = \frac{1}{\int_{x'} g(x')dx'} \cdot \frac{1}{\int_{v'} h(v')dv'} = \alpha_g \alpha_h, \tag{E.39}$$

where $\alpha_g = 1/\int g(x')dx'$ and $\alpha_h = 1/\int h(v')dv'$. Note also that the velocity distribution function is independent of time i.e. the integral

$$\int f(x, v, t = 0)\, dx = \int \alpha_h h(v) \cdot \alpha_g g(x)\, dx = \alpha_h h(v),$$

is equal to

$$\int f(x, v, t)\, dx = \int \alpha_h h(v) \cdot \alpha_g g(x - vt)\, dx = \alpha_h h(v).$$

This is to be anticipated because there is no force in Eq. E.23 to alter the velocity distribution.

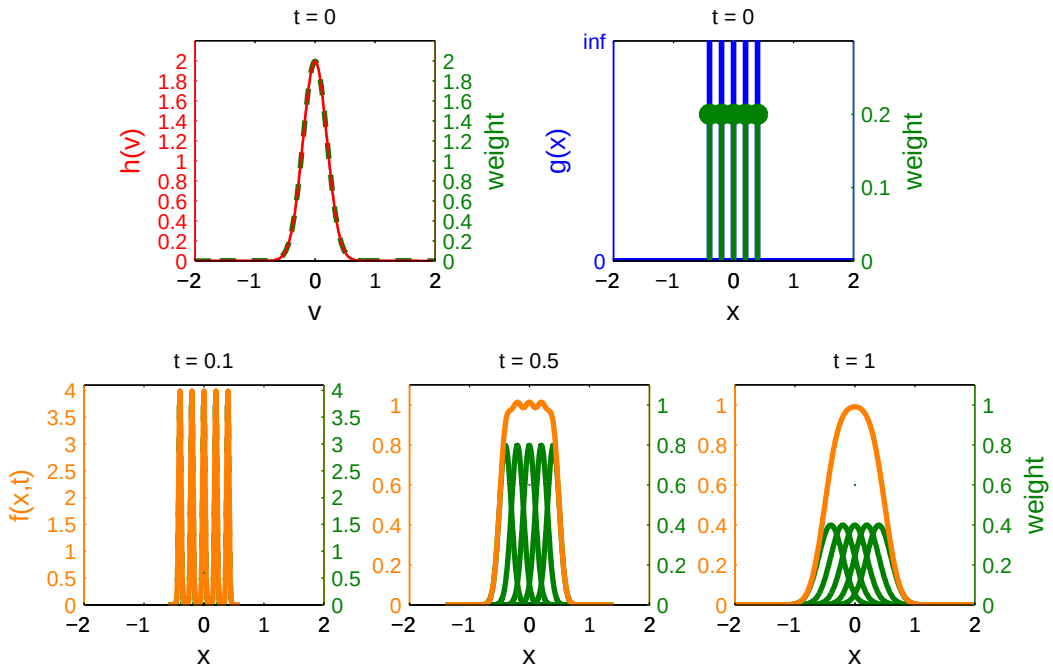

Figure E.6: The expansion is similar to the one in Fig. E.5 except that the weights of $g(x)$ resembles a flat top function. Compare this with the expansion in Fig. E.7.

E.4.2 Gaussian Expansion: Analytical vs Numerical Evaluation

To show how $f(x,t)$ is evaluated explicitly, we consider one analytical example when both initial spatial and velocity distribution are Gaussian. First, we start by noticing from Eq. E.26 and Eq. E.27 that at $t = 0$, $h(v) = h(v')$ and $g(x) = g(x')$. In other words, $h(v')$ and $g(x')$ can be considered as our initial distributions. Therefore we can write $h(v') = \exp\left(-v'^2/2\sigma_v^2\right)$ and $g(x') = \exp\left(-x'^2/2\sigma_x^2\right)$. Next, we evaluate $f(x,t)$ using Eq. E.31 i.e.

$$f(x,t) = \int_{-\infty}^{+\infty} \tilde{\alpha} g(x') h\left(v' \to \frac{x-x'}{t}\right) dx' \tag{E.40}$$

$$= \tilde{\alpha} \int_{-\infty}^{+\infty} \exp\left(-\frac{x'^2}{2\sigma_x^2}\right) \exp\left[-\frac{(x-x')^2}{2\sigma_v^2\, t^2}\right] dx' \tag{E.41}$$

$$= \tilde{\alpha} \int_{-\infty}^{+\infty} \exp\left[-\frac{x'^2}{2\sigma_x^2} - \frac{(x-x')^2}{2\sigma_v^2 t^2}\right] dx'$$

$$= \tilde{\alpha} \int_{-\infty}^{+\infty} \exp\left[\frac{-2\sigma_v^2 t^2 x'^2 - 2\sigma_x^2 (x-x')^2}{4\,\sigma_x^2\,\sigma_v^2\,t^2}\right] dx'. \tag{E.42}$$

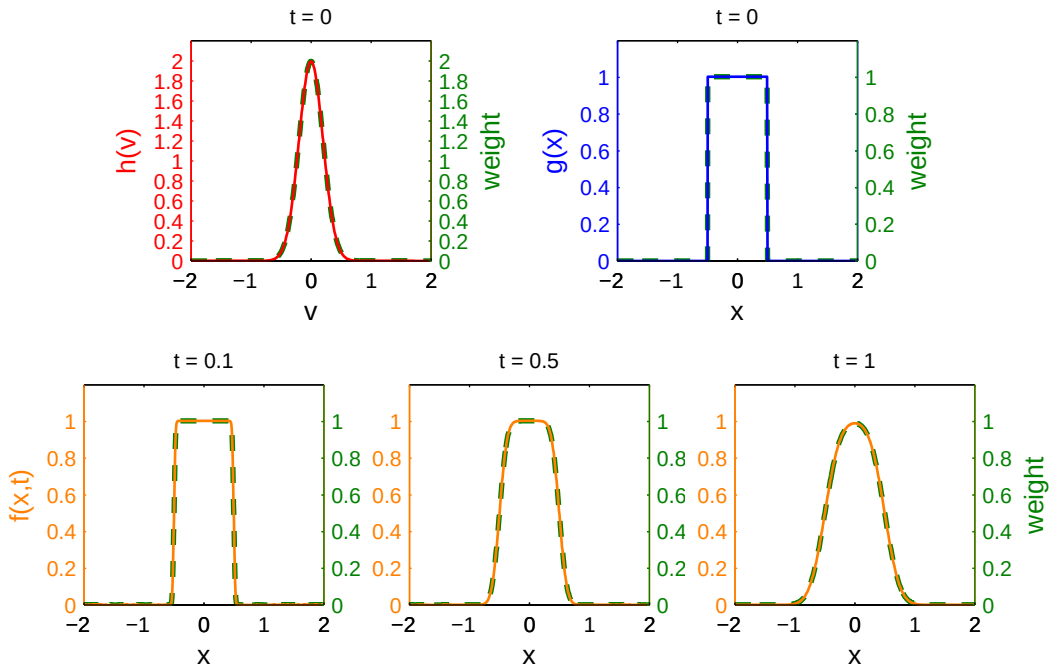

Figure E.7: The expansion in this figure is similar to the one in Fig. E.6 except that $g(x)$ is a piecewise function. The free expansion is obtained from a convolution of two continuous functions $g(x)$ and $h(v)$ as shown in Eq. E.31 and Eq. E.34.

The argument of the exponential function can be rearranged as shown below

$$\begin{aligned}
\frac{-2\sigma_v^2 t^2 x'^2 - 2\sigma_x^2 (x-x')^2}{4\,\sigma_x^2\,\sigma_v^2\,t^2} &= \frac{-(2\sigma_v^2 t^2 + 2\sigma_x^2)x'^2 + (4\sigma_x^2 x)x' - (2\sigma_x^2 x^2)}{4\,\sigma_x^2\,\sigma_v^2\,t^2} \\
&= \frac{-ax'^2 + bx' - c}{d} \\
&= -\frac{a}{d}\left(x'^2 - \frac{b}{a}x' + \frac{c}{a}\right) \\
&= -\frac{a}{d}\left[\left(x' - \frac{b}{2a}\right)^2 - \frac{b^2}{4a^2} + \frac{c}{a}\right], \qquad \text{(E.43)}
\end{aligned}$$

where $a = (2\sigma_v^2 t^2 + 2\sigma_x^2)$, $b = (4\sigma_x^2 x)$, $c = (2\sigma_x^2 x^2)$, and $d = (4\,\sigma_x^2\,\sigma_v^2\,t^2)$. Thus the integral in Eq. E.42 can then be rewritten as

$$\begin{aligned} I(x) &= \exp\left[-\frac{a}{d}\left(-\frac{b^2}{4a^2}+\frac{c}{a}\right)\right]\int_{-\infty}^{+\infty}\exp\left[-\frac{a}{d}\left(x'-\frac{b}{2a}\right)^2\right]dx' \\ &= \exp\left[-\frac{a}{d}\left(-\frac{b^2}{4a^2}+\frac{c}{a}\right)\right]\left[\frac{d}{a}\right]^{1/2}\pi^{1/2} \\ &= \left[\frac{\pi d}{a}\right]^{1/2}\exp\left[\left(\frac{b^2-4ac}{4ad}\right)\right] \\ &= \left[\frac{\pi 4\,\sigma_x^2\,\sigma_v^2\,t^2}{2\sigma_v^2 t^2+2\sigma_x^2}\right]^{1/2}\exp\left[\frac{4^2\sigma_x^4 x^2-4\,(2\sigma_v^2 t^2+2\sigma_x^2)2\sigma_x^2 x^2}{4\,(2\sigma_v^2 t^2+2\sigma_x^2)\,4\sigma_x^2\sigma_v^2 t^2}\right] \\ &= \sigma_x\sigma_v t\,\left[\frac{2\pi}{\sigma_v^2 t^2+\sigma_x^2}\right]^{1/2}\exp\left[-\frac{x^2}{2\,(\sigma_v^2 t^2+\sigma_x^2)}\right]. \end{aligned} \tag{E.44}$$

The distribution, $f(x,t)$, in Eq. E.42 can thus be written as

$$f(x,t) = \frac{\exp\left[-x^2/2\sigma_x^2(t)\right]}{(2\pi)^{1/2}\sigma_x(t)} \tag{E.45}$$

where we have used Eq. E.39 to evaluate $\tilde{\alpha}$ to be $(2\pi\sigma_x\sigma_v t)^{-1}$ and we define

$$\sigma_x^2(t) \equiv \sigma_x^2 + \sigma_v^2 t^2. \tag{E.46}$$

Note that the exponential function of the shifted coordinate $x - x'$ in Eq. E.41 has the same form as the Green function shown in the appendix section in [122].

Now let us consider the numerical evaluation of $f(x,t)$. Using Eq. E.34, $f(x,t)$ can be written as

$$f(x,t) = \tilde{\alpha}\,\tilde{\mathfrak{F}}\big\{\mathfrak{F}\{g(x)\}\cdot\mathfrak{F}\{h(x)\}\big\} \tag{E.47}$$

$$= \tilde{\alpha}\,\tilde{\mathfrak{F}}\left\{\mathfrak{F}\left\{\exp\left(-\frac{x^2}{2\sigma_x^2}\right)\right\}\cdot\mathfrak{F}\left\{\exp\left[-\frac{x^2}{2\sigma_v^2\,t^2}\right]\right\}\right\}. \tag{E.48}$$

In MATLAB, the last expression can be evaluated as

```
f = abs(ifftshift(ifft(fft(g).*fft(h))))/(sum(g)*t);
```

where `g` and `h` can be written as

```
g = exp(-x.^2/(2*sgmx^2))/(sqrt(2*pi)*sgmx);
h = exp(-x.^2/(2*(sgmv*t)^2))/(sqrt(2*pi)*sgmv);
```

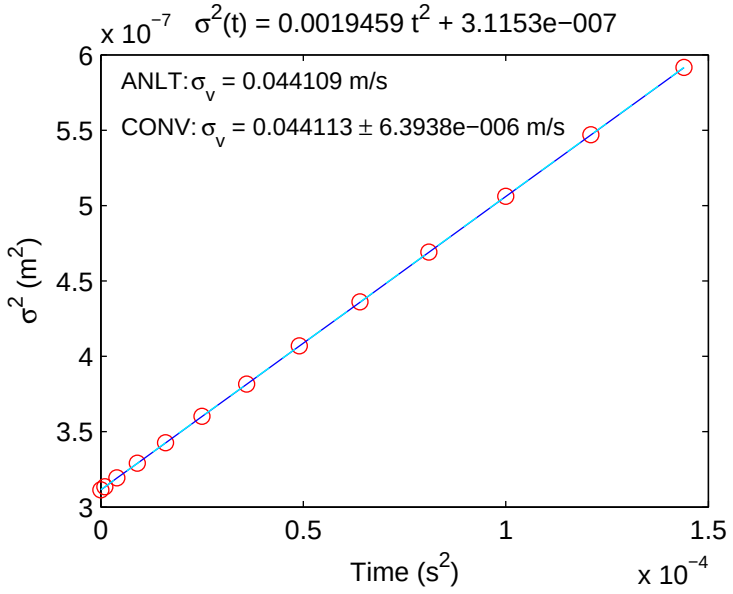

Figure E.8: Comparison of free expansion obtained from analytical calculation (blue line) and a 2D convolution method (red circle) of a Gaussian distribution as described in the text. The graph shows squared half-width of a Gaussian function (σ^2) vs. squared time (t^2).

Once we have `f`, we can fit it to our analytical Gaussian form and extract $\sigma_x(t)$. The plot of $\sigma_x^2(t)$ v.s. t^2 for both numerical and analytical calculation can then be compared. Note that the analytical and numerical evaluations above can be extended to the free expansion in two dimensions in Cartesian coordinates in the same manner as what we have done with the 1D expansion, i.e., for the analytical evaluation,

$$f(x,y,t) = \frac{1}{2\pi\sigma_x(t)\sigma_y(t)} \cdot \exp\left[-\frac{x^2}{2\sigma_x^2(t)} - \frac{y^2}{2\sigma_y^2(t)}\right], \tag{E.49}$$

and for the numerical evaluation,

$$f(x,y,t) \;=\; \tilde{\alpha}\,\tilde{\mathfrak{F}}\big\{\mathfrak{F}\{g(x,y)\}\cdot\mathfrak{F}\{h(x,y)\}\big\}, \tag{E.50}$$

where

$$g(x,y) = \frac{1}{2\pi\sigma_x\sigma_y}\exp\left[-\frac{x^2}{2\sigma_x^2} - \frac{y^2}{2\sigma_y^2}\right]$$

and

$$h(x,y) = \frac{1}{2\pi\sigma_{vx}\sigma_{vy}}\exp\left[-\frac{x^2}{2\sigma_{vx}^2t^2} - \frac{y^2}{2\sigma_{vy}^2t^2}\right].$$

The 2D convolution can be evaluated in MATLAB as

```
f = abs(ifft2c(fft2c(g).*fft2c(h)))/(sum(sum(g))*t^2);
```

where `fft2c(A)` and `ifft2c(A)` of a 2D matrix `A` can be written [172] as

```
fft2c(A) = fftshift(fft2(ifftshift(A)));
ifft2c(A) = ifftshift(ifft2(fftshift(A)));
```

The comparison of the 2D expansion for both evaluations is shown to be in agreement in Fig. E.8. For this expample, $\sigma_x^2 = \sigma_y^2 = 3.1153 \times 10^{-7}\text{m}^2$ and $\sigma_{vx}^2 = \sigma_{vy}^2 = \sigma_v^2 = 1.9459 \times 10^{-3}\text{m}^2/\text{s}^2$.

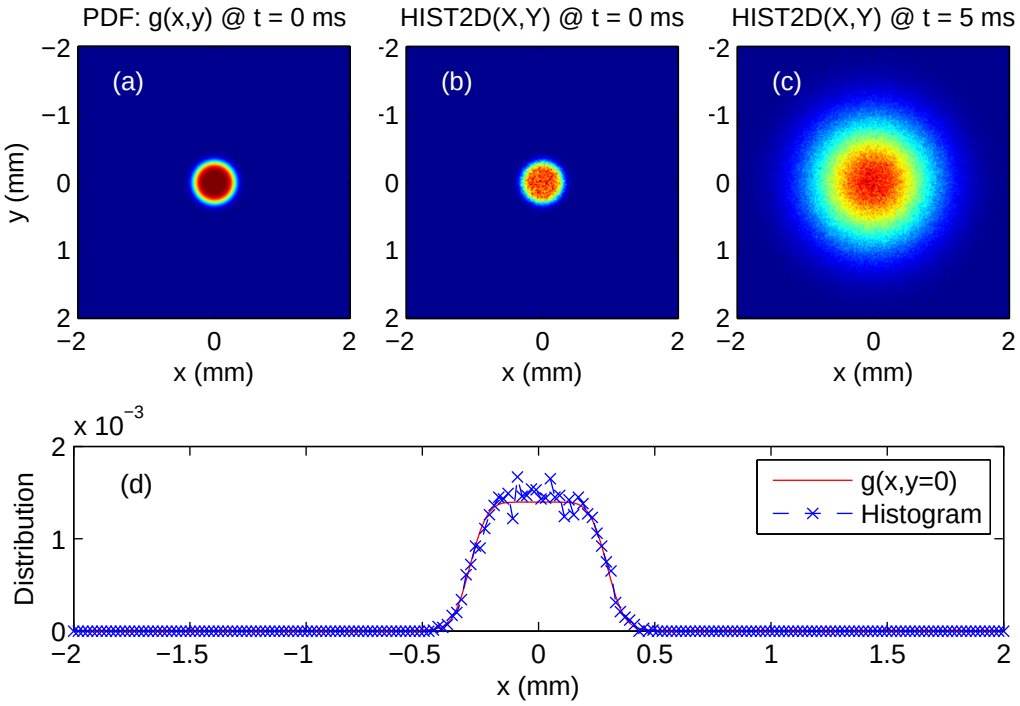

Figure E.9: Monte-Carlo Samples: (a) a probability distribution function $g(x, y)$ at $t = 0$, (b) a 2D histogram of a random variable (X, Y) drawn from the distribution in (a) as described in the text, and (c) the free expansion of (b) at $t = 5$ ms. The histogram in (b) contains 1×10^5 samples, while it is 2×10^6 in (c) to compensate for the spread of the distribution. The plots in (d) shows the distributions along the x-axis at $y = 0$ of the distribution in (a) (red) and (b) (blue).

E.4.3 Free Expansion: Monte Carlo vs. Convolution method

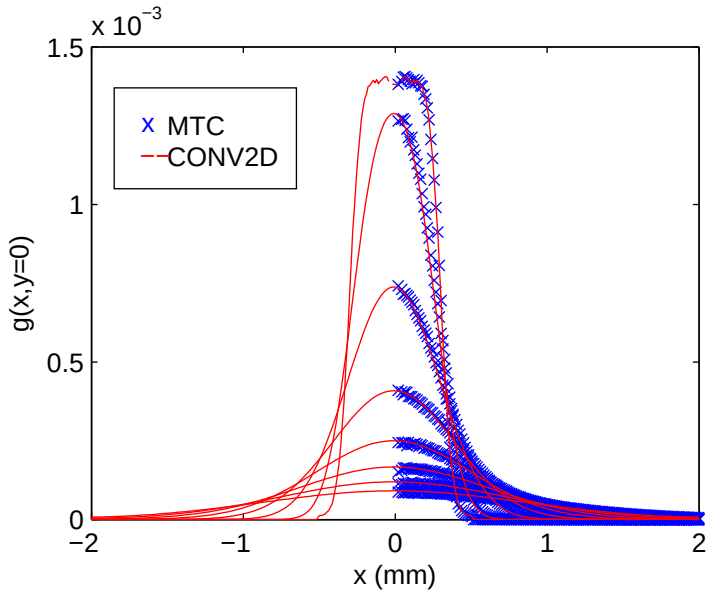

Figure E.10: A comparison of free expansion profiles obtained from a classical trajectory Monte-Carlo simulation (blue cross) and a 2D convolution method (red line). The profiles are obtained from the convolution between a non-Gaussian spatial distribution and a Gaussian velocity distribution as discussed in the text. As time increases, the width of the distribution increases while the amplitude decreases.

In the previous section, we consider free expansion of a distribution that is Gaussian in both spatial and velocity spaces and can be described analytically. In this section, we look at a non-analytical free-expansion which can be calculated numerically via a classical trajectory Monte-Carlo method (MC) derived from the first principle. We then can use the results from the MC to further check the validity of the convolution method mentioned in the previous section. If they are in good agreement, in some cases that the convolution method can be applied (e.g. when $h(v)$ does not depend on spatial coordinates or when the Gaussian expansion dominates at large t), it will be our method of choice because it is significantly computationally inexpensive compare to the MC method.

We begin our 2D Monte-Carlo method by sampling, at time $t = 0$, N random variable pairs of (X_i, Y_i) and (U_i, V_i) from two arbitrary spatial probability distribu-

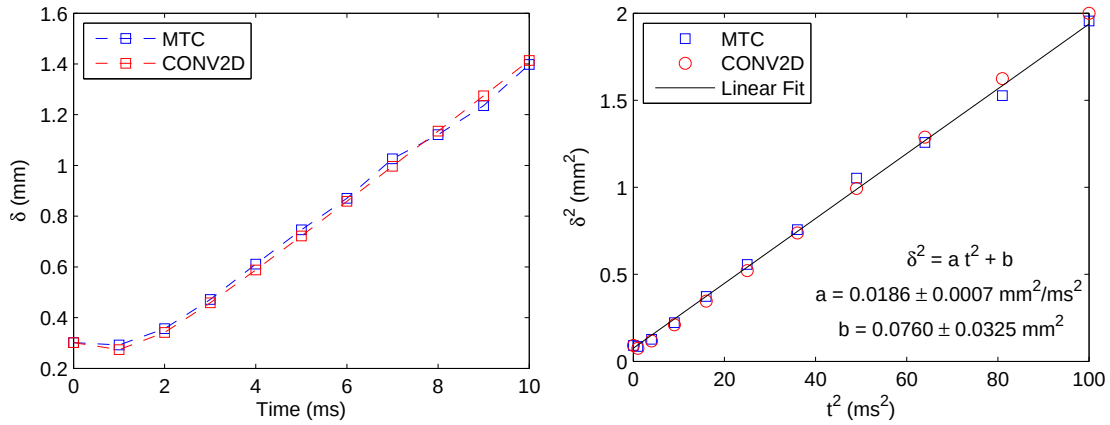

Figure E.11: A comparison of free expansion rates obtained from a classical trajectory Monte-Carlo simulation (blue square) and a 2D convolution method (red square) of the distributions displayed in Fig. E.10: (Left) the plots of the half-width- half- max, δ, vs. time, and (Right) the plots of δ^2, vs. squared time. The rates of expansion are obtained from slop of the later as discussed in the text.

tions, $g(x, y)$ and $h(u, v)$ respectively. In practice, the variables can be stored in a $2 \times N$-matrix (X, Y) and (U, V) accordingly. Next we note that for each quadruple (X_i, Y_i, U_i, V_i), we can find a new location $(X_i(t), Y_i(t)) = (X_i + U_i t, Y_i + V_i t)$ at time $t = n\Delta t$, where $n = 0, 1, 2, 3, \ldots$, and Δt is a time increment. The spatial distribution at t for each n, $f(x, y, n\Delta t)$, can be obtained by calculating a 2D-histogram of each updated (X, Y) [173]. As an example, we consider

$$g(x, y) = \alpha_g \exp\left\{-\alpha J_n^2[k\,(x^2 + y^2)^{1/2}]\right\}, \tag{E.51}$$

and

$$h(u, v) = \frac{1}{2\pi\sigma_v^2} \exp\left[-\frac{u^2 + v^2}{2\sigma_v^2}\right], \tag{E.52}$$

where $\alpha = 30$, $n = 4$, $k = 10.6351$ mm^{-1}, $g(x, y) = 0$ when $(x^2 + y^2)^{1/2} > 0.5$ mm and $\sigma_v = 0.1208$ mm/ms. A random spatial variable matrix (X, Y) is obtained numerically using MATLAB user-defined functions `randp2Dcs()` and `cs2randp2D()` as shown in Appendix G.7. For a random velocity variable matrix (U, V) the MATLAB built-in function `randn()` is used. A MATLAB code for the free expansion using the 2D convolution method and the Monte-Carlo simulation can be seen in

Appendix G.6 and Appendix G.7 respectively.

Some selected distribution's line profiles $f(x, y = 0, n\Delta t)$ for different values of n, from the Monte-Carlo simulation can be seen in Fig. E.10. As n increases, the half- width- half- max, δ, of the distribution also increases while the peak of the profile decreases. This is shown in the plot of δ vs. time in Fig. E.11. Both the line profiles and the plot of $\delta(t)$ are shown to be in good agreements with those obtained from the 2D convolution method as seen in the figures.

There is one remark to be pointed out here. For the expansion of the non-Gaussian distribution started initially as shown in Fig.E.9, the plot of $\delta^2(t)$ fits to a line. This is similar to the case where we start out with the Gaussian spatial distribution. If they both starts with the same δ, the slope of the fits for both cases are also similar. The Gaussian distribution expands $\sim 4\%$ faster. For a Gaussian distribution, the slope of the plot $\delta^2(t)$ vs t^2 is $2\ln(2)$ times the slope of $\sigma^2(t)$ vs t^2, which is σ_v^2. This allows us to assign σ_v^2 as a characteristic expansion parameter for the expansion of the initial profile that is Gaussian or the one shown in Fig. E.9. However, if the initial profile has side lobes as seen in Fig. E.12, the plot of $\delta^2(t)$ becomes drastically different and cannot be fit to a line (see Fig. E.13). This is to keep in mind because our experimental profiles also have side lobes. Therefore in general, it is not enough to conclude that a non-Gaussian expansion can be characterized by σ_v^2 that is obtained from $\delta^2(t)$.

E.5 Numerical Simulation of LE

So far, we only look at two limiting cases of LE i.e. the steady state LE and the force-free LE (a.k.a. free expansion). Now, we will look at the full LE, which is time dependent. The equation is generally hard to solve analytically (if not at all impossible), so we need to solve it numerically. There are several methods to do it. The most modern one is the lattice Boltzmann model. Here we will solve the equation using a split-operator method [120] to arrive at the same conclusion as what was done in [168, 169, 170] in the context of fractional steps and weak

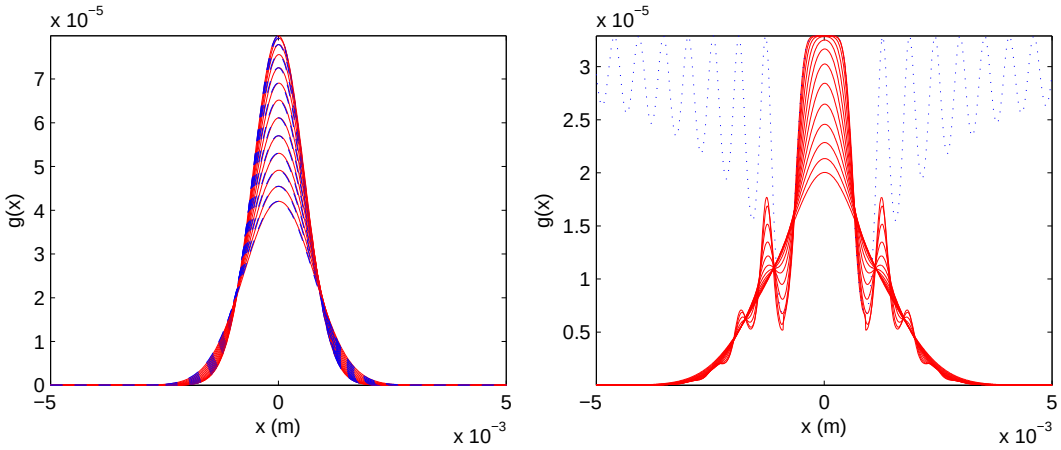

Figure E.12: A comparison of free expansion profiles of a Gaussian (left) and a non-Gaussian (right) distributions with the same δ at $t = 0$.

approximation [168]. Note that there are also routines for solving the Boltzmann equation including collision terms (which is the extension of the Liouville equation) available from astrophysics community. Some examples for these routines are ZEUS-2D [174] and ZEUS-3D [175].

The solution of the LE (Eq. E.1) in the operator form [176] is

$$f_{t+\Delta t} = \exp\left[-\int_{t}^{t+\Delta t} (\vec{v}\cdot\nabla_{\vec{r}} + \vec{a}\cdot\nabla_{\vec{v}})\, dt'\right] f_t. \tag{E.53}$$

This solution can be derived from the Dyson scheme as shown below [177]. Considering a distribution Ψ that satisfies an equation usually appears in physics,

$$\frac{1}{\alpha}\frac{\partial\Psi}{\partial t} = H\Psi, \tag{E.54}$$

where H is a linear operator that is implicit in time [176]. The solution can be written as

$$\Psi = \Psi_i + \alpha\int H\Psi dt \tag{E.55}$$

This implicit solution can be resolved using iteration to assemble an infinite series

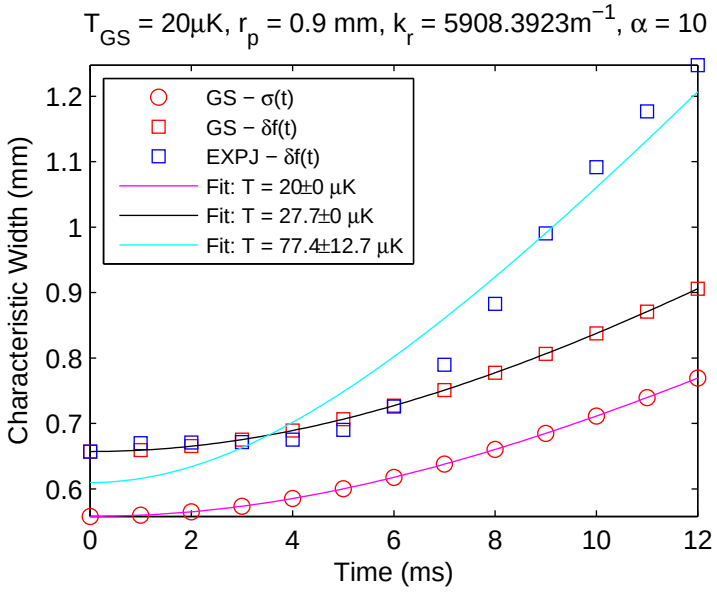

Figure E.13: In the figure, a plot of characteristic width or half- width- half- max δ vs. time of a Gaussian distribution (red square) is shown against that of a non-Gaussian distribution (blue square). They are obtained from the profiles in Fig. E.12. The plot of a non-Gaussian distribution does not follow the quadratic rule as described by Eq. E.46 unlike the plot from the Gaussian one. The width of the non Gaussian (with side lobes) starts to deviates greatly from the width of the Gaussian after a certain time ($t \geq 6$ ms) when the contribution from the side lobes start to affect the central distribution. Also seen the figure, the plot of the Gaussian half width $\sigma(t)$ that is $2\ln 2$ times lower than that of the Gaussian $\delta(t)$.

i.e.

$$\begin{aligned}
\Psi &= \Psi_i + \alpha \int_0^t dt_1 H(t_1)\Psi_i + \alpha^2 \int_0^t dt_1 \int_0^{t_1} dt_2 H(t_1)H(t_2)\Psi_i + ... \\
&= \Psi_i + \alpha \int_0^t dt_1 H(t_1)\Psi_i + \frac{1}{2!}\alpha^2 \left[\int_0^t dt_1 H(t_1)\right]^2 \Psi_i + ... \\
&= \exp\left(\alpha \int_0^t H dt'\right)\Psi_i. \qquad \text{(E.56)}
\end{aligned}$$

The factorial denominators in front of α are the combinatoric factor when changing the order of integration among dt_i.

The operator in Eq. E.53 can be split to second order in Δt as shown below

$$f_{t+\Delta t} = \exp\left(-\vec{v}\cdot\nabla_{\vec{r}}\,\Delta t/2\right)\exp\left(-\vec{a}\cdot\nabla_{\vec{v}}\,\Delta t\right)\exp\left(-\vec{v}\cdot\nabla_{\vec{r}}\,\Delta t/2\right)\,f_t. \tag{E.57}$$

The solution has an error of the third order in Δt ($O(\Delta t^3)$). The proof of the second-order accuracy of the splitting scheme above was shown in the Appendix A of [121].

The operator $\exp(\vec{v}\cdot\nabla_{\vec{r}}\,\Delta t/2)$ acting on f_t, i.e. $f^* = \exp(\vec{v}\cdot\nabla_{\vec{r}}\,\Delta t/2)\,f_t$ is equivalent to solving, over the time $\Delta t/2$, the following equation

$$\frac{\partial}{\partial t}f^* + \vec{v}\cdot\nabla_{\vec{r}}f^* = 0. \tag{E.58}$$

The solution of this equation is what we have seen before when we solved the free-expansion problem. The solution is $f^*(x,y,v_x,v_y) = f_t(x-v_x\Delta t/2, y-v_y\Delta t/2, v_x, v_y)$.

Similarly, the operator $\exp(\vec{a}\cdot\nabla_{\vec{v}}\,\Delta t)$ acting on the function on its right, f^*, is equivalent to solving, over time Δt,

$$\frac{\partial}{\partial t}f^{**} + \vec{a}\cdot\nabla_{\vec{v}}f^{**} = 0. \tag{E.59}$$

The solution is $f^{**}(x,y,v_x,v_y) = f^*(x,y,v_x - a_x\Delta t, v_y - a_y\Delta t)$. The last operator $\exp(\vec{v}\cdot\nabla_{\vec{r}}\,\Delta t/2)$ acting on f^{**}, is equivalent to solving, over the time $\Delta t/2$, the following equation

$$\frac{\partial}{\partial t}f_{t+\Delta t} + \vec{v}\cdot\nabla_{\vec{x}}f_{t+\Delta t} = 0. \tag{E.60}$$

The solution of this equation is, as before, $f_{t+\Delta t}(x,y,v_x,v_y) = f^{**}(x - v_x\Delta t/2, y - v_y\Delta t/2, v_x, v_y)$.

Thus we end up solving three equations in succession. The process of getting to the final solutions, $f_{t+\Delta t}(x,y,v_x,v_y)$, can be summarized through the steps as shown below.

$$\begin{aligned} f^*(x,y,v_x,v_y) &= f_t(x - v_x\Delta t/2, y - v_y\Delta t/2, v_x, v_y), \\ f^{**}(x,y,v_x,v_y) &= f^*(x,y,v_x - a_x\Delta t, v_y - a_y\Delta t), \\ f_{t+\Delta t}(x,y,v_x,v_y) &= f^{**}(x - v_x\Delta t/2, y - v_y\Delta t/2, v_x, v_y). \end{aligned} \tag{E.61}$$

Since the simulation is done on a discrete mesh, we need to extrapolate the distributions in order to shift them in time according to the steps shown above.

The extrapolations are implemented using a MATLAB function called `spline()` (slow method) or using `fft2()` (fast method). The MATLAB codes that is used to solve the LE is shown in Appendix G.8.

E.6 Ensemble Evolution with a Force Function: Monte-Carlo Simulation

The evolution of a collisionless MOT ensemble inside a optical potential can be simulated directly from the first principle similar to what we have described in Sec. E.4.3 for the case of the free expansion. However, in addition to drawing the initial random spatial and velocity variables from appropriate distribution functions, we also obtain acceleration

$$(AX_i, AY_i) = \left(-\frac{1}{m}\frac{\partial}{\partial x}U(x,y), -\frac{1}{m}\frac{\partial}{\partial y}U(x,y)\right)$$

of a potential $U(x,y)$ at a point $(x,y) = (X_i, Y_i)$ where m is the particle mass. The updated location at time t can be written as

$$(X_i(t), Y_i(t)) = \left(X_i + U_i t + \frac{1}{2}Ax_i t^2 \ , \ Y_i + V_i t + \frac{1}{2}Ay_i t^2\right),$$

the velocity pair is updated to

$$(U_i(t), V_i(t)) = (U_i + Ax_i t \ , \ V_i + Ay_i t)\,,$$

and the acceleration pair is updated to $(Ax_i(t), Ay_i(t))$ evaluated from $U(x,y)$ evaluated at the new location $(x,y) = (X_i(t), Y_i(t))$.

One distinct difference from the free expansion case is that, here the time increment cannot be arbitrary large because the potential changes the velocity of the particle depending on its location. The error from this method thus comes from the particle with high velocity or the one that locate at the place where the potential changes the velocity significantly. One way to reduce this error is to have the time increment small enough so that the particles that travel with rms velocity can only propagate not more than one simulation pixel for each update. A MATLAB code that implements this simulation can be found in Appendix G.9.

Appendix F

Split-Operator Method: Numerical Implementation

In this Appendix, we will follow Feit *et al.* [120] to show the split-operator method that we will use to solve the Schrödinger equation. In the following we will calculate eigen-energies and eigen-functions for the single- and multi- mode tunnel described in Chapter 6.

The time dependent Schrödinger equation can be written as

$$i\hbar\frac{\partial\Psi}{\partial t} = -\frac{\hbar^2}{2m}\nabla^2\Psi + U(x,y)\Psi, \tag{F.1}$$

and the solution of this equation can be written as

$$\begin{aligned}\Psi_{t+\Delta t} &= \exp\left[\int_t^{t+\Delta t}\left(-\frac{i\hbar}{2m}\nabla^2 + \frac{U(x,y)}{i\hbar}\right)\,dt\right]\Psi_t \\ &= \exp\left(-\frac{i\hbar\Delta t}{2m}\nabla^2 + \frac{U(x,y)}{i\hbar}\Delta t\right)\Psi_t.\end{aligned} \tag{F.2}$$

The exponential can be split to second order in Δt as

$$\Psi_{t+\Delta t}(x,y) = G^U_{\Delta t/2}G^K_{\Delta t}G^U_{\Delta t/2}\;\Psi_t(x,y), \tag{F.3}$$

where

$$G^U_{\Delta t/2} = \exp\left(\frac{1}{2}\frac{U(x,y)}{i\hbar}\,\Delta t\right),$$

and

$$G^K_{\Delta t} = \exp\left(-\frac{i\hbar}{2m}\nabla^2\,\Delta t\right).$$

We can evaluate Eq. F.3 numerically by first constructing a grid of spatial coordinates, (x,y), that the values of $\Psi_{t+\Delta t}(x,y)$ will be determined. The grid can be represented by discrete coordinates, (x_i,y_j), as shown below.

$$(x_i,y_j) = \left(-\frac{a_0}{2} + (i-1)\Delta x, -\frac{a_0}{2} + (j-1)\Delta y\right) \tag{F.4}$$

where $i, j = 1, 2, 3, \ldots,$ M. From this construction, we have the length of the simulation area equal to a_0. The coordinates run from $-a_0/2$ to $+a_0/2$ and are divided into M cells. Thus $\Delta x = \Delta y = \Delta q = a_0/(M-1)$ for a square grid.

Next, to evaluate Eq. F.3, we consider consecutively the operations of $G^K_{\Delta t}$ and $G^U_{\Delta t/2}$ on $\Psi_t(x, y)$ as represented on the grid, (x, y).

The operation $G^U_{\Delta t/2}$ on $\Psi_t(x, y)$ is straightforward since both $G^U_{\Delta t/2}$ and $\Psi_t(x, y)$ can be represented as arrays of numbers on the (x,y) grids. The operation is simply an element-by-element multiplication of both arrays i.e. an element of the arrays, $\Psi^U(x, y) = G^U_{\Delta t/2}\Psi_t(x, y)$, can be written as

$$\Psi^U(x_i, y_i) = G^U_{\Delta t/2}(x_i, y_j)\, \Psi_t(x_i, y_j).$$

After we get Ψ^U, the next step is to evaluate $\Psi^{KU} = G^K_{\Delta t}\Psi^U$. This is equivalent to solving the free-particle equation below

$$i\hbar\frac{\partial\Psi^{KU}(x, y)}{\partial t} = -\frac{\hbar^2}{2m}\nabla^2\Psi^{KU}(x, y). \tag{F.5}$$

Because the equation involves derivatives, we can solve it by applying the inverse Fourier transform of $\Psi^{KU}(x, y)$ as shown below.

$$\Psi^{KU}(x, y) = \frac{1}{2\pi}\int_{k_x=-\infty}^{+\infty}\int_{k_y=-\infty}^{+\infty}\Psi^{ku}(u, v)\exp(-iu\,x - iv\,y)\,du\,dv, \tag{F.6}$$

where u and v are the spatial frequencies complimentary to x and y respectively. Substitute Eq. F.6 into Eq. F.5, we have the equation for $\Psi^{ku}(u, v)$ in the uv-space as shown below

$$i\hbar\frac{\partial\Psi^{ku}(u, v)}{\partial t} = \frac{\hbar^2}{2m}(u^2 + v^2)\,\Psi^{ku}(u, v). \tag{F.7}$$

The solution for the equation above is

$$\begin{aligned}\Psi^{ku}(u, v) &= \exp\left[-\frac{i\hbar}{2m}(u^2 + v^2)\,\Delta t\right]\Psi^u(u, v)\\ &= G^k_{\Delta t}\Psi^u(u, v).\end{aligned} \tag{F.8}$$

The initial $\Psi^u(u, v)$ in the uv-space can be obtained by applying Fourier transform to initial $\Psi^U(x, y)$ in the xy-space i.e. $\Psi^u(u, v) = \mathfrak{F}\left\{\Psi^U(x, y)\right\}$ where we denote $\mathfrak{F}$

as the Fourier transform. Once the solution in the uv-space is obtained, we can use the inverse Fourier transform (Eq. F.6) to get back the solution, $\Psi^{KU}(x,y)$, in the xy-space. If we denote $\tilde{\mathfrak{F}}$ as the inverse Fourier transform, the process above can be summarized as $\Psi^{KU}(x,y) = \tilde{\mathfrak{F}}\left\{G^k_{\Delta t}\mathfrak{F}\left\{\Psi^U(x,y)\right\}\right\}$.

Finally, we evaluate $\Psi_{t+\Delta t}(x,y) = G^U_{\Delta t/2}\Psi^{KU}(x,y)$ in the same way as what we have done to $\Psi_t(x,y)$ earlier. The whole process for propagating $\Psi_t(x,y)$ from t to $t+\Delta t$ can be summarized as

$$\Psi_{t+\Delta t}(x,y) = G^U_{\Delta t/2}\tilde{\mathfrak{F}}\left\{G^k_{\Delta t}\mathfrak{F}\left\{G^U_{\Delta t/2}\Psi_t(x,y)\right\}\right\}. \tag{F.9}$$

Note that, due to the convention in the discrete Fourier transform, the length of the simulation in the uv-space is $2\pi/\Delta q$. The coordinates in the uv-space run from $-\pi/\Delta q$ to $+\pi/\Delta q$ and is also divided into M elements i.e. $\Delta u = \Delta v = 2\pi/(M-1)\Delta q = 2\pi/a_0$ for square grids. Thus, the coordinates in the uv-space, (u,v), can be written in a discrete form as:

$$\begin{aligned}(u_i, v_j) &= \left(-\frac{\pi}{\Delta q} + (i-1)\Delta u, -\frac{\pi}{\Delta q} + (j-1)\Delta v\right) \\ &= \left(\frac{\pi}{a_0}(2i - M - 1), \frac{\pi}{a_0}(2j - M - 1)\right) \end{aligned} \tag{F.10}$$

where $i, j = 1, 2, 3, \ldots,$ M.

We can get the eigen-energies by tracking a propagation of a wave packet in time via a correlation function, $P(t)$ below

$$P(t) = \langle \Psi_{t=0}(x,y) | \Psi_t(x,y) \rangle . \tag{F.11}$$

If we write the wave packet, $\Psi_t(x,y)$, in terms of eigen-functions, $u(x,y)$, as

$$\Psi_t(x,y) = \sum\nolimits_{n,j} a_{n,j} u_{n,j}(x,y) \exp(-iE_n t), \tag{F.12}$$

where j denotes degenerate states, E_n the eigen-energies and $u_{n,j}$ satisfies

$$-\frac{\hbar^2}{2m}\nabla^2 u_{n,j} + U(x,y)u_{n,j} = E_n u_{n,j}, \tag{F.13}$$

the correlation function can be rewritten as

$$P(t) = \iint \Psi^*_{t=0}(x,y)\Psi_t(x,y)\, dx\, dy \tag{F.14}$$

$$= \sum\nolimits_{n,j} |a_{n,j}|^2 \exp(-iE_n t). \tag{F.15}$$

By applying Fourier transform on $P(t)$ in Eq. F.15, we can get a profile of $P(E)$ that has several spikes (as shown in Fig. 6.4). The spikes peak at eigen-energies given by the equation below

$$P(E) = \sum\nolimits_{n,j} |a_{n,j}|^2 \, \delta(E - E_n). \tag{F.16}$$

In a discrete form, we can evaluate the integral $P(t)$ in Eq. F.14 by using a trapezoidal integration, i.e.

$$P(t) = \sum_i \sum_j \frac{\Delta x}{2} \frac{\Delta y}{2} \left(\chi(x_i, y_j) + \chi(x_{i+1}, y_{j+1}) \right) \tag{F.17}$$

where $\chi(x, y) = \Psi_0^*(x, y)\Psi_t(x, y)$. If we use $\Psi_{t+\Delta t}(x, y)$ from Eq. F.9, $P(t)$ will be discrete in time. In this case, P(t) has a finite length and $t = h\Delta t$, where $h = 0, 1, 2, \ldots, N_t - 1$. This makes the peaks of $P(E)$ not as sharp as those of the delta functions. We can modified $P(E)$ to accommodate this feature as shown below.

$$\begin{aligned} \tilde{P}(E) &= \int_{t=0}^{T} w(t) P(t) \exp(iEt) \, dt \\ &= \sum\nolimits_{n,j} |a_{n,j}|^2 \, \mathfrak{L}(E - E_n) \end{aligned} \tag{F.18}$$

where

$$w(t) = \begin{cases} 1 - \cos(2\pi t/T); & 0 \le t \le T, \\ \\ 0; & t > T, \end{cases}$$

and

$$\begin{aligned} \mathfrak{L}(E - E_n) &= \frac{1}{T} \int_0^T \exp\left[i(E - E_n)t \right] \, w(t) \, dt \\ &= -\frac{1}{2} \left[\frac{\exp\left[i(E - E_n)T + i2\pi \right] - 1}{i(E - E_n)T + i2\pi} + \frac{\exp\left[i(E - E_n)T - i2\pi \right] - 1}{i(E - E_n)T - i2\pi} \right] \\ &\quad + \frac{\exp\left[i(E - E_n)T \right] - 1}{i(E - E_n)T}. \end{aligned} \tag{F.19}$$

Because $P(t)$ is discrete, $P(E)$ is also discrete. The energy, E, ranges from $-\pi\hbar/\Delta t$ to $+\pi\hbar/\Delta t$ and has the same number of elements as in $P(t)$ i.e. N_t elements. Thus $E_{\max} - E_{\min} = 2E_{\max} = 2\pi\hbar/(N_t - 1)\Delta t$. As suggested by Feit *et al.* [120], Δt

should be small enough to cover the range of the potential used in the calculation and $\Delta t = 2\pi\hbar/3\,U_{max}$ is considered to be appropriate.

After we get the eigen-energies from the plot of $P(E)$, we can use them to find their eigen-functions as well. If we apply the Fourier transform to Eq. F.12, we will have

$$\begin{aligned} \Psi(x,y,E) &= \int \Psi(x,y,t)\exp(iEt)\,dt \\ &= \sum\nolimits_{n,j} a_{n,j}u_{n,j}(x,y)\delta(E-E_n) \end{aligned} \tag{F.20}$$

If $E = E_n$ and $\Psi(x,y,t)$ contains only non-degenerate states throughout the time of propagation, then $\Psi(x,y,E_n) = a_n u_n$. In other words, if we know E_n, we can get $\Psi(x,y,E_n)$ which is proportional to the eigen-function that corresponds to eigen-energy E_n. In the case of degenerate states, the initial wave packet should be chosen so that the degeneracy among states is broken toward the desired eigen-function. For example, if we have a degeneracy in a pair of angular momentum states, one rotates clockwise and the other counterclockwise, the degeneracy will be broken toward the clockwise state if we choose the initial wave function to be clockwise.

Note that in reality, a Fourier transform of $\Psi(x,y,t)$ does not produce a pure eigen-function (even when degenerate issue is already taken care of). The reason is that the uncertainties in eigen-energies are not zero because the propagation time of $\Psi(x,y,t)$ is finite. Therefore we need to modify Eq. F.20 further as shown below.

$$\tilde{\Psi}(x,y,E) = \int_{t=0}^{T} w(t)\Psi(x,y,t)\exp(iEt)\,dt \tag{F.21}$$

$$= \sum\nolimits_{n,j} a_{n,j}u_{n,j}(x,y)\mathfrak{L}(E-E_n) \tag{F.22}$$

Numerically, we typically use a trapezoidal integration to evaluate the integration in Eq. F.21 for a series of matrices, $\Psi(x,y,h\Delta t)$, that are discrete in time i.e.

$$\begin{aligned} \tilde{\Psi}(x,y,E_m) = &\frac{\Delta t}{2}\Bigg[w(0)\Psi(x,y,0) \\ &+ 2\sum_{h=1}^{N_t-1} w(h\Delta t)\Psi(x,y,\Delta t)e^{iE_m h\Delta t} \\ &+ w(N_t\Delta t)\Psi(x,y,N_t\Delta t)e^{iE_m N_t\Delta t}\Bigg]. \end{aligned} \tag{F.23}$$

Appendix G
Computer Codes

In this Appendix, we list names and descriptions of the softwares that we used to produce the work presented in this thesis so that an interested reader can investigate it or use it in his/her own work. The source codes are provided after this list, according to the order presented here.

G.1 Controlling Camera and DDG (C/C++ codes) – This code is written to control camera to grab shadow images and the digital delay generator to trigger mechanical shutters and AOMs. The code uses a library from XCAP to control a frame grabber (via a PIXCI board) and a National Instrument library to control the GPIB devices (via a GPIB card). The program reads a text file that contains series of numbers related to time delays for the pulses described in Chapter 3.

G.2 Grab images with MATLAB (MATLAB-C/C++) – This C/C++ code is used to take a snap short ($\sim 100\ \mu$s) of atom ensemble in our experiment. It integrates MATLAB library with libraries for a frame grabber and GPIB devices so that they can be controlled via MATLAB command window. To compile the code, links to grabimg.cpp, grabimg.def, mexversion.rc, and mexversion.rc are needed as described in the MATLAB document. The code can be compiled to "grabimg.dll" which is a dynamic library that can run in MATLAB in the same way as MATLAB built-in functions.

G.3 Image processing using MATLAB – This code is a MATLAB script that uses grabimg.dll described above to take pictures of shadow images and average them. The code shows how we typically use MATLAB to generate an averaged image.

G.4 Phase Mask Generating using MATLAB – This MATLAB function generates a phase mask to produce a Bessel beam as described in Sec. 2.2. For example, to generate a J_4-Bessel beam with $k_r = 10000$ m^{-1} and the ellipticity ratio $\eta_x/\eta_y = 1.03$ (as described in Sec. 2.4.6), the input command to MATLAB that stores the mask in a matrix `M` is

```
>> M = maskgen('charge',4,'kr',10000,'scalex',1.03,'scaley',1);.
```

G.5 Propagation of Scalar Field – This section shows three MATLAB scripts that demonstrate three different methods for field propagation as described in Sec. C. They are (1) an angular spectrum method using the Hankel transform, (2) a 2D angular spectrum using the fast Fourier transform (FFT), and (3) a 2D paraxial approximation method using the FFT.

G.6 Convolution Codes: 2D Free Expansion – This is a MATLAB script used to generate an example of 2D free expansion profiles similar to that describe in Appendix E.4.

G.7 Classical Trajectory Monte-Carlo Method: 2D Free Expansion – a MATLAB script in this section contains an example of a 2D free expansion as described in Appendix E.4.3.

G.8 Liouville's Equation Solver – The following code demonstrate an example that uses the function `cbe_get_fft_propagation()` or `cbe_get_propagation()` to solve the Liouville equation for a Bessel potential with $U_{max} = 300\mu$K high. The initial spatial distribution of an ensemble is Gaussian in both coordinate and velocity space. The temperature of the ensemble is also 300μK. The function `cbe_get_fft_propagation()` required user defined functions `fftc()` and `ifftc()` as shown in G.11 to interpolate the ensemble distribution in the phase space as described in Appendix E.5. This function is at least 10 times faster than `cbe_get_propagation()` which uses a function called `spline()` to interpolate the distribution.

G.9 Classical Trajectory Monte-Carlo Method: with Force Term – This MATLAB

script demonstrates classical trajectory Monte-Carlo Method with a non-zero force term as described in Sec. E.6.

G.10 Split-Operator Codes – The script `scp_so_get_en_wf.m` uses the split-operator calculation to find an eigen-energies and eigen-functions in the first ring of a Bessel potential described in Sec. 6.3 and Appendix F. The script obtained the grid of spatial coordinates and theirs spatial frequency from `so_get_grid()`. The spatial grid is used to construct the user-defined potential via the function `so_get_potential_ring()`. At the boundary of the simulation, a portion of the wavepacket that reaches the boundary get suppressed by the function `so_get_dampbound()` to eliminate reflection from the boundary (via FFT or IFFT). The initial wavepacket is generated by `so_get_initwavepacket()` and propagate by using `so_get_correlation()` under the propagator generated from the function `so_get_propagator()`. The eigen-energies and their eigen-functions are calculated from the function `so_get_eigenergy()` and the function `so_get_eigfunction()` respectively.

G.11 Miscellaneous – This section includes source codes used in some of the MATLAB scripts or functions shown in the list. They are (1) a 2D centered discrete Fourier transform (`fft2c`), (2) a 2D centered inverse discrete Fourier transform (`ifft2c`), (3) a radial scan script (`scp_rscan_pol2.m`), and (4) a radial scan function (`rscan_pol2`). The first and second ones are used to obtained the FFT that has zero frequency component in the middle of the Matrix instead of at the edge as is usually done in the normal FFT function. The third code is the script that use the fourth code to convert a distribution matrix into a radial profile in polar coordinates.

G.1 Controlling Camera and DDG (C/C++ codes)

SCRIPTGRAB103.CPP

```
#include <direct.h>
#include <stdlib.h>
#include <stdio.h>
#include <string.h>
#include <windows.h>
#include <conio.h>
#include <math.h>
extern"C"
{
#include "decl-32.h"    /* GPIB Library */
#include "xcliball.h"   /* PIXCI Library */
}
int Ch;
void SetupGpib(int);
void CloseGpib(int);
void OpenPixciBoard(void);
void ClosePixciBoard(void);
void SetDelayChnl(int,int,int,int);
void SvImg(int,int,int,int,int,int,int,int,char myfolder[50]);
FILE *stream;
FILE *streamout;
void main()
{
   int dpa1 = 14, dpa2 = 15, dg1, dg2;
   int numShft,numAvg;
   int dlyTmShft=0,bcgShft=0,myShft;
   int shftLoop, avgLoop, buffLoop;
   int iniDlyTmA,iniDlyTmA2;
   int iniDlyTmB,iniDlyTmB2;
   int iniDlyTmC,iniDlyTmC2;
   int iniDlyTmD,iniDlyTmD2;
   int iniBffgrp,lastBffgrp,iniBffSv,lastBffSv;
   int sleepTm1=5000,sleepTm2=5000;
   pxcoord_t ulx=0, uly=0, lrx=-1, lry=-1;
   char imgfolder[50];
   char logname[70];
   stream = fopen( "SG103param.txt","r+" );
   if( stream == NULL )
      printf( "The file SG102param.txt was not opened\n" );
   else
   {
      fseek( stream, 0L, SEEK_SET );
      fscanf( stream, "%d", &dpa1 );
      fscanf( stream, "%d", &numShft );
      fscanf( stream, "%d", &numAvg );
      fscanf( stream, "%d", &dlyTmShft );
      fscanf( stream, "%d", &bcgShft );
      fscanf( stream, "%d", &iniDlyTmA );
      fscanf( stream, "%d", &iniDlyTmB );
      fscanf( stream, "%d", &iniDlyTmC );
      fscanf( stream, "%d", &iniDlyTmD );
      fscanf( stream, "%d", &dpa2 );
      fscanf( stream, "%d", &iniDlyTmA2 );
      fscanf( stream, "%d", &iniDlyTmB2 );
      fscanf( stream, "%d", &iniDlyTmC2 );
      fscanf( stream, "%d", &iniDlyTmD2 );
      fscanf( stream, "%d", &iniBffgrp );
      fscanf( stream, "%d", &lastBffgrp );
      fscanf( stream, "%d", &iniBffSv );
      fscanf( stream, "%d", &lastBffSv );
      fscanf( stream, "%d", &sleepTm1 );
      fscanf( stream, "%d", &sleepTm2 );
      fscanf( stream, "%d", &ulx );
```

```
   fscanf( stream, "%d", &uly );
   fscanf( stream, "%d", &lrx );
   fscanf( stream, "%d", &lry );
   fscanf( stream, "%s", imgfolder );
   fclose( stream );
}
int myerr = _mkdir( imgfolder );
if( myerr == 0 )
{
   printf( "Directory %s was successfully created\n", imgfolder );
   // see _mkdir in MSVC Help|index|_mkdir
}
else if(myerr == -1)
{
   printf( "Problem creating directory %s\n", imgfolder );
   printf( "Message: %s\n", strerror(errno) );
   printf( "Error: %d\n", errno );
   exit(1);
}
strcpy( logname, imgfolder );
strcat( logname, "SG103param.txt" );
streamout = fopen( logname,"w+" );
if( streamout == NULL )
   printf( "The file %s was not opened\n",logname );
else
{
   printf( "The file %s was opened\n",logname );
   fprintf( streamout,"%d %d %d %d %d %d %d %d %d
   %d %d %d %d %d %d %d %d %d %d %d %d %d %d %d\n",
      dpa1,numShft,numAvg,dlyTmShft,bcgShft,
      iniDlyTmA,iniDlyTmB,iniDlyTmC,iniDlyTmD,
      dpa2,iniDlyTmA2,iniDlyTmB2,iniDlyTmC2,iniDlyTmD2,
      iniBffgrp,lastBffgrp,iniBffSv,lastBffSv,sleepTm1,
      sleepTm2,ulx,uly,lrx,lry );
   // Print configurations to file
   fclose( streamout );
}
printf("\nPlease unplug the cable to AOM\n");
printf("Setting Up Prompt (Enter to continue) : ");
Ch = getchar();
dg1 = ibdev (0, dpa1, NO_SAD, T10s, 1, 0);   /* open dev pad (dpa) */
dg2 = ibdev (0, dpa2, NO_SAD, T10s, 1, 0);   /* open dev pad (dpa) */
OpenPixciBoard();
SetupGpib(dg1);
SetupGpib(dg2);
ibwrt(dg1,"DL2,4,0",7); //Display AB loads
ibwrt(dg1,"TZ4,0",5);   //Set output impedance of AB to 50 ohms
Sleep(1000);
ibwrt(dg1,"OM4,3",5);    //Set +AB to VAR mode
ibwrt(dg1,"DL2,4,2",7); //Display AB Amplitude
ibwrt(dg1,"OA4,0.5",7); //Set +AB Output to 0.5 Volts
Sleep(1000);
ibwrt(dg1,"TM2",3); //Set Sigle Shot mode
printf("\nPlease make sure the cable to AOM is plugged in\n");
printf("We are ready to go (Enter to continue): ");
Ch = getchar();
for(avgLoop = 1; avgLoop<=numAvg; avgLoop++)
{
   myShft = iniDlyTmD; // Set initial time shift
   SetDelayChnl(dg1,2,1,iniDlyTmA); Sleep(500);
   // ^-- Set A to follow T0
   SetDelayChnl(dg1,3,2,iniDlyTmB); Sleep(500);
   // ^-- Set B to follow A
   SetDelayChnl(dg1,6,1,myShft); Sleep(500);
   // ^-- Set D to follow T0
   SetDelayChnl(dg1,5,6,iniDlyTmC); Sleep(500);
   // ^-- Set C to follow D
```

```
      SetDelayChnl(dg2,2,1,myShft+iniDlyTmA2); Sleep(500);
      // ^-- Set A2 to follow T0
      SetDelayChnl(dg2,3,2,iniDlyTmB2); Sleep(500);
      // ^-- Set B2 to follow A2
      SetDelayChnl(dg2,6,1,myShft+iniDlyTmD2); Sleep(500);
      // ^-- Set D2 to follow T0
      SetDelayChnl(dg2,5,6,iniDlyTmC2); Sleep(500);
      // ^-- Set C2 to follow D2
      printf("Initialization has been set\n\n");
      for(shftLoop = 1; shftLoop<=numShft; shftLoop++)
      {
         HANDLE hEvent = NULL;
         for(buffLoop = iniBffgrp; buffLoop<=lastBffgrp; buffLoop++)
            {
               pxd_doSnap(1,buffLoop,0);
            }
         SvImg(1,333,iniBffSv,lastBffSv,
               ulx,uly,lrx,lry,imgfolder);
         Sleep(500);
         hEvent = pxd_eventFieldCreate(1);
         if(hEvent)
         {
            /* take image */
            ibwrt(dg1,"SS",2);
            ibwrt(dg2,"SS",2);
            for(buffLoop = iniBffgrp; buffLoop<=lastBffgrp; buffLoop++)
            {
               pxd_doSnap(1,buffLoop,0);
            }
            SvImg(avgLoop,shftLoop,iniBffSv,lastBffSv,
               ulx,uly,lrx,lry,imgfolder);
         }
         Sleep(sleepTm1); //take a rest after taking an image
         SetDelayChnl(dg1,6,1,iniDlyTmD-bcgShft); //set delay for background
         Sleep(500);
         hEvent = pxd_eventFieldCreate(1);
         if(hEvent)
         {
            /* exec background */
            ibwrt(dg1,"SS",2);
            ibwrt(dg2,"SS",2);
            for(buffLoop = 1; buffLoop<=lastBffgrp; buffLoop++)
            {
               pxd_doSnap(1,buffLoop,0);
            }
            SvImg(avgLoop,shftLoop+125,iniBffSv,lastBffSv,
               ulx,uly,lrx,lry,imgfolder);
            Sleep(500); //take a rest after taking a background
         }
         /* Set Delay Accumulation */
         myShft -= dlyTmShft;
         SetDelayChnl(dg1,6,1,myShft);  //set D to follow T0
         SetDelayChnl(dg2,2,1,myShft+iniDlyTmA2); // set A2 to follow D
         SetDelayChnl(dg2,6,1,myShft+iniDlyTmD2); // set D2 to follow D
         Sleep(sleepTm2); //MOT build up
         printf("Shift Loop: %d finished\n",shftLoop);
      }
      printf("Average Loop: %d finished\n\n",avgLoop);
   }
   /* Ending Period */
   CloseGpib(dg1);
   ClosePixciBoard();
   printf("Have a nice picture!\n");
   printf("Please unplug the cable from DDG\n");
   printf("Press [Enter] to end this program");
   Ch = getchar();
}
```

```
void SetupGpib(int dg)
{
   ibclr(dg); /* clear GPIB board */
   ibwrt(dg,"CL",2);   /* clear DDG535 */
   if (ibsta & ERR)
   {
      printf("Cannot clear AT-GPIB/TNT(PnP) board\n");
      exit(1);
   }
   else
   {
      printf("AT-GPIB/TNT(PnP) board is clear\n");
      ibwrt(dg,"DS WELCOME",10);
      Sleep(1000);
      ibwrt(dg,"DS",2);
   }
}

void CloseGpib(int dg)
{
   ibwrt(dg,"CL",2);
   ibonl(dg,0);
   if (ibsta & ERR)
   {
      printf("Cannot close AT-GPIB/TNT(PnP) board\n");
      exit(1);
   }
   else
   {
      printf("AT-GPIB/TNT(PnP) board has been closed\n");
      ibwrt(dg,"DS BYE",6);
      Sleep(1000);
      ibwrt(dg,"DS",2);
   }
}

void OpenPixciBoard(void)
{
   int i;
   if    ((i=pxd_PIXCIopen("-DM 1","RS-170",""))!=0)
   {
      printf("Open PIXCI board: Error\n");
      pxd_mesgFault(1);
      exit(1);
   }
   printf("Open PIXCI board: OK\n");
   //end checking board status//
}

void ClosePixciBoard(void)
{
   int i;
   if    ((i=pxd_PIXCIclose())!=0)
   {
      printf("Close PIXCI board: Error\n");
      pxd_mesgFault(1);
      exit(1);
   }
   printf("Close PIXCI board: OK\n");
   //end checking board status//
}

void SetDelayChnl(int dg,int Chnl,int refChnl,int shift)
{
   int dlyLoop = 0;
   char intdly[16]="000000000000000";
```

```
   int lmtLngth = strlen(intdly) - 1;
   char myCommand[30];
   char chRef[7] = "DT0,0,";
   do
   {
      chRef[2]=(char)Chnl + '0';
      chRef[4]=(char)refChnl + '0';
      if(Chnl == refChnl)
      {
         printf("The reference channel cannot be\n");
         printf("the same as the delay channel\n");
         continue;
      }
      else if(Chnl == 1)
      {
         printf("T0 cannot be a delay channel\n");
         continue;
      }
      for (dlyLoop = 0; dlyLoop <= lmtLngth; dlyLoop++)
      {
         intdly[dlyLoop] += (char)fmod((shift*pow(10,dlyLoop-lmtLngth)),10);
      }
      strcpy( myCommand, chRef );
      strcat( myCommand, intdly );
      strcat( myCommand, "E-6" );
      printf( "Command sent: %s\n", myCommand );
      ibwrt(dg,myCommand,strlen(myCommand));
   }
   while((Chnl!=2)&&(Chnl!=3)&&(Chnl!=5)&&(Chnl!=6));
   switch(Chnl)
   {
   case 2: ibwrt(dg,"DL1,0,0",7);break;
   case 3: ibwrt(dg,"DL1,0,1",7);break;
   case 5: ibwrt(dg,"DL1,0,2",7);break;
   case 6: ibwrt(dg,"DL1,0,3",7);break;
   }
}

void SvImg(int code,int nShift,int iniBuff=0,int lastBuff=0,
         int ulxs=0,int ulys=0,int lrxs=1, int lrys=1,char myfolder[50]="\\")
{
   int bufLoop2;
   int namelngth = strlen(myfolder);
   char name[14]="000aaa000.bmp";
   char folder[70];
   strcpy( folder, myfolder );
   strcat( folder, name );
   for (bufLoop2=iniBuff; bufLoop2<=lastBuff; bufLoop2++)
   {
      name[0] = '0' + (char)((code/100)%10);
      name[1] = '0' + (char)((code/10)%10);
      name[2] = '0' + (char)((code/1)%10);
      name[3] = 'a' + (char)((nShift/100)%10);
      name[4] = 'a' + (char)((nShift/10)%10);
      name[5] = 'a' + (char)((nShift/1)%10);
      name[6] = '0' + (char)((bufLoop2/100)%10);
      name[7] = '0' + (char)((bufLoop2/10)%10);
      name[8] = '0' + (char)((bufLoop2/1)%10);
      strncpy( folder + namelngth, name, 14 );
      printf("image name = %s\n",folder);
      pxd_saveBmp(1,folder,bufLoop2,ulxs,ulys,lrxs,lrys,0,0);
   }
}
```

End of code

G.2 Grab images with MATLAB (MATLAB-C/C++)

GRABIMG.CPP

```
#include <direct.h>
#include <stdlib.h>
#include <stdio.h>
#include <string.h>
#include <windows.h>
#include <conio.h>
#include <math.h>
extern"C"
{
#include "mex.h"   /* MATLAB Library */
#include "xcliball.h"   /* PIXCI Library */
}
FILE *streamout;
void grabimg(char *outchar, char *inchar, double *nmloop, double *pr)
{
   strcpy( outchar, inchar );
   char logname[200];
   int nmsv = (int)*nmloop;
   int pxstat,avgcode,buffLoop,lastBffgrp;
   int namelngth = strlen(inchar);
   char name[14]="000aaa000.bmp";
   char folder[200];
   int mdflag = _mkdir( inchar );
   if( mdflag == 0 )
   {
      mexPrintf( "Directory %s was successfully created\n", inchar );
      // see _mkdir in MSVC Help|index|_mkdir
   }
   else if(mdflag == -1)
   {
      mexPrintf( "Problem creating directory %s\n", inchar );
      mexPrintf( "Message: %s\n", strerror(errno) );
      mexPrintf( "Error: %d\n", errno );
   }
   // Open PIXCI board
   if    ((pxstat=pxd_PIXCIopen("-DM 1","RS-170",""))!=0)
   {
      mexPrintf("Error %s\n",pxd_mesgErrorCode(pxstat));
      exit(1);
   }
   mexPrintf("Open PIXCI board: OK\n");
   lastBffgrp = pxd_imageZdim();
   strcpy( folder, inchar );
   strcat( folder, name );
   for (avgcode = 1; avgcode <= nmsv; avgcode++)
   {
      name[0] = '0' + (char)((avgcode/100)%10);
      name[1] = '0' + (char)((avgcode/10)%10);
      name[2] = '0' + (char)((avgcode/1)%10);
      for (buffLoop = 1; buffLoop<=lastBffgrp; buffLoop++)
      {
         pxd_doSnap(1,buffLoop,0);
         name[6] = '0' + (char)((buffLoop/100)%10);
         name[7] = '0' + (char)((buffLoop/10)%10);
         name[8] = '0' + (char)((buffLoop/1)%10);
         strncpy( folder + namelngth, name, 14 );
         pxd_saveBmp(1,folder,buffLoop,(int)pr[0],(int)pr[1],
            (int)pr[2],(int)pr[3],0,0);
         // pr[0] = ulxs; pr[1] = ulys; pr[2] = lrxs; pr[3] = lrys;
      }
   }
   strcpy( logname, inchar );
   strcat( logname, "grabimg.log" );
```

```
   streamout = fopen( logname,"w+" );
   if( streamout == NULL )
      mexPrintf( "The file %s was not opened\n",logname );
   else
   {
      mexPrintf( "The file %s was opened\n",logname );
      fprintf( streamout, "%d [numpic]\n", nmsv);
      fprintf( streamout, "%s [folder]\n", inchar);
      fprintf( streamout, "%d [ulxs]\n", (int)pr[0]);
      fprintf( streamout, "%d [ulys]\n", (int)pr[1]);
      fprintf( streamout, "%d [lrxs]\n", (int)pr[2]);
      fprintf( streamout, "%d [lrys]\n", (int)pr[3]);
      fprintf( streamout, "%d [lastBuff]\n", lastBffgrp);
      fclose( streamout );
   }
   mexPrintf("Image Aspect Ratio: %d\n",pxd_imageAspectRatio);
   mexPrintf("Image Bit Depth: %d\n",pxd_imageBdim);
   mexPrintf("Image Field Dimension: %d\n",pxd_imageIdim);
   mexPrintf("Image H-Dimension: %d\n",pxd_imageXdim);
   mexPrintf("Image V-Dimension: %d\n",pxd_imageYdim);
   if    ((pxstat=pxd_PIXCIclose())!=0)
   {
      mexPrintf("Error %s\n",pxd_mesgErrorCode(pxstat));
      exit(1);
   }
   mexPrintf("Close PIXCI board: OK\n");
}

void mexFunction( int nlhs, mxArray *plhs[],
                  int nrhs, const mxArray *prhs[] )
{
   char *outchar, *inchar;
   double *nmloop;
   double *pr;
   int buflen,status;
   /* Check for proper number of arguments. */
   if(nrhs != 3) {
      mexErrMsgTxt("Three input required.");
   } else if (nlhs > 1) {
      mexErrMsgTxt("Too many output arguments");
   }
   /* 1st Input must be a string. */
   if (mxIsChar(prhs[0]) != 1)
      mexErrMsgTxt("The first input must be a string.");
   /* Input must be a row vector. */
   if (mxGetM(prhs[0]) != 1 && mxGetM(prhs[2]) != 1)
      mexErrMsgTxt("Input must be a row vector.");
   if (mxGetN(prhs[2]) != 4)
      mexErrMsgTxt("Need 4 elements to define the picture's size.");
   /* Check data type of input argument. */
   if (!(mxIsDouble(prhs[1])) && (mxIsDouble(prhs[2])))
      mexErrMsgTxt("Input array must be of type double.");
   /* Get the length of the input string. */
   buflen = (mxGetM(prhs[0]) * mxGetN(prhs[0])) + 1;
   /* Allocate memory for input and output strings. */

   inchar = (char *)mxCalloc(buflen, sizeof(char));
   outchar = (char *)mxCalloc(buflen, sizeof(char));
   /* Copy the string data from prhs[1] into a C string
   * inchar. If the string array contains several rows,
   * they are copied, one column at a time, into one long
   * string array. */
   status = mxGetString(prhs[0], inchar, buflen);
   if (status != 0)
      mexWarnMsgTxt("Not enough space. String is truncated.");
   nmloop = mxGetPr(prhs[1]);
   /* Get the data. */
```

```
   pr = mxGetPr(prhs[2]);
   /* Call the C subroutine. */
   grabimg(outchar, inchar, nmloop, pr);
   /* Set C-style string output_buf to MATLAB mexFunction output*/
   plhs[0] = mxCreateString(outchar);
   return;
}
```

End of code

GRABIMG.DEF

```
LIBRARY grabimg.dll
EXPORTS mexFunction
```

End of code

MEXVERSION.RC

```
//* $Revision: 1.6 $  */
//        Mex versioning resource file
//  this should be compiled with the V5_COMPAT and ARRAY_ACCESS_INLINING
//  defines if they apply.
//
//  DO NOT EDIT        - this is for MATLAB use only
#define ML_VERSION   100
#define INLINING   101
//
// String Table
//
STRINGTABLE
BEGIN
#ifdef V5_COMPAT
    ML_VERSION,             "MATLAB 5 compatible"
#else
        ML_VERSION,           "MATLAB R13 native"
#endif
#ifdef ARRAY_ACCESS_INLINING
        INLINING,             "inlined"
#else
    INLINING,               "not inlined"
#endif
END
```

End of code

G.3 Image processing using MATLAB

GRABIMGAVG.M

```
function mypic = grabimgavg(savename,varargin)
% GRABIMGAVG: average images (use in conjunction with MEX grabimg)
% function grabimgavg(savename)
% Example:
% image = grabimgavg('d:/image001');
% imagesc(image);
steps = 1;
ulxs = 0;
ulys = 0;
lrxs = -1;
lrys = -1;
if exist('varargin','var')
 L = length(varargin);
 if rem(L,2) ~= 0, error('Parameters/Values must come in pairs.'); end
 for ni = 1:2:L
```

```
  switch lower(varargin{ni})
    case 'steps', steps = varargin{ni+1};
    case 'ulxs', ulxs = varargin{ni+1};
    case 'ulys', ulys = varargin{ni+1};
    case 'lrxs', lrxs = varargin{ni+1};
    case 'lrys', lrys = varargin{ni+1};
  end
 end
end
if exist('d:/temp/','dir')~=7, mkdir('d:/','/temp/'); end
folder = 'd:/temp/';
grabimg(folder,steps,[ulxs,ulys,lrxs,lrys]);
[param]=textread([folder,'grabimg.log'],'%s%*[^\n]');
numpic = str2num(param{1,1});
numbuf = str2num(param{7,1});
picadd = 0;
for rnpic = 1:numpic
 for rnbuf = 2:numbuf % start at buf2 in case of buf1 failure
   picnm = [folder, ...
            namecode('000',rnpic),'aaa', ...
            namecode('000',rnbuf),'.bmp'];
   mypic = imread(picnm);
   mypic = double(mypic(:,:,1));
   picadd = mypic + picadd;
 end
end
mypic = picadd/(numpic*(numbuf-1)); % start at buf2
if nargin == 1, save(savename,'mypic'); end
```

End of code

G.4 Phase Mask Generating using MATLAB

MASKGEN.M

```
function mask = maskgen(varargin)

%MASKGEN: Mask generator. Generate besselj(n,kr*rho).^2
% used in slmeffc experiments
%
% mask = maskgen(varargin)
%
% DEFAULT VALUES
% charge:           charge = 1;
% rotation:               ellprot = 0;
% resolution:       res = 768;
% colorlevel:       clev = 256;
% colormap:         cmap = 'gray';
% masklength:       L = 0.02;
% kr:                  kr = 5500;
% handlevisibility: hvis = 'off';
% quantize:          qnt = 'off';
% modulo:           modulo = 2*pi;
% scalex:           scalex = 1;
% scaley:           scaley = 1;
%
% Example:
% mask = maskgen('charge',2,'kr',300,'resolution',256);
% Copyleft 2004 Hill lab/Tor

% % Initialization
L=0.02; % Length of the mask in [m]
charge = 1; % charge of the vortex
res = 768; % resolution of the mask
```

```
clev = 256; % phase quantization of the mask
cmap = gray(clev); % colormap [MATLAB]
kr = 8000; % Coefficient in besselj(n,kr*rho).^2
beta = 0; % lens factor [arb. unit]
modulo = 2*pi; % bound phase
scalex = 1; % adjust x-axis scale
scaley = 1; % adjust y-axis scale
ellprot = 0; % rotation of the mask

% *** Set Configurations *** %
if exist('varargin','var')
    L = length(varargin);
    if rem(L,2) ~= 0, error('Parameters/Values must come in pairs.'); end
    for ni = 1:2:L
        switch lower(varargin{ni})
            case 'charge', charge = varargin{ni+1};
            case 'rotation', ellprot = varargin{ni+1};
            case 'resolution', res = varargin{ni+1};
            case 'colormap', cmap = varargin{ni+1};
            case 'colorlevel', clev = varargin{ni+1};
            case 'masklength', L = varargin{ni+1};
            case 'kr', kr = varargin{ni+1};
            case 'beta', beta = varargin{ni+1};
            case 'modulo', modulo = varargin{ni+1};
            case 'scalex', scalex = varargin{ni+1};
            case 'scaley', scaley = varargin{ni+1};
        end
    end
end

dL=L/(res-1);
[xx0,yy0] = meshgrid(-L/2:dL:L/2,-L/2:dL:L/2);

xx = xx0.*cos(ellprot) + yy0.*sin(ellprot);
yy = -xx0.*sin(ellprot) + yy0.*cos(ellprot);
[phi,rho] = cart2pol(scalex*xx,scaley*yy);
phi = mod(phi + pi,2*pi);
Phi = 0;
Phi = Phi + charge*phi;
Phi = Phi - min(min(Phi)); % for making negative vortex
Phi = Phi + kr*rho; % kr = (2*pi)/(r_p*rmax)
Phi = Phi + beta*(rho.^2);
mask = mod(Phi,modulo);

% Highest SLM Phase Quantization Level = 256
if clev >= 256,
   clev = 256;
else
   for rnclev = 1:clev
       upperphase = 2*pi*rnclev/clev;
       lowerphase = 2*pi*(rnclev-1)/clev;
       mask( mask > lowerphase & ...
           mask <= upperphase ) = lowerphase;
   end
end

mask = length(cmap)*mask/(2*pi);
image(mask);colormap(cmap);
axis image;axis off;
```

End of code

G.5 Propagation of Scalar Field

G.5.1 1D Angular Spectrum: Hankel Transform

MATLAB script Adapted from code by M. Guizar-Sicairos *et al.* [103].

SCP_1D_HT.M

```
% MATLAB SCRIPT
% Angular Spectrum 1D Hankel Transform
% Credit: Manuel Guizar Sicairos.
%
% % Link
% http://www.mathworks.com/matlabcentral/fileexchange/loadFile.do?objectId
% =6570&objectType=file
%
clear all; close all; clc;

R = 4;          %% Maximum sampled radius (time)
N = 500;        %% Number of sampling points
ord = 4;        %% Transformation order

%%%%%%%%%%%%%%%%%%%%%%%%%%%%%%%%%%
% % Matrix and vectors computing
%%%%%%%%%%%%%%%%%%%%%%%%%%%%%%%%%%
load c.mat; % -> get this file from the link provided above
aph = c(ord+1,1:N+1);

V = aph(N+1)/(2*pi*R);    % Maximum frequency
r = aph(1:N)'*R/aph(N+1);   % Radius vector
v = aph(1:N)'/(2*pi*R);   % Frequency vector
% S = 2*pi*R*V = aph(N+1);
[An,Am] = meshgrid(aph(1:N),aph(1:N));
bT1 = besselj(ord,An.*Am/aph(N+1));
Tmn = (2/aph(N+1))*bT1./(abs(besselj(ord+1,An)).*abs(besselj(ord+1,Am)));
% ^-- Tmn is the transformation matrix
J1 = (abs(besselj(ord+1,aph(1:N)))/R)';
%% ^-- J1 prepares input vector for transformation
% J2 = J1*R/V;
%% ^-- J2 prepares output vector for display
clear An Am
%
%%%%%%%%%%%%%%%%%%%%%%%%%%%%%%%%%%%%%%%%%%%
% % Propagation of the angular spectrum
%%%%%%%%%%%%%%%%%%%%%%%%%%%%%%%%%%%%%%%%%%%
charge = 4;
rpeak = 0.5; %% [mm] Distance from center to peak
kappa = const('Jrp',4)/rpeak;
lambda = 780e-6; % [mm]
focL = 0.5e3; %% [mm]
Nz = 500;
Z = 1.5*focL;
rg = 2; %% [mm] --> Gaussian Width
%
k = (2*pi/lambda);
Q_lens = -(k*r.^2)/(2*focL);
%
dz = Z/Nz;
zz = linspace(0,Z,Nz+1);
%
kr = 2*pi*v;
kz = sqrt(k^2 -kr.^2);
fr = besselj(charge,kappa*r); % --> [theta dependent is taken care of]
fr = fr.*exp(-0.5*(r/rg).^2); % --> [added to subpress bndry reflection]
```

```
fr = fr/max(max(fr));
fr = fr.*exp(i*(Q_lens + kappa*r));
Fr = fr./J1;
Hv0 = Tmn*Fr;
%
z = (1:Nz)*dz; %% [mm]
Gz = exp(i*kz*z); % --> Propagator
Hv = repmat(Hv0,1,length(z)).*Gz;
%
ur = (Tmn*Hv).*repmat(J1,1,length(z));
%
figurel(1);set(gcf,'position',[50 400 40*[6 5]]);
imagesc(z/1e3,([flipud(r);-r]),abs([flipud(ur);ur]).^2);
colormap(hot);
set(gca,'YDir','normal');
xlabel('z (m)');ylabel('x (mm)');
axis([0 0.75 -2 2]);
%
figurel(2);set(gcf,'position',[50 400 40*[6 5]]);
imagesc(z/1e3,r,abs(ur));
colormap(jet);
set(gca,'YDir','normal');
xlabel('z (m)');ylabel('r (mm)');
```

End of code

G.5.2 2D Angular Spectrum: FFT

SCP_2D_ANGSP.M

```
%% 2D - Angular Spectrum - CODE2025OCT192552
%% Propagation of the Bessel Beam

clear all; close all; clc;
charge = 4;
M = 512;
a0 = 8e-3;% %% [m] Sim Size
rpeak = 0.5e-3; %% [m] Distance from center to peak
kappa = const('Jrp',charge)/rpeak;
x = linspace(-a0/2,a0/2,M); x = x'; %% [m]
[xx,yy] = meshgrid(x,x);
[theta,rho] = cart2pol(xx,yy);
kx = (2*pi/a0)*linspace((-M)/2,(M-2)/2,M); kx = kx';
[kxx,kyy] = meshgrid(kx,kx);
%
Bnd = besselj(40,42.8*abs(rho)/x(end));
Bnd(rho>=0.933*x(end)) = max(max(Bnd));
Bnd = exp(-40*Bnd);
%%
lambda = 780e-9; % [m]
k = (2*pi/lambda);
kz = sqrt(k^2 - (kxx.^2 + kyy.^2));
dz = 0.7; % [m] % -> Propagation distance
focL = -0.5; %% [m] %% [+] Diverge [-] Converge
%
sigGss = 2e-3;
fxy = exp(-rho.^2/(2*sigGss^2)).*besselj(charge,kappa*rho);
%
Q_rho = +1*kappa*rho; % Conical Phase [Produce Bessel Beam]
Q_tht = charge*theta; % Vortex Phase
Q_lens = +(k*rho.^2)/(2*focL); % Lens
Q_Kx = 0*kappa*xx; % Transverse Shift
Q_kz = kz*dz; % Propagator Phase
%
% ---
```

```
fxy = fxy.*exp(i*(Q_tht+Q_lens));
% ^-- input profile can be changed here.
% ---
%
Gz = exp(i*Q_kz);
hxy = ifft2c((fft2c(fxy).*Gz));
%
figurel(1);set(gcf,'position',[50 500 300 300]);
imagesc(x*1e3,x*1e3,abs(hxy).^2);axis image;
colormap(hot);
xlabel('x (mm)');ylabel('y (mm)');
%
figurel(2);set(gcf,'position',[150 50 300 300]);
imagesc(x*1e3,x*1e3,angle(hxy));
xlabel('x (mm)');ylabel('y (mm)');
```

End of code

G.5.3 2D Paraxial Approximation: FFT

SCP_2D_PRXAP.M

```
%% 2D - Paraxial Approximation - CODE2256OCT192552
%% Propagation of the Bessel Beam

clear all; close all; clc;
charge = 4;
M = 512;% %% -> Resolution of the simulation
a0 = 8e-3;% %% [m] %% -> Sim Size
rmax = const('Jrp',charge); % %% peak position of unscaled J_n
rpeak = 0.5e-3;% %% [m] Distance from center to peak
kappa = rmax/rpeak; %% [m^-1]
x = linspace(-a0/2,a0/2,M); x = x'; %% [m] % spatial Grid 1D - Cartesian
[xx,yy] = meshgrid(x,x); % spatial Grid 2D - Cartesian
[th,rh] = cart2pol(xx,yy); % spatial Grid 2D - Polar
kx = (2*pi/a0)*linspace((-M)/2,(M-2)/2,M); kx = kx'; % spatial freq. Grid 1D
[kxx,kyy] = meshgrid(kx,kx); % spatial freq. Grid 2D
%
% v-- Added to suppress reflection from the boundary
Bnd = besselj(40,42.8*abs(rh)/x(end));
Bnd(rh>=0.933*x(end)) = max(max(Bnd));
Bnd = exp(-40*Bnd);
% %
szSLM = 8e-3; % [m] %% -> Apperture - Size of SLM
BndSLM = zeros(size(Bnd));
BndSLM(abs(xx)<=szSLM/2 & abs(yy)<=szSLM/2)=1;
figurel(10);imagesc(x,x,BndSLM);axis image;
%%
lambda = 780e-9; % [m]
k = (2*pi/lambda);
dz = 0.7;% % [m] % -> propagation distance
sigGss = 2e-3; % -> sigma of the input Gaussian
focL = 0.5;%inf;% %% [m] -> focal length of a lens
sgnL = +1; % --> Lens' signature: (+) == focused, (-) == diverge
%
AxyBssFlag = 1;
AxyGssFlag = 1;
%
if AxyBssFlag, AxyBss = besselj(charge,kappa*rh); else AxyBss = 1; end
if AxyGssFlag, AxyGss = exp(-rh.^2/(2*sigGss^2)); else AxyGss = 1; end
%
Axy = AxyBss.*AxyGss;
Axy = Axy/max(max(Axy));
figurel(11);imagesc(x,x,Axy);axis image;
%
```

```
Q_rho = kappa*rh; % Conical Phase
Q_tht = -charge*th; % Vortex Phase
Q_lens = sgnL*(k*rh.^2)/(2*focL); % Lens
%
fxy = BndSLM.*Axy.*exp(i*(Q_tht+Q_lens));
%
Gz = exp(i*(kxx.^2 + kyy.^2)*dz/(2*k)); % -> Propagator
%
hxy = ifft2c(fft2c(fxy).*Gz);
%
Ih = abs(hxy).^2;
figurel(1);set(gcf,'position',[50 500 300 300]);
imagesc(x*1e3,x*1e3,Ih);axis image;colormap(hot);
xlabel('x (mm)');ylabel('y (mm)');
%
figurel(2);set(gcf,'position',[50 50 300 300]);
imagesc(x*1e3,x*1e3,angle(hxy));axis image;
xlabel('x (mm)');ylabel('y (mm)');
```

End of code

G.6 Convolution Codes: 2D Free Expansion

A MATLAB script in this section contains an example of 2D free expansion as described in Appendix E.4. The initial distributions are written as

$$g(x,y) = \alpha_g \exp\left\{-\alpha J_n^2[k\,(x^2+y^2)^{1/2}]\right\} \quad \text{and} \quad h(u,v) = \frac{1}{2\pi\sigma_v^2}\exp\left[-\frac{u^2+v^2}{2\sigma_v^2}\right],$$

where $\alpha = 30$, $n = 4$, $k = 10.6351$ mm^{-1} and $\sigma_v = 0.1208$ mm/ms. The code below store the normalized initial spatial and velocity distribution in `Bp` and `Gp` respectively. The resulting spatial distribution at time t is stored in variable `Bpt`.

CBE MATLAB SCRIPT

```
%% CONV2D - FREE EXPANSION - CODE1646JAN062553
clear all; close all; clc;
NN = 501;
%% Spatial Distribution
x = 4*linspace(-1,1,NN); % [mm]
[xx,yy] = meshgrid(x,x); % [mm,mm]
[th,rh] = cart2pol(xx,yy); % [rad,mm]
sgmx = 1; % [mm]
Bp0 = exp(-30*besselj(4,10.6351*rh).^2);Bp0(rh>0.5) = 0;
figurel(1,0.7);imagesc(x,x,Bp0);axis image;
%
% % integration of Bp0 can be evaluated as
BsI = trapz(x,trapz(x,Bp0,2),1);
fprintf('AREA TRAPZ: %1.5f \n',BsI);
%%
%% Velocity Distribution
v = 2*linspace(-1,1,NN); % [mm/ms]
[vx,vy] = meshgrid(v,v); % [mm/ms,mm/ms]
[ph,vr] = cart2pol(vx,vy); % [rad,mm/ms]
%
sgmv = 0.1208; % [mm]
Gp0 = exp(-vr.^2/(2*sgmv^2));
```

```
figurel(1,0.7);imagesc(v,v,Gp0);axis image;
%
% % integration of Gp0 = 2*pi*sgmv^2
% % numerically this can be evaluated as
GsI = trapz(v,trapz(v,Gp0,2),1);
fprintf('GSS AREA ANALYT: %1.5f, TRAPZ: %1.5f \n',2*pi*sgmv^2,GsI);
%%
%% Normalize Bp and Gp
Bp = Bp0/BsI;
Gp = Gp0/GsI;
%% CONV2D @ time t
t = 4; % [ms] % -> Expansion Time
%%
Gpt = exp(-(rh.^2)/(2*(sgmv*t)^2))/(GsI);
Bpt = real(ifft2c(fft2c(Gpt).*fft2c(Bp)))/(sum(sum(Bp))*(t^2));
BsIt = trapz(x,trapz(x,Bpt,2),1);
fprintf('AREA TRAPZ: %1.5f \n',BsIt);
%%
figure(1);imagesc(Bpt);axis image;

```

End of code

G.7 Classical Trajectory Monte-Carlo Method: 2D Free Expansion

A MATLAB script in this section contains an example of a 2D free expansion as described in Appendix E.4.3. The initial distribution functions are written as

$$g(x,y) = \alpha_g \exp\left\{-\alpha J_n^2[k\,(x^2+y^2)^{1/2}]\right\} \quad \text{and} \quad h(u,v) = \frac{1}{2\pi\sigma_v^2}\exp\left[-\frac{u^2+v^2}{2\sigma_v^2}\right],$$

where $\alpha = 30$, $n = 4$, $k = 10.6351$ mm^{-1} and $\sigma_v = 0.1208$ mm/ms. The code below stores the random variables of initial spatial and velocity coordinates in `xn`, `yn`, `un` and `vn` respectively. The updated values at time t are restored in the same variables. The 2D distribution from the updated location $(x(t), y(t))$ is calculated using `histogram2d` [173]. The script uses function `randp2Dcs()` and `cs2randp2D()` to sample random variable from an arbitrary probability distribution. The functions are shown below after the script.

MTC MATLAB SCRIPT

```
%% MTC - FREXPSN - SHORT VERSION - CODE1803JAN062553
%% Initialization
clear all; close all; clc;
cc.Nxy = 200; % [#] -- size of simulation (spatial)
cc.Nvr = 200; % [#] -- size of simulation (velocity)
cc.Nn = 100000; % [#] -- number of random samples
cc.Ne = 20; % [#] -- number of average
cc.xlim = 2; % [mm] -- x-range = [-xlim,xlim]
cc.nu_j = 4; % [#] -- besselj index (charge)
cc.rp = 0.5; % [mm] -- besselj peak radius
cc.kp = const('Jrp',cc.nu_j)/cc.rp; % [mm^-1]
cc.Temp = 150; % [uK] -- Temperature associated with h(v)
```

```
Kb = 1.3807e-023; % [J K-1] -- Boltzmann constant
mRb = 1.4192e-025; % [kg] -- mass of Rubidium atom
cc.sgmu = sqrt(Kb*cc.Temp*1e-6/mRb); % [mm/ms]
cc.sgmv = sqrt(Kb*cc.Temp*1e-6/mRb); % [mm/ms]
cc.alpSPIE = 30;
cc.dx = 2*cc.xlim/(cc.Nxy-1); % [mm]
%
x = linspace(-cc.xlim,cc.xlim,cc.Nxy); % [mm]
[xx,yy] = meshgrid(x); % [mm,mm]
[th,rh] = cart2pol(xx,yy); % [rad,mm]
%
%%
% Define EXPJ2 - Spatial Distribution Function
fxy0 = exp(-cc.alpSPIE*besselj(cc.nu_j,cc.kp*rh).^2);
fxy0(rh > cc.rp) = 0;
fxy0 = fxy0/sum(sum(fxy0));
%
figurel(1);imagesc(x,x,fxy0);
axis image; colorbar;
xlabel('x (mm)');ylabel('y (mm)');
title('Distribution Function g(x,y)');
%
Cs = cs2randp2D(fxy0);
[X,Y] = randp2Dcs(Cs,cc.Nn);
%
fxy = histogram2d(x(X),x(Y),x,x)/cc.Nn;
%
figurel(2);imagesc(x,x,fxy);
axis image; colorbar;
fprintf('sum(fxy(:)) = %1.1f\n',sum(fxy(:)));
xlabel('x (mm)');ylabel('y (mm)');
title('Histogram of random variable (X,Y)');
%
figurel(3); clf; hold on; box on;
xc = round(cc.Nxy/2);
plot(x,fxy0(xc,:),'r',x,fxy(xc,:),'b');
xlabel('x (mm)');ylabel('g(x)');
legend('g(x)','Histogram');
%
%%
fxyAvg = zeros(size(fxy));
dt = 5; % ms
for nE = 1:cc.Ne;
    [X,Y] = randp2Dcs(Cs,cc.Nn);
    xn = x(X); % [mm]
    yn = x(Y); % [mm]
    %
    un = cc.sgmu*randn(1,cc.Nn); % [mm/ms]
    vn = cc.sgmv*randn(1,cc.Nn); % [mm/ms]
    %
    % Throw away out of bound values
    excidx = find(abs(xn) > cc.xlim-cc.dx | abs(yn) > cc.xlim-cc.dx );
    xn(excidx) = []; yn(excidx) = []; un(excidx) = []; vn(excidx) = [];
    %
    xn = xn + un*dt;
    yn = yn + vn*dt;
    %
    fxy = histogram2d(xn,yn,x,x);
    fxyAvg = fxyAvg + fxy;
    %
    figurel(4);imagesc(x,x,fxy);
    axis image; colorbar;
    fprintf('sum(sum(fxy)) = %1.1f\n',sum(sum(fxy)));
    xlabel('x (mm)');ylabel('y (mm)');
end
fxyAvg = fxyAvg/cc.Ne;
figurel(5);imagesc(x,x,fxyAvg);
```

```
axis image; colorbar;
fprintf('sum(sum(fxy)) = %1.1f\n',sum(sum(fxy)));
xlabel('x (mm)');ylabel('y (mm)');
title('Averaged Distribution');
%%
```

End of code

RANDP2DCS.M

```
function [X,Y] = randp2Dcs(Cs,Nn)

% Input an arbitrary distribution + appropriate cummulative sum
% RANDP2DCS - pick random values with relative probability
%
% Cs  - Structured Input from cs2randp2D()
%
% Adapted from RANDP() by Jos van der Geest
% Ref: http://www.mathworks.com/matlabcentral/fileexchange/8891
%
% Idea for 2D arbitrary distribution by
% Herman Tulleken (herman.tulleken@gmail.com)
% Ref:
% http://code-spot.co.za/2009/04/15/
% generating-random-points-from-arbitrary-distributions-for-2d-and-up/
%
% see also: randp, gDiscrPdfRnd, rndpdf, randp2D,  randp2Dcs, cs2randp2D

error(nargchk(2,Inf,nargin));

try
    X = rand(1,Nn);
    Y = rand(1,Nn);
catch
    E = lasterror ;
    E.message = strrep(E.message,'rand','randp') ;
    rethrow(E) ;
end

if isempty(Cs.Cx) || sum(Cs.Cx)==0
    warning([mfilename ':ZeroProbabilities'],'All zero probabilities') ;
    X(:) = 0;
    Y(:) = 0;
else
    [junk,X] = histc(X,[0 ; cumsum(Cs.Cx(:))] / sum(Cs.Cx));
    [junk,V] = histc(Y+X-1,Cs.CyL);
    Y = V - size(Cs.cf,1)*(X-1);
end
```

End of code

CS2RANDP2D.M

```
function Cs = cs2randp2D(fxy0)

% CS2RANDP2D - Provide output structure for RANDP2DCS()
%    fxy0 -- arbitrary distribution function
%      Cs -- Structure input for RANDP2DCS()
%    Cs.cf -- Commulative Distribution
%      Cs.Cx -- use to find random variable X
%    Cs.CyL -- use to find random variable Y
%
% related to: randp2Dcs, rand, randn

if any(any(fxy0 < 0)),
    error('All probabilities should be 0 or larger.') ;
end
```

```
cf0 = cumsum(fxy0,1);
sm = repmat(cf0(end,:),size(cf0,1),1);
cf = cf0./sm; cf(sm==0) = 0;
% % any(any(isinf(cf)))
% % any(any(isnan(cf)))
cf(end,:) = ones(1,size(cf,2)); % always make end rows prob = 1
Cs.cf = [zeros(1,size(cf,2));cf];
Cs.Cx = cf0(end,:);
v1 = cumsum(Cs.cf(end,:));
m1 = [0,v1(1:end-1)];
m2 = repmat(m1,size(Cs.cf,1),1);
Cs.CyL = reshape(Cs.cf+m2,numel(Cs.cf),1);
%
if nargout == 0, figurel(2);plot(Cs.CyL); end
```

End of code

G.8 Liouville's Equation Solver

The following code demonstrates an example that uses the function `cbe_get_fft_propagation()` or `cbe_get_propagation()` to solve the Liouville equation for a Bessel potential with $U_{max} = 300$ μK high. The initial spatial distribution of an ensemble is Gaussian in both coordinate and velocity space. The temperature of the ensemble is also 300 μK.

The function `cbe_get_fft_propagation()` required user defined functions `fftc()` and `ifftc()` as shown in G.11 to interpolate the ensemble distribution in the phase space as described in Appendix E.5. This function is at least 10 times faster than `cbe_get_propagation()` which uses a function called `spline()` to interpolate the distribution.

CBE MATLAB SCRIPT

```
1  %% GET F(U,X,t) from F(U,X,0)
2  %  CODE1923JUN162552
3  clear all; close all; clc;
4  %% Get Grid
5  cc.Nx = 500; % [#:INT]
6  cc.Nv = 500; % [#:INT]
7  cc.xlim = 8; %% [mm]
8  cc.vlim = 0.8;%1; %% [mm/ms]
9  %
10 grd.x = cc.xlim*linspace(-1,1,cc.Nx); %% [mm]
11 grd.v = cc.vlim*linspace(-1,1,cc.Nv); %% [mm/ms]
12 grd.kx = (pi/cc.xlim) * linspace(-cc.Nx/2,(cc.Nx-2)/2,cc.Nx);
13 grd.kv = (pi/cc.vlim) * linspace(-cc.Nv/2,(cc.Nv-2)/2,cc.Nv);
14 %
15 %% Get Potential
16 cc.TUlim = 77;% % [uK]
17 cc.rp = 0.893;% % [mm]
18 cc.charge = 4; % [#:INT]
19 %
20 rpj = const('Jrp',cc.charge);
```

```
TU = besselj(cc.charge,(rpj/cc.rp)*abs(grd.x)).^2;  %% [uK] %%
TU = cc.TUlim*TU/const('Jsqmx',cc.charge); %% [uK] %% TUx = Ux/k_B
TU2 = repmat(TU,cc.Nv,1);  % [uK]
%
%% Get Initial Distribution
cc.Tmot = 150; % [uK]
cc.sgmv = 1e-3*sqrt(const('Kb')*cc.Tmot/const('mRb87')); % [mm/ms]
cc.sgmx = 0.72; % [mm]
%
fx = exp(-(grd.x.^2)/(2*(cc.sgmx^2)));
fv = exp(-(grd.v.^2)/(2*(cc.sgmv^2)));
fvfx0 = fv'*fx;
%
%% Get Dump Boundary
cc.xlTDB = 3*cc.xlim/4; % [mm]
cc.sgmTDB = 0.5; % [mm]
%
bDB = zeros(size(grd.x));
iDx = find(abs(grd.x) < cc.xlTDB);
bDB(iDx) = 1;
iDxL = iDx(1);
iDxR = iDx(end);
bDB(1:iDxL) = exp(-((grd.x(1:iDxL)+cc.xlTDB).^2)/(2*(cc.sgmTDB^2)));
bDB(iDxR:end) = exp(-((grd.x(iDxR:end)-cc.xlTDB).^2)/(2*(cc.sgmTDB^2)));
bDB = repmat(bDB,cc.Nv,1);
%
%% Get Distribution Evolution
cc.NN = 400; % [#]
cc.thold = 20; % [ms]
cc.dt = cc.thold/cc.NN; % [ms]
%
for n = 1:cc.NN
   %% GET F(U,X,dt) from F(U,X,0)
   fvfx1 = cbe_get_fft_propagation(grd,cc,TU,fvfx0); % -> [FAST]
   %fvfx1 = cbe_get_propagation(grd,cc,TU2,fvfx0); % -> [MEDIUM]
   %
   save(['c:\CBE01\fvfxt',num2str(n)],'fvfx1');
   %
   %% Dump outflow atoms at the boundary
   fvfx0 = fvfx1.*bDB;
end
save('c:\CBE01\cc','cc');
```

End of code

CBE_GET_FFT_PROPAGATION.M

```
function [fvfx1] = cbe_get_fft_propagation(mygrid,coeff,TU1d,fvfx0)

ax = -(1e-3*8.3145/(coeff.m0))*gradient(TU1d,mygrid.x(2)-mygrid.x(1));

%% Propagator
dx = (coeff.dt/2)*mygrid.v;
gA = mygrid.kx'*dx; gA = gA';
Ga = exp(-i*gA);
%
dv = (coeff.dt)*ax;
gB = mygrid.kv'*dv;
Gb = exp(-i*gB);
%
%% Velocity: Spatial Shift
FvFx0 = fftc(fvfx0,[],2);
fvfx1 = ifftc(Ga.*FvFx0,[],2); fvfx1 = real(fvfx1);
%
%% Acceleration: Velocity Shift
FvFx0 = fftc(fvfx1,[],1);
fvfx1 = ifftc(Gb.*FvFx0,[],1); fvfx1 = real(fvfx1);
```

```
%
%% Velocity: Spatial Shift
FvFx0 = fftc(fvfx1,[],2);
fvfx1 = ifftc(Ga.*FvFx0,[],2); fvfx1 = real(fvfx1);
```

End of code

CBE_GET_PROPAGATION.M

```
function [fvfx1] = cbe_get_propagation(mygrid,coeff,TU,fvfx0)

ax = -(1e-3*8.3145/(coeff.m0))*gradient(TU,mygrid.x(2)-mygrid.x(1));
% ^-- Define U = k_B T

%% Velocity: Spatial Shift
xv = mygrid.xx - (coeff.dt/2)*mygrid.vv;
fvfx1 = zeros(coeff.Nv,coeff.Nx);
for nn = 1:coeff.Nv
    cs = spline(mygrid.x,fvfx0(nn,:));
    fvfx1(nn,:) = ppval(cs,xv(nn,:));
end
%
%% Acceleration: Velocity Shift
va = mygrid.vv - coeff.dt*ax;
va = va';
fxfv1 = fvfx1';
for nn = 1:coeff.Nx
    cs = spline(mygrid.v,fxfv1(nn,:));
    fxfv1(nn,:) = ppval(cs,va(nn,:));
end
fvfx1 = fxfv1';
%
%% Velocity: Spatial Shift
for nn = 1:coeff.Nv
    cs = spline(mygrid.x,fvfx1(nn,:));
    fvfx1(nn,:) = ppval(cs,xv(nn,:));
end
```

End of code

G.9 Classical Trajectory Monte-Carlo Method: with Force Term

This MATLAB script demonstrates classical trajectory Monte-Carlo Method with a non-zero force term as described in Sec. E.6

The script obtained random variables from `MTC_GET_AXNZYN` and use `PROPAGATE2D` to propagate them in time.

PIC MATLAB SCRIPT

```
%% INITIALIZATION
clear all; close all; clc;
cc.Nsim = 6; % [#] --> simulation number (for a set of config)
cc.Nxy = 500; % [#]
cc.xlim = 4; % [mm] range_x = [-xlim,xlim]
cc.Nvr = 500;
cc.vlim = 0.5; % [mm/ms] range_vr = [0,vlim]
cc.nu_j = 4; % [#] % --> besselj index (charge)
cc.rp = 0.67*4/3; % [mm] - peak radius
cc.kp = const('Jrp',cc.nu_j)/cc.rp; % [mm^-1]
```

```
cc.U0 = 86; % [uK]
cc.dt = 0.01; % [ms]
cc.dt_sv = 1; % [ms] --> time to save data
%
rdir = 'c:\';
simdir = ['mtc',namecode('000',cc.Nsim)];
nmdirsv = fullfile(rdir,simdir);
mkdir(rdir,simdir);
%
%% GET GRID
mygrid.x = linspace(-cc.xlim,cc.xlim,cc.Nxy); % [mm]
mygrid.vr = linspace(0,cc.vlim,cc.Nvr); %% [mm/ms]
mygrid.ux = linspace(-cc.vlim,cc.vlim,2*cc.Nvr);
[mygrid.xx,mygrid.yy] = meshgrid(mygrid.x); % [mm,mm]
[mygrid.th,mygrid.rh] = cart2pol(mygrid.xx,mygrid.yy); % [rad,mm]
%
cc.dx = abs(mygrid.x(2)-mygrid.x(1)); % [mm]
cc.zr_idx = find((mygrid.x)>=0,1); % [#]
%
%% GET POTENTIAL
U2d = besselj(4,cc.kp*mygrid.rh).^2;
U2d = cc.U0*U2d/max(max(U2d)); % [uK]
%
[ax,ay] = gradient(U2d,cc.dx); % [uK/mm]
cc_T2a = 1e-6*const('Kb')/const('mRb87'); % [mm/ms^2] * [mm/uK]
ax = -cc_T2a*ax; % [mm/ms^2]
ay = -cc_T2a*ay; % [mm/ms^2]
%
%% GET INITIAL DISTRIBUTION
cc.Nn = 100000;
cc.Tmot = 150; % [uK]
cc.sgmx = 0.72; % [mm]
cc.sgmy = 0.72; % [mm]
cc.sgmu = sqrt(const('Kb')*cc.Tmot*1e-6/const('mRb')); % [mm/ms]
cc.sgmv = sqrt(const('Kb')*cc.Tmot*1e-6/const('mRb')); % [mm/ms]
%%
%
for Ntrial = 1:20;
    %
    xn = cc.sgmx*randn(1,cc.Nn); % [mm]
    yn = cc.sgmy*randn(1,cc.Nn); % [mm]
    un = cc.sgmu*randn(1,cc.Nn); % [mm/ms]
    vn = cc.sgmv*randn(1,cc.Nn); % [mm/ms]
    %
    [axn,ayn] = mtc_get_axnayn(cc,xn,yn,ax,ay);
    %
    %% SAVE INITIAL DISTRIBUTION
    time = 0;
    tmtxt = ['t = ',num2str(time),' ms'];
    nmsv = fullfile(nmdirsv, ...
        ['fxyuva_',num2str(time),'ms_v',num2str(Ntrial)]);
    save(nmsv,'xn','yn','un','vn','axn','ayn','time');
    disp(tmtxt);
    disp(['SAVED: ',nmsv]);
    %
    cc.Nt = 2000;
    %
    tic
    for nt = 1:cc.Nt
        % ELIMINATE OUTFLOW ATOMS
        excidx = find(abs(xn) > cc.xlim-cc.dx | abs(yn) > cc.xlim-cc.dx );
        %
        xn(excidx) = [];
        yn(excidx) = [];
        un(excidx) = [];
        vn(excidx) = [];
        %
```

```
        % GET AXN & AYN
        [axn,ayn] = mtc_get_axnayn(cc,xn,yn,ax,ay);
        % %
        [xn,yn,un,vn] = mtc_propagate2D(xn,yn,un,vn,axn,ayn,cc.dt);
        %
        time = cc.dt*nt; % [ms]
        %
        if mod(time,cc.dt_sv) == 0
            nmsv = fullfile(nmdirsv, ...
                ['fxyuva_',num2str(time),'ms_v',num2str(Ntrial)]);
            save(nmsv,'xn','yn','un','vn','axn','ayn','time');
            disp(tmtxt);
            disp(['SAVED: ',nmsv]);
        end
    end
    toc
end
%%
save(fullfile(nmdirsv,'cc'),'cc');
```

End of code

MTC_GET_AXNAYN.M

```
function [axn,ayn] = mtc_get_axnayn(cc,xn,yn,ax,ay)

% GET SPATIAL DEPENDENT ACCELERATION

xn_idx_frac = cc.zr_idx + xn/cc.dx;
xn_idxL = floor(xn_idx_frac);
xn_idxU = xn_idxL+1;
%
yn_idx_frac = cc.zr_idx + yn/cc.dx;
yn_idxL = floor(yn_idx_frac);
yn_idxU = yn_idxL+1;
%
dxy = sqrt((xn_idx_frac-xn_idxL).^2 + (yn_idx_frac-yn_idxL).^2);
%
axnL = ax(cc.Nxy*(xn_idxL-1)+yn_idxL);
axnU = ax(cc.Nxy*(xn_idxU-1)+yn_idxU);
axn = axnL + ((axnU-axnL).*dxy)/sqrt(2);
%
aynL = ay(cc.Nxy*(xn_idxL-1)+yn_idxL);
aynU = ay(cc.Nxy*(xn_idxU-1)+yn_idxU);
ayn = aynL + ((aynU-aynL).*dxy)/sqrt(2);
```

End of code

PROPAGATE2D.M

```
function [x,y,u,v] = propagate2D(x0,y0,u0,v0,ax,ay,dt)

% PROPAGATION OF A CLASSICAL TRAJECTORY

x = x0 + u0*dt + 0.5*ax*(dt^2);
y = y0 + v0*dt + 0.5*ay*(dt^2);
u = u0 + ax*dt;
v = v0 + ay*dt;
```

End of code

G.10 Split-Operator Codes

The script `scp_so_get_en_wf.m` below uses the split-operator calculation to find an eigen-energies and eigen-functions in the first ring of a Bessel potential described in Sec. 6.3 and Appendix F. The script obtains the grid of spatial coordinates and theirs spatial frequency from `so_get_grid()`. The spatial grid is used to construct the user-defined potential via `so_get_potential_ring()`. At the boundary of the simulation, a portion of the wavepacket that reaches the boundary get suppressed by `so_get_dampbound()` to eliminate reflection from the boundary (via FFT or IFFT). The initial wavepacket is generated by `so_get_initwavepacket()` and propagate by using `so_get_correlation()` under the propagator generated from `so_get_propagator()`. The eigen-energies and their associated eigen-functions are calculated from `so_get_eigenergy()` and `so_get_eigfunction()` respectively.

SCP_SO_GET_EN_WF.M

```
% SPLIT-OPERATOR: MATLAB SCRIPT
%% scp_so_get_en_and_wf.m
clear all; close all; clc;
%
%% Get Grid
clear coeff;
coeff.a0 = 4;%5;%  %% [rscale m] Length (size of simulation)
coeff.Ng = 256;%128;  %% size of matrix
coeff.rscale = 1e-6; %% [micro] prefix of length in [m]
mygrid = so_get_grid(coeff);
%
%% Get Potential
coeff.charge = 1;
coeff.rpeak = 0.5;
coeff.tempUmax = 2.5e-6;%0.24e-6;%5e-6;%100e-6;% % [K]
V = so_get_potential_ring(mygrid,coeff);
%
%% Get Damp Boundary
coeff.nb = 40;
coeff.cj = 42.8;
coeff.cg = 0.933;
coeff.cexp = 40;
Bnd = so_get_dampbound(mygrid,coeff);
%
%% Get Initial Wave Packet
coeff.amp = -1;  %% amp of initial wavepacket
coeff.wd = 0.3*abs(mygrid.x(1)); %% width of initial wavepacket
coeff.nwp = 16; %% vortical index of initial wavepacket
Phi0 = so_get_initwavepacket(mygrid,coeff,V);
%
%% Get Propagators
coeff.Kb = const('Kb');
coeff.hbar = const('hbar');
coeff.mRb = const('mRb87');
coeff.dt_sim = (2*pi*coeff.hbar/(6*coeff.Kb*coeff.tempUmax)); %% [s] Time increment
prpg = so_get_propagator(mygrid,coeff,V,Bnd);
%
```

```
%% Get Correlation Function
coeff.NPt = 10000;% 16384;% %% Total number of time steps
coeff.Ndisp = round(coeff.NPt/10);%  %% Step interval to display
coeff.sstep = 1; %% sampling step
corr = so_get_correlation(mygrid,coeff,Phi0,prpg);
disp('Correlation Function Done');
%
%% Get Eigen-Energy
coeff.Elow = -coeff.Kb*coeff.tempUmax;
coeff.Ehgh = 0;
coeff.lnPeoBase = -30;%-20;%
eEn = so_get_eigenergy(coeff,corr);
%
%% Save Eig-Energy
cd('G:\myddrive\my_matlab\split_operator_2');
Vctxt = namecode('00',coeff.charge);
Vrtxt = namecode('000',coeff.rpeak);Vrtxt(Vrtxt=='.')='_';
VTtxt = namecode('000',coeff.tempUmax*1e6);VTtxt(VTtxt=='.')='_';
nwptxt = namecode('00',coeff.nwp);
ntrialtxt = namecode('00',1); % <-- [trial number label]
namesaved = ['so_ring_j',Vctxt,'r',Vrtxt,'umT',VTtxt,'uK_nwp',nwptxt, ...
    'ver',ntrialtxt];
save(namesaved,'coeff','corr','eEn');
disp(['Eig-Energy: ',namesaved]);
%
%% Get Wave-Function
nE = 1; % %% <-- [Change Here!]
En = eEn.E_eig_corrected(nE);
eFn = so_get_eigfunction(mygrid,coeff,Phi0,prpg,corr,En);
endsound;
%
%% Save Wave-Function
nEtxt = namecode('00',nE);
myvarname = ['eFn_nE',nEtxt];
eval([myvarname,' = eFn;']);
save(namesaved,myvarname,'-append');
disp(['Wave-Function: ',namesaved,': ',myvarname]);
```

End of code

SO_GET_GRID.M

```
function mygrid = so_get_grid(coeff)

% see also: so_get_en
if nargin < 1,
    coeff.a0 = 5;  %% [rscale m] Length (size of simulation)
    coeff.Ng = 256;%128;  %% size of matrix
    coeff.rscale = 1e-6; %% prefix of length in [m]
end

%%% COORDINATES
mygrid.x = (coeff.rscale)*linspace(-coeff.a0/2,coeff.a0/2,coeff.Ng);
mygrid.x = mygrid.x';
% ^-- dx = rscale*a0/(Ng-1) = x(2)-x(1);
[mygrid.xx,mygrid.yy] = meshgrid(mygrid.x,mygrid.x);
[mygrid.theta,mygrid.rho] = cart2pol(mygrid.xx,mygrid.yy);
%
mygrid.kx = (2*pi/(coeff.rscale*coeff.a0))* ...
    linspace((-coeff.Ng)/2,(coeff.Ng-2)/2,coeff.Ng);
mygrid.kx = mygrid.kx';
[mygrid.kxx,mygrid.kyy] = meshgrid(mygrid.kx,mygrid.kx);
```

End of code

SO_GET_POTENTIAL_RING.M

```
function V = so_get_potential_ring(mygrid,coeff,dispFlag)
%
if nargin < 3,
    dispFlag = 1;
end
if nargin < 2,
    coeff.rscale = 1e-6; % [micro]
    coeff.charge = 4;
    coeff.rpeak = 1;
    coeff.tempUmax = 100e-6;
end
if nargin < 1,
    mygrid = so_get_grid;
end
%
rpeak = (coeff.rscale*coeff.rpeak);
rmax = const('Jrp',coeff.charge);
rzro = const('Jrz',coeff.charge);
alpha = (1/rpeak)*rmax;
%
%%% POTENTIAL
Rho = alpha*mygrid.rho;
V = besselj(coeff.charge,Rho).^2;
Vmax = max(max(V));
V(Rho > rzro) = 0;
V = -const('Kb')*coeff.tempUmax*V/Vmax;
%
% Display
if dispFlag
figurel(1);clf;set(gcf,'position',[33 47 241 759]);
subplot(3,1,1);
contour(mygrid.x,mygrid.x,V,14);axis square;
ylabel('Potential''s Contour (Top view)');
subplot(3,1,2);
imagesc(mygrid.x,mygrid.x,V);axis square;
ylabel('Potential: V(x,y)');
subplot(3,1,3);
yhlf_pxl = round(size(V,1)/2);
plot(mygrid.x,V(yhlf_pxl,:));
axis([mygrid.x(1) mygrid.x(end) min(V(yhlf_pxl,:)) max(V(yhlf_pxl,:))]);
ylabel('Potential: V(x,0)');
end
```

End of code

SO_GET_DAMPBOUND.M

```
function Bnd = so_get_dampbound(mygrid,coeff)
%
if nargin < 2,
    coeff.nb = 40;
    coeff.cj = 42.8;
    coeff.cg = 0.933;
    coeff.cexp = 40;
end
if nargin < 1,
    mygrid = so_get_grid;
end


Bnd = besselj(coeff.nb,coeff.cj*abs(mygrid.rho)/mygrid.x(end));
Bnd(mygrid.rho>=coeff.cg*mygrid.x(end)) = max(max(Bnd));
Bnd = Bnd - min(min(Bnd));
Bnd = Bnd/max(max(Bnd));
Bnd = exp(-coeff.cexp*Bnd);
```

```
%
figurel(1);clf;imagesc(mygrid.x,mygrid.x,Bnd);
% surf(mygrid.x,mygrid.x,Bnd);shading(gca,'interp')
title('Damping Boundary');
```

End of code

SO_GET_INITWAVEPACKET.M

```
function Phi0 = so_get_initwavepacket(mygrid,coeff,V)
%
if nargin < 3,
    disp('SO_GET_INITWAVEPACKET() needs 3 arguments');
    disp('Enter DEMO Mode:')
    mygrid = so_get_grid;
    coeff.amp = 1;  %% amp of initial wavepacket
    coeff.wd = 0.3*abs(mygrid.x(1)); %% width of initial wavepacket
    coeff.nwp = 1; %% vortical index of initial wavepacket
    V = exp(-0.5*((mygrid.rho/coeff.wd).^2));
end
%%-----------------------------------------------------------------------
%
%%% INITIAL WAVE PACKET
%%% nwp --> defined in PARAMETERS
% Pamp = coeff.amp*exp(-0.5*((Rhoh/coeff.wd).^2));
% Pamp = coeff.amp*sin(3*mygrid.rho/abs(mygrid.x(1))).*V/max(max(abs(V)));
% Pamp = coeff.amp*cos(3*mygrid.rho/abs(mygrid.x(1))).*V/max(max(abs(V)));
Pamp = coeff.amp*V/max(max(abs(V)));
Phi0 = coeff.amp*Pamp.*exp(1i*coeff.nwp*mygrid.theta);
%
figurel(101);
% contour(xx,yy,V,14);hold off;
% imagesc(abs(Phi0));hold off;
imagesc(Pamp);hold off;
%
figurel(102);clf;hold on;box on;grid on;
V1d = V(round(size(V,1)/2),:);
V1d = V1d/max(abs(V1d));
P1d = Pamp(round(size(Pamp,1)/2),:);
P1d = P1d/max(P1d);
plot(mygrid.x,V1d,'r');
plot(mygrid.x,P1d+min(V1d),'b--');
```

End of code

SO_GET_PROPAGATOR.M

```
function output = so_get_propagator(mygrid,coeff,V,Bnd)

%%% PROPAGATORS
% GK1 = (exp(-(i*hbar*dt_sim/(4*mRb))*(kxx.^2 + kyy.^2)));
% ^-- dt_sim/2 kinetic energy propagator
output.GK2 = exp(-(i*coeff.hbar*coeff.dt_sim/(2*coeff.mRb))* ...
    (mygrid.kxx.^2 + mygrid.kyy.^2));
% ^-- dt_sim/1 kinetic energy propagator
% GV0 = exp(-i*dt_sim*(V - i*Bnd)/hbar);
% ^-- Potential: spatial interaction
% ^-- V = V - i*Bnd;  %% Absorption at simulation boundary
output.GV1 = Bnd.*exp(-i*coeff.dt_sim*(V)/(2*coeff.hbar));
% ^-- half spatial operator: spatial interaction
% ^-- V = V - i*Bnd;  %% Absorption at simulation boundary
```

End of code

SO_GET_CORRELATION.M

```
function output = so_get_correlation(mygrid,coeff,Phi0,Propg)

% GET CORRELATION

%%% CALCULATIONS
Phi0c = conj(Phi0); % real(Phi0)- i*imag(Phi0);
Pt = zeros(1,coeff.NPt); % <-- allocating memory
Pt(1) = trapz(mygrid.x,trapz(mygrid.x,Phi0c.*Phi0,2),1); % @t = 0
%
t = coeff.dt_sim*(0:1:coeff.NPt-1);
% T_sim = dt_sim*(NPt-1); % T_sim = t(end);
% ^-- dt_sim = (t(n)-t(n-1)) = T / (NPt-1)
%
figure(10);set(gcf,'position',[20 100 320 700]);
Phi = Phi0;
for nrn = 2:coeff.NPt
    iPhi = fft2c(Propg.GV1.*Phi);
    Phi = Propg.GV1.*ifft2c(iPhi.*Propg.GK2); %% <-- Evaluate @ dt_sim
    Pt(nrn) = trapz(mygrid.x,trapz(mygrid.x,Phi0c.*Phi,2),1);
    if mod(nrn,coeff.Ndisp) == 0
        figure(10);
        subplot(2,1,1);contour(mygrid.xx,mygrid.yy, real(Phi),10);
        title(['\Phi_x  t_{',num2str(nrn),'} = ',num2str(t(nrn))]);
        xlabel('x');ylabel('y');
        subplot(2,1,2);contour(mygrid.kxx,mygrid.kyy,(real(iPhi)),10);
        title('\Phi_k');
        xlabel('kx');ylabel('ky');
        drawnow;
    end
end

Pto = Pt(1:coeff.sstep:coeff.NPt);
tmo = t(1:coeff.sstep:coeff.NPt);
dto = coeff.sstep*coeff.dt_sim; %abs(tmo(2)-tmo(1));
% ^-- new dt_sim (after changing sampling step)
To = tmo(end);
% ^-- new T (after changing sampling step)
No = length(tmo);

output.t = t;
output.Pt = Pt;
output.Pto = Pto;
output.tmo = tmo;
output.dto = dto;
output.To = To;
output.No = No;
%
figure(21);clf;box on;grid on;
plot(tmo,abs(Pto));
title('Correlation Function ');xlabel('Time'); axis tight;
```

End of code

SO_GET_EIGENERGY.M

```
function output = so_get_eigenergy(coeff,corr)

% GET EIGEN-ENERGY

Eo = (2*pi*coeff.hbar/corr.To)* ...
         (linspace((-corr.No)/2,(corr.No-2)/2,length(corr.Pto)));
Peo = fliplr(abs(fftshift(fft(((1-cos(2*pi*corr.tmo/corr.To)).* ...
         corr.Pto/corr.To)))));
lnPeo = log(Peo);
%
```

```
figure(22);clf;box on;grid on;
plot(Eo,lnPeo,'rx-');
title('Energy Spectrum');xlabel('Energy');ylabel('Power');
pause(1);
%
%%% FIND EXTREMA
%%% External file:
%%% http://www.mathworks.com/matlabcentral/fileexchange: EXTREMA
idx = find((Eo >= 1.2*coeff.Elow) & (Eo <= 1.2*coeff.Ehgh) & (lnPeo > coeff.lnPeoBase));
Ebnd = Eo(idx);
Pebnd = Peo(idx);
lnPebnd = lnPeo(idx);
%
[lnPEmax,imax,lnPEmin,imin] = extrema(lnPebnd);
idxmax = sort(imax);
if idxmax(1) == 1, idxmax(1) = []; end
if idxmax(end) == length(idx), idxmax(end) = []; end
idxmin = sort(imin);
if idxmin(1) == 1, idxmin(1) = []; end
if idxmin(end) == length(idx), idxmin(end) = []; end
E_eig = Ebnd(idxmax);
lnPebnd_eig = lnPebnd(idxmax);
E_bottom = Ebnd(idxmin);
lnPebnd_bottom = lnPebnd(idxmin);
%
idx2 = find(E_eig > coeff.Ehgh | E_eig < coeff.Elow);
idx3 = find(E_bottom > coeff.Ehgh | E_bottom < coeff.Elow);
idxmax(idx2)=[];
lnPebnd_eig(idx2)=[];
E_eig(idx2)=[];
lnPebnd_bottom(idx3)=[];
E_bottom(idx3)=[];
%
figurel(22);hold on;
plot(E_eig,lnPebnd_eig,'go');
plot(E_bottom,lnPebnd_bottom,'yo');
plot(repmat(coeff.Elow,1,2),[0 -60],'k:');
plot(repmat(coeff.Ehgh,1,2),[0 -60],'k:');
disp('E_eig ([K]): ');
disp(num2str(E_eig'/coeff.Kb));
%
%%% LINESHAPE-FITTING CORRECTION
%%% Hanning window func: w(t) = (1-cos(2*pi*t/T))
%
R = (Pebnd(idxmax+1))./(Pebnd(idxmax-1));
% Ebnd(idxmax+1) % Ebnd(idxmax) % Ebnd(idxmax-1)
rr = (1+R)./(1-R);
mysign = sign(R-1);
del = (3*rr + mysign.*sqrt(9*(rr.^2)-8))/2;
dE = - 2*pi*del*coeff.hbar/corr.To;
E_eig_corrected = E_eig + dE;
disp('E_eig_corrected ([K]): ');
disp(num2str(E_eig_corrected'/coeff.Kb));
fprintf('There are %d bound states\n',length(E_eig_corrected))
%
for m = 1:length(E_eig),%7;
    fprintf('E%d\n',m);
    fprintf('E(m) = %1.10e\n',Ebnd(idxmax(m)));
    fprintf('E(m+1) = %1.10e\n',Ebnd(idxmax(m)+1));
    fprintf('E(m-1) = %1.10e\n',Ebnd(idxmax(m)-1));
    fprintf('E_corrected = %1.10e\n',E_eig_corrected(m));
    fprintf('dE = %1.10e\n',dE(m));
    fprintf('rr = %1.10e\n',rr(m));
    fprintf('R = %1.10e\n\n',R(m));
end
%
%%% OUTPUTS
```

```
output.Eo = Eo;
output.Peo = Peo;
output.lnPeo = lnPeo;
output.E_eig = E_eig;
output.lnPebnd_eig = lnPebnd_eig;
output.E_bottom = E_bottom;
output.lnPebnd_bottom = lnPebnd_bottom;
output.E_eig_corrected = E_eig_corrected;
output.rr = rr;
output.R = R;
```

End of code

SO_GET_EIGFUNCTION.M

```
function eFn = so_get_eigfunction(mygrid,coeff,Phi0,prpg,corr,En)
%
% GET EIGEN-FUNCTION
% CALCULATIONS
%
figure(3); clf; set(gcf,'position',[30 100 240 500]);
subplot(2,1,1);set(gca,'fontsize',8);set(gca,'fontname','verdana');
subplot(2,1,2);set(gca,'fontsize',8);set(gca,'fontname','verdana');
annt = annotation(gcf,'textbox','Edgecolor','none', ...
    'string','t(0) = 0 s', ...
    'HorizontalAlignment','left', ...
    'VerticalAlignment','middle', ...
    'fontname','verdana','fontsize',8);
set(annt,'position',[0.3 0.4 0.4 0.05]);
%
T_sim = corr.t(end); % T_sim = dt_sim*(NPt-1); %
wt = (1-cos(2*pi*corr.t/T_sim));
Phi = Phi0;
eFn = 0;
for nrn = 1:length(corr.t)  % length(corr.t) = coeff.NPt
    PhiE = Phi*wt(nrn)*exp(i*En*corr.t(nrn)/coeff.hbar);
    eFn = eFn + 2*PhiE;
    iPhi = fft2c(prpg.GV1.*Phi);
    Phi = prpg.GV1.*ifft2c(iPhi.*prpg.GK2); %% <-- Evaluate @ coeff.dt_sim
    if mod(nrn,coeff.Ndisp) == 0
        figure(3);
        subplot(2,1,1);contour(mygrid.xx,mygrid.yy,abs(PhiE),10);
        title('PhiE(t) = 2 \Phi(t) w(t) exp(i*E_n*t)');
        xlabel('x');ylabel('y');axis tight;
        subplot(2,1,2);contour(mygrid.xx,mygrid.yy,real(eFn),10);
        title(['Eigen function @ E = ',num2str(En)]);
        xlabel('x');ylabel('y');axis tight;
        mytimetxt = ['t(',num2str(nrn),') = ',num2str(corr.t(nrn)),' s'];
        set(annt,'string',mytimetxt);
        drawnow;
    end
end
%
% NOTE: TRAPAZOIDAL INTEGRATION
%
% eFn = \int_{t=0}^{T} \Phi(t) w(t) exp(i*E_n*t) dt
% eFn = [ \frac{PhiE(0) + PhiE(1*dt)}{2} + \frac{PhiE(1*dt) + PhiE(2*dt)}{2}
%         + ... + \frac{PhiE((N-1)*dt) + PhiE(N*dt)}{2} ] * dt
% eFn = [ PhiE(0) + 2*PhiE(1*dt) + ... + 2*PhiE((N-1)*dt) + PhiE(N*dt) ]
%         * \frac{dt}{2}
%
% PhiE(0) = 0; % b/c w(0) = 0;
% PhiE(N*dt) = 0; b/c w(N*dt) = 0;
%
% eFn = [eFn - 0/2 - 0/2]*dt/2;
eFn = eFn*coeff.dt_sim/2;
%
```

```
so_disp_eigfunction(mygrid,corr,eFn,En);
```

End of code

G.11 Miscellaneous

This section includes source codes used in some of the MATLAB scripts or functions shown earlier. They are (1) a 2D centered discrete Fourier transform (`fft2c`), (2) a 2D centered inverse discrete Fourier transform (`ifft2c`), (3) a radial scan script (`scp_rscan_pol2.m`), and (4) a radial scan function (`rscan_pol2`). The first and second ones are used to obtained the FFT that has zero frequency component in the middle of the Matrix instead of at the edge as is usually done in the normal FFT function. The third code is the script that use the fourth code to convert a distribution matrix into a radial profile in polar coordinates.

G.11.1 2D Centered Discrete Fourier Transform

FFT2C.M

```
function x = fft2c(x,varargin)
%FFTC Centered discrete Fourier transform.

%   Usage see: IFFTC, FFT, IFFT, FFT2, IFFT2, FFTSHIFT.
%   v1.0, 6/25/01, Michael Butterfield, <gte881s@prism.gatech.edu>
%   v1.1, 6/26/01, Erik Zeek, <zeekec@mad.scientist.com>
%      Updated help.  Changed to VARARGIN implementation.
%   $Revision: 1.3 $ $Date: 2002/04/18 22:05:29 $
%   $Log: fftc.m,v $
%   Revision 1.3  2002/04/18 22:05:29  zeekec
%   Reused the input as the output.
%   Revision 1.2  2001/07/10 01:10:00  zeekec
%   Library cleanup.  Added, deleted, and moved files.
%
x = fftshift(fft2(ifftshift(x),varargin{:}));
```

End of code

G.11.2 2D Centered Inverse Discrete Fourier Transform

IFFT2C.M

```
%IFFT2C Centered inverse discrete Fourier transform.

%   Usage see: IFFTC, FFT, IFFT, FFT2, IFFT2, FFTSHIFT.
%   v1.0, 6/25/01, Michael Butterfield, <gte881s@prism.gatech.edu>
%   v1.1, 6/26/01, Erik Zeek, <zeekec@mad.scientist.com>
%      Updated help.  Changed to VARARGIN implementation.
%   $Revision: 1.3 $ $Date: 2002/04/18 22:05:29 $
%   $Log: fftc.m,v $
```

```
%   Revision 1.3  2002/04/18 22:05:29  zeekec
%   Reused the input as the output.
%   Revision 1.2  2001/07/10 01:10:00  zeekec
%   Library cleanup.  Added, deleted, and moved files.
%
x = ifftshift(ifft2(fftshift(x),varargin{:}));
```

End of code

G.11.3 Radial Scan Script

This script shows the usage of the function "rscan_pol2" (down below).

SCP_RSCAN_POL2.M

```
%% Generate 2D Profile to scan
clear all; close all; clc;
charge = 4;
M = 256;
a0 = 10e-3;% %% [m] Sim Size
kappa = 8000;
x = linspace(-a0/2,a0/2,M); x = x'; %% [m] % 1D Cartesian Grid
dx = abs(diff(x(1:2))); % Grid Spacing
[xx,yy] = meshgrid(x,x);  % 2D Cartesian Grid
[th,rh] = cart2pol(xx,yy); % 2D Polar Grid
Axy = besselj(charge,kappa*rh).^2;
figure(1);imagesc(Axy);axis image;
[rBin,yPavg,yPstd,rPr,yPr] = rscan_pol2(Axy,rh,dx);
figure(2);plot(rBin,yPavg);axis tight;
```

End of code

G.11.4 Radial Scan Function

RSCAN_POL2.M

```
function [rBin,yPavg,yPstd,rPr,yPr] = rscan_pol2(M,rh,dr)

% M -- 2D Matrix
% rh -- polar rho Matrix (e.g. from cart2pol)
% dr -- grid spacing of rh

rP = sortrows([rh(:),M(:)]);
rP = unique(rP,'rows');

drP = [1;diff(rP(:,1));1];
idx = find(drP~=0);

rPr = zeros(1,length(idx)-1);
yPr = zeros(1,length(idx)-1);
for nn = 1:(length(idx)-1)
    rPr(1,nn) = rP(idx(nn),1);
    yPr(1,nn) = mean(rP(idx(nn):(idx(nn+1)-1),2));
end

rPc = rPr;
yPc = yPr;

rMx = max(rPr);
Nr = ceil(rMx/dr); % -> might become a bug in the future

rBin = dr*(0:1:Nr);
```

```
yPavg = zeros(1,Nr);
yPstd = zeros(1,Nr);
for nrn = 1:Nr
    [ida]=find( rPc >= rBin(nrn) & rPc < rBin(nrn+1) );
    yPavg(nrn) = mean(yPc(ida));
    yPstd(nrn) = std(yPc(ida));
    rPc(ida) = []; yPc(ida) = [];
end
rBin(end) = [];
rBin = rBin+0.5*dr;

if nargout == 0
figurel(10);clf;hold on;box on;
% errorbar(rBin,yPavg,yPstd,'b--');
plot(rBin,yPavg,'r');
end
```

End of code

Appendix H

Color-Mappings

The color of the figures (excluding real images from the experimental setup) in this thesis presented by the value according to the following color-mappings. All the mappings are generated from MATLAB.

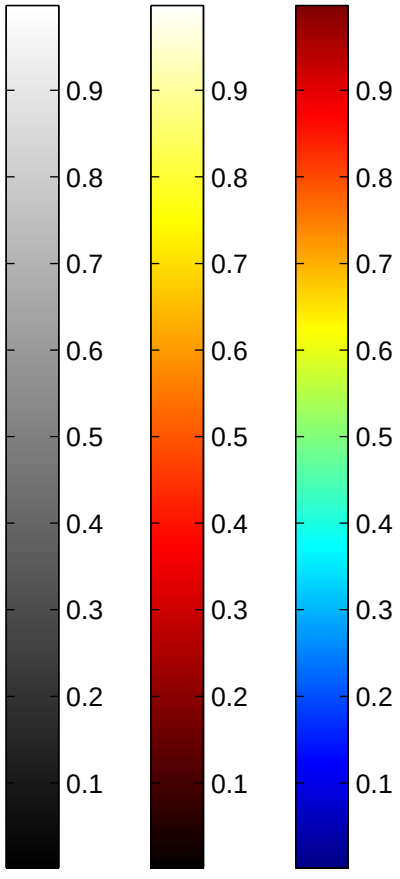

Figure H.1: Color mappings of figures presented in this thesis. The maximum value shown here is normalized to one. The name of the color mappings from left to right are “gray”, “hot”, and “jet” according to MATLAB.

Bibliography

[1] E. L. Raab, M. Prentiss, A. Cable, S. Chu, and D. E. Pritchard, "Trapping of Neutral Sodium Atoms with Radiation Pressure," Phys. Rev. Lett. **59**(23), 2631.

[2] T. W. Hänsch and A. L. Schawlow, "Cooling of gases by laser radiation," Opt. Commun. **13**, 68 (1975).

[3] D. J. Wineland and H. Dehmelt, "Proposed 1014 Delta Upsilon Less Than Upsilon Laser Fluorescence Spectroscopy on T1+ Mono-Ion Oscillator III," Bull. Am. Phys. Soc. **20**, 637 (1975).

[4] S. Chu, "Manipulation of neutral particles," Rev. Mod. Phys. **70**, 685 (1998).

[5] C. N. Cohen-Tannoudji, "Manipulating atoms with photons," Rev. Mod. Phys. **70**, 707 (1998).

[6] W. D. Phillips, "Laser cooling and trapping of neutral atoms," Rev. Mod. Phys. **70**, 721 (1998).

[7] M. G. Raizen, "Compression of atomic phase space using an asymmetric one-way barrier," PRL **94**, 053,003 (2005).

[8] E. Narevicius, "An atomic coilgun: using pulsed magnetic fields to slow a supersonic beam," New J. Phys. **9**, 358 (2007).

[9] M. G. Raizen, "Comprehensive control of atomic motion," Science **324**, 1403 (2009).

[10] S. C. Doret, C. B. Connolly, W. Ketterle, and J. M. Doyle, "Buffer-gas cooled Bose-Eistein condensate," Phys. Rev. Lett. **103**, 103,005 (2009).

[11] B. T. Seaman, M. Krämer, D. Z. Anderson, and M. J. Holland, "Atomtronics: ultracold-atom analogs of electronics devices," Phys. Rev. A **75**, 023,615 (2007).

[12] R. A. Pepino, J. Cooper, D. Z. Anderson, and M. J. Holland, "Atomtronic circuits of diodes and transistors," Phys. Rev. Lett. **103**, 140,405 (2009).

[13] A. Ruschhaupt and J. G. Muga, "Atom diode: a laser device for a unidirectional transmission of ground-state atoms," Phys. Rev. A **70**, 061,604(R) (2004).

[14] J. Hu, C. Wu, and X. Dai, "Proposed design of a Josephson diode," Phys. Rev. Lett. **99**, 067,004 (2007).

[15] V. M. Akulin, Y. E. Lozovik, I. E. Mazets, A. G. Rudavets, and A. Sarfati, "Tunneling electroconductance of atomic Bose-Einstein condensates," Phys. Rev. A **79**, 063,614 (2009).

[16] J. Y. Vaishnav, J. Ruseckas, C. W. Clark, and G. Juzeliūnas, "Spin field effect transistors with ultracold atoms," Phys. Rev. Lett. **101**, 265,302 (2008).

[17] B. P. Anderson, K. Dholakia, and E. M. Wright, "Atomic-phase interference devices based on ring-shaped Bose-Einstein condensates: Two-ring case," Phys. Rev. A **67**, 033,601 (2003).

[18] V. M. Kaurov and A. B. Kuklov, "Josephson vortex between two atomic Bose-Einstein condensates," Phys. Rev. A **71**, 011,601(R) (2005).

[19] Z. Y. Wang, Z. Zhang, and Q. Lin, "Atom interferometers manipulated through the toroidal trap realized by the interference patterns of Laguerre-Gaussian beams," Eur. Phys. J. D. **53**, 127 (2009).

[20] A. Ramanathan, K. C. Wright, S. R. Muniz, M. Zelan, W. T. Hill, III, C. J. Lobb, K. Helmerson, W. D. Phillips, and G. K. Campbell, "Superflow in a toroidal Bose-Einstein condensate: an atom circuit with a tunable weak link," Phys. Rev. Lett. **106**, 130,401 (2011).

[21] M. H. Anderson, J. R. Ensher, M. R. Matthews, C. E. Wieman, and E. A. Cornell, "Observation of Bose-Einstein condensation in a dilute atomic vapor," Science **269**, 198 (1995).

[22] A. D. Cronin, J. Schmiedmayer, and D. E. Pritchard, "Optics and interferometry with atoms and molecules," Rev. Mod. Phys. **81**, 1051 (2009).

[23] R. Dumke, T. Mather, M. Volk, W. Ertmer, and G. Birkl, "Interferometer-type structures for guided atoms," Phys. Rev. Lett. **89**, 220,402 (2002).

[24] Y. Shin, C. Sanner, G.-B. Jo, T. A. Pasquini, M. Saba, W. Ketterle, D. E. Pritchard, M. Vengalattore, and M. Prentiss, "Interference of Bose-Einstein condensates split with an atom chip," Phys. Rev. A **72**, 021,604(R) (2005).

[25] D. E. Miller, J. R. Anglin, J. R. Abo-Shaeer, K. Xu, J. K. Chin, and W. Ketterle, "High-contrast interference in a thermal cloud of atoms," Phys. Rev. A **71**, 043,615 (2005).

[26] Y.-J. Wang, D. Z. Anderson, V. M. Bright, E. A. Cornell, Q. Diot, T. Kishimoto, M. Prentis, R. A. Saravanan, S. R. Segal, and S. Wu, "Atom Michelson interferometer on a chip using a Bose-Einstein condensate," Phys. Rev. Lett. **94**, 090,405 (2005).

[27] J. Denschlag, D. Cassettari, A. Chenet, S. Schneider, and J. Schmiedmayer, "A neutral atom and a wire: towards mesoscopic atom optics," Appl. Phys. B **69**, 291 (1999).

[28] D. Müller, D. Z. Anderson, R. J. Grow, P. D. D. Schwindt, and E. A. Cornell, "Guiding neutral atoms around curves with lithographically patterned current-carrying wires," Phys. Rev. Lett. **83**, 5194 (1999).

[29] D. Müller, E. A. Cornell, P. D. D. Schwindt, A. Zozulya, and D. Z. Anderson, "Waveguide atom beam splitter for laser-cooled neutral atoms," Opt. Lett. **25**, 1382 (2000).

[30] D. Cassettari, A. Chenet, R. Folman, A. Haase, B. Hessmo, P. Krüger, T. Maier, S. Schneider, T. Calarco, and J. Schmiedmayer, "Micromanipulation of neutral atoms with nanofabricated structures," Appl. Phys. B. **70**, 721 (2000).

[31] D. Cassettari, B. Hessmo, R. Folman, T. Maier, and J. Schmiedmayer, "Beam splitter for guided atoms," Phys. Rev. Lett. **85**, 5483 (2000).

[32] R. Folman, P. Kruger, D. Cassettari, B. Hessmo, T. Maier, and J. Schmiedmayer, "Controlling cold atoms using nanofabricated surfaces: Atom chips," Phys. Rev. Lett. **84**, 4749 (2000).

[33] N. H. Dekker, C. S. Lee, V. Lorent, J. H. Thywissen, S. P. Smith, M. Drndic, R. M. Westervelt, and M. Prentiss, "Guiding Neutral Atoms on a Chip," Phys. Rev. Lett. **84**, 1124 (2000).

[34] O. Houde, D. Kadio, and L. Pruvost, "Cold atom beam splitter realized with two crossing dipole guides," Phys. Rev. Lett. **85**, 5543 (2000).

[35] I. V. Arakelyan, N. Chattrapiban, S. Mitra, and W. T. Hill, III, "Versatile element for free-space dividing and redirecting neutral-atom clouds," Phys. Rev. A **75**, 061,604(R) (2007).

[36] Y. Song, D. Milam, and W. T. Hill, III, "Long, narrow all-light atom guide," Opt. Lett. **24**, 1805 (1999).

[37] R. Grimm, M. Weidemüller, and Y. B. Ovchinnikov, *Optical Dipole Traps for Neutral Atoms*, vol. 42 of *Advances In Atomic, Molecular, and Optical Physics*, pp. 95 – 170 (Academic Press, New York, 2000). B. Bederson and H. Walther, ed.,.

[38] M. D. Barrett, J. A. Sauer, and M. S. Chapman, "All-optical formation of an atomic Bose-Einstein condensate," Phys. Rev. Lett. **87**, 1515 (2001).

[39] J.-P. Yin, W.-J. Gao, H.-F. Wang, Q. Long, and Y.-Z. Wang, "Generation of dark hollow beams and their applications in laser cooling of atoms and all optical-type Bose-Einstein condensation," Chin. Phys. **11**, 1157 (2002).

[40] J.-P. Yin, W.-J. Gao, and Y. F. Zhu, *Generation of dark hollow beams and their applications*, vol. 45 of *Progress in Optics*, pp. 119 – 204 (Elsevier Science B. V., Amsterdam, the Netherlands, 2003). Editor: E. Wolf.

[41] S. Barreiro, J. W. R. Tabosa, J. P. Torres, Y. Deyanova, and L. Torner, "Four-wave mixing of light beams with engineered orbital angular momentum in cold cesium atoms," Opt. Lett. **29**, 010,404 (2004).

[42] J.-P. Yin, "Realization and research of optically-trapped quantum degenerate gases," Phys. Reports **430**, 1 (2006).

[43] N. Chattrapiban, E. A. Rogers, I. V. Arakelyan, R. Roy, and W. T. Hill, III, "Laser beams with embedded vortices: Tools for atom optics," JOSA B **23**, 94 (2006).

[44] S. Marksteiner, C. M. Savage, and P. Zoller, "Coherent atomic waveguides from hollow optical fiber: quantized atomic motion," Phys. Rev. A **50**, 2680 (1994).

[45] F. K. Fatemi and M. Bashkansky, "Cold atom guidance using a binary spatial light modulator," Opt. Express **14**, 1368 (2006).

[46] V. Boyer, R. M. Godun, G. Smirne, D. Cassettari, C. M. Chandrashekar, A. B. Deb, Z. J. Laczik, and C. J. Foot, "Dynamic manipulation of Bose-Einstein condensates with a spatial light modulator," Phys. Rev. A **73**, 031,402(R) (2006).

[47] F. K. Fatemi, M. Bashkansky, and Z. Dutton, "Dynamic high-speed spatial manipulation of cold atoms using acousto-optic and spatial light modulation," Opt. Express **15**, 3589 (2007).

[48] K. Henderson, C. Ryu, C. MacCormick, and M. B. Boshier, "Experimental demonstration of painting arbitrary and dynamic potentials for Bose-Einstein condensates," New J. Phys. **11**, 043,030 (2009).

[49] M. J. Renn, D. Montgomery, O. Vdovin, D. Z. Anderson, C. E. Wieman, and E. A. Cornell, "Laser-Guided atoms in hollow-core optical fibers," Phys. Rev. Lett. **75**, 3253 (1995).

[50] M. J. Renn, A. A. Zozulya, E. A. Donley, E. A. Cornell, and D. Z. Anderson, "Optical-dipole-force fiber guiding and heating of atoms," Phys. Rev. A **55**, 3684 (1997).

[51] J.-P. Yin, Y.-F. Zhu, W.-H. Jhe, and Z. Wang, "Atom guiding and cooling in a dark hollow laser beam," Phys. Rev. A **58**, 509 (1998).

[52] J. Yin, Y. Lin, K.-L. Lee, H. Nha, H.-R. Noh, and Y. Wang, "Guiding of atoms in a dark-hollow laser beam," J. Korean Phys. Soc. **33**, 362 (1998).

[53] J.-P. Yin, Y.-F. Zhu, and Y.-Z. Wang, "Evanescent light-wave atomic funnel: A tandem hollow-fiber, hollow-beam approach," Phys. Rev. A **57**, 1957 (1998).

[54] H. J. Davies and C. S. Adams, "Transferring laser-cooled atoms to a spatially separated magnetic trap using a far-off resonance optical guide," J. Phys. B: At. Mol. Opt. Phys. **33**, 4079 (2000).

[55] S. R. Mishra, S. P. Ram, S. K. Tiwari, and S. C. Mehendale, "Enhanced atom transfer in a double magneto-optical trap setup," Phys. Rev. A **77**, 065,402 (2008).

[56] X. Xu, V. G. Minogin, K. Lee, Y. Wang, and W. Jhe, "Guiding cold atoms in a hollow laser beam," Phys. Rev. A **60**, 4796 (1999).

[57] X. Xu, Y. Wang, and W. Jhe, "Theory of atom guidance in a hollow laser beam: dressed-atom approach," JOSA B **17**, 1039 (2000).

[58] X. Xu, K. Kim, W. Jhe, and N. Kwon, "Efficient optical guiding of trapped cold atoms by a hollow laser beam," Phys. Rev. A **63**, 063,401 (2001).

[59] B. T. Wolschrijn, R. A. Cornelussen, R. J. C. Spreeuw, and H. B. van Linden van den Heuvell, "Guiding of cold atoms by red-detuned laser beam of moderate power," New J. Phys. **4**, 69.1 (2002).

[60] Y. Song, "Hollow Beam Atom Tunnel," Phd thesis, University of Maryland (1999).

[61] L. Pruvost, D. Marescaux, O. Houde, and H. T. Duong, "Guiding and cooling of cold atoms in a dipole guide," Opt. Commun. **166**, 199 (1999).

[62] D. Rhodes, D. Gherardi, J. Livesey, D. McGloin, H. Melville, T. Freegarde, and K. Dholakia, "Atom guiding along high order Laguerre-Gaussian light beams formed by spatial light modulation," J. Mod. Opt. **53**, 547 (2006).

[63] M. Mestre, F. Diry, B. V. de Lesegno, and L. Pruvost, "Cold atom guidance by a holographically-generated Laguerre-Gaussian laser mode," Eur. Phys. J. D **57**, 87 (2010).

[64] K. Bongs, S. Burger, S. Dettmer, D. Hellweg, J. Arlt, W. Ertmer, and K. Sengstock, "Waveguide for Bose-Einstein condensates," Phys. Rev. A **63**, 031,602(R) (2001).

[65] P. Verkerk, B. Lounis, C. Salomon, C. Cohen-Tannoudiji, J.-Y. Courtois, and B. Grynberg, "Dynamics and spatial order of cold cesium atoms in a periodic optical potential," Phys. Rev. Lett. **68**, 3861 (1992).

[66] P. S. Jessen, C. Gerz, P. D. Lett, W. D. Phillips, S. L. Rolston, R. J. C. Spreeuw, and C. I. Westbrook, "Observation of quantized motion of Rb atoms in an optical field," Phys. Rev. Lett. **69**, 49 (1992).

[67] J. S. Sebby, "Demonstration of dense mesoscopic atomic clouds in a holographic atom," Phd thesis, University of Wisconsin-Madison (2004).

[68] H. Kogelnik and T. Li, "Laser beams and resonators," Appl. Opt. **5**, 1550 (1966).

[69] J. R. Leger, D. Chen, and G. Mowry, "Design and performance of diffractive optics for custom laser resonators," Appl. Opt. **34**, 2498 (1995).

[70] P. Pääkkönen and J. Turunen, "Resonators with Bessel-Gauss modes," Opt. Commun. **156**, 359 (1998).

[71] U. T. Schwarz, M. A. Bandres, and J. C. Gutiérrez-Vega, "Observation of Ince-Gaussian modes in stable resonators," Opt. Lett. **29** (2004).

[72] J. Yin, Y. Zhu, W. Jhe, and Z. Wang, "Atom guiding and cooling in a dark hollow laser beam," Phys. Rev. A **58**, 509 (1998).

[73] D. Gabor, *Holography, 1948-1971*, pp. 11–44, Nobel Lectures, Physics 1971–1980 (World Scientific Publishing Co., Singapore, 1992). Editor Stig Lundqvist.

[74] F. Zernike, *How I discovered phase contrast*, p. 239, Nobel Lectures, Physics 1942–1962 (Elsevier Publishing Co., Amsterdam, 1964).

[75] C. A. Alonzo, P. J. Rodrigo, and J. Glückstad, "Photon-efficient grey-level image projection by the generalized phase contrast method," New J. Phys. **9**, 1 (2007).

[76] R. W. Gerchberg, "A new approach to phase retrieval of a wave front," J. Mod. Opt. **49**, 1185 (2002).

[77] E. R. Dufresne, G. C. Spalding, M. T. Dearing, S. A. Sheets, and D. G. Grier, "Computer-generated holographic optical tweezer arrays," Rev. Sci. Instrum. **72**, 1810 (2000).

[78] D. Cojoc, E. Di-Fabrizio, L. Businaro, S. Cabrini, F. Romanato, L. Vaccari, and M. Altissimo, "Design and fabrication of diffractive optical elements for optical tweezer arrays by means of e-beam lithography," Microelectron. Eng. **61–62**, 963 (2002).

[79] A. Vasara, J. Turunen, and A. T. Friberg, "Realization of general nondiffracting beams with computer-generated holograms," J. Opt. Soc. Am. A **6**, 1748 (1989).

[80] N. R. Heckenberg, "Generation of optical phase singularities by computer-generated holograms," Opt. Lett. **17**, 221 (1992).

[81] D. V. Petrov, F. Canal, and L. Torner, "A simple method to generate optical beams with a screw phase dislocation," Opt. Commun. **143**, 265 (1997).

[82] I. Freund, "Vortex flowers," Opt. Commun. **196**, 63 (2001).

[83] J. Durnin, "Exact solutions for diffracting beams. I. The scalar theory," J. Opt. Soc. Am. A (1987).

[84] J. A. Davis, E. Carcole, and D. M. Cottrell, "Intensity and phase measurements of nondiffracting beams generated with a magneto-optic spatial light modulator," Appl. Opt. **35**, 593 (1996).

[85] N. Chattrapiban, E. A. Rogers, D. Cofield, W. T. Hill, III, and R. Roy, "Generation of nondiffracting Bessel beams by use of a spatial light modulator," Opt. Lett. **28**, 2183 (2003).

[86] J. W. Goodman and A. M. Silvestri, "Some effects of Fourier-domain phase quantization," IBM J. Res. Develop. **14**, 478 (1970).

[87] L. Allen, S. M. Barnett, and M. J. Padgett, *Optical angular momentum* (Institute of Physics Publishing, Bristol, UK, 2003). ISBN 0-7503-0901-6.

[88] D. Akamatsu and M. Kozuma, "Coherent transfer of orbital angular momentum from an atomic system to a light field," Phys. Rev. A **67**, 023,803 (2003).

[89] M. F. Andersen, C. Ryu, P. Clad, V. Natarajan, A. Vaziri, K. Helmerson, and W. D. Phillips, "Quantized rotation of atoms from photons with orbital angular momentum," Phys. Rev. Lett. **97**, 170,406 (2006).

[90] K. Volke-Sepulveda and R. Jauregui, "All-optical 3D atomic loops generated with Bessel light fields," J. Opt. B: At. Mol. Opt. Phys. **42**, 085,303 (2009).

[91] V. Milner, J. L. Hanssen, W. C. Campbell, and M. G. Raizen, "Optical billiards for atoms," Phys. Rev. Lett. **86**, 1514 (2001).

[92] S. H. Tao, W. M. Lee, and X.-C. Yuan, "Dynamic optical manipulation with a higher-order fractional Bessel beam generated from a spatial light modulator," Opt. Lett. **28**, 1867 (2003).

[93] J. F. Nye and M. V. Berry, "Dislocations in wave trains," Proc. R. Soc. Lond. A **336**, 165 (1974).

[94] J.-Y. Lu and J. F. Greenleaf, "Nondiffracting X waves-exact solutions to free-space scalar wave equation and their finite aperture realizations," IEEE Trans. Ultrason. Ferroelectr. Freq. Control **39**, 19 (1992).

[95] J.-Y. Lu and J. F. Greenleaf, "Experimental verification of nondiffracting X waves," IEEE Trans. Ultrason. Ferroelectr. Freq. Control **39**, 441 (1992).

[96] C. A. Alonzo, P. J. Rodrigo, and J. Glückstad, "Helico-conical optical beams: a product of helical and conical phase fronts," Opt. Express **13**, 1749 (2005).

[97] J. W. Goodman, *Introduction to Fourier Optics* (The McGraw-Hill Co., Inc., New York, 2002). ISBN 0-07-024254-2.

[98] G. B. Arfken and H. J. Weber, *Mathematical Methods for Physicists, Fourth Edition* (Academic Press, California, 1995). ISBN 0-120-59815-9.

[99] A. E. Siegman, *Lasers* (University Science, Mill Valley, CA, 1986). ISBN 0-935702-11-5.

[100] S. Chávez-Cerda, "A new approach to Bessel beams," J. Mod. Opt. **46**, 923 (1999).

[101] J. Arlt and K. Dholakia, "Generation of high-order Bessel beams by use of an axicon," Opt. Commun. **177**, 297 (2000).

[102] J. E. Curtis and D. G. Grier, "Structure of Optical Vortices," Phys. Rev. Lett. **90**, 133,901 (2003).

[103] M. Guizar-Sicairos and J. C. Gutierrez-Vega, "Computation of quasi-discrete Hankel transforms of integer order for propagating optical wave fields," J. Opt. Soc. Am. A **21**, 53 (2004).

[104] A. Burvall, "Axicon imaging by scalar diffraction theory," Phd thesis, Royal Institute of Technology (2004).

[105] A. Burvall, K. Kolacz, A. V. Goncharov, Z. Jaroszewicz, and C. Dainty, "Lens axicons in oblique illumination," Appl. Opt. **46**, 312 (2007).

[106] A private communication with Dr.J. E. Curtis in Spring, 2005.

[107] E. Hecht, *Optics* (Addison Wesley, California, 2002). ISBN 0-321-18878-0.

[108] G. Indebetouw, "Optical vortices and their propagation," J. Mod. Opt. **40**, 73 (1993).

[109] D. Rozas, C. T. Law, and G. A. Swartzlander, "Propagation dynamics of optical vortices," J. Opt. Soc. Am. B **14**, 3054 (1997).

[110] G. Molina-Terriza, J. Recolons, and L. Torner, "The curious arithmetic of optical vortices," Opt. Lett. **25**, 1135 (2000).

[111] S. Orlov and A. Stabinis, "Propagation of superpositions of coaxial optical Bessel beams carrying vortices," J. Opt. A: Pure Appl. Opt. **6**, S259 (2004).

[112] C. Wieman, G. Flowers, and S. Gilbert, "Inexpensive laser cooling and trapping experiment for undergraduate laboratories," Am. J. Phys. **63**, 317 (1995).

[113] S. Bali, K. M. O'Hara, M. E. Gehm, S. R. Granade, and J. E. Thomas, "Quantum-diffractive background gas collisions in atom-trap heating and loss," Phys. Rev. A **60**, R29 (1999).

[114] K. B. MacAdam, A. Steinbach, and C. Wieman, "A narrow-band tunable diode laser system with grating feedback, and a saturated absorption spectrometer for Cs and Rb," Am. J. Phys. **60**, 1098 (1992).

[115] D. P. Rhodes, "Experimental Studies of Cold Atom Guiding Using Hollow Light Beams," Phd thesis, University of St Andrews (2005).

[116] W. Demtröder, *Laser Spectroscopy* (Springer-Verlag, Berlin, Germany, 2002).

[117] I. Arakelyan, "Two Experiments with Cold Atoms: I. Application of Bessel Beams for Atom Optics, and II. Spectroscopic Measurements of Rydberg Blockade Effect," Phd thesis, University of Maryland (2010).

[118] W. T. Hill, III, N. Chattrapiban, I. V. Arakelyan, S. Mitra, and Y. Song, "All-optical manipulation of neutral atomic ensembles," Proc. SPIE - Int. Soc. Opt. Eng. (USA) **6644**, 664,411 (2007).

[119] L. Allen, M. Babiker, W. K. Lai, and V. E. Lembessis, "Atom dynamics in multiple Laguerre-Gaussian beams," Phys. Rev. A **54**, 4259 (1996).

[120] M. D. Feit, J. A. F. Jr., and A. Steiger, "Solution of the Schrodinger equation by a spectral method," J. Comp. Phys. **47**, 412 (1982).

[121] J. A. Fleck, Jr., J. R. Morris, and M. D. Feit, "Time-Dependent Propagation of High Energy Laser Beams through the Atmosphere," Appl. Phys. **10**, 129 (1976).

[122] D. S. Weiss, E. Riis, Y. Shevy, P. J. Ungar, and S. Chu, "Optical molasses and multilevel atoms: experiment," JOSA B **6**, 2072 (1989).

[123] Y. B. Ovchinnikov, I. Manek, A. I. Sidorov, G. Wasik, and R. Grimm, "Gravito-optical atom trap based on a conical hollow beam," Europhys. Lett **43**, 510–515 (1998).

[124] H. Perrin, A. Kuhn, I. Bouchoule, and C. Salomon, "Sideband cooling of neutral atoms in a far-detuned optical lattice," Europhys. Lett. **42**, 395 (1998).

[125] R. Dumke, M. Volk, T. Müther, F. B. J. Buchkremer, G. Birkl, and W. Ertmer, "Micro-optical realization of arrays of selectively addressable dipole traps: a scalable configuration for quantum computation with atomic qubits," Phys. Rev. Lett. **89**, 097,903 (2002).

[126] D. McGloin, G. C. Spalding, H. Melville, W. Sibbett, and K. Dholakia, "Applications of spatial light modulators in atom optics," Opt. Express **11**, 158 (2003).

[127] M. Schiffer, M. Rauner, S. Kuppens, M. Zinner, K. Sengstock, and W. Ertmer, "Guiding, focusing, and cooling of atoms in a strong dipole potential," Appl. Phys. B **67**, 705 (1998).

[128] S. Kuppens, M. Rauner, M. Schiffer, K. Sengstock, W. Ertmer, F. E. van Dorsselaer, and G. Nienhuis, "Polarization-gradient cooling in a strong doughnut-mode dipole potential," Phys. Rev. A **58**, 3068 (1998).

[129] J. Arlt, T. Hitomi, and K. Dholakia, "Atom guiding along Laguerre-Gaussian and Bessel light beams," Appl. Phys. B **71**, 549 (2000).

[130] J. Arlt, K. Dholakia, J.Soneson, and E. M. Wright, "Optical dipole traps and atomic waveguides based on Bessel light beams," Phys. Rev. A **63**, 063,602 (2001).

[131] C. O'Dwyer, G. Gay, B. V. de Lesegno, and J. Weiner, "Atomic nanolithography patterning of submicron features: writing an organic self-assembled monolayer with cold, bright Cs atom beams," Nanotechnology **16**, 1536 (2005).

[132] B. Rohwedder, "Resource letter AON-1: atom optics, a tool for nanofabrication," Am. J. Phys. **75**, 394 (2007).

[133] D. N. Matsukevich and A. Kuzmich, "Quantum State Transfer Between Matter and Light," Science **306**, 663 (2004).

[134] Z. Dutton and J. Ruostekoski, "Transfer and Storage of Vortex States in Light and MatterWaves," Phys. Rev. Lett. (2004).

[135] C. Ryu, M. F. Andersen, P. Clade, V. Natarajan, K. Helmerson, and W. D. Phillips, "Observation of persistent flow of a Bose-Einstein condensate in a toroidal trap," Phys. Rev. Lett. **99**, 260,401 (2007).

[136] A. Vaziri, G. Weihs, and A. Zeilinger, "Experimental Two-Photon, Three-Dimensional Entanglement for Quantum Communication," Phys. Rev. Lett. **89**, 240,401 (2002).

[137] D. N. Matsukevich, T. Chanelière, M. Bhattacharya, S.-Y. Lan, S. D. Jenkins, T. A. B. Kennedy, and A. Kuzmich, "Entanglement of a photon and a collective atomic excitation," Phys. Rev. Lett. **95**, 040,405 (2005).

[138] S. Franke-Arnold and A. S. Arnold, "Twisting light to trap atoms," Amer. Scientist **96**, 226 (2008).

[139] Z. Yan, "General thermal wavelength and its applications," Eur. J. Phys. **21**, 625 (2000).

[140] W. Guerin, J.-F. Riou, J. P. Gaebler, V. Josse, P. Bouyer, and A. Aspect, "Guided quasicontinuous atom laser," Phys. Rev. Lett. **97**, 200,402 (2006).

[141] A. Couvert, M. Jeppesen, T. Kawalec, G. Reinaudi, R. Mathevet, and D. Guéry-Odelin, "A quasi-monomode guided atom laser from an all-optical Bose-Einstein condensate," EPL **83**, 50,001 (2008).

[142] R. G. Dall, S. S. Hodgman, M. T. Johnsson, K. G. H. Baldwin, and A. G. Truscott, "Transverse mode imaging of guided matter waves," Phys. Rev. A **81**, 011,602(R) (2010).

[143] Private communications with Prof.M. Edwards with technical helps from J. Heward.

[144] A. S. Arnold, C. S. Garvie, and E. Riis, "Large magnetic storage ring for Bose-Einstein condensates," Phys. Rev. A **73**, 041,606(R) (2006).

[145] S. Gupta, K. W. Murch, K. L. Moore, T. P. Purdy, and D. M. Stamper-Kurn, "Bose-Einstein condensation in a circular waveguide," Phys. Rev. Lett. **95**, 143,201 (2005).

[146] J. E. Mooij, T. P. Orlando, L. Levitov, L. Tian, C. H. van der Wal, and S. Lloyd, "Josephson persistent-current qubit," Science **285**, 1036 (1999).

[147] C. H. vander Wal, A. C. J. ter Haar, F. K. Wilhelm, R. N. Schouten, C. J. P. M. Harmans, T. P. Orlando, S. Lloyd, and J. E. Mooij, "Quantum superposition of macroscopic persistent-current states," Science **290**, 773 (2000).

[148] L. Amico, A. Osterloh, and F. Cataliotti, "Quantum many particle systems in ring-shaped optical lattices," Phys. Rev. Lett. **95**, 063,201 (2005).

[149] A. R. Carter, M. Babiker, M. Al-Amri, and D. L. Andrews, "Generation of microscale current loops, atom rings, and cubic clusters using twisted optical molasses," Phys. Rev. A **73**, 021,401(R) (2006).

[150] S. E. Olson, M. L. Terraciano, M. Bashkansky, and F. K. Fatemi, "Cold-atom confinement in an all-optical dark ring trap," Phys. Rev. A **76**, 061,404(R) (2007).

[151] D. Jaksch and P. Zoller, "The cold atom Hubbard toolbox," Ann. Phys. **315**, 52 (2005).

[152] J. Ka and S. Shin, "Tunneling dynamics in a double-well: numerical studies with thermal wavepackets," J. Mol. Struc. (Theochem) **623**, 23 (2003).

[153] C. J. Pethick and H. Smith, *Bose-Einstein condensation in dilute gases* (Cambridge University Press, Cambridge, UK, 2002). ISBN 0-521-66580-9.

[154] S. Geltman and A. Bambini, "Triplet scattering lengths for Rubidium and their role in Bose-Einstein condensation," Phys. Rev. Lett. **86**, 3276 (2001).

[155] J. Javanainen and J. Ruostekoski, "Symbolic calculation in development of algorithms: split-step methods for the Gross-Pitaevskii equation," J. Phys. A: Math. Gen. **39** (2006).

[156] C. A. Regal, C. Ticknor, J. L. Bohn, and D. S. Jin, "Creation of ultracold molecules from a Fermi gas atoms," Nature **424**, 47 (2003).

[157] M. Greiner, C. A. Regal, and D. S. Jin, "Emergence of a molecular Bose-Einstein condensate from a Fermi gas," Nature **426**, 537 (2003).

[158] H. J. Metcalf and P. V. der Straten, *Laser cooling and trapping* (Springer-Verlag New York Inc., New York, New York, 2002). ISBN 0-387-98728-2.

[159] E. Arimondo, W. D. Phillips, and F. Strumia, *Proceedings of the International School of Physics (Enrico Fermi): Laser Manipulation of Atoms and Ions* (North-Holland, Elsevier Science Publishers B. V., Amsterdam, 1992). ISBN 0-444-89993-6.

[160] G. R. Fowles and G. L. Cassiday, *Analytical Mechanics* (Saunders College Publishing, Orlando, FL, 1993). ISBN 0-03-096022-3.

[161] Daniel A. Steck, "Rubidium 85 D Line Data," available online at `http://steck.us/alkalidata` (revision0.2,1 September 2008).

[162] Daniel A. Steck, "Rubidium 87 D Line Data," available online at `http://steck.us/alkalidata` (revision0.2,1 September 2008).

[163] J. J. Sakurai, *Modern Quantum Mechanics* (Addison-Wesley Publishing Company, Inc., New York, 1994). ISBN 0-201-53929-2.

[164] J. Allen, M. J. Padgett, and M. Babiker, *Progress in optics XXXIX edited by E. Wolf: The orbital angular momentum of light*, vol. XXXIX (Elsevier science B.V., Amsterdam, 1999). ISBN 0-444-50104-5.

[165] J. Allen, M. J. Padgett, and M. Babiker, *The orbital angular momentum of light*, p. 294 (Elsevier science B.V., Amsterdam, 1999).

[166] M. R. Teague, "Deterministic phase retrieval: a Green's function solution," J. Opt. Soc. Am **73**, 1434 (1983).

[167] P. Bauer, "The collisionless Boltzmann equation," (2004). The note was accessed online on 1/25/2007. The url no longer exists.

[168] C. Z. Cheng and G. Knorr, "The Integration of Vlasov Equation in Configuration Space," J. Comp. Phys. **22**, 330 (1976).

[169] T. Fujiwara, "Integration of the collisionless Boltzmann equation for spherical stellar systems," Publ. Astron. Soc. Japan **35**, 547 (1983).

[170] G. Manfredi and P.-A. Hervieux, "Vlasov simulations of electron dynamics in metallic nanostructures," Comp. Mat. Sci. **35**, 327 (2006).

[171] C. Kittel and H. Kroemer, *Thermal Physics* (W. H Freeman and Company, New York, 1998). ISBN 0-7167-1088-9.

[172] E. Zeek and M. Butterfield, `ff2c()` and `ifft2c()` are obtained from the MATLAB File Exchange repertoire available online at `http://www.mathworks.com/matlabcentral/fileexchange/` (revision 1.3, 18 April 2002), retrieved 9 September 2004.

[173] L. Balkay, the MATLAB function `histogram2d()` is obtained from the MATLAB File Exchange repertoire available online at `http://www.mathworks.com/ matlabcentral/ fileexchange/ 9896-2d-histogram- calculation`.

[174] J. M. Stone and M. L. Norman, "ZEUS-2D: A radiation magnetohydrodynamics code for astrophysical flows in two space dimensions: I. The hydrodynamic algorithms and tests," Astrophys. J. Suppl. **80** (1992).

[175] D. A. Clarke, "A consistent method of characteristics for multidimensional magnetohydrodynamics," Ap. J. **457**, 291 (1996).

[176] D. J. Tannor, *Introduction to quantum mechanics: a time-dependent perspective*, p. 193 (University Science Books, California, 2007).

[177] G. Baym, *Lectures on Quantum Mechanics*, p. 142 (Addison-Wesley Publishing Company, Redwood City, CA, 1994).